How Does Calcium Oscillate?

An Interdisciplinary Approach

DISSERTATION

zur Erlangung des akademischen Grades
doctor rerum naturalium
(Dr. rer. nat.)
im Fach Biologie

eingereicht an der
Mathematisch-Naturwissenschaftlichen Fakultät I
Humboldt-Universität zu Berlin

von
Herr Dipl.-Phys. Alexander Skupin
geboren am 7.5.1976 in Braunschweig

Präsident der Humboldt-Universität zu Berlin:
Prof. Dr. Dr. h.c. Christoph Markschies

Dekan der Mathematisch-Naturwissenschaftlichen Fakultät I:
Prof. Dr. rer. nat. Lutz-Helmut Schön

Gutachter:

1. Prof. Dr. H. Herzel
2. Priv.-Doz. Dr. M. Falcke
3. Prof. Dr. C.W. Taylor

eingereicht am:	15. Januar 2009
Tag der mündlichen Prüfung:	3. Juni 2009

Abstract

Ca^{2+} is the most important second messenger in living cells serving as a critical link between a variety of extracellular stimuli and their intra- and intercellular responses. The external signals are translated most often into repeated increases of the cytosolic Ca^{2+} concentration. Due to their importance and frequent appearance, Ca^{2+} oscillations have been extensively studied in experiments and most of the involved physiological elements are identified. Despite this knowledge, the link between these microscopic elements and the cellular dynamics is only vaguely understood.

An important mechanism for generating cytosolic Ca^{2+} transients is Ca^{2+} release by channels from internal storage compartments, mainly from the endoplasmic reticulum and the sacroplasmic reticulum. A common channel type present in many cells is the inositol 1,4,5-trisphosphate receptor (IP_3R) which opens and closes randomly in dependence on binding and dissociation of IP_3 and Ca^{2+}. The open probability of IP_3R exhibits a nonlinear dependence on the cytosolic Ca^{2+} concentration leading to Ca^{2+} induced Ca^{2+} release, the key element of Ca^{2+} signaling. An initial opening of a single channel increases the open probability of adjacent channels, and Ca^{2+} release spreads throughout the whole cell until channel inhibition caused by high Ca^{2+} concentrations terminates the release.

This work uses an interdisciplinary approach combining experimental techniques from biology, analytical tools from theoretical physics and computer simulations to clarify the question of the oscillation mechanism and how cells can generate globally coordinated Ca^{2+} signals originated from local stochastic channel dynamics. In this context, the spatial inhomogeneous distribution of IP_3Rs, forming channel clusters which are separated by 1-7 µm, plays a key role. Together with Ca^{2+} pumps, this induces huge concentration gradients close to open clusters, leading to a hierarchical organization of Ca^{2+} signals. In combination with the random behavior of single IP_3Rs, this might generate a stochastic medium, which is known from pattern formation.

Starting from this knowledge, Ca^{2+} oscillations are predicted to be stochastic as well as to consist of repetitive wave nucleation and hence to have a spatial character. This hypothesis is justified experimentally in the first part of this thesis by analyzing Ca^{2+} oscillations of four different cell types in terms of their mean periods and standard deviations exhibiting a linear dependence. Hence, Ca^{2+} signaling constructively uses thermal noise to build global signals. Thereby the molecular fluctuations are carried on the level of the cell by the hierarchical signaling structure rendering Ca^{2+} oscillations stochastic. This contradicts the current opinion of the last decades of Ca^{2+} being a representative cellular oscillator. Moreover, this makes Ca^{2+} a first natural example of array enhanced coherent resonance, a phenomenon theoretically predicted by statistical physics. The knowledge of the oscillation mechanism allows

as well for determination of intrinsic cell properties by global observations. To illuminate the structure of the signaling mechanism, the data are also analyzed with respect to information processing.

Furthermore, the temperature dependence of Ca^{2+} signaling in astrocytes is analyzed experimentally. The findings show that the reported difference between cultured astrocytes and astrocytes in acute brain slices are mainly caused by the different temperatures at which cells are used to be measured. This leads again to a more general interrogation as to how temperature is recognized. Are the decreased Ca^{2+} signals at higher temperature caused by an increased pump activity and hence spatially controlled or does temperature mainly change local properties like the channel dynamics?

In the modeling part of this work, a physiological model for intracellular Ca^{2+} dynamics in three spatial dimensions is developed that takes the spatial arrangement of cells seriously. In contrast to most models of Ca^{2+} dynamics using ordinary differential equations, it uses a detailed channel model for the discrete release sites and takes into account diffusion and buffer interaction of Ca^{2+}. The model is based on separation of the two involved length scales. On the microscopic scale, the IP_3Rs are described by Markov chains, the dynamics of which depend on the local Ca^{2+} concentration. The Ca^{2+} concentration is determined on its part by the channel states acting as source terms of the corresponding reaction diffusion system (RDS) describing the macroscopic scale. The two model segments are coupled by a hybrid version of a Gillespie algorithm.

For an efficient simulation tool, the RDS is linearized and solved analytically by a three component Green's functions describing cytosolic free Ca^{2+}, mobile and immobile Ca^{2+} buffers, respectively. The linear RDS allows for an elegant parallel algorithm enabling detailed physiological simulation of intracellular Ca^{2+} dynamics. In dependence on physiological motivated parameters, the developed *Green's cell algorithm* generates in a natural way the whole spectrum of experimentally known Ca^{2+} signals and fits the experimental data of the first part in an almost perfect manner.Thus, the temperature dependence of astrocytic Ca^{2+} signals are in line with an increased pump activity and highlights once more the spatial character of Ca^{2+} signaling. In simulations that go beyond the experimental possibilities, the role of IP_3R clustering in Ca^{2+} signaling is studied and the influence of intrinsic channel properties on Ca^{2+} signals is analyzed. These investigations may lead to the design of new experiments.

Although this work is inspired by Ca^{2+} dynamics, the general concept how cells can generate predictable behavior from noisy molecular properties may also hold for other signaling pathways, especially for those exhibiting spatial concentration gradients as well, such as cyclic adenosine monophosphate (cAMP). Moreover, the derived methods and modeling tools can be used in other scientific disciplines, too.

Zusammenfassung

Ca^{2+} ist der wichtigste intrazelluläre Botenstoff, der extrazelluläre Signale in intrazelluläre Antworten übersetzt. Meistens werden die externen Signale in wiederholte Anstiege der zytosolischen Kalziumkonzentration übersetzt. Wegen ihres häufigen Auftretens und ihrer elementaren physiologischen Bedeutung sind diese Kalziumoszillationen intensiv experimentell untersucht und die meisten involvierten physiologischen Elemente charakterisiert worden. Trotz dieses umfangreichen Wissens ist der Zusammenhang zwischen dem mikroskopischen Verhalten und der zellulären Dynamik nur unzureichend verstanden.

Zytosolische Ca^{2+}–Transienten werden oft durch Ca^{2+}–Freisetzung aus intrazellulären Speichern, hauptsächlich aus dem sakroplasmatischen und dem endoplasmatischen Retikulum, mittels Membrankanälen generiert. Ein weit verbreiteter Kanaltyp ist der Inositol-1,4,5-trisphosphate Rezeptor (IP_3R), der in Abhängigkeit von gebundenem Ca^{2+} und IP_3 zufällig öffnet und schließt. Das Schlüsselelement des Ca^{2+}–Signalweges ist die nicht linear von der zytosolischen Ca^{2+}–Konzentration abhängende Öffnungwahrscheinlichkeit des IP_3R, die zu Ca^{2+} induziertem Ca^{2+}–Einfluss führt. Dabei wird durch das Öffnen eines einzelnen Kanals die Kalziumkonzentration und damit die Öffnungswahrscheinlichkeit an benachbarten Kanälen erhöht, wodurch in der gesamten Zelle Ca^{2+} ins Zytosol eintritt.

Diese interdisziplinäre Arbeit kombiniert biologische Experimente, analytische Methoden der theoretischen Physik und Computersimulationen, um den Oszillationsmechanismus zu charakterisieren und die offene Frage zu klären, wie Zellen aus lokal stochastischem Kanalverhalten zellweit koordinierte Signale generieren können. Von wesentlicher Bedeutung ist dabei die räumlich inhomogene Verteilung der IP_3Rs, die Kanalcluster mit Abständen zwischen 1-7 μm bilden. Dies induziert zusammen mit den Ca^{2+}–Pumpen große Konzentrationsgradienten in der Nähe von offenen Kanalclustern, was zu einer hierarchischen Organisation von Ca^{2+}–Signalen führt. In Kombination mit dem stochastischen Verhalten einzelner IP_3Rs wird diese Hierarchie ein stochastisches Medium generieren, das aus der Theorie der Musterbildung bekannt ist.

Unter diesem Gesichtspunkt erwartet man, dass Ca^{2+}–Oszillationen stochastisch sind und aus wiederholter Wellennukleation hervorgehen, was ihnen einen räumlichen Aspekt gibt. Diese Hypothese wird im ersten Teil dieser Arbeit experimentell verifiziert, indem Ca^{2+}–Oszillationen vier verschiedener Zellarten bezüglich ihrer mittleren Periode und Standardabweichungen analysiert werden. Die gefundenen linearen Abhängigkeiten der beiden Oszillationscharakteristika zeigen, dass der Ca^{2+}–Signalweg thermisches Rauschen konstruktiv dazu verwendet, globale Signale zu

bilden. Dabei werden die molekularen Fluktuationen durch die hierarchische Signalstruktur auf die zelluläre Ebene gehoben, was Ca^{2+}–Oszillationen einen stochastischen Charakter verleiht. Dies steht im Gegensatz zu der jahrzehntelang weitläufigen Auffassung, dass Ca^{2+} ein repräsentatives Beispiel eines zellulären Oszillators ist. Des weiteren macht dieses Ergebnis Ca^{2+} zu einem ersten natürlichen Beispiel für "array enhanced coherent resonance", einem Phänomen, das theoretisch in der statistischen Physik vorhergesagt worden ist. Die Kenntnis des Oszillationsmechanismus' ermöglicht das Abschätzen intrinsischer Zelleigenschaften aus globalen Beobachtungen. Um mögliche Strukturprinzipien zu beleuchten, werden die Daten auch aus dem Blickwinkel der Informationsverarbeitung betrachtet.

Außerdem wird die Temperaturabhängigkeit von Ca^{2+}–Signalen in Astrozyten experimentell untersucht. Die Ergebnisse zeigen, dass die berichteten Unterschiede zwischen Astrozyten in Kultur und in akuten Gehirnschnitten hauptsächlich durch die verschiedenen Temperaturen, bei denen die Zellen gewöhnlich gemessen werden, bedingt sind. Das führt wiederum zu der allgemeineren Frage, wie die Temperatur detektiert wird. Sind die verringerten Ca^{2+}–Signale bei höheren Temperaturen durch eine höhere Pumpaktivität bedingt und damit ein räumliches Phänomen oder modifiziert Temperatur eher lokale Eigenschaften wie die Kanaldynamik?

Im Modellierungsteil dieser Arbeit wird ein physiologisches Modell für die intrazelluläre Ca^{2+}–Dynamik entwickelt, das die dreidimensionale Struktur von Zellen berücksichtigt. Das Modell beinhaltet im Gegensatz zu den üblichen Modellen, die gewöhnlich Differentialgleichungen verwenden, sowohl die Wechselwirkung mit Puffern als auch die Diffusion von Ca^{2+} und verwendet eine mikroskopische Kanaldynamik. Das entwickelte Zellmodell basiert auf der Separierung der beiden beteiligten Längenskalen. Auf der mikroskopischen Längenskala werden die IP_3Rs durch Markovketten beschrieben, deren Dynamik von den lokalen Ca^{2+}–Konzentrationen abhängt. Die Ca^{2+}–Konzentration wird ihrerseits durch die Kanalzustände bestimmt, die als Quellterme in einem Reaktions–Diffusions–System (RDS) wirken, das die makroskopische Längenskala beschreibt. Die beiden Modellsegmente werden durch eine hybride Version des Gillespiealgorithmus' gekoppelt.

Um ein effizientes Modellierungsprogramm zu entwickeln, wird das RDS linearisiert und mittels einer drei komponentigen Green's Funktion, die freies zytosolisches Ca^{2+}, mobilen Puffer und inmobilen Puffer beschreibt, analytisch gelöst. Das lineare RDS ermöglicht einen eleganten parallelen Algorithmus zur detaillierten Modellierung physiologischer Ca^{2+}–Dynamik. Der implementierte *Green's cell algorithmus* generiert auf natürliche Art und Weise in Abhängigkeit von physiologischen Parametern das gesamte Spektrum der experimentell bekannten Ca^{2+}–Signale und spiegelt die experimentellen Daten des ersten Teils in nahezu perfekter Weise wider. Die experimentell gefundene Temperaturabhängigkeit der Ca^{2+}–Signale kann beispielsweise in den Simulationen mit einer gesteigerten Pumpaktivität erklärt werden, was erneut den räumlichen Aspekt des Ca^{2+}–Signalweges unterstreicht. In Simulatio-

nen, die über die experimentellen Möglichkeiten hinaus gehen, wird die Rolle der IP_3R–Clusterbildung untersucht und der Einfluss intrinsischer Kanaleigenschaften analysiert.

Auch wenn diese Arbeit von der intrazellularen Ca^{2+}–Dynamik inspiriert ist, wird das generelle Konzept, wie Zellen aus verrauschter molekularer Dynamik koordinierte Signale generieren, ebenso für andere Signalpfade gelten, besonders für solche, die auch räumliche Konzentrationsgradienten aufweisen, wie zum Beispiel zyklisches Anedosinmonophosphat (cAMP). Außerdem können die hier entwickelten Methoden und das Modellierungsprogramm in anderen wissenschaftlichen Bereichen von Nutzen sein.

Contents

List of Figures

Abbreviations

Abbreviations	Explanation
AECR	Array enhanced coherent resonance
ATP	Adenosine tri-phosphate
BAPTA	Bis-(o-aminophenoxy) ethane-tetraacetic acid
$[Ca^{2+}]_0$	Cytosolic Ca^{2+} base level
$[Ca^{2+}]_i$	Intracellular Ca^{2+} concentration
CaM	Calmodulin
cAMP	Cyclic adenosine monophosphate
CCh	Carbamyl choline
CICR	Calcium induced calcium release
CV	Coefficient of variation
DAG	Diacylglycerol
DKM	DeYoung-Keizer model
EGTA	Ethylen glycol-bis(2-aminoethylether)-tetraacetic acid
ER	Endoplasmic reticulum
FES	Finite element solver
FHN	FitzHugh-Nagumo
GCA	Green's cell algorithm
GCM	Green's cell model
GFP	Green fluorescent protein
GPCR	G-protein coupled receptor
HEK cells	Human embryonic kidney cells
HEPES	4-(2-Hydroxyethyl)-1-piperazine(2-ethanesulphonic) acid
IP_2	Inosistol 1,4-biphosphate
IP_3	Inositol 1,4,5-trisphosphate
$[IP_3]$	Inositol 1,4,5-trisphosphate concentration
IP_4	Inosistol 1,3,4,5-tetrakisphosphate
IP_3R	Inositol 1,4,5-trisphosphate receptor
ISI	Interspike interval
LTD	Long-term depression
LTP	Long-term potentiation

Abbreviations	Explanation
MPI	Message passing interface
NAADP	Nicotinic acid adenine dinucleotide phosphate
NCX	$Na^+ - Ca^{2+}$ exchanger
NO	Nitric oxide
ODE	Ordinary differential equation
P_0	Stationary open probability
PDE	Partial differential equation
PIP_2	Phosphatidylinosistol 4,5-biphosphate
PKA	Protein kinase A
PKB	Protein kinase B
PKC	Protein kinase C
PLA cells	Processed lipoaspirate cells
PLC	Phospholipase C
PM	Plasma membrane
PMCA	Plasma membrane calcium ATPase
PMCC	Plasma membrane calcium channel
RDS	Reaction diffusion system
ROC	Receptor-operated channel
RT	Room temperature
RTK	Receptor tyrosin kinases
RyR	Ryanodine receptor
SCC	Serial correlation coefficient
s.e.	Standard error or standard deviation of the mean
SERCA	Sacro-endoplasmic reticulum ATPases
SNOG	S-nitrosoglutathione
SR	Sacroplasmic reticulum
SW	Spike width
VOC	Voltage-operated channel

Chapter 1

Introduction

"Biology will be to the 21st Century what physics and chemistry were to this century."

John Naisbitt, American forecaster, 1992

Its scorching development within the last decades makes biology today the most exciting discipline in science. New experimental methods allow deep insights into life on both a molecular level as e.g. by real time Polymerase Chain Reaction and a mesoscopic scale, on which for instance brain activity can be measured by Magnetic Resonance Imaging techniques. The recently completed decoding of the human genome marks a milestone in this successful story. But at the same time it unbosoms the challenge biology faces: To extract from an enormous amount of data the underlying mechanisms that nature uses to perform versatile tasks. The example of the Human Genome Project illustrates further, that the fundamental principles probably have a structural character. Considering the high complexity of the human organism the number of 30,000 to 40,000 genes identified in the human genome is amazingly small compared e.g. with 26,000 genes found in the flower arabidopsis. This discrepancy can be solved by assuming complex control mechanisms of the involved elements leading to a highly developed system.

To understand these complex systems the approach of "systems biology" had its breakthrough at the millennium. Systems biology tries to help understanding biological processes at the level of systems. The roots of systems biology go back to the beginning of the last century. The Lotka-Volterra equations derived in 1931 to describe predator-prey dynamics can be seen as a first systematical approach in ecology. Also Erwin Schrödinger tried in his book *"What is life?"* [201] to put biology on to a basis of physically motivated principles. A first successful application of systems biology was the mathematical description of neuronal action potentials by Alan Lloyd Hodgkin and Andrew Huxley in 1952.

According to Kitano [105], systems biology focuses today on the four key characteristics and their related questions of biological systems:

- **Systems structure:** What are the biological components and their structural relation ships?
- **Systems dynamics:** How does the system behave under different internal and external conditions?
- **Systems control:** What are the relevant control mechanisms?
- **Design principles:** How does the structure rule to the dynamics and what might be the fundamental reasons for that organization?

Due to the complexity of biological processes an easy and linear answer to these questions is in general far out of reach. Thus systems biology relies on an iterative process of knowledge generation depicted in Figure 1.1. It starts from the biological phenomenon mostly given in a purely qualitative manner. As a next step, this phenomenon must be quantified by experiments, e.g. due to different stimuli, chemical manipulations or knockout experiments. These data can be used to build a first mathematical model from which hypotheses of the process can be drawn. This is the starting point of the iterative knowledge generation. The model must be tested on the one hand by *in vivo* and *in vitro* experiments, leading to new experimental data and possibly new hypotheses and on the other hand, the model can be studied theoretically by analytical techniques or computer simulations, which correspond to *in silico* experiments. By repeated adjustment of these two parallel investigations, the hypotheses or the model will be refined, leading to a deeper understanding of the corresponding system.

This interplay between experiment and theory was extensively used in physics and chemistry during the last century and has led to a deep understanding of dead matter. As biology is the complex interplay of these two sciences, a systematical analysis of biological processes needs an interdisciplinary approach of biology, physics, chemistry, mathematics and computer science, connecting their knowledge, methods and communities. Additionally, the pure scientific disciplines may profit from that exchange, as new methods within the biological context may have an impact on other research areas, too.

Within this framework the present work is located at the border between biology and physics using methods from chemistry, mathematics and informatics. From a physical point of view the time evolution of a macroscopic system in thermal equilibrium is determined by the thermodynamic laws, energy conservation and the fundamental principle of irreversibility leading to a clearly predictable behavior in the thermodynamic equilibrium. But biological systems are open systems far away

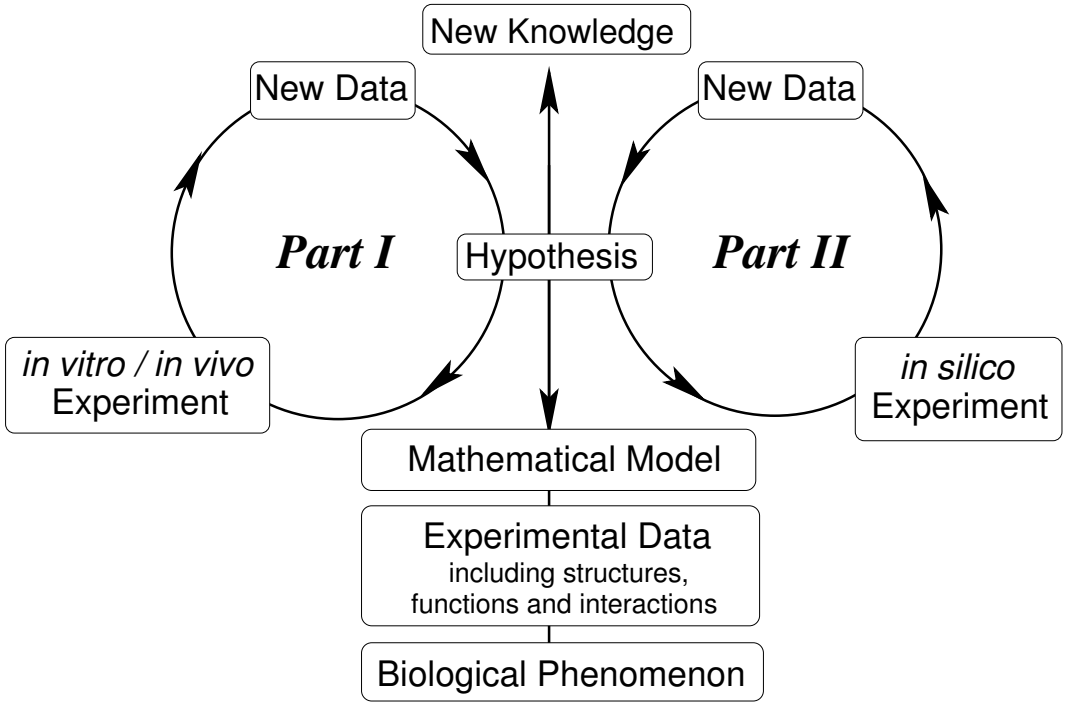

Figure 1.1: The process of knowledge generation in systems biology. Starting from the physiological phenomenon and a first mathematical model the knowledge is increased by both, theoretical investigations and experimental studies and the adjustments between them. This work uses both, the *in vitro* loop in Part I and the *in silico* loop in Part II (Figure inspired by [70]).

from equilibrium and often exhibit nonlinear properties. The nonlinearities enable complex control mechanisms, since small changes in the amplitude of a perturbation can lead to dramatic changes in the system's response. Far from equilibrium nonlinearities lead to symmetry breaking, multi-stability and feedback loops facilitating a versatile dynamical behavior and complexity. These are the mechanisms of evolution and life [158, 89, 55].

Nonlinearities are essential for cell communication and particularly for cell signaling [103]. An important example of a nonlinear property is excitability, the mechanism well known in the description of neurons. A neuron integrates signals coming from surrounding neurons with its axon hill. If the integrated signal exceeds a threshold, the neuron will fire an action potential that can be detected by other neurons. A key element for the biological excitability are membranes. Together with ion transporters they allow for concentration differences between distinct parts of a cell or between the interior and the extracellular space and are thus means to keep cells far away from the thermodynamic equilibrium.

Cell signals are often transmitted by specific molecules, e.g. neurotransmitters or hormones. They can bind to corresponding receptors in the plasma membrane. Such a signal leads to intracellular signalling pathways, which exhibit amplification by excitability, feedback loops and interactions with other pathways and represent complex regulatory mechanisms that control the behavior of individual cells and entire organisms.

Thus, a detailed understanding of signaling pathways is essential to explain the characteristics of biological systems. The molecular origin of cell signaling given by the stochastic binding of agonists to receptors as well as fluctuations of the environment lead to intrinsic and extrinsic noise in biological processes. Due to the nonlinear properties these fluctuations may have a large influence on the dynamics. In Neuroscience noise has become an accepted element to describe neuronal dynamics and it has been shown that noise is essential for the function of the nervous system [269, 268]. Within most other areas of biology noise is still neglected and is assumed to be averaged out by the large number of involved molecules. Especially control mechanisms as signaling pathways are treated deterministically according to current paradigms of systems biology.

Within this work we investigate the Ca^{2+} signaling pathway, which is the most predominant intracellular pathway. We will focus on the dynamic structure of the Ca^{2+} signaling network and only briefly introduce its physiological function in Chapter 2. Due to its importance and frequent appearance, Ca^{2+} signaling has been under scientific investigation for about 130 years now leading to a profound knowledge of biological elements involved. Together with the rich spectrum of dynamical behavior, which this pathway shows, this has led to a zoo of different modeling approaches. Most of them use a top-down approach explaining the experimental data by heuristic models. These models can describe the dynamics from a bird's-eye view, but do not resolve the microscopic level, i.e. the molecular behavior. But this is exactly the scale, where cell signalling is happening. Therefore we are interested in a bottom-up approach, where the cellular dynamics originates from the microscopic properties of specific proteins.

Thanks to preliminary experimental and theoretical results the following investigation starts at the level of the hypotheses within the picture 1.1 of the knowledge generation in systems biology. To answer the question of our bottom-up approach, as to how the molecular properties influence the cellular dynamics, we will go into both cycles of Figure 1.1, in the experimental (*in vitro*) and in the theoretical (*in silico*) one and compare their results.

This work elucidates new results in relation to Ca^{2+} signaling in experimental and theoretical fashions. We focus on the questions:

(i) *How are random molecular events orchestrated into reliable cellular behavior?*

(ii) *What are the possible design principles and consequences of the underlying*

mechanism?

(iii) *How do we have to model systems exhibiting spatial gradients including Ca^{2+} dynamics?*

We will start in Part I with the experimental investigation and use its outcome to build a physiological bottom-up model in Part II, the results of which can be compared to the experimental findings.

In accordance with Kitano [105] we begin with the systems structure in Chapter 2 with a brief overview of intracellular Ca^{2+} signaling, where we introduce the physiological elements known to be involved in Ca^{2+} dynamics together with a short compendium of models developed so far. Different approaches of how cells can transform molecular fluctuations into more regular global signals are discussed and lead to our hypotheses. To clarify the kind of mechanism we start with some experimental investigations in Part I.

In Chapter 3 we introduce our experimental materials and methods including a brief description of the different cell types used in experiments. In addition, both the experimental data generation as well as the theoretical tools to analyze them are described. For the latter we give a brief overview of how stochastic processes can be characterized and what are reasonable quantities for experimental data.

With these methods we will analyze the calcium oscillations of four different cell types in Chapter 4, where we start with some general theoretical hypotheses motivated by the physiological facts given in Chapter 2. The results are discussed on a single cell level as well as in a cell population manner using methods from information theory and stochastic dynamics.

While the previous chapter had a quite general approach we focus in Chapter 5 on a more specific one. Here we try to understand the role of temperature in Ca^{2+} signaling within astrocytes and its implication in Neuroscience. We see, that the difference observed between Ca^{2+} signals in cultured cells and in cells from acute brain slices are mainly due to the different temperatures at which cells are normally measured. During the experiments the question arose as to whether the temperature dependence is caused by biochemistry (namely due to nitric oxid signaling) or has a more structural character, since pumps work faster at higher temperatures and therefore might abolish global signals.

The experimental results have clearly shown that Ca^{2+} signaling is a spatial phenomenon in smaller cells too and that the local stochastic behavior of channels determines the global behavior of cells. Thus modeling must be spatially resolved and must take the stochastic character of channels into account. For that reason we develop in Chapter 6 an adequate model for Ca^{2+} signaling in three dimensions by means of Green's functions for the cellular dynamics, which is coupled by a Gillespie algorithm to a detailed model of the release channels. Altogether this leads to a reasonably physiological model for the intracellular Ca^{2+} dynamics.

The model is used in Chapter 7 to perform cell specific simulations. We simulate the experimental results from the first part and can verify the results found in Chapter 4 and even illuminate the reason for the temperature dependence found in Chapter 5. Another application that goes beyond the experimental possibilities is the analysis of different channel arrangements and how the intrinsic channel properties effect global signals.

This work uses Ca^{2+} dynamics as an representative example of an intracellular signaling pathway but the fundamental results how cells produce global signals from molecular fluctuations can be generalized to other cellular processes like cyclic adenosine monophosphate (cAMP) signaling [282, 118, 254, 271, 102]. Even the physical approach how to deduce microscopic processes from global signals by tools from statistical physics may inspire future experimental studies.

From a physical point of view the findings are fascinating since we observe the constructive use of noise in an excitable and spatially extended system. Thus, global signals are orchestrated by the interplay of microscopic fluctuations and the spatial inhomogeneity. Stochasticity and excitability are common features in many nonlinear physical systems far away from thermodynamic equilibrium ranging from lasers and chemical reactions to climate and neuron dynamics. In this sense the derived analysis methods and the developed modeling tool are not restricted to Ca^{2+} signaling but might also be used in other frameworks.

Chapter 2

Calcium signaling

The first evidence of a physiological function of Ca^{2+} was reported by Sidney Ringer in 1883 [33]. He studied the contractions of isolated rat hearts in a saline medium for which he used the hard London tap water. After replacing the tap water with distilled water the beautiful contractions became progressively weaker and finally stopped after 20 minutes. Ringer found out that he could re-evoke these contractions by adding Ca^{2+} salts to the medium. By then Ca^{2+} was considered exclusively as a structural element needed for bones and teeth. The accidental finding gave Ca^{2+} a completely novel function: It carried the signal for heart contraction. Unexpectedly this pioneering observation did not cause wide interest, and it took about 60 years until K. Bailey explained the Ca^{2+} dependent contraction of muscle fibers by the ATPase activity of myosin caused by Ca^{2+} liberation nearby. From this time on the interest in the signaling role of Ca^{2+} increased. An important contribution in this context was the development of Ca^{2+} chelators and Ca^{2+} sensitive fluorescent dyes that make possible a variety of experiments illuminating the predominant role of Ca^{2+} in cell signaling.

Thus we know today that Ca^{2+} is the most important second messenger in living cells, serving as a critical link between extracellular signals and intracellular responses. The influence ranges from bacteria to highly specialized cells and occurs at every stage of cell life. Although a complete representation would go beyond the scope of this work we will give a short overview of the fascinating versatility of Ca^{2+} signaling without the claim of completeness in the next section. Afterwards we will compile the functional elements known today to take part in Ca^{2+} signaling and investigate the physiology of cells. The question will arise as to how Ca^{2+} signals occur and how we can understand and interpret them. This work will contribute to casting a light on that issue.

2.1 Calcium in physiology

Ca^{2+} comes into the game of life at the very beginning: If a spermatozoa enters an egg, a Ca^{2+} wave is initiated that runs through the egg starting a variety of processes. Among others a membrane detaches from the egg and isolates it from the environment to prevent another fertilization [4]. In the next step cell profileration and differentiation connected with gene regulation occur, which are again controlled by calcium [120, 51].

Dolmetsch and coworkers have shown in experiments with T cells that Ca^{2+} determines the expression level of interleukin 2 (IL2) and some transcription factors such as NFκB. In their experiments they were able to force cells to oscillate with different frequencies by changing the suspending medium. Cells were superfused with a medium containing the Ca^{2+} chelator Ethylene glycol-bis(2-aminoethylether)-tetraacetic acid (EGTA), that suppresses intracellular Ca^{2+} signals (for reasons we will explain in Chapter 4). They switched to a medium with a high Ca^{2+} concentration inducing a transient Ca^{2+} signal within the cell by using a computer controlled valve. They analyzed the cells with respect to the level of IL2 and transcription factors, from which they determined the corresponding gene expression. They found that faster oscillations increase gene expression and that oscillations have an amplifying effect. For the latter result they performed a control experiment, in which cells were exposed to a constant Ca^{2+} concentration that corresponds to the average concentration of the oscillation experiment. They found an expression level up to eight times higher in cells with the oscillatory behavior than in cells with a corresponding constant Ca^{2+} concentration.

As another example of the functional role of Ca^{2+}, we may invoke its influence on synaptic plasticity, the mechanism of memory. A synapse connects two neurons representing the smallest structural unit in information processing in the brain. Organisms can deal with different tasks due to specific wiring of neurons. One important feature is adaptation of behavior according to the environment, i.e. learning and memory. The latter is explained by the change of the synaptic transmission strength resulting from the interplay of long-term potentiation (LTP) and long-term depression (LTD). LTP is the prolonged increase in transmission efficiency induced by high frequency stimulation of the synapse. LTD is caused by short activation of an excitatory pathway leading to a sustained decrease in synaptic transmission. Experiments have shown that Ca^{2+} influences both, LTP and LTD in dependence on the magnitude of the transient Ca^{2+} signal. Things become even more complicated as neurons are not isolated but are embedded in an environment of glia cells, of which astrocytes are the predominant part. These are non excitable cells that exhibit intra and intercellular Ca^{2+} signals by which they are bidirectionally coupled to neurons. We will come to this point later in Section 3.2.

Ca^{2+} is a major control element also at the end of a cells life. Apoptosis is accompanied by Ca^{2+} signals [161]. Altogether this has led to the paradigm of Ca^{2+} being a life and death signal [17].

2.2 Ca^{2+} signals

The universality of Ca^{2+} signaling is astonishing, as Ca^{2+} is an obviously simple bivalent cation that can control very specific tasks. The reason for the universality of Ca^{2+} signaling is its versatility. Cells can specify the meaning of Ca^{2+} signals by the choice of plasma membrane receptors inheriting Ca^{2+} signals and the target molecules of these signals. Additionally cells can create different spatio-temporal signals by their distinct components and the combination of those [18, 25]. Most often, the Ca^{2+} driven processes are initiated by the increase of the intracellular free Ca^{2+} concentration from a resting level of the order of tens of nM. Some Ca^{2+} sensitive processes, such as muscle contraction, need a rapid and localized Ca^{2+} signal with high amplitudes, whereas other processes require prolonged and more global signals.

The targets of Ca^{2+} signals are mostly Ca^{2+}-binding proteins. Some of them such as paravalbunim, act as Ca^{2+} buffers and absorb most of the free Ca^{2+} and shape the amplitude and the duration of Ca^{2+} transients as well as minimizing toxic effects [161]. Other proteins like calmodulin (CaM) and calcinerin have a downstream character, i.e. they decode the information carried by the Ca^{2+} signal and pass it on to targets. This is achieved by a conformational change after Ca^{2+} binding which allows for the function as a committed separate subunit of a single enzyme or as a subunit that is associated reversibly with different proteins. CaM for instance becomes more hydrophobic after Ca^{2+} binding and can then react with the binding domain of a skeletal muscle myosin light chain kinase that induces muscle contraction and explains Ringer's experiment mentioned above on a molecular level.

The cytosolic Ca^{2+} signals must be contemplated within the context of the toxic effect of Ca^{2+} on many proteins and other functional elements. Prolonged high cytosolic Ca^{2+} levels can lead to necrosis and apoptosis [161], the two types of cell death. Therefore Ca^{2+} waves and oscillations, i.e. repeated transients of the cytosolic Ca^{2+} concentrations are common ways to translate external signals into cellular responses, as they expose the cell only briefly to high Ca^{2+} concentrations. As we have seen from the example of gene expression, Ca^{2+} signaling is often frequency encoded, i.e. different external signals are encoded in different oscillation periods and sometimes in variable amplitudes. Two experimental examples of Ca^{2+} spiking are shown in Figure 2.1.

The Ca^{2+} spikes occur by repeated increase of the cytosolic Ca^{2+} concentration and a subsequent removal of Ca^{2+} as depicted in Figure 2.2. The increase might be

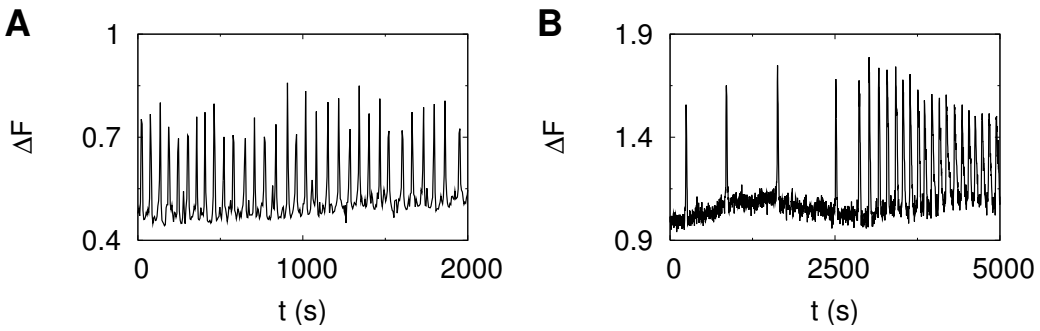

Figure 2.1: Representative examples of cytosolic Ca^{2+} oscillations in a stimulated HEK cell (**A**), and spontaneous oscillation in a PLA cell (**B**), where ΔF is the fluorescent signal corresponding to the cytosolic Ca^{2+} concentration. See Chapter 3 for more details. The spontaneous signal suddenly changes its behavior which is a typical evidence for apoptosis.

caused by Ca^{2+} entry from the extracellular space, where the typical concentrations are in the order of mM and thus three to four orders of magnitude higher than the cytosolic resting concentration which is in the range of tens of nM. Another possibility to increase the cytosolic Ca^{2+} concentration is the release from intracellular stores by channels, especially from the endoplasmic reticulum (ER) and its counterpart in muscle cells, the sarcoplasmic reticulum (SR), where typical concentrations are also in the mM range. Cells have several mechanisms of Ca^{2+} extrusion.

2.2.1 Ca^{2+} extrusion

Corresponding to the Ca^{2+} increase, cells extrude Ca^{2+} into the extracellular space as well as into the internal stores. They have active transporters using Adenosine tri-phosphate (ATP) to remove Ca^{2+} actively into the extracellular space by plasma membrane Ca^{2+}-ATPases (PMCAs) and into the intracellular stores by Sacro-endoplasmic reticulum ATPases (SERCAs) [197]. Besides these two main Ca^{2+} transporters cells have additionally Na^+/Ca^{2+} exchangers (NCX) located in the plasma membrane. The bidirectional NCX works in dependence on the Ca^{2+} and Na^+ gradients across the membrane. In its forward mode it transports one Ca^{2+} ion out and lets three Na^+ ions in. The NCX primarily plays a role in heart cells and neurons. Another internal Ca^{2+} extrusion element is mitochondria. They can take up Ca^{2+} by the mitochondrial Ca^{2+} unitransporter (MCU) and can shape Ca^{2+} signals [64, 191].

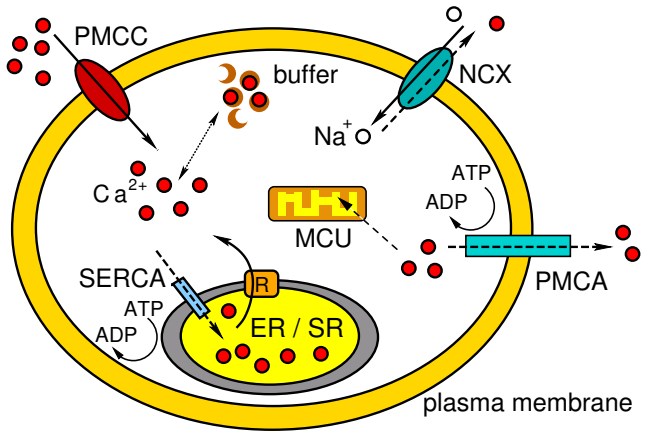

Figure 2.2: Scheme of main Ca^{2+} fluxes within cells, where solid arrows correspond to cytosolic influx and dashed arrows to efflux, respectively. Ca^{2+} can enter the cytosol by plasma-membrane Ca^{2+} channels (PMCC) (dark red) from the extracellular space or from internal stores (ER resp. SR) by receptor channels (R) located in the ER/SR membrane. Ca^{2+} extrusion occurs through the membrane by plasma-membrane Ca^{2+} ATPases (PMCA) or sodium-Ca^{2+} exchangers (NCX). Ca^{2+} uptake into the internal stores is done by SERCA pumps. In addition Ca^{2+} is taken up by mitochondria due to their mitochondrial Ca^{2+} universal transporter (MCU) and is bound by buffers.

2.2.2 Ca^{2+} entry through the plasma membrane

Due to the high concentration difference between the interior and the outside of a cell and the hyperpolarized resting membrane potential of about -70 mV Ca^{2+} entry is encouraged. The Ca^{2+} influx through the plasma membrane occurs by several plasma-membrane Ca^{2+} channels (PMCC), which can be classified into four groups according to their activation [24]. Thus we distinguish between voltage-operated channels (VOCs) opening in response to depolarization of the plasma membrane, receptor operated channels (ROCs) activated by extracellular agonist binding, second-messenger operated channels (SMOC) that open in response to intracellular second messengers and capacitive calcium entry channels (CCECs) [26]. The latter open in response to depletion of the internal Ca^{2+} stores, which might be caused by pharmacological manipulations such as with thapsigargin or by physiological stimulation. The best studied Ca^{2+} flux of the CCECs is the Ca^{2+}-release activated Ca^{2+}current (J_{CRAC}) found in many cell types [166]. The mechanism of the CCECs activation and the corresponding refilling of the internal stores has been under investigation for a long time without satisfying answers have been found. Recently two molecular key elements have been found [101]: Stromal-interacting molecule-1 (STIM1), a protein in the ER membrane with a single transmembrane domain, and Orai located

in the plasma membrane. In the resting state STIM1 and Orai are uncorrelated in the cell. After store depletion the STIM1 molecules relocate to the ER region close to the plasma membrane. If STIM1 and Orai co-localize, J_{CRAC} is initiated and Ca^{2+} enters the cytosol, where it can fill the internal stores. This recently found mechanism has lead to the picture of an ER-plasma membrane synapse.

2.2.3 Ca^{2+} release from internal stores

Ca^{2+} release from internal stores, most often from the ER and the SR, is mediated mainly by two major channel families: the Ryanodine receptor (RyR) and the inositol 1,4,5-trisphosphate receptor (IP_3R). RyRs dominate in excitable cells like neurons and heart cells, whereas IP_3R are more common in non-excitable cells, but mostly the two families coexist.

RyR are expressed in three different isoforms (RyR1-3) coded by different genes. While RyR1 and RyR2 are predominantly present in skeletal muscle cells, RyR3 is found in different cell types. The initiation to open a RyR is not clarified at all. RyR1 is activated by depolarization of the SR and the corresponding conformational change of L-type channels that is thought to be transmitted mechanically to RyR1 and causes it to open. In cardiac myocytes RyR2s open in dependence on the Ca^{2+} concentration. The typical scenario is a local Ca^{2+} influx through the plasma membrane initiated by its depolarization and a subsequent opening of RyR2.

Release of intracellular Ca^{2+} by IP_3R occurs in response to the second messenger IP_3. Since the following investigations focus on this channel type we give a more detailed description of its physiological structure and of the corresponding pathway in the next section. Nicotinic acid adenine dinucleotide phosphate (NAADP) is also known to initiate Ca^{2+} release from internal [38] stores by a still unknown channel type.

2.3 The IP_3 pathway

According to the systems biological approach described in the introduction, we present in this section the recent relevant knowledge of the IP_3 pathway, which we need for the following investigation. We introduce the structure of the signaling pathway and depict the properties of the biological system and its main elements.

The IP_3 signaling pathway is present in almost all eukaryotic cells [235, 134, 148]. It translates external signals into intracellular responses by the second messenger IP_3, that is produced by a specific phospholipase C (PLC) following stimulation of G-protein coupled receptors (GPCR) and some receptor tyrosin kinases (RTK). Typical agonists are growth factors or hormones like serotonin, but ATP also stimulates receptors in some cells as e.g. astrocytes. Stimulation of GPCR leads to PLCβ and

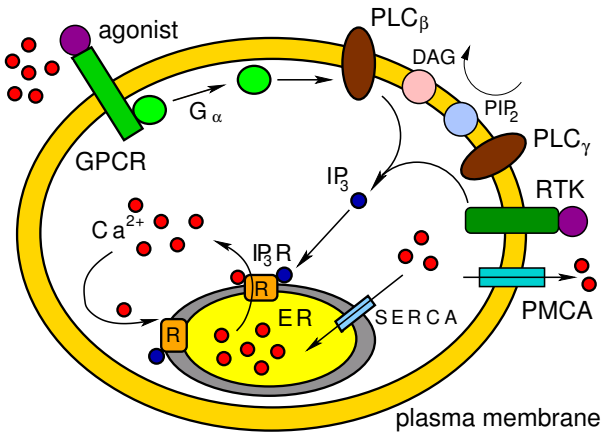

Figure 2.3: Scheme of the IP_3 pathway. If a PM receptor bind its specific agonist it induces a phospholipase C that produces IP_3 (blue) at the plasma membrane. From there IP_3 diffuses into the cytosol and can be detected by IP_3R. If IP_3 and Ca^{2+} are bound to IP_3R it might open and Ca^{2+} diffuses from the ER into the cytosol and can open adjacent channels, too. SERCA pumps and PMCA remove the liberated Ca^{2+} from the cytosol. For more details see text.

stimulated RTK induces the activation of PLCγ. Both active PLC isoforms catalyze the hydrolysis of phosphatidylinosistol-4,5-biphosphate (PIP_2) into diacylglycerol (DAG) and IP_3 [4]. DAG stays in the plasma membrane, where it can activate some protein kinase C (PKC) that activates other Ca^{2+} dependent pathways. DAG can also be metabolized to arachidonic acid, which regulates store-operated Ca^{2+} entry pathways [246]. IP_3 diffuses from the plasma membrane through the cytosol, where it binds to IP_3Rs located in the membrane of the ER or SR respectively. After the fast rise of the IP_3 concentration due to stimulation IP_3 is subsequently metabolized to inosistol-1,4-biphosphate (IP_2) and to inosistol 1,3,4,5-tetrakisphosphate (IP_4) with a time constant of about $\tau = 13$ s [264]. IP_4 may itself act as a second messenger, regulating Ca^{2+} entry or protecting IP_3 from degradation, but its role is still under investigation.

If IP_3 and Ca^{2+} are bound to an IP_3R, it may open and Ca^{2+} will enter the cytosol. There it can diffuse to adjacent channels and causes them to open too. This self amplifying process is known as Ca^{2+} induced Ca^{2+} release (CICR) observed in many cell types. The mechanism of CICR and its relation to the IP_3 pathway is shown in Figure 2.3. From the cytosol the released Ca^{2+} is pumped back into the ER by SERCA pumps and is extruded into the extracellular space as described in Section 2.2.1.

2.4 The IP_3R channel

The key element of CICR is the IP_3R channel. Due to stochastic binding of Ca^{2+} and IP_3 it opens and closes randomly. The open probability of IP_3Rs depends on the IP_3 concentration and the calcium concentration in the cytosol [245, 184, 62]. It increases with increasing IP_3 concentration. It is low for low calcium concentration, increases with increasing Ca^{2+} concentration and finally decreases again for even higher concentrations. This nonlinearity represents a major control element in Ca^{2+} signaling, as it allows Ca^{2+} to terminate its own release by channel inhibition at high Ca^{2+} concentrations leading to a negative feedback loop required for oscillations [270].

IP_3R structure: From atomic force measurements we know, that an IP_3R consists of four identical subunits [234, 149, 145, 185] as shown in Figure 2.4D. Theses subunits together form a glycoprotein with approximately 2700 amino acids per subunit. IP_3Rs share many functional characteristics with RyRs [75]. IP_3Rs are expressed in mammals in three different isoforms (IP_3R1-3) encoded by different genes. They exhibit a similarity of about 60-80 % in their amino acid sequence but differ in their properties of activation by Ca^{2+} and IP_3 as well as in their distribution. Most cells express more than one subtype [157, 78] but in different relative abundance [245] probably caused by differential transcription [178]. For a summary we refer here to [247]. The cerebellum is the richest region of IP_3Rs, mainly expressing IP_3R1 but also both other isoforms. Glia cells express mainly IP_3R3 [88], whereas type 2 predominates e.g. in pancreatic cells [273].

Although it is known that each subunit has a single site for IP_3 binding [246, 129], the number of Ca^{2+} binding sites and their relation to the channel state has not yet been established in detail [247]. In IP_3R1 seven Ca^{2+} binding sites have been found, but there might be more indirect sites, as other sites e.g. for calmodulin and several phosphorylation sites have been identified, too. The IP_3 binding site lies towards the N-terminus [147, 247] close to the pore of the channel and thus allows for communicating IP_3 binding of one subunit to adjacent subunits. The N-terminus and the channel domain are separated by a relatively large segment of about 1600 amino acids. This regulatory domain has binding sites for versatile regulatory factors as Ca^{2+} and calmodulin. The other end of the subunit, the C-terminus probably consists of six helices traversing the membrane of the ER. The spatial arrangement of the four subunits leads to a pore with an estimated diameter of 0.6-0.8 nm.

IP_3R regulation: The general opinion of IP_3R activation assumes that an IP_3R opens if a minimal number $n_{\min}$ of subunits is activated by Ca^{2+} and IP_3 binding [245, 73, 19]. The stochastic character of binding to a few discrete binding sites and the small number of subunits makes the IP_3R to a stochastic element. Thus it opens not deterministically but with a specific open probability P_o depending

on the binding rates and the corresponding cytosolic concentrations of IP_3 and Ca^{2+}. Many experiments were performed to specify the concrete dependence of P_o [132, 22, 151, 150] and to analyze the differences between the subtypes. It turned out, that the activation dependence on IP_3 seems to be similar for type 1 and type 3 receptor, whereas the latter exhibits a higher sensitivity to Ca^{2+} than IP_3R1.

The IP_3R closes if the number of active subunits drops below the minimal number $n_{\min}$. IP_3R have two mechanisms to close: Stochastic attrition and inhibition. The first describes the dissociation of IP_3 or Ca^{2+} bound to the activating sites. Inhibition is the source of the nonlinear behavior of P_o. It is assumed that inhibition occurs by Ca^{2+} binding to an inhibitory site on the receptor or to other accessory proteins as e.g. calmodulin that acts upon Ca^{2+} binding inhibitorically on the channel. High Ca^{2+} concentrations therefore inhibit release through IP_3Rs and prolong the close time, since Ca^{2+} first has to dissociate from the dominant inhibiting site and the Ca^{2+} activating site must still be occupied or occupied again. Inhibition was found in all three isoforms of the IP_3R, although its mechanisms may differ. Typically half times for Ca^{2+} dependent inhibition are in the range of tens of milliseconds and decrease with increasing Ca^{2+} concentrations [73, 2, 236].

Beside these regulation mechanisms there are several experimental evidences of other influences on the channel dynamics like phosphorylation [115], ATP concentration [94, 131] and diverse accessory proteins [32]. Furthermore, IP_3 binding seems to be Ca^{2+} dependent [277, 278, 98] and the lumenal Ca^{2+} concentration might regulate IP_3R dynamics, too [174].

But these effects do not dominate the behavior of IP_3R and some are still controversially discussed. Therefore we focus here on the two major aspects: The biphasic behavior of P_o in dependence on the Ca^{2+} concentration and its excitable and stochastic dynamics. For the biphasic behavior we will assume in the following two binding sites for Ca^{2+} at each subunit as shown in Figure 2.4D. One with a high affinity that activates the subunit and another one with a lower affinity that inhibits the subunit and is dominant, i.e. that a subunit is active only in the case of IP_3 binding if the first Ca^{2+} binding site is occupied and the latter is free.

2.4.1 Cellular arrangement

The IP_3Rs are embedded in the membrane of the endoplasmic reticulum. An important physiological function of the ER is the synthesis and folding of several secretory and membrane proteins. It is also the main intracellular Ca^{2+} store, which is linked to the first property, as Ca^{2+} modulates protein production and proteins influence the Ca^{2+} dynamics by buffering and triggering specific control mechanisms.

The endoplasmic reticulum: Deviating from the schemes in Figures 2.2 and 2.3 the ER is a tubular network of bilayer membranes spreading throughout the whole cell as depicted in Figure 2.4A for a COS7 cell, which is from a monkey cell

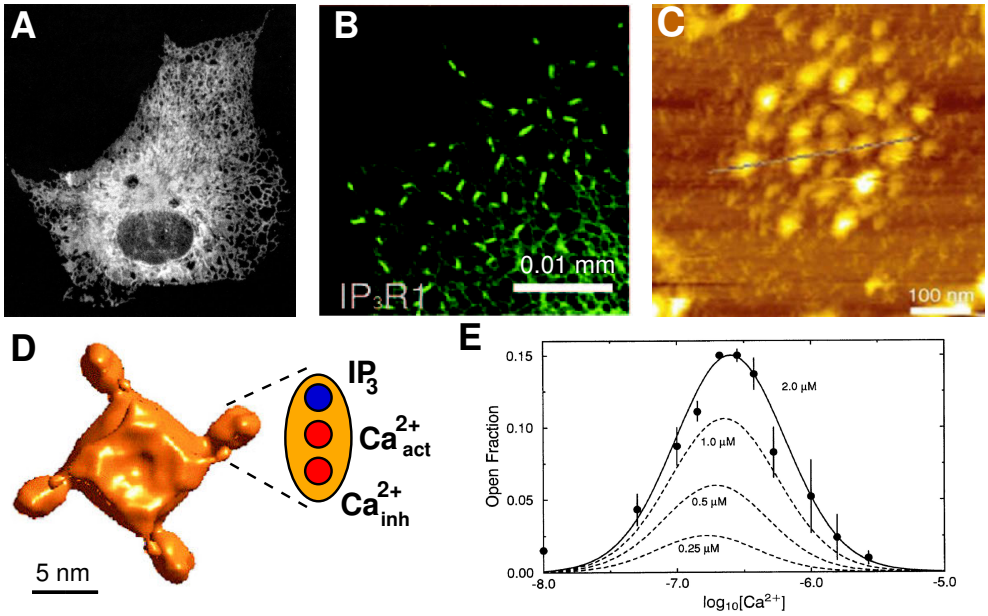

Figure 2.4: Summary of the physiological elements involved in the intracellular Ca^{2+} dynamics. Deviating from the scheme in Figure 2.3 the ER is a tubular network spreading through out the hole cell (**A**) (picture taken from [192]). On the membrane of the ER IP_3Rs form separated channel clusters (**B**) (picture from [244]). A single cluster consists of 1-40 localized channels as shown in experiments by Suhara (**C**) (picture from [234]). A single channel consists of four identical subunits (**D**) each having binding sites for IP_3, activating and inhibiting Ca^{2+} (channel picture taken from [185]). The ambivalent character of Ca^{2+} binding leads to a biphasic open probability (**E**) of IP_3Rs representing a key element of CICR (picture from [48]).

line (picture taken from [192]). The ER structure was visualized by transfecting the cell with an ER targeted red fluorescent protein (dsRed 2) exhibiting a typical higher density around the nucleus (see [192] for more details). The ER comprises up to 10 % of the cell volume [164] and exhibits free Ca^{2+} concentration of hundreds of µM [142, 76, 152]. Moreover, most of the Ca^{2+} within the ER is bound to buffers like calsequestrin and calreticulin [142, 144] increasing the effective Ca^{2+} capacity. The latter is important as free lumenal Ca^{2+} concentration determines the strength of release.

The SERCA pumps: SERCAs are the most important intracellular Ca^{2+} removing element with high affinity and low capacity. They bind two Ca^{2+} ions at the cytosolic site, which are transported by ATP consuming phosphorylation into the lumen. By a subsequent dephosphorylation the pumps return in their initial state [197, 69]. SERCAs are expressed in different isoforms and cell specific

distributions. SERCA1 is only expressed in fast contracting muscle cells, SERCA2 is mainly present in cardiac muscle cells but it is also co-expressed with SERCA3 in non-muscle tissues [128, 128, 29]. Typical concentration of SERCAs within cells are in the range of μM [95]. Together with their estimated pump rate of about 10 ions per second, this leads to a pump flux capacity of tens of μM s^{-1}, which depends on the temperature: The SERCA activity increases with temperature for all subtypes [50, 112].

The IP_3R cluster: Another important property of the IP_3 pathway is the spatially inhomogeneous distribution of the IP_3Rs. They form channel clusters, which are scattered randomly on the ER membrane with typical distances of 1-7 μm [244, 136] as shown in Figure 2.4B (taken from [244]). Another example of the IP_3R distribution in PLA cells used in the experiments in Chapter 4 is shown in Figure A.1. Each cluster contains typically between 1-40 channels, which are separated by approximately tens of nanometers. Figure 2.4C shows an example of a cluster measured by Suhara and coworkers [234].

The spatial inhomogeneity of IP_3R distribution together with the SERCA pumps and Ca^{2+} buffers causes huge concentration gradients close to open clusters and has led to the picture of a hierarchical structure of Ca^{2+} dynamics.

2.5 Ca^{2+} modeling

In this section we briefly summarize the main concepts of Ca^{2+} modeling and their relation to the hierarchical organization of Ca^{2+} signaling. That is, in relation to Figure 1.1, the last step before we come to our hypotheses.

Ca^{2+} oscillations have been extensively studied in experiments due to their frequent appearance and importance and most of the elements involved are identified as summarized in the previous section. Moreover, Ca^{2+} signaling is simple enough to be cast into treatable mathematical models, which allows for systematic investigation. In combination with the fascinating spatio-temporal behavior this has put Ca^{2+} dynamics into the focus of theoretical investigations for about 20 years now.

2.5.1 Deterministic ODE models

Most models to date assume cells as well stirred reactors and describe Ca^{2+} dynamics by fluxes between the two compartments, the cytosol and the ER. These fluxes occur under the control of the functional elements described in Figure 2.2 and are most often assumed as linear.

One of the first modeling approaches was suggested by Meyer and Stryer [143] in 1988. They identified two of the key features in intracellular Ca^{2+} dynamics: cooperative Ca^{2+} release induced by IP_3 and a feedback of Ca^{2+} somewhere in the

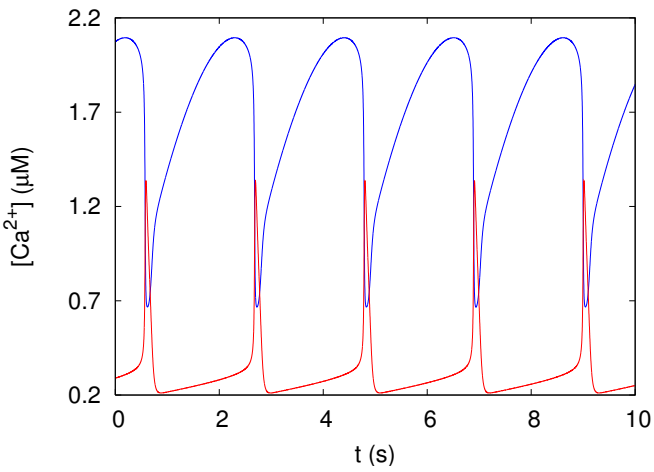

Figure 2.5: Ca^{2+} oscillation simulated by the Goldbeter ODE model described by eqs. (2.1). The cytosolic (red) and lumenal (blue) Ca^{2+} concentration oscillate in phase and are of the same magnitude.

pathway. They introduced a positive feedback of Ca^{2+} on PLC activation leading to an enhanced IP_3 production. Although this model exhibits Ca^{2+} oscillations it also predicts an indispensably oscillating IP_3 concentration that oscillates in phase with Ca^{2+}. This could not be verified in experiments [16].

A more self-sustained model was introduced two years later by Goldbeter and coworkers [84]. Their model is based on the existence of two Ca^{2+} pools, one of which is sensitive to IP_3 and the other not, representing the ER and the cytosol, respectively. Increasing IP_3 triggers Ca^{2+} release from the ER into the cytosol inducing further CICR by a positive feedback. After emptying the ER, Ca^{2+} is pumped back by pumps into the ER. Repeating this scenario leads to oscillations with similar properties observed in experiments. Due to its success, this model became the origin of many enhanced models and Ca^{2+} oscillations have been the representative example of a cellular oscillator for years.

Because of its importance and its reference character we will briefly review this model to illustrate the foundation of Ca^{2+} modeling. The governing equations read

$$\dot{Z} = J_0 + J_1\beta - J_2 + J_3 + k_f Y - kZ \tag{2.1a}$$

$$\dot{Y} = J_2 - J_3 - k_f Y \ , \tag{2.1b}$$

where Z denotes the cytosolic and Y the lumenal Ca^{2+} concentration respectively. The two pools are coupled by a constant flux J_2 from the cytosol into the ER, J_3 corresponds to the flux from the ER into the cytosol and k_f corresponds to a leak flux through the membrane of the ER. Additionally the cytosolic Ca^{2+} concentration increases by a leak influx through the plasma membrane J_0 and an influx from IP_3-insensitive stores, and it is decreased by an efflux across the plasma membrane. The fluxes J_2 and J_3 corresponding to the pumps and the channels respectively are

described by the nonlinear relations in the form of Hill functions as

$$J_2 = V_{M_2} \frac{Z^n}{K_2^n + Z^n} \tag{2.2a}$$

$$J_3 = V_{M_3} \frac{Y^m}{K_R^m + Y^m} \frac{Z^p}{K_A^p + Z^p} \ , \tag{2.2b}$$

where V_{M_i} are the maximal rates of Ca^{2+} transport, K_i correspond to threshold constants and the coefficients n, m and p determine the cooperativeness of the corresponding Ca^{2+} transporter. Note that the channel dynamics is here given by a meanfield approach. Thus, the channel dynamics is nonlinear, but neither inhibition nor the discrete transition from close to open state are considered.

This model and its modifications describe Ca^{2+} oscillations by repeating emptying and refilling the two pools as shown in Figure 2.5 for standard parameters ($J_0 = 1$ μM/s,$J_1 = 7.3$ μM/s, $\beta = 0.3$, $k = 10$ s^{-1}, $k_f = 1$ s^{-1}, $V_{M_2} = 65$ μM/s, $V_{M_3} = 500$ μM/s, $K_2 = 1$ μM, $K_R = 2$ μM, $K_A = 0.9$ μM, $n = m = 2$ and $p = 4$). On the one hand, Equations (2.1) exhibit a good agreement with experiments on a global scale and demonstrate the principles of cell signaling: cooperativeness and feedback regulation. But on the other hand it requires store depletion during each oscillatory period, which could not be justified by more detailed experiments.

Other points of criticism arose as these ODE models produce generally Ca^{2+} oscillation with short regular periods of about 10-60 s. But in experiments slower and more irregular oscillations are observed as well. To include such behavior models means including stochastic gating of the IP_3R, regulation of IP_3R by phosphorylation or slow buffers [58, 228]. Also the feedback of Ca^{2+} on the IP_3 production was revived in this context.

2.5.2 Spatially extended models

The models mentioned above have substantially increased our understanding of the regulatory mechanisms that cells can use for signaling. Thus they have explained CICR and pointed out the need for more realistic channel models including stochastic transitions from open to closed states.

A general drawback of all these point models is their incapability to explain the hierarchical structure of Ca^{2+} signaling [253, 26] and waves. The hierarchical picture arose upon observation of random release events from single channel clusters called "puffs" [15, 24, 135, 136, 62]. They can be considered as the elemental events of intracellular Ca^{2+} dynamics. According to the hierarchical concept, random opening of a single channel in a cluster causes the other channels of the same cluster to open thus generating a puff. This puff may cause neighboring clusters to open, too. If a supercritical number of puffs arises, release spreads through the whole cell.

This behavior is shown in Figure 2.6 depicting an experiment performed by Marchant and coworkers [135]. They measured the cytosolic Ca^{2+} concentration in Xenopus oocytes with Ca^{2+} sensitive fluorescent dyes on the same line of a cell over time. Blue corresponds to low and red to high cytosolic Ca^{2+} concentrations, respectively. At the white line they uncaged IP_3 by an UV flash to sensitize the cell. After approximately 1.5 s, they observed an isolated puff in (A), but this opening of a single cluster does not initiate a global wave. Only if more of these local events come together and exceed a critical number a global wave is set off. Once the wave is initiated it exhibits a deterministic behavior, as the wave travels with constant velocity. That can be seen by the behavior of the wave front, which corresponds to the two turquoise straight lines that extend diagonally upward and downward from the initiating site.

The delay of the wave initiation from the IP_3 uncaging and the failure of the isolated puff to initiate a wave was explained in former models by a negative feedback of IP_3 on Ca^{2+}. To investigate this hypothesis Marchant *et al.* tried to trigger a wave rather shortly after IP_3 release. This is shown in panel B, where they triggered a Ca^{2+} wave by applying a short localized laser pulse approximately 1 s after the UV flash indicated by the arrow in Figure 2.6B. The laser pulses cause small holes in the membrane of pigments through which Ca^{2+} enters the cytosol. The long lasting Ca^{2+} release induces a Ca^{2+} wave at a shorter time than the failure of wave initiation of the isolated puff in panel A occurs. Hence, the delay is not caused by a negative feedback of IP_3 on Ca^{2+} release, but occurs due to the space-temporal interplay of the release sites, the IP_3R cluster. Moreover, we can deduce from the comparison with penal A, that the stochastic nature of Ca^{2+} signaling is mainly given by the natural triggering event, the wave nucleation.

These findings indicate the hierarchical structure of Ca^{2+} signaling. A global Ca^{2+} signal originates from the stochastic opening of a single channel. This blip can now be amplified by the properties of IP_3Rs , since the released Ca^{2+} increases the open probability of other channels within the same cluster leading to a puff. This single localized Ca^{2+} release may initiate a global wave by itself (as in Figure 2.6B) or contribute to a nucleus of several puffs inducing a global signal as shown in panel A. Hence, the global signal consisting of a cooperative opening of channels is determined by the molecular properties of single IP_3Rs and their coupling by diffusion of Ca^{2+}.

To model this hierarchical signal, we rely on spatially extended models to incorporate its spatial character. In general, Ca^{2+} dynamics is described by a reaction diffusion system coupling the cytosol and the ER and considering buffer reaction

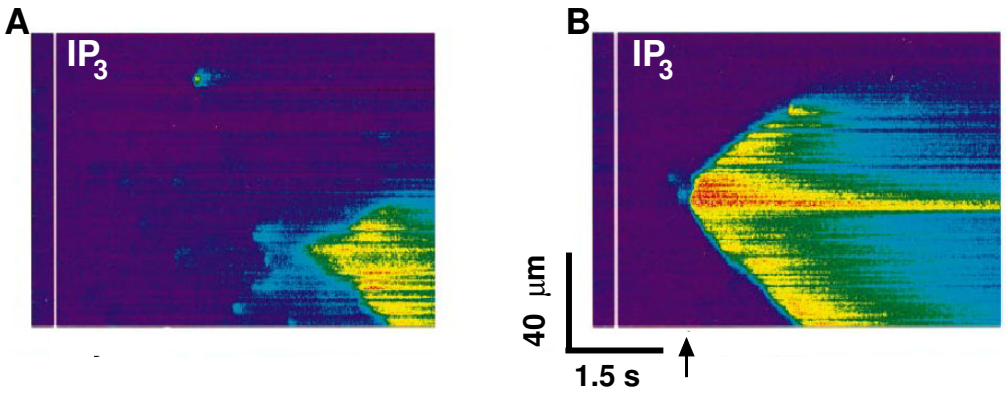

Figure 2.6: Experimental example of wave nucleation. In the experiment the cytosolic Ca^{2+} concentration of Xenopus oocytes was measured by a line scan with Ca^{2+} sensitive dye. Blue corresponds to low and red to high cytosolic Ca^{2+} concentrations. At the white line IP_3 was added to the cell. If several local events come together a global wave nucleates by CICR (**A**). In panel **B** a hole was burned into the ER membrane after uncaging IP_3 at the time indicated by the arrow. This triggering event initiated the global Ca^{2+} wave. (picture taken from [135])

and channel transitions. Thus, the general form reads

$$\frac{\partial[\mathrm{Ca}^{2+}]}{\partial t} = D_c \nabla^2[\mathrm{Ca}^{2+}] + \mathcal{F}\left([\mathrm{Ca}^{2+}], [\mathrm{IP}_3], [E], P_{\mathrm{IP}_3\mathrm{R}}, P_p, P_l\right) + \sum_j R_j \tag{2.3a}$$

$$\frac{\partial[E]}{\partial t} = D_E \nabla^2[E] - \gamma\mathcal{F}\left([\mathrm{Ca}^{2+}], [\mathrm{IP}_3], [E], P_{\mathrm{IP}_3\mathrm{R}}, P_p, P_l\right) + \sum_k R_k \tag{2.3b}$$

where the first equation describes the cytosolic and the second one the endoplasmic Ca^{2+} concentration. Ca^{2+} of the two compartments diffuses with their compartment dependent diffusion coefficient D_i and is coupled by a general function $\mathcal{F}$ which depends on the pumps P_p, the leak flux across the ER membrane and the states of the IP_3Rs. The latter depend on the cytosolic Ca^{2+} concentration as well as on the IP_3 concentration. Their action, i.e. the flux induced by open channels as well as the leak flux, depends on the concentration in both compartments. Furthermore, Ca^{2+} reacts with compartment specific buffers denoted by the reaction terms R_j and R_k for the cytosol and the ER, respectively. These buffers may diffuse as well.

Several specific models of this structure were used to study wave nucleation and to estimate the influence of buffer properties [65, 59, 228, 183, 229, 223, 226, 225]. Most of the models are restricted to one or two dimensions and use simplified IP_3R models. A popular example are fire-diffuse fire models [39, 252] in which the release sites are described by a threshold dynamics, i.e. a channel opens if the Ca^{2+} concentration exceeds a specific value and closes after a fixed time.

But a model in three dimensions with a microscopic IP_3R model is still lacking. Especially investigations in regards to the spiking behavior are mostly on a toy model level.

2.6 Aims

Despite the substantial experimental knowledge and various modeling approaches, the links between IP_3R behavior and Ca^{2+} oscillations are poorly understood. Is oscillatory behavior a feature of individual IP_3Rs and their local interaction with Ca^{2+} and IP_3, with channels opening and closing in oscillatory fashion? Or do oscillations arise from properties that depend upon a higher level of organization involving many IP_3Rs?

Although the hierarchical structure of Ca^{2+} signals is accepted in general [253, 15, 24, 27] and clearly shown in larger cells as e.g. within *Xenopus oocytes* [135], the current opinion still assumes Ca^{2+} oscillations to be a deterministic process with small deviations occurring by some unspecific intrinsic noise. The basis of these ideas originates from the assumption that the IP_3R clusters in smaller cells are coupled globally by the cytosolic Ca^{2+}, i.e. that the diffusion length is large compared with the inter cluster distances.

Consequently, these models neglect the spatial character and assume IP_3R clusters to open in an oscillatory fashion. Combined with the global coupling this leads to a system of coupled phase oscillators, which are intensively studied in chemical reactions [110, 196, 207, 208] or neural dynamics [243, 241, 242] and represent a prototype of limit cycle oscillators. An important consequence of that assumption is that the frequency of Ca^{2+} oscillations stays constant for different coupling strengths but the amplitude weakens with decreasing coupling.

This picture stands opposite to results from cellular pattern formation [114, 116, 63, 227] and physical knowledge of spatial inhomogeneous media. They often exhibit stochastic dynamics and are described as stochastic media which are predicted theoretically for reaction diffusion systems [182, 99, 122, 60, 39]. From their properties one would expect Ca^{2+} oscillations to consist of repeated wave nucleation leading to a spiking structure as shown in the experimental examples in Figure 2.1. Indeed, first simulations of intracellular Ca^{2+} dynamics predicted that mechanism to apply. The regime of rather regular oscillations appears in this model by array enhanced coherence resonance (AECR) [182, 99, 122, 60, 39], where wave initiation is frequent enough to ensure that waves emerge as soon as the refractory period has passed. These mechanisms would explain the observed stochastic Ca^{2+} spiking on a molecular level and would overthrow the established conception of deterministic Ca^{2+} signals.

Within this work, we would like to clarify the question whether Ca^{2+} oscillations

are limit cycle oscillations or if Ca^{2+} spikes occur by repeated nucleation of puffs to a global wave even in smaller cells. The latter would lead to the general question whether cells can build regular behavior from molecular fluctuations by AECR and would make Ca^{2+} signaling to a first biological relevant example. Within this context the differences between induced Ca^{2+} oscillations, i.e. cellular responses evoked by stimulation, and spontaneous Ca^{2+} signals may indicate the structure of the signaling network.

Therefore, we investigate the properties of Ca^{2+} signals of different cell types under different experimental conditions in the first part of this thesis. The results put a new complexion on Ca^{2+} signaling and demonstrate a lack of understanding of previous models. Thus, we extract the most relevant biological elements found in the experimental part and build a physiological model that can be used for cell specific simulation in the second part. The comparison of the simulations with our experimental data can illuminate open questions of the cellular dynamics.

Part I

Experiment

Chapter 3

Materials and methods

In this chapter the experimental materials and methods used for the investigation are described. We start with how the cytosolic Ca^{2+} concentration was measured in four different cell types. For each cell type we give a brief physiological description and the experimental details as medium compositions and setup components.

In Section 3.5 we then present how to extract relevant quantities from the raw data for our analysis. This analysis is based on methods from statistical physics. Thus, we give with a brief review of stochastic processes and experimentally accessible measures and demonstrate their relation to the raw data.

All experiments with HEK cells were performed by Steve C. Tovey, most experiments with microglia cells were done by Ulrike Winkler, and experiments with acute brain slices in Chapter 5 were performed by Antje Heidemann. All other experiments and the whole data analysis were exclusively performed by myself.

3.1 Measurements of cytosolic Ca^{2+} concentration by dyes

To determine the cytosolic Ca^{2+} concentration we used different Ca^{2+} sensitive fluorescent dyes. The dyes were loaded into the cell by using an acetoxymethylester modification that allows the transport through the plasma membrane. Within the cytosol, the ester group is split off by enzymes leading to the active form of the dye and prevents a further transport through membranes, e.g. back into the extracellular space or into the ER.

Cells were illuminated by monochromatic light. This light may induce excited states of the dye molecules, i.e. the energy of the light is absorbed by the molecule and transformed into intramolecular oscillations. As molecules may have an inhomogeneous charge distribution, these oscillations lead to electrical dipole oscillations yielding an emission of light. The emitted light has in general distinct spectral

properties different from the excitation light and can therefore be filtered out by appropriate filters and recorded by CCD cameras.

A common feature of fluorescent dyes is a change of the fluorescent intensity by a factor up to 100 upon binding of Ca^{2+} ions. Two different kinds of dyes are discerned. Nonratiometric dyes have only a single excitation and a single emission wavelength.The dye molecules change their configuration due to Ca^{2+} binding , which allows for excited molecular oscillations and subsequent emission of light. These dyes cannot be used to determine the real Ca^{2+} concentration, as the signal exhibits only relative changes and depends on the unknown total amount of dye that has entered the cell. In this work, the measured fluorescent signals F of nonratiometric dyes are normalized to the initial signal strength F_0 leading to the observable $\Delta F = F/F_0$.

Ratiometric dyes have two wavelengths λ_1 and λ_2, one for the Ca^{2+} free and another one for the Ca^{2+} bound case respectively. This property can be used to calibrate the signal to concrete Ca^{2+} concentrations, since the ratio of the two signals does not depend on the absolute dye concentration. In the case of ratiometric dyes, we describe the signal by the ratio of the single signals, i.e. $\Delta F = F_{\lambda_2}/F_{\lambda_1}$.

3.2 Glia cells

Glia cells are non-excitable cells within the central nervous system, which exhibit Ca^{2+} signals. Their name "glia" was coined by Rudolph Virchow in 1856 for the interstitial, cement-like substances surrounding neurons in the brain. The name already points to the assumed function as neuronal glue. While Virchow used the term not for single cells but for the whole substance, further investigations discovered that glia consists of different cell types. Thus we discern to date three main types of glia cells: astrocytes, oligodendrocytes and microglia, where the first two cell types are often subsumed under macroglia[1]. The knowledge about their physiological function has changed dramatically within the last decades from a pure passive role to a more controlling function that goes far beyond the structural support. They exhibit intercellular signals within astrocytes networks as well as signals between astrocytes and neurons, transmitted by glutamate and more importantly by Ca^{2+}.

The importance of glia cells for higher brain functions is indicated by the increasing ratio of glia to neuron within the phytogenetic tree. In *C. elegance*, ten neurons are surrounded by one glia cell, in mice we find a ratio of 1:1 and in the human brain 90 % of cells are glia cells. Moreover, glia differentiation is greatest in

[1]Recently a fourth glia type was found, the NG2+ glia cell [159]. These complex cells are in contact with the axons of neurons. Very recently it was reported that NG2+ cells can fire axon potentials [162, 109] what contradicts the dogma that only neurons are excitable in the brain. These results are still discussed controversially.

higher vertebrates.

3.2.1 Microglia

Cells of the immune system can not reach the brain due to the blood-brain barrier. Therefore microglia cells are the immuno-component cells of the central nervous system. They have several states between which they switch in response to their environment. Thus, they may exhibit transitions from ramified resting cells into active, cytotoxic and phagocytic cells [180]. The origin of microglia was discussed controversially, but to date their mesodermal origin seems to by clarified. They are related to the macrophages within the blood with which they share a similar antigen spectrum, but differ in other cell properties.

3.2.2 Astrocytes

Macroglia cells are divided into astrocytes and oligodendrocytes. The latter build the myelin sheet around neuronal axons and their functional damage leads to multiple sclerosis. The majority of glia cells within the human brain are astrocytes comprising 80 % of all cells. They are named in accordance to their often star like shape.

Astrocytes are characterized by glutamate synthetase, expression of the Ca^{2+} binding protein S-100β and of the intermediate filament protein glia fibrillary acidic protein (GFAP) [138]. Furthermore, they express connexin 43 hemi channels which can form gap junctions. Due to these gap junctions, astrocytes can form cellular networks leading to intercellular signals reaching about 200 µm and activating up to hundreds of cells.

But astrocytes are not a homogeneous cell type. They are subdivided into stellate astrocytes found predominantly in white matter and protoplastic astrocytes mainly located in the gray matter. Astrocytes also differ in their properties in dependence on their locations within the brain. Astrocytes within the cortex often exhibit gap junctions, whereas in the hippocampus astrocytes are coupled mainly by signals translated by the extracellular space.

Physiological role of astrocytes: Since astrocytes play a key role within this thesis and are studied in Chapter 5 in a more physiological manner, we give here a brief overview of their role in the brain.

Astrocytes have a variety of physiological functions including metabolic, homeostatic, trophic and signaling ones besides their old known structural property. They contribute to the blood-brain barrier and are involved in angiogenisis, in development and repair processes [97].

Astrocytes are typically in contact with neurons on the one side and with blood vessels on the other side, and thus a medium to couple neuronal activity and metabolism [283, 284, 7, 154, 172]. They give nutritional support to neurons by

storing most of the glycogen within the brain and are probably responsible for the fast energy supply to neurons by lactate [179].

Furthermore, astrocytes are key elements for the regulation of the cerebrospinal fluid with regard to Ca^{2+}, K^+ and H^+ concentrations [189, 215] and remove free radicals in order to support neuronal functionality. As part of the extracellular medium astrocytes contribute to neuronal migration and formation of nuclei [261, 137] in development. In adult brains they influence synapse formation and maintenance as well as regulate synaptic efficiency [261, 49], i.e. LTP and LTD, which are the mechanism of memory.

Astrocyte-neuron coupling: Especially the last point has moved astrocytes into the focus of recent scientific investigations. Two main properties of astrocytes are important: Their direct contact with neuronal synapses and the expression of neurotransmitter receptors [260, 259].

Astrocytes were thought to seal up the synaptic cleft in order to minimize the free space, through which neurotransmitters have to diffuse from the pre-synapse to the post-synapse. In this location astrocytes are able to remove neurotransmitters and especially glutamate from the synapse and to convert it to glutamine. The glutamine is provided back to the neurons having no enzyme for glutamine synthetase. That is known as the "glutamate-glutamine circle" [267] contributing to the termination of neural signals.

Due to their neurotransmitter receptors, astrocytes can be activated by neuronal signals transmitted at the synapse [199, 71]. Binding of a neurotransmitter does not induce an action potential like in neurons but leads to a Ca^{2+} signal e.g. by the IP_3 pathway. The astrocytic signals can differ in dependence on the neurotransmitter concentration [260, 175].

Astrocytic Ca^{2+} signals exhibit a feedback on neuronal activity by the capability of astrocytes to release glutamate [21, 9, 96, 177] and other neuromodulatory substances like ATP [231], D-Serine [165] or nitric oxide (NO) [119] into the extracellular space upon activation, many of which in a Ca^{2+} dependent manner. The release is controlled by both, the frequency and the amplitude of the astrocytic Ca^{2+} oscillations [283, 176]. The frequency on its part is determined by the neuronal activity leading to a bidirectional astrocyte-neuron coupling and has led to the model of the "tripartite synapse" [262, 10].

Together with the astrocytic network formed by connexin 43 gap junctions that leads to long range signals, this tripartite synapse leads to an amplifying mechanism and may play the role of a delayed feedback. Furthermore, astrocytes exhibit spontaneous activity *in vitro* [172, 156, 240] and *in vivo* [93], i.e. Ca^{2+} signals occur without stimulation. Thus astrocytes may represent a slow time scale in information processing or correspond to control of other signaling systems as e.g. the immune system.

3.2.3 Measurements of $[Ca^{2+}]_i$ in glia

Glia culture preparation: Glial cell cultures were prepared from brains of newborn NMRI mice [127] using whole brains for microglia, but only cortex for astrocyte cultures. Briefly, brain tissue was freed from blood vessels and meninges, trypsinised and gently triturated with a fire-polished pipette in the presence of 0.05% DNAase (Worthington Biochem. Corp., Freehold, NY, USA). After washing twice, cells were plated directly on poly-L-lysine (PLL; 100 μg/ml; Sigma, Deisenhofen, Germany) coated glass coverslips ($\emptyset$ 15 mm) at densities of 3 to 5×104 cells/coverslip, kept in $\emptyset$-10-cm-dishes using Dulbecco's modified Eagle's medium (DMEM) supplemented with 10% fetal calf serum (FCS), 2 mM L-glutamine, 100 units/ml penicillin, and 100 μg/ml streptomycin. One day later, cultures were washed twice with Hank's balanced salt solution (HBSS) to remove cellular debris.

Cells were maintained for at least 4 days and after reaching a subconfluent state, microglial cells and oligodendrocytes as well as their early precursors were dislodged by manual shaking and removed by washing with HBSS. The purity of the astrocytes was routinely determined by immunofluorescence using an antibody against glial fibrillary acidic protein (GFAP, Sigma), a specific astrocytic marker. The cultures typically showed more than 90% cells positive for GFAP.

Brain slice preparation: Some experiments in Chapter 5 were performed in acute brain slices by Antje Heidemann. All experiments were performed according to the guidelines of the German Animal Protection Law. For slice preparations 10-14 day old mice (NMRI mice) were decapitated and their brains were removed. Cortical slices of 250 µm thickness were cut in ice-cold bicarbonate buffer (134 mM NaCl, 2.5 mM KCl, 2 mM $CaCl_2$, 1.3 mM $MgCl_2$, 26 mM $NaHCO_3$, 1.25 mM K_2HPO_4 and 10 mM glucose) using a vibratome (HM 650 V, Microm; Walldorf, Germany). By gassing with carbogen, the pH was adjusted to 7.4. Slices were stored at room temperature in gassed buffer for at least 45 min prior to staining.

Ca^{2+} imaging: Cultured cells plated on glass coverslips were incubated with the Ca^{2+} indicator dye Fluo-4-acetoxymethylester (Fluo-4 AM, 5 µM, Molecular Probes, Eugene, USA) for 30 min at room temperature in HEPES buffer (148.9 mM NaCl, 5.4 mM KCl, 1 mM $MgCl_2$, 10 mM $CaCl_2$, 10 mM HEPES, 5 mM D-glucose, pH 7.4) containing 0.01% Pluronic-127 (Molecular Probes). Subsequently cells were washed and kept in bath solution (HEPES buffer) for 15-20 min prior to the measurements with the conventional imaging system at a frequency of 0.33 Hz. Cultures were fixed within the microscope chamber of an upright microscope (Axioskop FS, Zeiss, Oberkochen, Germany) equipped with a 20x water immersion objective (UMPlanFl, numeric aperture: 0.5, Olympus, Hamburg, Germany) by a U-shaped platinum wire and superfused with HEPES buffer normally at 20 °C. Substances were applied by changing the perfusate. Cells were illuminated (495 nm) from a monochromator (T.I.L.L. Photonics) and fluorescent images (515-545 nm) collected

every 3 s with a 12 bit camera (SensiCam) on an upright microscope and visualized with ImagingCellsEasily software.

Slices were also incubated with Fluo4-AM (10 μM, Molecular Probes, Eugene, USA) in bicarbonate buffer containing 0.02 % Pluronic-127 (Invitrogen, Paisley, UK) at room temperature for 40-50 min. This loading protocol has previously been shown to selectively load astrocytes in this type of slices. Slices were transferred to a perfusion chamber on the upright microscope and fixed in the chamber using a U-shaped platinum wire with a grid of nylon threads. Slices were superfused with gassed bicarbonate buffer at a flow rate of 4-6 ml/min. All other imaging details are the same as for the cultured cells.

3.3 Processed lipoaspirate (PLA) cells

Processed lipoaspirate cells are human adult stem cells derived from adipose tissues [286]. The features of stem cells are their self-renewal capacity, long-term viability and multilineage potential that makes them highly interesting for medical therapies. PLA cells exhibit stable growth and profileration kinetics in culture and can differentiate in vitro towards the osteogenic, adipogenic, myogenic and chondrogenic lineage when treated with established lineage-specific factors [285]. These factors may influence intracellular signals as for instance Ca^{2+} oscillations that lead to the specific cell types.

The study conforms to the Declaration of Helsinki and all cell donors gave their informed written consent to use part of their fat tissue for the generation of processed lipoaspirate cells.

3.3.1 Measurements of $[Ca^{2+}]_i$ in PLA cells

PLA cells were cultured in 25 cm^2 flasks in 5 % CO_2, humidified air at 37 °C in Ham's F-10 medium (Biochrom, Berlin, Germany) supplemented with 10 % fetal calf serum (Sigma), 2 mM glutamine, 0.1 mM β-mercaptoethanol, 1 to 100 non-essential amino acids (Biochrom), 100 units/ml penicillin and 100 μg/ml streptomycin (Invitrogen). Subconfluent cell cultures were dissociated with a 0.2 % trypsin-0.05 % EDTA solution and subcultured onto 12 mm coverslips. For Ca^{2+} measurements, subconfluent cells on coverslips were incubated for 30 min with 10 μM fluo3-AM (Invitrogen) and then washed once in culture medium. Fluo-3 fluorescence was recorded in single cells by confocal laser scanning microscopy (LSM 510 Meta, Zeiss) using a 25× objective with a numerical aperture of 0.8 (Plan Neofluor, Zeiss). Excitation was at 488 nm and emission was recorded using a 515 nm longpass filter.

3.4 Human embryonic kidney (HEK) cells

HEK293 cells are a cell line derived from Human Embryonic Kidney cells in the early 70s in the lab of Alex van der Eb in Leiden, Netherlands. Cells were obtained from an aborted fetus cultured by van der Eb and transformed by DNA from human adenovirus by Frank Graham. The number 293 corresponds to the consecutive numbering of Grahams experiments.

Although HEK cells are not a particularly good model for normal cells as an experimentally transformed cell line their easy handling has led to a wide distribution. They are easy to culture and to transfect and are often used in experiments where the cumulative behavior of a cell is not of interest. Among other issues, HEK cells became a reference character for IP_3R mediated signals comparable to the harmonic oscillator in theoretical physics.

3.4.1 Measurements of $[Ca^{2+}]_i$ in HEK cells

HEK293 cells were cultured in Dulbecco's modified Eagle's medium/Ham's F-12 supplemented with fetal bovine serum (10 %) and L-glutamine (2 mM), in a humidified athmosphere (95 % air, 5 % CO_2, 37 °C). Medium was replaced every third day, and cells were passaged when they reached 80 % confluence. For single cell imaging, cells were plated onto 22 mm round glass coverslips coated with 0.01 % poly-L-lysine and used after 2 days. They were loaded with 2 µM fura-2-AM in HEK medium (HM: 135 mM NaCl, 5.9 mM KCl, 1.2 mM $MgCl_2$, 1.5 mM $CaCl_2$, 11.6 mM HEPES, 11.5 mM D-glucose, pH 7.3) supplemented with 1 mg/ml bovine serum albumin and 0.02 % Pluronic F-127. Cells were loaded for 45 min at 20 °C and then washed for 45 min in HEK medium to allow de-esterification of the fura-2-AM. Measurements of $[Ca^{2+}]_i$ in single cells were performed as previously described [209], with fluorescence collected at intervals of 5 s. Fluorescence ratios were calculated after correction for autofluorescence.

3.5 Data analysis

The stochasticity of the data originates from the stochastic opening and closing of single IP_3Rs as explained in Section 2.4. These fluctuations may be carried on the level of the cell by the inhomogeneous arrangement of channels (see Section 2.4.1). The global signal occurs by cooperative channel behavior induced by Ca^{2+} diffusion and CICR as described in Section 2.5.2 leading to the hierarchical structure of Ca^{2+} signals as mentioned in Section 2.5.2 and 2.6. The resulting assumption of Ca^{2+} being a repeated wave nucleation processes expresses itself in the unpredictability of a Ca^{2+} spike. Hence, we rely on tools to characterize random behavior.

3.5.1 Characterization of stochastic processes

A stochastic variable X is defined either by a set of possible realizations, i.e. the set of states, or by a probability distribution over this set. This duality connects experiment and theory. In experiments it is only possible to measure concrete realizations of a specific process like throwing a coin N times and counting heads and tails. We will never predict the result of a specific event, but if we know the underlying process we may estimate its outcome. This knowledge is obtained by a large sample space, i.e. by repeating the corresponding experiment many times. From these realizations we can find its statistical characteristics. Thus, we know the stochastic process, if we know the statistical data, which completely characterize it, the *moments* μ_ν of X, where the order ν required for a complete description depends on the process.

Moments and cumulants: A stochastic variable is determined by its probability distribution density, or short, probability density $p(X)$, since the expectation value or average of any function $f(X)$ is given by

$$\langle f(X)\rangle = \int f(x)p(x)dx \; . \tag{3.1}$$

Hence the moments $\mu_\nu = \langle X^\nu\rangle$ of a variable are determined due to the probability density by

$$\mu_\nu = \int x^\nu p(x)dx \; . \tag{3.2}$$

Since the probability density describes a probability, it must be normalized to one, i.e.

$$\int p(x)dx = 1 \; . \tag{3.3}$$

The probability density corresponds to the relative frequency in experiments and the probability that a particular realization of the random variable is in the interval $(x_1, x_1 + \Delta x)$ is given by $p(x)\Delta x$. But in experiments it is more convenient to determine the *central moments* which are related to the *cumulants* c_ν. The second and third cumulants are given by

$$c_\nu = \langle (\; x - \langle x\rangle \;)^\nu\rangle \quad , \quad \nu = 2, 3 \; . \tag{3.4}$$

An easy general definition of c_ν is not possible, but they are connected with the moments by the characteristic function $\mathcal{C}(s)$, which is given on the one hand by

$$\mathcal{C}(s) = \left\langle e^{isx}\right\rangle = \int e^{isx}p(x)dx \; , \tag{3.5}$$

which means that $p(x)$ is simply the Fourier transform of $\mathcal{C}$. The generating function $\tilde{\mathcal{C}}(s)$ for cumulants is defined by $\tilde{\mathcal{C}}(s) = \log\left(\mathcal{C}(s)\right)$.

On the other hand, $\mathcal{C}(s)$ can be defined by the moments μ_ν and the cumulants c_ν as

$$\mathcal{C}(s) = 1 + \sum_{\nu=1}^{\infty} \frac{(is)^\nu}{\nu!}\mu_\nu = \exp\left[\sum_{\nu=1}^{\infty} \frac{(is)^\nu}{\nu!}c_\nu\right] , \tag{3.6}$$

and comparison leads to the known identities

$$\begin{aligned} c_1 &= \mu_1 , \qquad c_2 = \mu_2 - \mu_1^2 , \\ c_3 &= \mu_3 - 3\mu_1\mu_2 + 2\mu_1^3 , \\ c_4 &= \mu_4 - 3\mu_2^2 - 4\mu_1\mu_3 + 12\mu_1^2\mu_2 - 6\mu_1^4 , \quad \ldots . \end{aligned} \tag{3.7}$$

Hence, the first moment equals the first cumulant and is just the mean value, the most important characteristics of the stochastic variable. The second cumulant is the variance and therefore strictly connected to the standard deviation $\sigma = c_2^{1/2}$, which characterizes the variability. The smaller σ the more exactly we can predict a variable. The third cumulant describes the symmetry of the probability distribution. In principle we need all moments or cumulants for a complete description of the stochastic variable, but higher order cumulants describe rather negligible details and we can therefore focus on the first orders.

Correlations: Another fundamental property is the correlation $\mathbf{K}$ between stochastic variables X_i with $i = 1, 2, ..., N$. If we know some realization of X_i, say $X_k, ..., X_N$, correlation leads to an information gain, i.e. larger predictability of the unknown variable $X_1, X_2, ...X_{k-1}$. The most compact definition can again be given by the characteristic function defined as Equation (3.5), in the case of several variables by

$$\mathcal{C}(s_1, s_2, ...s_N) = \langle \exp i\left[s_1X_1 + ... + s_NX_n\right]\rangle , \tag{3.8}$$

as the inverse Fourier transform of the joint probability distribution $p(X_1, ...X_N)$. The multiple correlation of order N is then defined by

$$\mathbf{K}(X_1, ...X_N) = \frac{1}{i^N}\frac{\partial^N \log \mathcal{C}(s_1, ...s_N)}{\partial s_1 ...\partial s_N}\bigg|_{s_1=...=s_N=0} . \tag{3.9}$$

A well known example is the *covariance* or *cross correlation* between two variables $\mathbf{K}(X_1, X_2) = \langle X_1X_2\rangle - \langle X_1\rangle \langle X_2\rangle$ which is often normalized by the standard deviations of the two variables leading to the dimensionless correlation coefficient

$$\rho = \frac{\mathbf{K}(X_1, X_2)}{\sigma(X_1)\sigma(X_2)} . \tag{3.10}$$

Stochastic process: So far we considered only stochastic variables X. But biological processes are embedded in time and our observables are random functions in time $X(t)$. Thus, we have a probability density not only depending on the realizations X_i, but additionally on the time t_i of their occurrence leading to $p_N(X_1, ..., X_N\,; t_1, ..., t_N)$. One might assume t_i as the recording time and X_i as the measured quantity like the fluorescent signal. The random function $X(t)$ is therefore determined by the infinite sequence of probability densities

$$p_1(X_1; t_1)\ , \quad p_2(X_1, X_2; t_1, t_2)\ , \quad p_3(X_1, X_2, X_3; t_1, t_2, t_3)\ , \quad ...\ , \tag{3.11}$$

whereby higher order densities do always contain the information of lower order densities. It is convenient to introduce *moment functions* m_ν and *correlation functions* k_ν

$$m_\nu(t_1, ..., t_\nu) = \langle X_{t1}, ..., X_{t_\nu} \rangle \tag{3.12}$$

and

$$k_\nu(t_1, ..., t_\nu) = \mathbf{K}\left[X_{t_1}, ..., X_{t_\nu}\right]\ . \tag{3.13}$$

A stochastic process is completely characterized by the infinite sequence of (3.12) or (3.13).

In this case, the characteristic function is given by a functional that connects the two characteristics m_ν and k_ν analogously to Equation (3.6) by the following definition. Consider a natural number v and fix v arbitrary numbers $z_1, ..., z_v$ and v positive times $t_1, ..., t_v$ and the characteristic functional $\mathcal{C}(z_1, ..., z_v; t_1, ..., t_v)$ is given by

$$\begin{aligned} 1 + \sum_{s=1}^{\infty} \frac{i^s}{s!} \sum_{\alpha,...,\omega=1}^{v} m_s(t_\alpha, ..., t_\omega) z_\alpha ... z_\omega = \\ = \exp\left(\sum_{s=1}^{\infty} \frac{1}{s!} \sum_{\alpha,...,\omega=1}^{v} k_s(t_\alpha, ..., t_\omega) z_\alpha ... z_\omega \right)\ . \end{aligned} \tag{3.14}$$

To derive explicit relations between m_ν and k_ν, both sides of (3.14) have to be differentiated over all z_i and a subsequent setting of $z_i = 0$. By doing so, we find for the first three pairs the relations

$$\begin{aligned} m_1(t_1) &= k_1(t_1) \\ m_2(t_1, t_2) &= k_2(t_1, t_2) + k_1(t_1) k_1(t_2) \\ m_3(t_1, t_2, t_3) &= k_3(t_1, t_2, t_3) + 3\{k_1(t_1) k_2(t_2, t_3)\}_s + k_1(t_1) k_2(t_2) k_3(t_3)\ , \end{aligned} \tag{3.15}$$

whereby $\{...\}_s$ denotes symmetrization with respect to all permutations of its arguments.

3.5.2 Point processes

For the analysis of Ca^{2+} oscillations, we are mainly interested in the times between Ca^{2+} spikes, since they point out the main characteristics of the underlying process. Another possibility would be a description of the detailed signals with the methods derived above, but this is not a very promising strategy as the whole signal contains too many fluctuations, which may originate from other processes than the one we are interested in. Hence we reduce the signal to the times t_i at which we observe a Ca^{2+} spike, from which we can determine the *waiting times* and the corresponding density.

These times lead to a set of randomly distributed points on the time axis. Such a set of points with random positions in space is called *point process* [42]. Typical examples of point processes are times at which customers enter a shop, incandescent lamps in a house fall out or stock prices of different companies intersect. Due to their frequent appearance, point processes have been extensively studied during the last decades [256, 232, 43, 42, 41].

Alternatively to the moment functions m_ν, a point process can be completely characterized by an infinite sequence of distribution functions [256]

$$n_1(t_1)\ , \quad n_2(t_2,t_1)\ , \quad n_l(t_l,...,t_2,t_1)\ , \quad ....\ , \tag{3.16}$$

determining the probability $n_\nu(t_1,t_2,...,t_\nu)dt_1...dt_2dt_\nu$ that at least one point falls in every of the ν non-overlapping intervals $(t_1,t_1+dt_1),...(t_\nu,t_\nu+dt_\nu)$. Corresponding to Subsection 3.5.1 the process can be also described by the correlation functions k_ν.

A powerful tool derived by Stratonovich [232] in the theory of random points is the generating function

$$L_T\left[v(t)\right] = \left\langle \prod_{i=1}^{n} [1+v(t_i)] \right\rangle \tag{3.17}$$

on the interval $0<t<T$, whereby n is the number of points falling in this interval at positions t_i and $v(t)$ denotes a rather unspecific function. By performing the averaging explicitly in Equation (3.17), we find the relation

$$L_T\left[v(t)\right] = 1+\sum_{s=1}^{\infty}\frac{1}{s}\int_0^T ... \int_0^T n_s(t_1,...,t_s)v_1(t_1)...v_s(t_s)dt_1...dt_s \tag{3.18}$$

that connects the generating function with the probability functions n_s.

The waiting time density $\mathcal{P}(T)$ of a point process is connected to the generating function [256] by

$$\mathcal{P}(T) = -\frac{d}{dT}L_T\left[-1\right] = \sum_{s=1}^{\infty}\frac{(-1)^s}{s!}\int_0^T ... \int_0^T n_s(t_1,...,t_s)dt_1...dt_s\ , \tag{3.19}$$

what can be used to determine $\mathcal{P}$.

Independent process: The most simple case of a point process is a set of *independent* random points, i.e. the intervals are identically distributed with a specific density. Then the distribution functions factorize, i.e. $n_l(t_1, ..., t_l) = n_1(t_1), ..., n_1(t_l)$ and hence all correlation function k_l vanish for $l > 1$ and the process is completely determined by $n_1(t)$, since it gives the probability of an event per unit time and denotes the *rate* of the process. The waiting time density in the case of independent random points obtained from Equation (3.19) is

$$\mathcal{P}(T) = n_1(T) \exp\left(-\int_0^T n_1(t)dt\right) . \tag{3.20}$$

Stationary process: A random process is called stationary if its statistical characteristics are invariant under time shifts, i.e.

$$n_l(t_1, ..., t_l) = n_l(t_1 + \tau, ..., t_l + \tau) \tag{3.21}$$
$$k_l(t_1, ..., t_l) = k_l(t_1 + \tau, ..., t_l + \tau) . \tag{3.22}$$

That implies that the correlation functions only depend on time differences and particularly that $n_1(t) = k_1(t) = n_0$ does not depend on time.

The stationary system of independent random points having a constant rate n_0 is the Poisson process. Famous examples are the radioactive decay or how rain drops fall on earth. A more mathematical description is given by taking a large interval $[i_a, ..., i_e]$ and mark uniformly a fixed number N_m of ciphers $\{i_1, i_2, ..., i_{N_m}\}$. In a short interval $[j_a, ..., j_e]$, i.e. $i_e - i_a \gg j_e - j_a$, the ciphers i_i lying within this interval are Poisson distributed. The waiting time density of a Poisson process is given by

$$\mathcal{P}_{\text{poi}}(T) = n_0 \exp(-n_0 T) . \tag{3.23}$$

An important tool for stochastic processes is the *power spectral density* or shorter the power spectrum $S(X, \omega)$ of a stochastic process X defined by

$$S(X, \omega) = 2 \int_{-\infty}^{\infty} e^{i\omega\tau} \langle X(t)X(t + \tau)\rangle \, d\tau , \tag{3.24}$$

which is determined by the autocorrelation function $\langle X(t)X(t + \tau)\rangle$. The power spectrum shows how much power of a signal is given by specific frequencies ω. For a Poisson process $S(X, \omega)$ is constant and equals the rate n_0, thus it is white noise.

Characteristic measures: Although the probability density respectively the waiting time density $\mathcal{P}$ characterizes the process completely, it is complicated to measure this in experiments directly. Therefore, we introduce alternative tools used for the analysis and show their connections to the more theoretical distribution densities.

The relative scattering of the intervals of the point process can be characterize with the *Coefficient of Variation*

$$CV = \frac{\sqrt{c_2}}{c_1} = \frac{\sigma}{\mu_1} \,, \tag{3.25}$$

sometimes called the normalized standard deviation. For a Poisson process $CV = 1$ holds and is a reference value.

Correlations between point intervals can be quantified by the *serial correlation coefficient* (SCC) ρ_k defined by

$$\rho_k = \left\langle \frac{\mathrm{Cov}(X_i, X_{i+k})}{\sigma_i \sigma_{i+k}} \right\rangle_i \,. \tag{3.26}$$

A *renewal process* is a specific independent process with vanishing ρ_k for $k > 0$.

Another useful measure is a random counting variable $N(t_1, t_2)$ representing the number of points falling in the interval (t_1, t_2). For the interval $(0, T)$ we denote $N(0, T) = N$ and express the moments in terms of the distribution function. By setting $v(t) = z$ in the generating functional (3.17), we find $L_T[z] = \left\langle (1+z)^N \right\rangle$ and consequently

$$\left.\frac{\partial L_T[z]}{\partial z}\right|_{z=0} = \left\langle N(1+z)^{N-1} \right\rangle |_{z=0} = \langle N \rangle \,, \quad \left.\frac{\partial^2 L_T[z]}{\partial z^2}\right|_{z=0} = \left\langle N^2 \right\rangle - \langle N \rangle \,. \tag{3.27}$$

With the definition (3.18) and the particular choice for v we can express the moments of N by the distribution functions using the results (3.27) as

$$\langle N \rangle = \int_0^T n_1(t) dt, \quad \left\langle N^2 \right\rangle = \langle N \rangle + \int_0^T \int_0^T n_2(t_1, t_2) dt_1 dt_2 \,. \tag{3.28}$$

These quantities can be used for another measure, the Fano factor $F(T)$ [66], that describes the relative dispersion of of the random counting variable N by

$$F(T) = \frac{\langle N^2 \rangle - \langle N \rangle^2}{\langle N \rangle} \,. \tag{3.29}$$

Hence, the Fano factor is a function of T and can characterize variability on all experimentally accessible time scales, whereas the Coefficient of Variation describes the variability on the time scale of the mean $\langle X \rangle$.

For experimental data we divide the time course into M non-overlapping time intervals of length T. The number of points in each interval is denoted by N_i, and we can calculate the first two moments as

$$\langle N \rangle = \lim_{M \to \infty} \frac{1}{M} \sum_{i=1}^{M} N_i, \quad \left\langle N^2 \right\rangle = \lim_{M \to \infty} \frac{1}{M} \sum_{i=1}^{M} N_i^2 \,. \tag{3.30}$$

For $M \to \infty$ the Fano factor is given by $F(T) = 1 - n_0 T$, i.e. for $T \to 0$ $F(T)$ equals one. For increasing T, $F(T)$ decreases linearly and the time scale at which F derivates from that linear decay denotes the minimal interval.

3.5.3 Spike train analysis

For the methods derived in the previous section we rely on point processes. Thus we reduce the data to a spike train which consists of the superposition of δ- pulses

$$\varsigma = \sum_{i=1}^{N} \delta(t - t_i) \ , \tag{3.31}$$

where t_i is the time at which the spike occurs and N corresponds to the number of spikes that occur during the observation time $\mathcal{T}$.

The rate r and the instantaneous rate $n_1(t)$ are the basic statistical measures of a spike train [107]. The rate averaged over the time of the observation $\mathcal{T}$ is defined by

$$r = \frac{N}{\mathcal{T}} = \frac{1}{\mathcal{T}} \int_0^{\mathcal{T}} \varsigma(t) dt \ , \tag{3.32}$$

and the instantaneous rate is given by the ensemble average of different realizations of the spike train as

$$n_1(t) = \lim_{\Delta t \to 0} \frac{1}{\Delta t} \int_t^{t+\Delta t} \langle \varsigma(t') \rangle \, dt' \ . \tag{3.33}$$

Here, $n_1(t)$ is the probability to observe a spike in the interval $(t, t + dt)$. For stationary processes with a time-independent firing rate $n_1(t) = const.$, the relation $n_1 = \lim_{\mathcal{T} \to \infty} r$ is valid.

An important statistical model is the renewal process [41]. The probability for a spike depends only on the elapsed time since the last spike, i.e. the systems do not have a long range memory and no significant correlations. Thus the intervals between successive spikes are statistically independent. In the case of a renewal spike train the *interspike intervals* (ISIs) describe the process sufficiently by the probability density function $p(T)$ of the interspike intervals T. But if the renewal assumption does not hold, the process must be defined by the infinite sequence of all joint ISI probability densities $p(T_1, ..., T_l)$ with $l = 1, 2, ...$.

The essential and experimentally accessible quantities are the mean $\mathrm{T_{av}}$ and the variance $\langle \Delta T \rangle = \sigma^2$ of the ISIs

$$\mathrm{T_{av}} = \lim_{N \to \infty} \frac{1}{N-1} \sum_{i=2}^{N} (t_i - t_{i-1}) \tag{3.34}$$

$$\sigma^2 = \langle \Delta T \rangle = \lim_{N \to \infty} \frac{1}{N-1} \sum_{i=2}^{N} (t_i - t_{i-1})^2 - \mathrm{T_{av}^2} \ . \tag{3.35}$$

These relations can be equivalently expressed in terms of the ISI probability distribution $p(t)$ as

$$\mathrm{T_{av}} = \int_0^\infty tp(t)dt \tag{3.36}$$

$$\sigma^2 = \langle \Delta T \rangle = \int_0^\infty t^2 p(t)dt - \mathrm{T_{av}^2} \,, \tag{3.37}$$

connecting the experimental data and their theoretical counterparts in correspondence to the two compatible definitions of a stochastic process by a large set of realizations or the distribution density as discussed in the beginning of Section 3.5.

In general, the mean is connected to the rate of a process by

$$\mathrm{T_{av}} = \lim_{\mathcal{T}\to\infty} \left(\frac{1}{\mathcal{T}} \int_0^{\mathcal{T}} \varsigma(t)dt \right)^{-1} \,, \tag{3.38}$$

which reduces to $\mathrm{T_{av}} = 1/r$ for stationary spike trains, i.e. the mean equals the reciprocal rate.

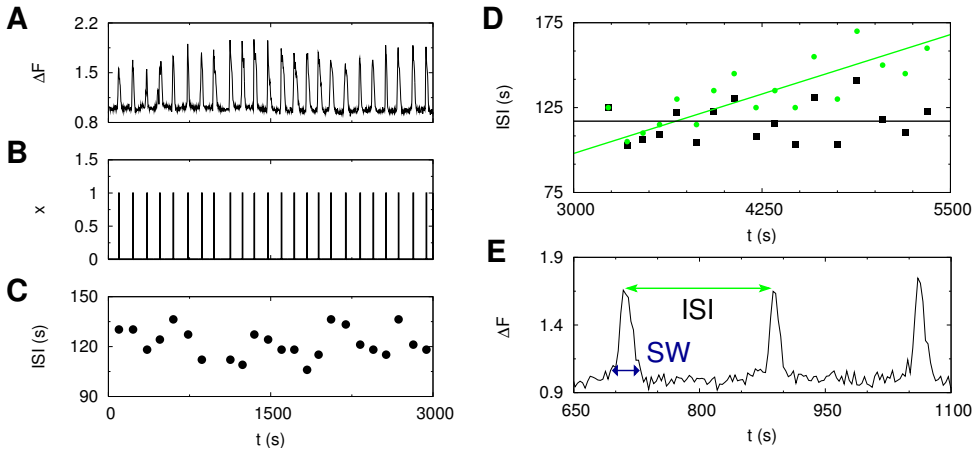

Figure 3.1: Data generation for analysis. From the fluorescence signal (**A**) we determine the corresponding spike train (**B**) by the fluorescence maxima. From that we can determine uniquely the ISI following each spike (**C**). To obtain stationary spike trains from non stationary data which are often produced by stimulated cells we remove trends from original data (green dots) and obtain the corrected data (black dots) (**D**). The spike width (SW) is defined by the full width at 10 % of the maximum as depicted by the blue arrow in **E**.

Spike train generation: In the following investigation we will analyze ISIs of Ca^{2+} oscillations to deduce the underlying mechanism. The ISIs are obtained from the fluorescence data by translating the raw data into a spike train as shown

in Figure 3.1A and B. Here, we define as a spike the event that the fluorescence signal exceeds a threshold of 20 % above the base level and the spike time t_i by the location of the fluorescence maximum. The characteristics of the spike trains do not differ too much by changing the threshold to 10 % or 40 %. From the spike trains we can determine the interspike intervals and the mean and the standard deviation by Equations (3.34). The use of ISIs is the reason why we can use non ratiometric dyes, since we are not interested in the absolute Ca^{2+} concentration but in the time between two spikes.

The analysis demonstrates that even rather regular oscillations exhibit variations in the ISIs as can be seen in Figure 3.1C, where each dot corresponds to the ISI following the actual spike. The ISI are not constant and do neither show a smooth time course as they would do for a deterministic process, but are scattered around the average ISI T_{av} of about 120 s.

These sequences of ISIs are used to decipher the spike generating process. The serial correlation coefficient (3.26) of a spike train l takes thus the concrete form

$$\rho_k^{(l)} = \frac{\sum_{i=1}^{N-k}\left[\left(\mathrm{ISI}_i - \frac{1}{N-k}\sum_{j=1}^{N-k}\mathrm{ISI}_j\right)\left(\mathrm{ISI}_{i+k} - \frac{1}{N-k}\sum_{j=1}^{N-k}\mathrm{ISI}_{j+k}\right)\right]}{\sqrt{\sum_{i=1}^{N-k}\left(\mathrm{ISI}_i - \frac{1}{N-k}\sum_{j=1}^{N-k}\mathrm{ISI}_j\right)^2 \sum_{i=1}^{N-k}\left(\mathrm{ISI}_{i+k} - \frac{1}{N-k}\sum_{j=1}^{N-k}\mathrm{ISI}_{j+k}\right)^2}}. \tag{3.39}$$

Stationary spike train: The above methods of analysis are meaningful for stationary processes only. However, most experimental records of stimulated HEK cells have a slight trend and eventually stop oscillating. We reduced that trend by leaving out parts of the ISI series in the beginning and end showing very obvious trends and removed linear trends from the remaining series before, we calculated the average ISI T_{av}, the standard deviation σ and correlations. This is illustrated in Figure 3.1D.

To ensure that the spike trains are really stationary, we monitor the behavior of both, the mean T_{av} and the standard deviation σ while averaging over the sequence of ISI. During the average procedure we determine T_{av} and σ of the spike train for each ISI that is added to the analysis leading to saturating functions for T_{av} and σ in dependence on the number of interspike intervals N_{ISI} born in mind. We only include those spike trains in our analysis, which exhibit merely deviations smaller than 5 % in $T_{av}(N_{\mathrm{ISI}})$ and $\sigma(N_{\mathrm{ISI}})$ for the last three ISIs.

Spike width (SW) and activity change: The spike width of single Ca^{2+} transients was determined (when analyzed) as the full width of the Ca^{2+} transient at 10 % of its maximum as depicted in Figure 3.1E. We determined the duration of a single calcium transient at 10 % of its maximal ΔF value, where we considered calcium transient duration from 4 s to 120 s as single calcium spikes. Sometimes,

we observed calcium transients lasting longer. These transients were also considered when counting the number of cells exhibiting calcium activity, but they were not included in the analysis of the spike width. This alternative definition reflects the active phase of cells much better than determining the full width at half maximum (FWHM) would do.

3.5.4 Statistical analysis

Most of the analysis is based on the characteristic measures introduced in the previous section for stochastic processes. For the analysis in Chapter 5 we use additionally the following methods.

Reacting cell number: To characterize the cell behavior in dependence on the temperature, we count the number of cells which exhibited a Ca^{2+} signal during a drop in temperature.

As acute tissues much more prone to photo damage we used shorter recording times for slices. For experiments in slices, time windows of 5 min for each different condition where analyzed. For experiments in cultures 10 min time windows were used. The number of active cells exhibiting a Ca^{2+} signal at higher temperature was expressed as a percentage of the number of cells responding within the reference measurement. The results obtained from different experiments for a given condition were averaged.

As a second measure, an activity parameter was evaluated and compared for the different conditions: in contrast to calcium activity which describes the general observation of calcium transients, the 'Ca^{2+} signaling activity' was defined as the average change in the ΔF value of single cells. The obtained value under control conditions was set to 100 %. The 'Ca^{2+} signaling activity' served as a general measure for activity to obtain an 'average activity profile' of the recordings including all cells and not only to compare the activity of active cells between the control and experimental conditions.

Statistical tests: All values are expressed as mean $\pm$ standard deviation if not stated otherwise. Further statistical analysis of the data was performed with the SPSS software (SPSS Inc.). For revealing significant differences between reacting cell numbers and average activity, the multiple Kruskal-Wallis Test was used to test for significant differences between all groups within a set of groups and if it was positive, each group was separately compared with its respective control by the paired Mann-Whitney Test. These tests are only suitable for independent variables. Since the values of the activity changes were dependent, significance between the different time windows was tested by the two-tailed Student's T-test for unequal variance or by the Wilcoxon Test. Significance was generally defined as $p < 0.05$, high significance as $p < 0.005$.

3.6 Summary

In this chapter we have introduced the tools we will use in the next chapters to explore the mechanism of cytosolic Ca^{2+} oscillations. Besides a brief description of the four different cell types, the experimental and analysis methods are introdued leading to the following way of proceeding:

- The cytosolic Ca^{2+} concentration of different cell types is measured over time by fluorescent dyes leading to time series of the fluorescent signal ΔF.
- From the obtained data, spike trains are generated by determining the event times of the fluorescent maxima.
- The resulting interspike intervals (ISIs) defined by the time between two succesive spikes describe the assumed point process.
- To characterize the process we rely on stationary processes, and hence eventually trends in the ISIs are removed.
- The remaining data are analyzed with respect to their variability by determining the moments of the spike trains and correlations between ISIs.

This procedure is used next to characterize the cellular behavior and the underlying mechanism.

Chapter 4

Oscillation mechanism

In this chapter[1] we would like to clarify the open question of the oscillation mechanism of intracellular Ca^{2+}. This is embedded in the more general framework of how random molecular events are orchestrated into reliable cellular behavior. If many molecules are involved, it is generally assumed that the cell behaves like a continuously object and the law of large numbers guaranties predictable behavior [256]. That is what most models in Ca^{2+} dynamics adopt [203, 62, 83] as described in Section 2.5. They assume the cell as a well stirred reactor and neglect the physiological arrangement of channel clusters summarized in Figure 2.4. Especially the spatial inhomogeneity of release sites leads to a hierarchical signal generation. Global oscillations arise from Ca^{2+} waves initiated locally [167, 135, 23, 248, 136]. Such a local mechanism is predicted to lead to stochastic oscillations because although each cell has many IP_3Rs and Ca^{2+} ions, the law of large numbers does not apply to the initiating event [62, 60], which is restricted to very few IP_3Rs by steep Ca^{2+} concentration gradients [23, 136, 249], that are shaped by SERCA pumps.

Oscillations of intracellular Ca^{2+} exhibit a spiking behavior, which appears rather regular by casual inspection as the examples in Figure 2.1 show. This led to the formulation of models with an oscillatory deterministic regime [203, 62, 83], but cells might exhibit stochastic dynamics which produce very similar global signals. This type of dynamics, often described as a stochastic medium [182, 99, 122, 60, 39], was predicted theoretically for reaction-diffusion systems with discrete stochastic sources of the diffusing species. Intracellular Ca^{2+} dynamics may be perceived as a stochastic medium: the diffusing species is cytosolic Ca^{2+} and the discrete stochastic sources are ion channels. Such systems generate spatio-temporal structures by wave nucleation due to thermal noise. In general, that leads to random spike sequences. The randomness does not arise from small numbers of molecules in the system, but rather from the fact that global events are initiated locally. Stochastic media exhibit

[1]The chapter is adopted in parts from [219] and [218]

almost regular oscillations in the regime of array enhanced coherence resonance (AECR) [182, 99, 122, 60, 39]. Here wave initiation is frequent enough to ensure that waves emerge as soon as the refractory period has passed. While there is experimental and theoretical evidence for the nucleation of global events by local events [23, 136, 249], we investigate in the following the function of spatial coupling of IP_3Rs by Ca^{2+} diffusion and whether Ca^{2+} spike sequences are random caused by repeated wave nucleation. This would make Ca^{2+} signaling the first biological example of AECR.

4.1 Theoretical prediction

As described in Section 2.3, release of Ca^{2+} occurs by intracellular Ca^{2+} channels, notably inositol 1,4,5-trisphosphate receptors (IP_3R), and Ca^{2+} is then resequestered into the ER by Ca^{2+} pumps (SR/ER Ca^{2+}-ATPases, SERCA). IP_3Rs are regulated by the Ca^{2+} they conduct, such that fast activation by cytosolic Ca^{2+} and slower inhibition lead to a bell-shaped Ca^{2+}-dependence of the stationary open probability of the IP_3R [20, 246, 130] as shown in Figure 2.4E. Within the membrane of the ER, clusters of IP_3Rs are separated by perhaps 1-7 μm [248, 136, 234], and clustering is also dynamically regulated [244, 34]. These clusters of channels generate global concentration spikes via a hierarchy of Ca^{2+} release events [167, 135, 23] that depend upon Ca^{2+} diffusing between IP_3Rs to activate successive clusters [62, 18]. The smallest Ca^{2+} release events, "blips" [167], probably reflect random openings of single IP_3Rs. Larger events, "puffs", lasting tens of milliseconds and restricted to a volume of less than 0.5 fl, reflect the almost simultaneous opening of a few IP_3Rs within a cluster [167, 248, 136, 234]. Many coordinated puffs form oscillations and waves [62, 193, 36]. Ca^{2+} oscillations therefore may depend upon both the spatial organization of IP_3Rs and their regulation by Ca^{2+} [246, 130, 2].

There are two obvious possibilities to orchestrate these elemental events. With an oscillatory dynamics arising from local interactions between individual IP_3Rs and their ligands, each IP_3R cluster is also an oscillator because channels within a cluster are synchronized by Ca^{2+} diffusion [249]. Characteristics of the global oscillation, like period and amplitude, would be determined by local parameters such as channel state dynamics. Spatial coupling of channel clusters by Ca^{2+} diffusion would serve only to synchronize the oscillations leading to a description by coupled phase oscillators. The global oscillation would be deterministic: it has regular ISI and the timing of each spike is predictable. But recent theoretical studies suggest that IP_3R clusters are not deterministic oscillators [60, 250]. A deterministic model generates oscillations only if IP_3Rs are exposed to Ca^{2+} concentrations similar to those that cause their half-maximal regulation (ca. 0.1-10 μM) [20, 246, 130, 2]. Local Ca^{2+} concentrations near open IP_3Rs are much higher and do not therefore

allow for deterministic oscillations [249, 250, 211, 14].

Another possibility is that stochastic fluctuations render IP_3R clusters oscillatory. Stochastic behavior of IP_3R clusters is observed experimentally as Ca^{2+} puffs [135, 136]. Simulations show that random binding and dissociation of Ca^{2+} and IP_3 to IP_3Rs are sufficient sources of stochastic fluctuations to explain the random generation of Ca^{2+} puffs [60, 238, 213]. However, these fluctuations alone cannot generate the observed time scale of global oscillations because puff durations and frequencies are 3 to 100 times faster than the ISI in cells [135]. Processes occurring within a single IP_3R cluster do not, therefore, transform random molecular behavior into oscillations. Local processes are not oscillatory, and so the idea that channel clusters are oscillators is untenable. A higher level of spatial organization is required to generate oscillations. The next spatial level is the cell, with its array of IP_3R clusters each capable of generating Ca^{2+} puffs.

4.1.1 Hypotheses

The previous considerations suggests that intracellular Ca^{2+} behaves as a stochastic medium. Experimental and theoretical studies show that Ca^{2+} puffs can initiate global Ca^{2+} spikes [62, 135, 23, 136, 60]. But theoretical analysis suggests that cells would not oscillate deterministically, instead they would produce random sequences of global Ca^{2+} release events [62, 60, 250, 251].

From this knowledge we expect Ca^{2+} oscillation to show four characteristic traits:

- **Existence of a minimal ISI:** After a Ca^{2+} spike the cell needs a more or less fixed time T_{cell} to return into the excitable state. This time is needed to pump back the released Ca^{2+} from the cytosol into the ER and to bring channels from the inhibited state to the excitable state. This property can be seen in Section 4.2.1.

- **Relation of the mean and the standard deviation:** Wave nucleation occurs through multiple puffs within a limited space. This corresponds to rare and independent events and leads to the characteristics of a Poisson like process. Hence, we expect the system to obey the main characteristic of Poisson like processes. A Poisson process has a waiting time density of the form

$$\mathcal{P}_{\text{poi}}(t) = \lambda e^{-\lambda t} \,. \tag{4.1}$$

  The most dominant property of a Poisson process is the equality of the mean and the standard deviation $\mu = \sigma = \lambda^{-1}$ leading to $CV = 1$ as described in Section 3.5.2. Together with the existence of a minimal ISI that would lead to a linear dependence of the standard deviation on the mean for the measured ISIs, as studied in Section 4.2.1.

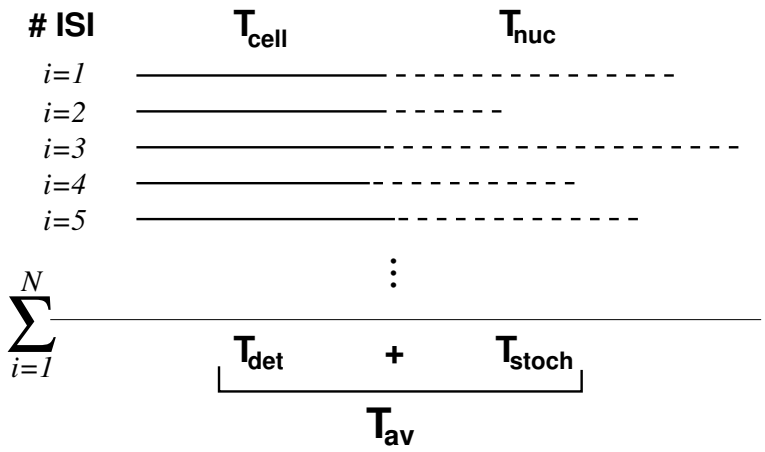

Figure 4.1: Assumption of ISIs and average procedure. The Ca^{2+} oscillation respectively the corresponding spike train has varying ISIs. Each ISI consists of two parts, a cell specific deterministic part, that blocks the cell for a time T_{cell}, and a stochastic time T_{nuc} that is needed to build a critical nucleus of puffs leading to a global Ca^{2+} spike. To characterize the process we average over all ISIs leading to the mean period $T_{av} = T_{det} + T_{stoch}$.

- **No correlation of successive ISIs:** Since we assume a stationary Poisson like process, we predict vanishing correlations between successive ISIs as shown in Section 3.5.2. This property of a renewal process characterized by a vanishing serial correlation coefficient (3.26) $\rho_k = 0$ for $k > 0$ is investigated in Section 4.2.2.

- **Influence of spatial coupling:** Modifying the spatial coupling would change the nucleation rate λ in Equation (4.1) and thus affect both frequency and the ability to oscillate [62, 60]. Moreover, we conclude from (4.1) that decreasing λ would lead to slower and more irregular oscillations, which is tested in Section 4.2.3.

Summing up these predictions we expect the ISIs to consist of two parts as depicted in Figure 4.1. The first part corresponds to a cell specific deterministic part, that blocks the cell for a time T_{cell}. The other part is a stochastic time T_{nuc} that is needed to build a critical nucleus of puffs and is determined by the nucleation rate λ. The first part does not vary too much compared to the second one, since it depends on rather constant properties of the cell like pump flux and recovery from inhibition. The second part exhibits larger fluctuations, as wave nucleation has a Poisson like character and is thus a stochastic process with high unpredictability. To analyze this process, we average over all ISIs resulting in the mean period $T_{av} = \langle ISI \rangle = T_{det} + T_{stoch}$, which consists of an average deterministic time T_{det} and a

mean nucleation time. The first is assumed to be rather fixed, whereas the latter part may exhibit a large variability.

For spontaneous oscillations we expect that the second part dominates the ISIs, since without external stimulation the cellular IP_3 level will be low and the probability of a single puff is low and thus the nucleation probability is low. For rather regular oscillations as invoked by stimulation we expect T_{nuc} to be smaller than T_{det} leading to AECR.

4.1.2 Predicted probability density

We first focus on the stochastic component of the ISI and include the deterministic time T_{det} afterwards. From the experimental observation that cells exhibit a relaxation time after a spike [31], we extend the pure Poisson process by a regeneration rate ξ. This regeneration leads to a time dependent nucleation rate Λ of the form

$$\Lambda(t) = \lambda\left(1 - e^{-\xi t}\right) , \tag{4.2}$$

which is zero directly after the last spike and relaxes to λ for large times. ξ could describe e.g. the recovery from inhibition [61] or refilling of the ER. The probability of observing a global wave at time t after the previous spike is given by

$$\mathcal{P}_\xi(t) = \lambda\left(1 - e^{-\xi t}\right) \exp\left[-\int_0^t \lambda\left(1 - e^{-\xi t'}\right) dt'\right] , \tag{4.3}$$

having the form shown in Figure 4.2A. For $\xi \gg \lambda$, $\mathcal{P}_\xi(t)$ converges to a pure Poisson process as shown for $\xi = 1$ and $\lambda = 0.02$ (dotted line) and $\lambda = 0.007$ (dash dotted line). With decreasing ξ, the maximum of the distribution shifts to higher values of t. For fixed $\xi = 0.01$ the width increases with decreasing λ, e.g. $\lambda = 0.06$ (solid line) and $\lambda = 0.01$ (dashed line). From expression (4.3) we can calculate the first two moments as

$$T_{av} = \int_0^\infty t\lambda\left(1 - e^{-\xi t}\right) \exp\left[-\int_0^t \lambda\left(1 - e^{-\xi t'}\right) dt'\right] dt \tag{4.4}$$

$$\left\langle T^2 \right\rangle = \int_0^\infty t^2\lambda\left(1 - e^{-\xi t}\right) \exp\left[-\int_0^t \lambda\left(1 - e^{-\xi t'}\right) dt'\right] dt. \tag{4.5}$$

This can be integrated by parts:

$$T_{av} = \int_0^\infty te^{-f(t)} f'(t)dt = -te^{-f(t)}\Big|_0^\infty + \int_0^\infty e^{-f(t)}dt , \tag{4.6}$$

where the first term vanishes leading to

$$T_{av} = \int_0^\infty e^{-\lambda\left(t + \frac{1}{\xi}e^{-\xi t} - \frac{1}{\xi}\right)}dt \tag{4.7}$$

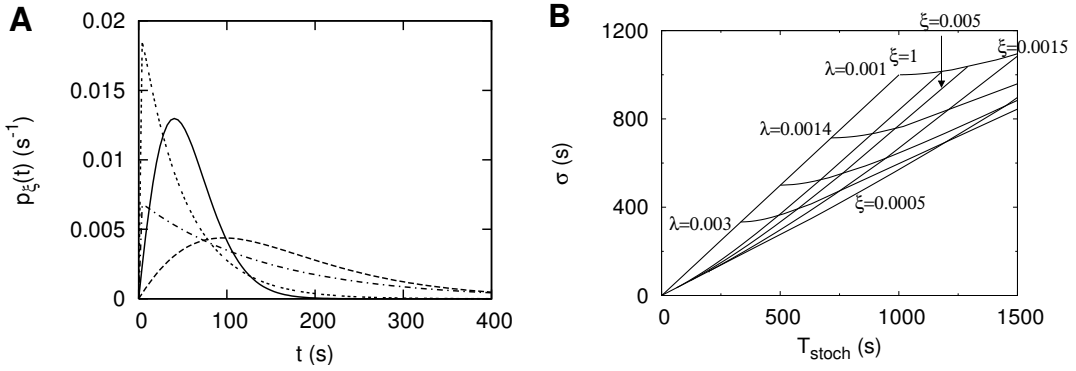

Figure 4.2: **A:** The density (4.3) for different parameters. See text for more details. **B:** σ-T_{stoch} relation for the waiting time density (4.3) resulting from equations. (4.7) and (4.8). The σ -T_{av} relation occurs by shifting the lines to the right by T_{det}.

The second moment $\langle T^2 \rangle$ is given by

$$\begin{aligned} \left\langle T^2 \right\rangle &= \int_0^\infty t^2 e^{-f(t)} f'(t) dt = 2 \int_0^\infty t e^{-f(t)} dt \\ &= 2 \int_0^\infty t e^{-\lambda\left(t + \frac{1}{\xi} e^{-\xi t} - \frac{1}{\xi}\right)} dt \ . \end{aligned} \tag{4.8}$$

Integration yields

$$T_{av} = \frac{e^{\frac{\lambda}{\xi}} \left(\frac{\lambda}{\xi}\right)^{1-\frac{\lambda}{\xi}}}{\lambda} \left[\Gamma\left(\frac{\lambda}{\xi}\right) - \Gamma\left(\frac{\lambda}{\xi}, \frac{\lambda}{\xi}\right)\right] \tag{4.9}$$

$$\left\langle T^2 \right\rangle = \frac{2e^{\frac{\lambda}{\xi}}}{\lambda^2} {}_2F_2\left[\left(\frac{\lambda}{\xi}, \frac{\lambda}{\xi}\right), \left(1 + \frac{\lambda}{\xi}, 1 + \frac{\lambda}{\xi}\right), -\frac{\lambda}{\xi}\right] \ , \tag{4.10}$$

where $\Gamma(x)$ denotes the Euler's Γ-function, $\Gamma(x, y)$ the incomplete Gamma function and ${}_2F_2(\mathbf{x})$ is the generalized hypergeometric function [1]. With the relation for the standard deviation

$$\sigma = \sqrt{\langle T^2 \rangle - {T_{av}}^2} \tag{4.11}$$

we obtain the T_{av}-σ relations shown in Figure 4.2B. Lines $\xi = constant$ arise by varying λ. They start at (0,0) with $\lambda = \infty$ and converge to T_{av}=σ with increasing ξ. The lines $\lambda = constant$ start on T_{av}=σ= λ^{-1} with $\xi \gg \lambda$ very large. Note that the σ-T_{av} relation becomes linear for $\lambda/\xi \to 0$ or $T_{av} \to \infty$ and $\sigma \to \infty$, and that the slope decreases from 1 for $\xi \to 0$. ξ and λ are measured in s^{-1}.

We did not consider a deterministic part T_{det} of the ISI in the above calculations which represents an absolute refractory part of the ISI. Such a deterministic

part simply moves the curves in Figure 4.2 to larger values of T_{av}. The complete distribution including T_{det} is:

$$\mathcal{P}_\xi(t) = \begin{cases} 0 & , \quad t < T_{\text{det}} \\ \lambda\left(1 - e^{-\xi(t-T_{\text{det}})}\right) \exp\left[-\int_{T_{\text{det}}}^{t} \lambda\left(1 - e^{-\xi(t'-T_{\text{det}})}\right) dt'\right] & , \quad t \geq T_{\text{det}} \end{cases} . \tag{4.12}$$

The analysis of experimental data show that T_{av}, σ and T_{det} vary between individual cells of the same cell type, as we will illustrate in the next section.

4.2 Experimental results

To establish whether intracellular Ca^{2+} oscillations are noisy limit cycle oscillations based on deterministic dynamics or repeated stochastic waves, we performed comprehensive measurements of ISI series in different cell types. In each case, IP_3Rs evoke the Ca^{2+} oscillations as shown in [72, 67, 210] for astrocytes, microglia and HEK cells, as well as in Figure A.1 for PLA stem cells from human adipose tissue. Figure 4.3 shows representative time series of global oscillations in astrocytes, microglia, PLA and human embryonic kidney (HEK) cells.

These examples show that ISIs are not regular, as can be seen in the lower panels in which each dot denotes the time from the actual spike to the next one, the following ISI. The length of the ISIs changes randomly, although in different extent. For the spontaneous oscillations in microglia the ISIs vary between 40 s and 400 s, whereas stimulation induced oscillations in HEK cells do only differ in the range from 50 s to 80 s. The ISIs derived from records like those were used to characterize the oscillation mechanism by determining the serial correlation coefficients ρ_k, mean values T_{av} and the standard deviations σ of the corresponding spike trains.

4.2.1 Experimental σ-T_{av} relation

For a systematic analysis we determine the mean and the standard deviation of many cells for each cell type. The individual cells may differ in a variety of properties. Parameters that act locally on the IP_3R clusters are the IP_3 and the Ca^{2+} base level concentrations that determine the probability of the initiating event P_{puff} of a first puff. The strength of Ca^{2+} extrusion is a main property determined by the expression level of SERCAs and PMCA. Experiments with Ca^{2+} free buffers do not exhibit a significant change of the oscillatory behavior indicating that cells can in general regulate their Ca^{2+} base level sufficiently to low levels in the range of tens of nM. Hence, we expect a similar low Ca^{2+} base level in different cells, which prevents toxic effects.

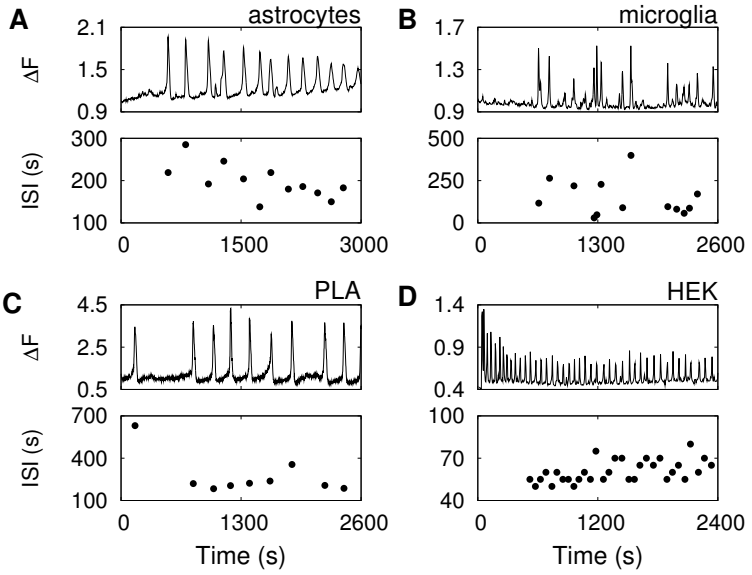

Figure 4.3: IP_3R-mediated Ca^{2+} spikes in various cell types. Representative examples of oscillation time series for astrocytes (**A**), microglia (**B**), PLA cells (**C**), and HEK cells stimulated with 30 µM CCh (carbamyl choline) (**D**). Lower panels show the ISI following each spike, with ISI defined as the interval between consecutive fluorescence maxima.

We expect a larger cell diversity caused by different cell arrangements. First of all, the expression level of IP_3R as well as their spatial arrangement and the localization of the ER have a huge impact. The spatial separation of clusters determines the communication between adjacent clusters. If the release sites are close to each other, a triggering puff can most likely induced a global signal. If the IP_3R clusters are more widely spread the probability of a triggering event P_{trig} is lower, since the nucleation probability of a wave P_{wave} is low. Ca^{2+} has to diffuse over long distances, where it is pumped back into the ER. Other global properties are therefore the pump strength and the buffer amount because they decrease the spatial communication and suppress a cooperative behavior.

The cell individuality leads to different parameters of the waiting time density (4.3) and hence to different mean periods T_{av} and standard deviation σ. This is shown in Figure 4.4 for the four different cell types, where each dot corresponds to the spike train of a single cell.

The standard deviation σ increases with the mean period T_{av} for all cell types and all different stimulation strengths. Another obvious characteristic is the offset of data points on the T_{av}-axis. That indicates the deterministic time T_{det} predicted by our first hypothesis in Section 4.1.1. Further we see that T_{av} and σ exhibit indeed

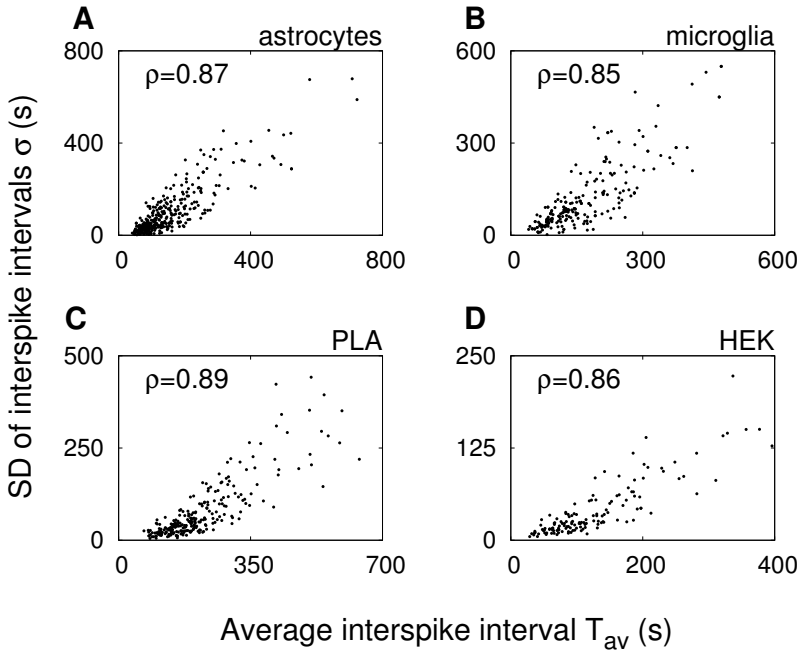

Figure 4.4: Ca^{2+} spikes occur randomly. Dependence of the standard deviation σ of ISI on the average ISI T_{av} for 366 astrocytes (**A**), 224 microglia (**B**), 270 PLA cells (**C**) and 137 HEK cells stimulated with 30 µM CCh (**D**). σ and T_{av} were obtained from time series of single cells by temporal averaging. The correlation coefficient ρ shows that σ and T_{av} are highly correlated in all four cases. A further example for hepatocytes is shown in Figure A.4A.

a linear relation as indicated by the linear correlation coefficient ρ which is close to 0.9 for all cell types.

Standard deviations are of the same order of magnitude as averages for most points, and for large T_{av}, σ and T_{av} are similar. Hence, the uncertainty in predicting the occurrence of a spike is of the same order of magnitude as the mean ISI: Ca^{2+} spikes are random events. If spikes represented the active phase in a deterministic oscillation, the standard deviation of ISI would instead be in the range of the global inter*puff* interval, i.e. between a few hundred milliseconds for short T_{av} and a few seconds for long T_{av}.

Comparison with the predicted σ-T_{av} relation in Figure 4.2B exhibits a good agreement if we include a deterministic time T_{det}. A good test of the model is the slope of the σ-T_{av} dependence.

The time-dependence of the global nucleation rate differs between the different cell types as revealed by the slopes of the relationship between σ and T_{av}. Figure 4.5A shows values of the parameters of the time-dependent global nucleation

rate (Equation 4.2) for the different cell types. The spontaneous oscillations in astrocytes and microglia have a slope of the σ-T_{av}-relation close to 1 and an asymptotic nucleation rate λ much smaller than the relaxation rate ξ. Despite the relatively fast recovery from the previous spike, these oscillations are neither fast nor regular since the asymptotic nucleation rate λ of these cells is small. The stimulated oscillations in HEK cells show the inverse relation between λ and ξ.

Recovery from the previous spike is relatively slow in HEK cells. This corresponds to the initial decline in spike amplitudes in Fig. 4.3 during which the cell reaches a state corresponding to incomplete recovery from a spike during each ISI. One possibility is that insufficient recovery from inhibition or incomplete refilling of the ER causes the decline. We might then suggest that immediately after stimulation, Ca^{2+} re-uptake during the ISI fails to keep pace with release during a spike and successive Ca^{2+} transients decrease in amplitude. But during the stationary phase of oscillations, the two fluxes balance such that Ca^{2+} uptake by the stores during the ISI matches the amount released during the preceding spike. The time-dependent nucleation rate $\Lambda(t)$ reaches only 60 % of λ during an average ISI due to the small value of ξ. However, since the asymptotic nucleation rate λ is rather large, the oscillations in HEK cells have smaller σ than astrocyte oscillations. The values for λ and ξ of PLA cells lie between those for astrocytes and HEK cells.

With the fitted rates λ and ξ we can calculate the mean and the standard deviation by Equations (4.7) and (4.11) and determine the expected CV. In Figure 4.5 CV is shown in dependence on λ and ξ. We see how CV decreases with decreasing ξ and increasing λ. For the fitted rates we obtain values, which correspond to the experimental population slopes in Figure 4.4.

4.2.2 Correlations

The findings above suggest a Poisson process. Especially the σ-T_{av} relation of spontaneous oscillations in glia cells substantiate this hypothesis, since they exhibit a slope of 1, which corresponds to the CV of a pure Poisson process. But also the lower slope for the HEK cells is in agreement with the time dependent Poisson process. Thus we expect that the uncertainty in spike timing is also visible in vanishing correlations between consecutive ISIs. To test that, we calculate the serial correlation coefficient ρ_k defined by Equation (3.39) of the ith and $(i+k)$th ISI of cell individual spike trains. Figure 4.6 depicts ρ_k averaged over a cell population of HEK cells. Similar results are obtained for PLA cells and astrocytes in Figure A.2.

The results demonstrate that consecutive intervals are not correlated, indicating the randomness of the spike-generating mechanism. To confirm that the vanishing correlations are not caused by annulling of opposite correlations of individual cells we merge the ISIs of all cells by normalize them to the corresponding mean period T_{av}. With the resulting spike train we can perform second order statistic. Therefore

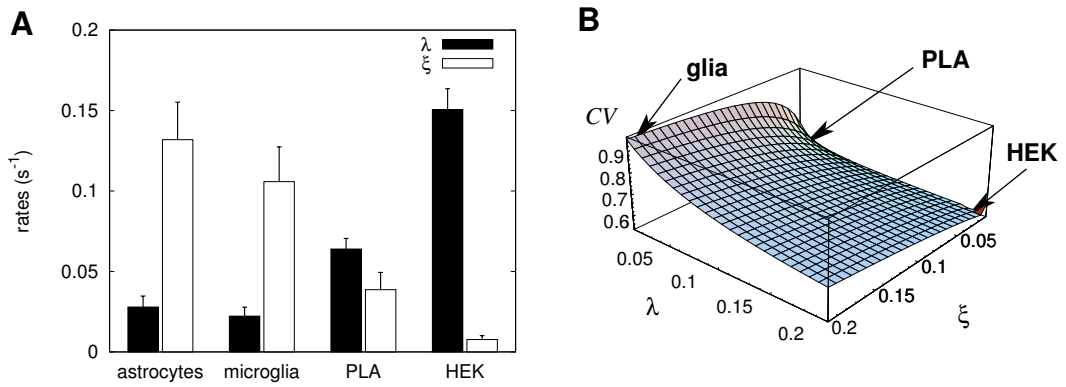

Figure 4.5: Fitted values λ and ξ of the time-dependent global nucleation rate Equation 4.2 for the different cell types and the corresponding CV. **A**: The values were obtained by fitting σ and T_{av} of individual time series to Equations (4.9) and (4.11) to obtain λ and ξ, which were then averaged across all cells of the same type. We have approximated T_{det} by the smallest value of T_{av} observed for the corresponding cell type in the fitting procedure. Error bars show standard errors (s.e.). **B**: Dependence of CV on the parameters of the waiting time density (4.3). The cell specific CV determined by the fitted values for λ and ξ from A are indicated by the arrows and exhibit a good agreement with the population slopes of the σ-T_{av} relation, which correspond to CV without T_{det}.

we calculate the joint distribution density $\mathcal{P}_2(\mathrm{ISI_i}, \mathrm{ISI_{i+1}})$ shown in the first row of Figure 4.7 for the different cell types.

The joint probability distribution exhibits only very small deviations from white correlation, which corresponds to a circular dependence. Moreover, we see that the width is in the range of T_{av}, as expected by the estimated coefficient of variations CV. In this context the narrower distribution of the HEK cells is related to the smaller CV.

Another property we can proof by $\mathcal{P}_2(\mathrm{ISI_i}, \mathrm{ISI_{i+1}})$ is the renewal assumption, i.e. that spikes occur independently from the previous one. Therefore, we calculate the correlation map defined by the difference of the joint distribution density and the product of the single densities

$$\mathcal{P}_2(\mathrm{ISI_i}, \mathrm{ISI_{i+1}}) - \mathcal{P}(\mathrm{ISI_i})\,\mathcal{P}(\mathrm{ISI_{i+1}}) \tag{4.13}$$

shown in the second row of Figure 4.7. Although we obtain a structure of the second order correlation their values are infinitesimally small, namely in the range of 10^{-7}.

The influence of the population averaging on the serial correlation coefficient is shown in the last row of Figure 4.7, where the distribution of the first correlation coefficient ρ_1 is shown. We see that the correlations are centered around zero and

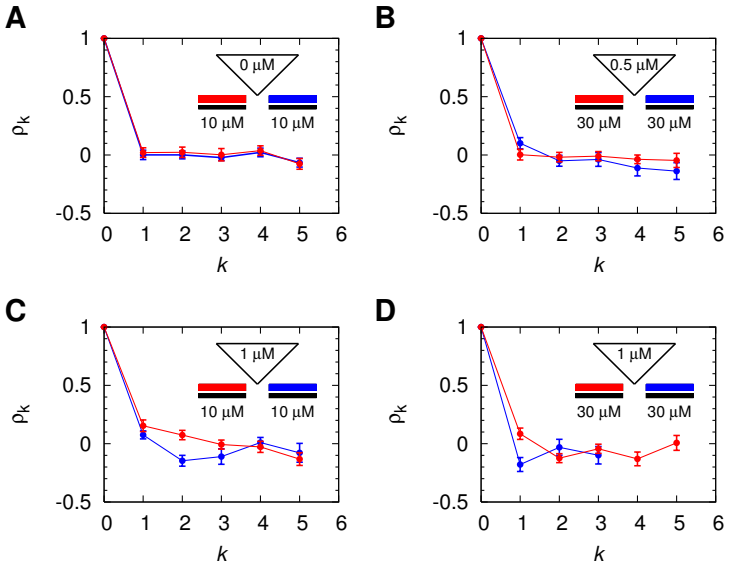

Figure 4.6: Successive ISIs are not correlated in HEK cells. **A-D:** Serial correlation coefficient ρ_k between the ith and $(i+k)$th ISI averaged across time series for HEK cells before (red) and after (blue) loading with additional Ca^{2+} buffer. The first and second periods of recording each lasted 45 min and were interrupted for 10 min to load cells with the concentrations of BAPTA-AM shown within the triangles and then 5 min to allow hydrolysis of the ester. CCh concentrations are shown beneath the black bars. The number of time series measured for the first and the second periods were, respectively: **A:** $n_1 = 35$, $n_2 = 35$; **B:** $n_1 = 35$, $n_2 = 28$; **C:** $n_1 = 31$, $n_2 = 22$ **D:** $n_1 = 29$, $n_2 = 18$. Error bars denote s.e. for averaging over n time series. Correlations for PLA cells and astrocytes are shown in Figure A.2.

that more than 80 % of ρ_1 have an amplitude smaller than 0.25. This does also hold for higher k as can be seen in the representative example of 35 HEK cells in Figure A.3 where the first six serial correlation coefficient are shown color coded for individual cells.

Hence, the vanishing correlations are not predominantly caused by averaging but by the vanishing correlations between single ISIs indicating the stochastic nature of Ca^{2+} oscillations as predicted by our third hypothesis in Section 4.1.1.

Thus we conclude that global oscillations result from a sequence of randomly occurring global Ca^{2+} spikes. The data show also that σ almost vanishes at the smallest values of T_{av}, indicating that almost regular oscillations with ISIs close to T_{det} do exist. The results are similar for spontaneous oscillations in astrocytes, microglia and PLA cells, and for oscillations evoked by different levels of stimulation in HEK cells, suggesting that IP_3-evoked Ca^{2+} oscillations are sequences of stochastic spikes in many cell types.

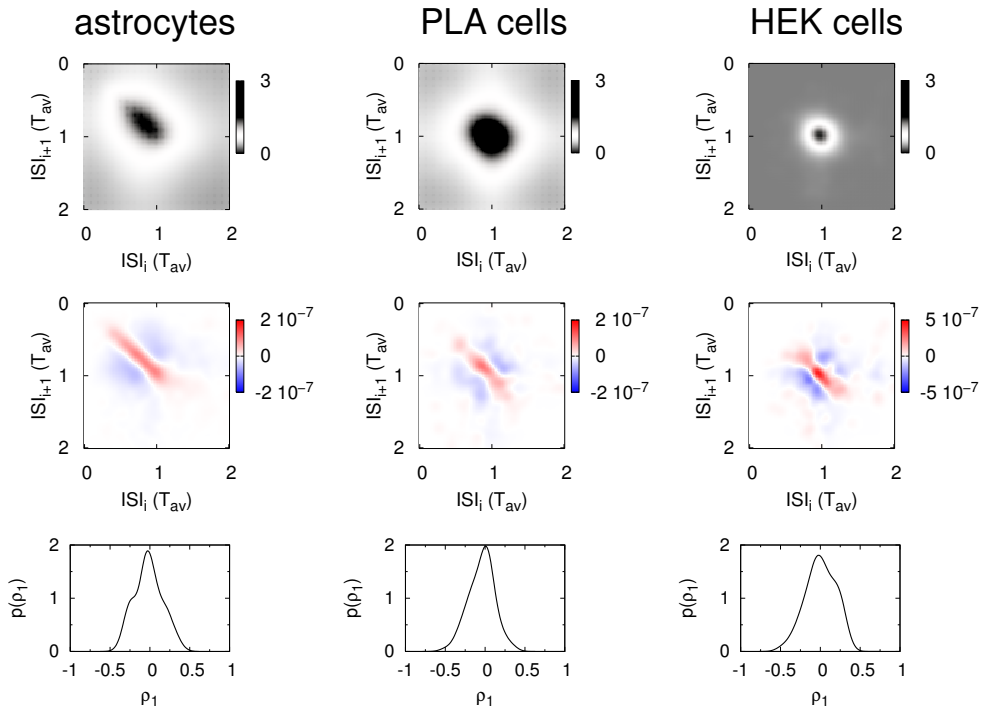

Figure 4.7: Second order statistics for astrocytes (first column), PLA cells (second column) and HEK cells (third column). The joint distribution density $\mathcal{P}_2\left(\mathrm{ISI_i}, \mathrm{ISI_{i+1}}\right)$ of two successive ISIs (first row) for merged spike trains normalized by $\mathrm{T_{av}}$ exhibit the structure of white, i.e. not correlated data for all cell types. Also the correlation map (second row) indicates only very small dependences. This is confirmed by the distribution of the correlation coefficients ρ_1 (third row) obtained from individual spike trains. This does also hold for higher k as can be seen in the representative example of 35 HEK cells in Figure A.3.

Our conclusion is compatible with the idea that each Ca^{2+} spike reflects the passage of a Ca^{2+} wave across the cell driven by successive activation of IP_3R clusters by Ca^{2+} diffusing between them [135, 23, 136]. This mechanism can generate the spectrum of observed shapes of oscillations [62, 60]. The results show that waves initiate randomly. The time of initiation is not set by a deterministic process, such as recovery from Ca^{2+}-inhibition or a progressive sensitization of IP_3Rs by Ca^{2+}.

Stochastic models of repetitive waves show that if σ is of the same order as $\mathrm{T_{av}}$, it is dominated by the probability P_{trig} of triggering a wave after the cell has recovered from the previous one [60]. The smaller the value of P_{trig}, the longer it takes on average for the next wave to occur, and the larger is the value of σ. For such repetitive triggering of waves, σ increases linearly with $\mathrm{T_{av}}$, and $\sigma = 1/P_{\mathrm{trig}} = \mathrm{T_{stoch}}$ holds for large values of $\mathrm{T_{av}}$. Even if P_{trig} relaxes exponentially from 0 immediately

after a spike to an asymptotic value, the linear relation between σ and T_{av} for large T_{av} still holds and it has a slope < 1 (see Fig. 4.2 and Fig. 4.4, D). Such a relaxation of P_{trig} appears to apply also to wave initiation reported in [136]. Almost regular oscillations arise when P_{trig} is very large, because then as soon as the cell has recovered from one spike, the next one is triggered. We refer to the length of the ISI of these regular oscillations as the deterministic part T_{det} of the ISI. It might be set by a variety of processes depending on the cell type, for example store refilling, IP_3R inhibition or Ca^{2+}-feedback to the IP_3 concentration. Each of these processes may also cause a time-dependence of P_{trig} such as that described in a simplified way by the relaxation with time constant ξ in Equation 4.2.

4.2.3 Influence of spatial coupling

We can further examine the stochastic component of wave triggering by manipulating the probability of wave initiation, for example by increasing the Ca^{2+}-buffering capacity of the cytosol [60, 249]. Decreasing P_{trig} increases the average ISI, but if wave triggering is random, the standard deviation σ should also increase. P_{trig} is actually the probability of two sequential events: that a puff occurs (P_{puff}) and then that the puff generate a wave (P_{wave}). The latter turns the puff frequency into the smaller wave frequency ($P_{trig} = P_{puff}P_{wave}$) and the standard deviation of inter*puff* intervals into the standard deviation of inter*spike* intervals. P_{wave} is expected to decrease when diffusion of free Ca^{2+} between clusters (the spatial coupling) is reduced by buffers [249]. The precise effect depends on the dynamic regime of the cell. With slow irregular waves, a slight decrease in coupling is predicted to increase T_{av} and σ, while larger decreases are predicted to abolish the self-amplifying mechanism required for oscillations leaving only moderate puff activity [60, 249]. Oscillations are predicted to be very sensitive to addition of Ca^{2+} buffers with fast binding and dissociation rates, and with K_D^{Ca} similar to resting cytosolic Ca^{2+} concentration, because such buffers effectively reduce diffusion of free Ca^{2+} at distances similar to the likely spacings of IP_3R clusters [249]. Because the buffers we use do not change the resting cytosolic free Ca^{2+} concentration, the IP_3 concentration or the interactions between IP_3Rs within clusters [47], we do not expect them to affect P_{puff}.

We measured the effect of Ca^{2+}-buffering on oscillations in astrocytes, HEK cells and PLA cells. Oscillations were first recorded to establish T_{av} and σ. The buffering capacity of the cells was then increased by incubating cells with BAPTA-AM or EGTA-AM, before continuing measurements of $[Ca^{2+}]_i$. BAPTA loading caused most of the astrocytes and HEK cells to stop oscillating. For those cells that resumed oscillations (about 10 % of astrocytes loaded with 20 nM BAPTA-AM and 50 % for HEK cells loaded with 0.5 or 1 μM BAPTA-AM), T_{av} and σ were both increased as indicated by the representative time series and the corresponding ISIs, which are shifted from short and rather regular values (red dots) to prolonged times with larger

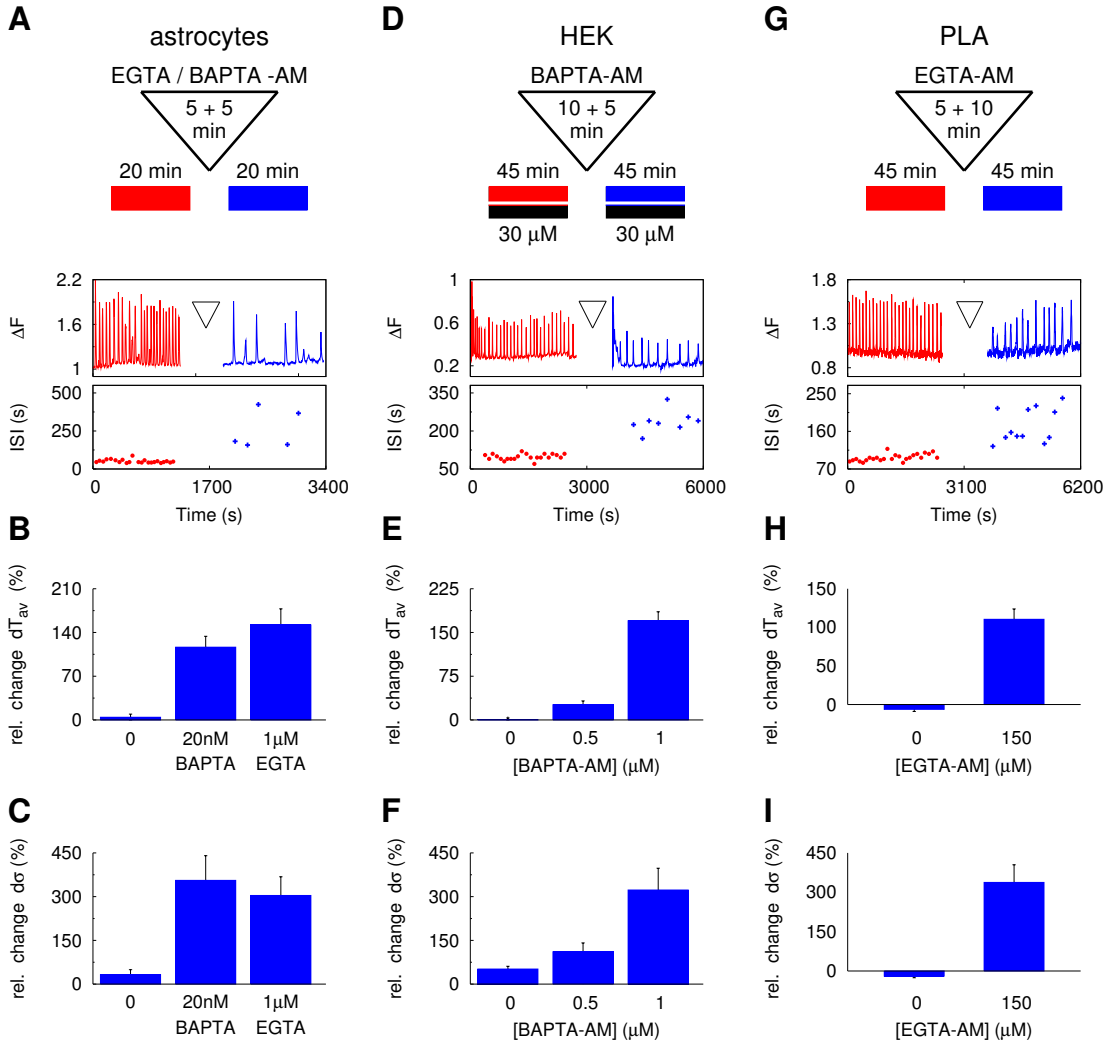

Figure 4.8: Ca^{2+} buffers render spike times even less predictable. Results show Ca^{2+} spikes in astrocytes (**A**-**C**), HEK cells stimulated with 30 µM CCh (**D**-**F**) and PLA cells (**G**-**I**) before (red) and after (blue) loading with additional Ca^{2+} buffer. The protocols and typical results are shown in panels (**A**), (**D**) and (**G**), the duration of the loading and subsequent hydrolysis times are shown in the triangles. Change to concentrations of EGTA-AM or BAPTA-AM are shown in the histograms. For the 50% of cells that resumed Ca^{2+} spiking, changes dT_{av} and $d\sigma$ in T_{av} and σ are shown relative to the values obtained before incubation with the Ca^{2+} buffer. Error bars show s.e. from different cells and experiments.

deviations (blue crosses) shown in Figure 4.8. HEK cells exhibit a concentration-dependent increase of T_{av} and σ compared to the control experiment in which the same protocol was used but without additional buffer loading. Figure 4.8 E-F show the population averaged increase of T_{av} and σ for the two different buffer concentrations. The larger effect for higher concentrations is in accordance with theoretical predictions [58]. The control experiment indicated by the zero of the corresponding concentration does only exhibit a slight difference to the reference measurement.

EGTA loading of PLA cells and astrocytes also caused oscillations to terminate in about 80 % of cells, and increased again both T_{av} and σ in the cells that resumed oscillations (Fig. 4.8 A-C, G-I), whereas control experiments do not exhibit significant changes.

For astrocytes we used two different kinds of buffers, BAPTA and EGTA with different concentrations. The tiny concentration of BAPTA-AM of 20 nM has a similar effect as the fifty times higher EGTA-AM loading concentration of 1 µM. This amazing result can be understood by consideration of the buffer properties. While EGTA has a relatively small capture rate k^+ leading to slow buffer dynamics with a dissociation constant in the range of µM, BAPTA has a higher k^+ and a dissociation constant in the nM range.

The characteristic length scale of the system is given by the diffusion length L, i.e. the stroke a Ca^{2+} ion covers in unit time. As we will see in Section 6.4, the diffusion length of the corresponding reaction diffusion system is given by $L^2 = D_{Ca}/(k^+[B]_T)$, where D_{Ca} denotes the diffusion coefficient of Ca^{2+}, $[B]_T$ describes the total buffer concentration and k^+ is the capture rate of the buffer. Interestingly the capture rates of BAPTA and EGTA differ by the reciprocal factor of the two different concentrations used, i.e. the diffusion length is affected in both experiments in a similar manner.

A possible objection of the experimental protocol is a potential influence of the increased buffer concentration on the Ca^{2+} base level $[Ca^{2+}]_0$. Due to the increased buffer capacity, $[Ca^{2+}]_0$ might be decreased leading to a decreased probability of an initial puff P_{puff}. This point of criticism is probably inappropriate by two reasons. First, we used rather small extracellular buffer concentrations in the range of tens of nM up to 1 µM and short loading times of several minutes, which should lead to a rather small increase of the cytosolic buffer concentration. Since we load the buffer in the presence of Ca^{2+}, these small additional buffer concentrations should not change the base level. In this context the Ca^{2+} regulating elements, especially the SERCA pumps and PMCAs, are important which remove Ca^{2+} from the cytosol in a Ca^{2+} dependent manner. Thus, measurements with a Ca^{2+} free medium do not exhibit significant differences regarding oscillation periods compared to experiments using media containing Ca^{2+}. Hence, we do not expect a dependence of $[Ca^{2+}]_0$ on the low buffer concentrations. Moreover, the measurements of HEK cells with the ratiometric dye fura2 do not exhibit a uniform significant change in the fluorescent

base level signal F_0.

These results demonstrate both the exquisite sensitivity of Ca^{2+} oscillations to Ca^{2+} buffering, whether provided by fast (BAPTA) or slow (EGTA) Ca^{2+} buffers, and the increase in both T_{av} and σ, predicted for a stochastic mechanism dependent on repetitive Ca^{2+} waves [60].

4.3 Theoretical analysis

So far we have proven all our hypotheses that were based on theoretical considerations of the underlying biological processes. Thus, Ca^{2+} oscillations are stochastic and occur by repeated wave nucleation and are consequently a spatial phenomenon. The latter is a prerequisite for AECR. Oscillations with small standard deviations are other circumstantial evidences for AECR.

The results above have induced a scientific discussion of the underlying mechanism. Dupont and coworkers report about stimulated Ca^{2+} oscillations within hepatocytes which exhibit coefficients of variation of about $CV = 0.35$ for moderate stimulation levels and even smaller values of about $CV \approx 0.15$ for strong stimulations [52]. From that the authors claim that stimulated Ca^{2+} oscillations are deterministic and revive the discussion of noisy limit cycle oscillators. At first glance this discussion might appear artificial, but it touches the very fundamental principles of cell signaling. Do cells use the spatial extension to build specific signals or is the spatial arrangement a side effect and signals correspond to responses of point objects?

To pick up this critical comment and to deepen our understanding of the underlying process we will in the following analyze the data presented above in more detail and demonstrate possible design principles. In this analysis the deterministic time T_{det} will play a central role for both the small CV and for AECR. Hence we turn first to the characteristics of T_{det}.

4.3.1 Determination of the deterministic time

From the offset of the σ-T_{av} relation in Figure 4.4 we confirmed our hypothesis of the two parts contributing to an individual ISI, the deterministic and the stochastic part predicted in Figure 4.1. But as mentioned before the deterministic part may vary between different cells. Thus an ISI is given by the sum of a cell dependent recovery time and a stochastic time as

$$\mathrm{ISI} = T_{cell} + t \ , \tag{4.14}$$

where t is taken from the probability density (4.3). Consequently the average period is determined by

$$\mathrm{T_{av}} = \langle \mathrm{T_{cell}} \rangle + \int_0^\infty t\mathcal{P}(t)dt = \mathrm{T_{det}} + \mathrm{T_{stoch}}\,. \tag{4.15}$$

The spread of data points in Figure 4.4 represents properties of individual cells. They differ firstly in $\mathrm{T_{det}}$ generating spread in the direction of $\mathrm{T_{av}}$ and secondly in the properties of the stochastic process, shifting them in the σ-$\mathrm{T_{av}}$ plane along curves parameterized by characteristics of the stochastic process, namely λ and ξ of the density (4.3). In order to decompose the measured $\mathrm{T_{av}}$ according to expression (4.15) into its parts $\mathrm{T_{stoch}}$ and $\mathrm{T_{det}}$ we have to distinguish between spreads caused by cell specific $\mathrm{T_{det}}$ and those given by the stochastic part.

For the simplifying assumption of a pure Poisson process, i.e. $\xi \to \infty$ and $\mathrm{T_{det}} = 0$, the data points in Figure 4.4 should be scattered on a straight line through the origin with slope one, since $\mathrm{T_{stoch}} = \sigma = 1/\lambda$. For various finite values of $\mathrm{T_{det}}$ the data structure could be explained by an array of lines with slope one. Indeed the structure of the astrocytes and microglia cells might be explained in that way as demonstrated in Figure A.5A.

Hence, we can determine the cell specific time $\mathrm{T_{det}}$ by Equation (4.15) by setting $\mathrm{T_{stoch}} = \sigma$ as

$$\mathrm{T_{det}} = \mathrm{T_{av}} - \sigma\,. \tag{4.16}$$

But the data in Figure 4.4 for HEK and PLA cells seem to disobey this interpretation since their population slopes indicate small regeneration rates ξ in correspondence to Figure 4.2B.

To clarify this issue we include an investigation of the population slopes $\mathrm{m_{pop}}$ determined by linear regression averaging over the cell population. The stochastic part $\mathrm{T_{stoch}}$ depends on the nucleation rate λ and we can consequently characterize the stochastic process by changing λ and study the impact on σ and $\mathrm{T_{av}}$. λ depends strongly on the concentration of Ca^{2+} binding proteins (buffers) in the cytosol as they determine the diffusion length of free Ca^{2+} and hence the strength of spatial coupling between channel clusters [62]. Higher buffer concentrations yield lower nucleation rates as seen in Section 4.2.3.

We do not expect the small buffer concentrations used to have an influence on the regeneration rate ξ or on the deterministic time $\mathrm{T_{det}}$ since both are not very sensitive to the cytosolic buffering capacity. Hence, we predict cells to be shifted on lines corresponding to $\xi = \textit{constant}$ in Figure 4.2B by lowering λ.

To proof this assumption we use buffer experiments like those described in Section 4.2.3. We denote the slope of the σ-$\mathrm{T_{av}}$ relation estimated from the data points before and after buffer addition as m_{shift}. If the population slopes before and after

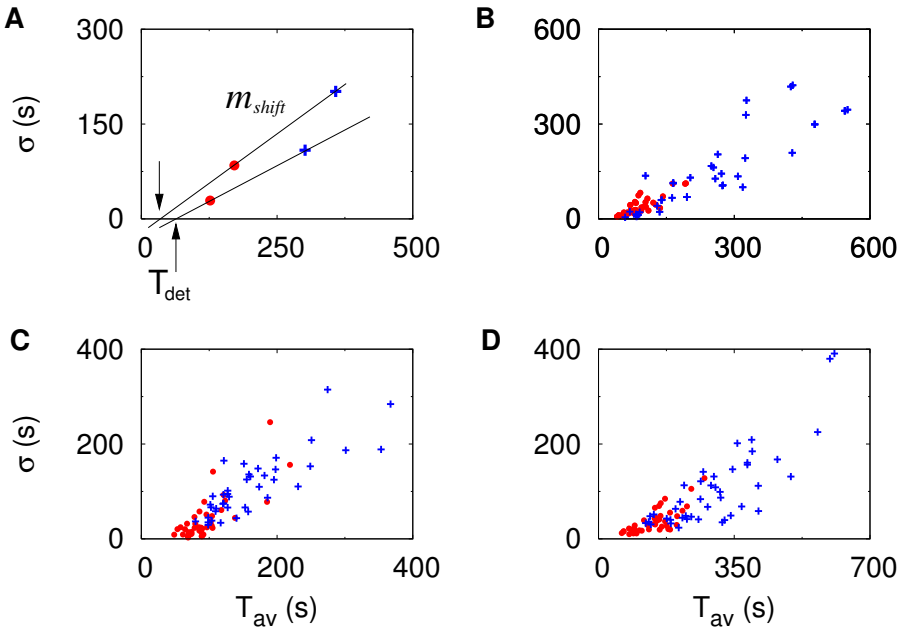

Figure 4.9: σ-T_{av} relation in buffer experiments. Ca^{2+} buffers influence both σ and T_{av} since the reference values before buffer loading (red dots) are shifted in σ and T_{av} directions due to buffers leading to blue crosses. From these shifts we determine the individual shifting slopes $m_{\mathrm{shift,i}}$ by drawing a line through the two data points corresponding to the ith cell. The intersection of this line with the T_{av} axis is used to estimate the deterministic time T_{det} indicated by the arrows (**A**). For astrocytes loaded with 20 nM BAPTA-AM (**B**) as well as with 1 µM EGTA-AM (**C**) and HEK cells loaded with 1 µM BAPTA-AM (**D**) cells seem to be shifted in the direction of the population, i.e. $\langle m_{\mathrm{shift},i} \rangle_i \approx m_{\mathrm{pop}}$, which is confirmed in Table 4.1.

adding additional buffer are in the same range as m_{shift}, we can take them as an estimate of the slope of the σ-T_{av} relation.

The resulting data of the experiments are shown in Figure 4.9, where again the standard deviation σ is plotted over T_{av} for astrocytes (B, C) and HEK cells (D) before (red dots) and after (blue crosses) buffer loading.

For the analysis we determined the population slopes m_{pop} by linear regression and the average shifting slope m_{shift} derived from cell individual slopes $m_{\mathrm{shift},i}$ as depicted in Figure 4.9A. We find that the population slopes are self consistent and in good agreement with the shifting slopes. Despite the variability of m_{shift} shown in Table 4.1, we nevertheless find a separation between the astrocytes and the HEK cells indicating the different dynamical regimes of both populations.

This means that cells of the same type seem to work at similar ξ values leading to a cell type specific slope of the σ-T_{av} relation. The analysis in Section 4.1.2 has

kind of experiment	m_{shift}	m^b_{pop}	m^a_{pop}
astrocytes with 10 nM BAPTA	1.01 ± 0.16	0.84	0.91
astrocytes with 20 nM BAPTA	0.94 ± 0.23	1.04	0.89
astrocytes with 1 µM EGTA	0.88 ± 0.19	0.86	0.79
HEK cells with 1 µM EGTA	0.49 ± 0.21	0.56	0.58
HEK cells with 0.5 µM EGTA	0.52 ± 0.18	0.59	0.57

Table 4.1: Comparison between the population slopes m^b_{pop} before and m^a_{pop} after buffer application and the average shifting slope m_{shift}.

shown that for small regeneration rates the slope of the σ-$\mathrm{T_{av}}$ relation decreases and can be approximated for large $\mathrm{T_{av}}$ and σ by the coefficient of variation CV. By inserting (4.9) into Equation (4.11), we obtain the functional dependence of the form

$$m \approx CV = \frac{\sigma}{\mathrm{T_{av}}} = f\left(\frac{\lambda}{\xi}\right) , \tag{4.17}$$

which depends on the ratio $r = \lambda/\xi$ only. From this we conclude that the stimulated HEK cells have high λ and small ξ.

We now return to the decomposition of $\mathrm{T_{av}}$. From the results above we expect that relation (4.16) should work for astrocytes, i.e. that the distributions $p(\mathrm{T_{det}})$ obtained for data without and with additional buffer should coincide. In addition they should be comparable with the distribution resulting from the behavior of cells due to buffer loading. This distribution comes from the intersection of the individual shifting lines with the $\mathrm{T_{av}}$ axis as shown in Figure 4.9A. Figure 4.10A illustrates this idea, where the three distribution have a similar shape and posture of their maxima. The naive use of Equation (4.16) for HEK cells will fail as can be seen in Figure 4.10B caused by different parameters for HEK cells in relation (4.3). Rescaling of σ by the inverse of the corresponding m_{pop} leads again to a nice consistency of the distribution as shown in the inset of 4.10B. The small contributions to $p(\mathrm{T_{det}})$ with negative $\mathrm{T_{det}}$ probably occur due to spike trains which are not yet equilibrated.

We have thus confirmed that stimulated HEK cells have distinct stochastic properties than spontaneously oscillating astrocytes and that this difference can be estimated by the structure of the population data. Based on this we presented how to extract the intrinsic property $\mathrm{T_{det}}$ of a cell out of the global observations of σ and $\mathrm{T_{av}}$. The agreement between the distributions further corroborates our assumption of the oscillation mechanism.

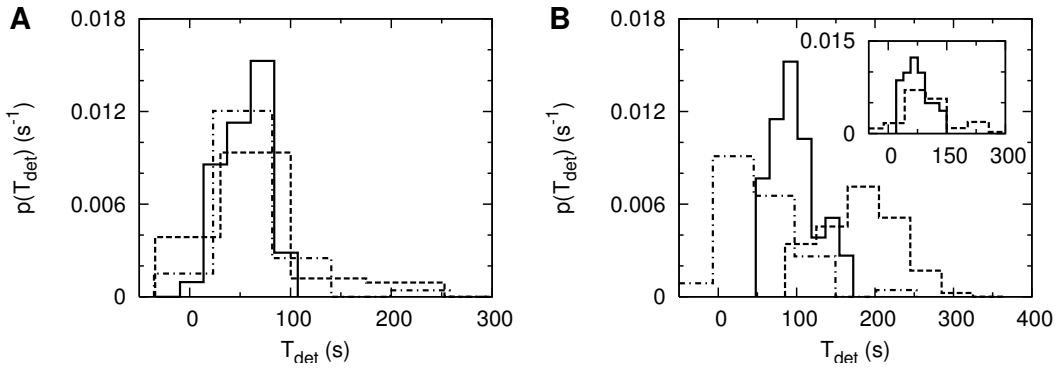

Figure 4.10: Comparison of distribution densities $p(\mathrm{T_{det}})$ obtained by (4.16) before and after buffer application (solid and dashed lines, respectively) and the density determined by shifting lines (dash dotted lines) for astrocytes (**A**) loaded with 20 µM BAPTA and HEK cells (**B**) loaded with 1 µM BAPTA. The distributions coincide very well for astrocytes, whereas they diverge for HEK cells, caused by the fact that the latter have a time dependent nucleation rate. The inset shows the corrected distributions taking that into account.

4.3.2 Role of deterministic time

We return now to the question of a small coefficient of variation CV found in stimulated cells. We expect that the deterministic time plays a key role under these circumstances. If the stochastic time is small or in the same range as the refractory period $\mathrm{T_{det}}$, the standard deviation is small compared to the average ISI $\mathrm{T_{av}}$.

We start again with the simple case of a pure Poisson process enhanced by the deterministic time leading to a waiting distribution of the form

$$\mathcal{P}_{\mathrm{poi}}(t) = \lambda \exp\left[-\lambda(t - \mathrm{T_{det}})\right] \ , \ t > \mathrm{T_{det}} \ . \tag{4.18}$$

With this distribution the mean ISI $\mathrm{T_{av}}$ and the standard deviation are given by

$$\mathrm{T_{av}} = \mathrm{T_{det}} + \frac{1}{\lambda} \quad , \qquad \sigma = \frac{1}{\lambda} \ , \tag{4.19}$$

and hence $CV = (1 + \lambda \mathrm{T_{det}})^{-1}$. From that it immediately follows that the oscillations become more regular for increasing λ and $\mathrm{T_{det}}$, as shown in Figure 4.11A. To check if our data do really exhibit this dependence we replot the data of Figure 4.4 as the CV over the reciprocal σ, which corresponds to the rate λ. Indeed, the data exhibit a comparable behavior, as can be seen in the representative example of the PLA cells in Figure 4.11B and for stimulated hepatocytes in Figure A.4B. The scattering of the data points is caused by different $\mathrm{T_{det}}$. The fitted line indicates an average refractory period of 144 s and the dashed lines correspond to different

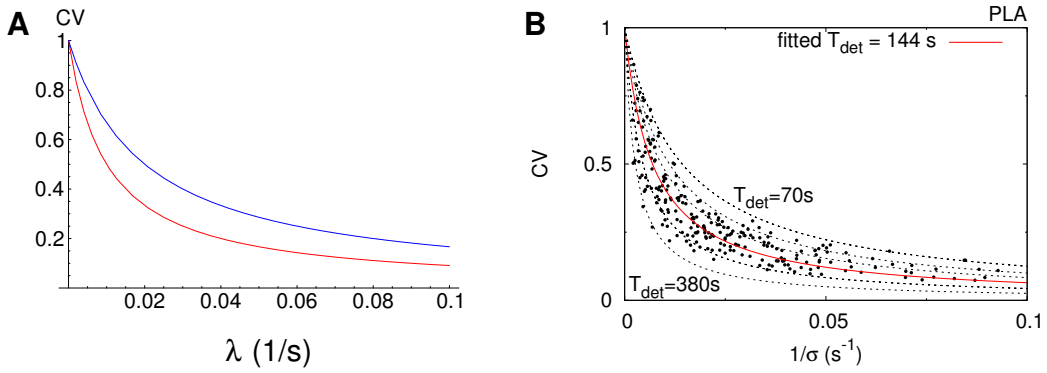

Figure 4.11: Dependence of CV on λ and $\mathrm{T_{det}}$. For a Poisson process with a recovery period the coefficient of variation decreases with increasing λ and $\mathrm{T_{det}}$ as shown for $\mathrm{T_{det}} = 50$ s (blue) and $\mathrm{T_{det}} = 100$ s (red) in **A**. The data of our measurements exhibit such a behavior as shown for the PLA cells **B**, where the dashed lines correspond to different $\mathrm{T_{det}}$. This methods can be used to determine the cell specific property.

deterministic times, which are in a reasonable range. This methods allows for determination of the intrinsic deterministic time from measurements of global properties.

This explains the CV found in stimulated hepatocytes by Dupont and coworkers in [52]. They do not indicate a deterministic regime but AECR, which has still a stochastic character despite of observed regularity.

Although AECR is a spatial phenomenon, it exhibits an effect on the global scale. As the name already suggests we expect to find a resonant property. To analyze this behavior we use the power spectrum introduced in Section 3.5.2 that quantifies how much power of a signal is placed in a frequency band $(\omega, \omega + d\omega)$. The power spectrum of a stationary spike train can be defined alternatively to Equation (3.24) in accordance to the Wiener-Khinchin theorem [81] by

$$S(\omega) = \langle \varsigma(\omega)\varsigma^*(\omega) \rangle \ , \tag{4.20}$$

where $\varsigma(\omega)$ is the Fourier transform of the spike train $\varsigma(t)$ defined by

$$\varsigma(\omega) = \int_{-\infty}^{\infty} e^{2\pi i \omega t} \varsigma(t) dt \ . \tag{4.21}$$

For renewal processes the power spectrum can be expressed by the Fourier transform of the waiting time density $\tilde{\mathcal{P}}(\omega)$ as follows [232]:

$$S_{\mathrm{ren}}(\omega) = r \frac{1 - \left|\tilde{\mathcal{P}}(\omega)\right|^2}{\left|1 - \tilde{\mathcal{P}}(\omega)\right|^2} \qquad (\omega > 0) \ , \tag{4.22}$$

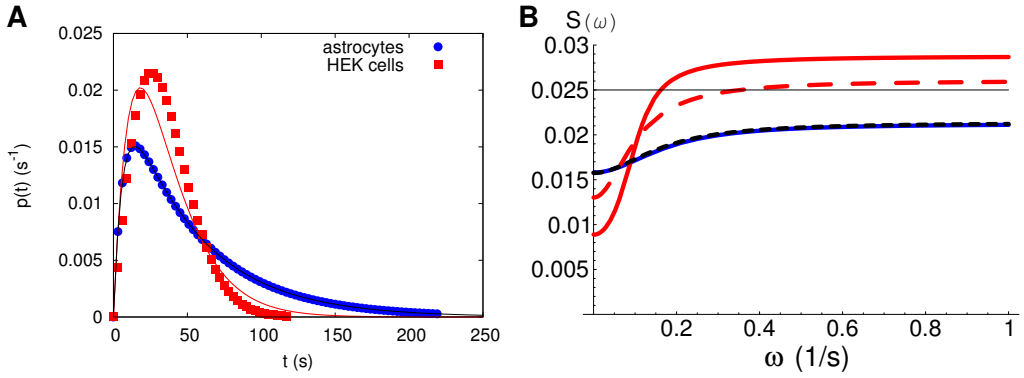

Figure 4.12: Approximated distribution and power spectra. **A**: The time dependent Poisson density (4.3) with the parameters determined in Figure 4.5A for HEK cells (red squares) and astrocytes (blue dots) can be approximated by the double exponential density (4.23) (solid lines) with $\lambda_1 = 0.167$ and $\lambda_2 = 0.02$ for HEK cells and with $\lambda_1 = 0.134$ and $\lambda_2 = 0.01$ for astrocytes. **B**: Corresponding power spectra for $\mathcal{P}_\xi$ (4.3) denote by solid lines and $S(\omega)$ obtained by $\mathcal{P}_{\text{app}}(t)$ (dashed lines) exhibit slight mismatch for HEK cells (red) and nearly perfect agreement for astrocytes (blue and black).

where r denotes the stationary rate which equals the inverse mean period $r = 1/\mathrm{T}_{\text{av}}$.

The Poisson process is a special renewal process and its exponential probability density leads to a flat spectrum that equals the rate $S_{\text{poi}} = r$. For the density of the time dependent Poisson process defined by Equation (4.3) we can determine the Fourier transform in the case of $\mathrm{T}_{\text{det}} = 0$ and thus calculate the spectrum $S(\omega)$. For a non vanishing deterministic time, the Fourier transform cannot be found in closed form. Therefore, we approximate it by a simpler distribution density consisting of to exponential functions, which reflects the most important property, the peaked structure. The approximated density takes the form

$$\mathcal{P}_{\text{app}}(t) = \alpha \left(e^{-\lambda_1 t} - e^{-\lambda_2 t} \right) \qquad (t > 0) \tag{4.23}$$

where α is the normalization factor determined by

$$\int_0^\infty \mathcal{P}_{\text{app}}(t) dt = 1 \qquad \Rightarrow \qquad \alpha = \frac{\lambda_1 \lambda_2}{\lambda_2 - \lambda_1} \,. \tag{4.24}$$

For the cell type specific values λ and ξ obtained in Figure 4.5A we can fit the parameters λ_1 and λ_2 as shown in Figure 4.12A for astrocytes and HEK cells. For astrocytes the approximation fits perfectly whereas for HEK cells the distribution exhibits small deviations.

With these distributions (4.23) we can calculate the power spectra shown in Figure 4.12B by Equation (4.22) and compare them with the spectra obtained by the

original distributions $\mathcal{P}_\xi$ defined by Equation (4.3). A dominant difference between the flat spectrum of a pure Poisson process with $\lambda = 0.025$ shown by the black line and the spectra obtained by the peaked densities is the dip for low frequencies ω. It occurs since the probability to observe a spike directly after the previous one is zero. That induces a characteristic in the spike train on long time scales, since after the refractory period a spike occurs at randomly times with non specific frequencies and hence the lack during the refractory period leads to holes on low frequencies. Moreover, we observe that the relaxation rate ξ respectively the corresponding approximated double exponential density decreases the asymptotic value of $\lim_{\omega\to\infty} S(\omega)$, as the fitted value for astrocytes in Figure 4.5A is the same as for the pure Poisson process, i.e. $\lambda = 0.025$. In this case the spectra of the approximated and the original density coincide, whereas for the HEK cells the approximated density leads to a smoother spectrum compared to the one originated from $\mathcal{P}_\xi(t)$. The latter induces a spectrum with a deeper hole by exhibiting smaller values for small ωs and a higher saturated level. These flat parts of the spectrum indicate the Poisson character.

So far we have only considered different kinds of smooth probability densities in our power spectrum analysis. The peaked form of the experimentally observed distributions leads to dips at low frequencies. A resonant behavior is characterized by specific frequencies. A simple example is a deterministic signal of the form $f(t) = \sin(\omega_0 t)$. Here the single frequency ω_0 characterizes the whole process, and the power spectrum consists of delta functions of ω_0 and its higher harmonics, $S(\omega) = \sum_{n=1}^{\infty} \delta(n\omega_0)$. In terms of predictability, this leads to perfect correlations since it is a deterministic process.

For AECR we are interested in the range where the recovery time is of the same order or even larger than the stochastic component $\mathrm{T}_{\mathrm{stoch}}$. Therefore we include $\mathrm{T}_{\mathrm{det}}$ in the approximated density

$$\mathcal{P}_{\mathrm{app}}(t) = \frac{\lambda_1\lambda_2}{\lambda_2-\lambda_1}\left(e^{-\lambda_1(t-\mathrm{T}_{\mathrm{det}})} - e^{-\lambda_2(t-\mathrm{T}_{\mathrm{det}})}\right) \quad , \quad (t > \mathrm{T}_{\mathrm{det}}) \, , \tag{4.25}$$

which now can be used to calculate the spectral density for the two parameter sets corresponding to the averaged astrocyte population and to the HEK cells. The spectrum calculated by Equation (4.22) reads

$$S(\omega) = r\,\frac{1 - \frac{\lambda_1^2\lambda_2^2}{(\lambda_1^2+\omega^2)(\lambda_2^2+\omega^2)}}{\left|1 + \frac{\lambda_1\lambda_2}{(\omega-i\lambda_1)(\omega-i\lambda_2)} e^{-i\omega \mathrm{T}_{\mathrm{det}}}\right|^2} \quad , \quad r = \frac{\lambda_1\lambda_2}{\mathrm{T}_{\mathrm{det}} + \lambda_1 + \lambda_2} \, . \tag{4.26}$$

and is shown in Figure 4.13A for λ values determined in Figure 4.12 for HEK cells (red) and astrocytes (blue). For better comparison, we set $r = 1$ in Equation (4.26).

We can also determine the experimental power spectrum of the merged spike train by Equation (4.20). This is shown in Figure 4.13B, where the ISIs were scaled by the mean of the spike train.

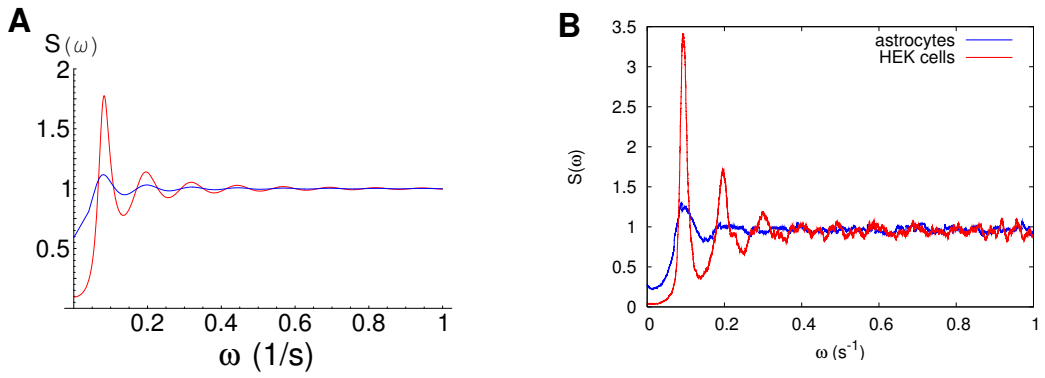

Figure 4.13: Comparison of theoretical and experimental power spectra. **A**: Power spectrum defined by Equation (4.26) with $r = 1$ of the probability density (4.25) for parameter sets describing astrocytes (blue) and HEK cells (red) determined in Figure 4.12 and $T_{det} = 40$ s. **B**: Power spectral density derived from experimental data by Equation (4.20).

These spectra exhibit similar properties like those in Figure 4.12B. They have a dip for small frequencies and saturate to a constant level for large ω indicating the Poisson character. The new feature introduced by the absolute recovery period is the existence of maxima. They indicate resonances. For large λs the probability to observe a spike directly after T_{det} is high and thus the power of the corresponding frequency band is high. For decreasing λ this effect decreases and reaches a flat spectrum for very small values of λ compared to the inverse deterministic time.

Such a behavior can be seen by the two examples of HEK cells (red) and astrocytes (blue) in both, the theoretically calculated spectra in Figure 4.13A and from the experimentally determined spectrum in Figure 4.13B. Here we observe a more resonant behavior for the HEK cells indicated by the higher peaks in Figure 4.13 as expected by their larger nucleation rate compared to the astrocytes. Astrocytes exhibit only a small peak in their spectrum and are dominated by the relaxation rate ξ inducing the hole at low ωs and by the Poisson like behavior leading to the flat spectrum for higher frequencies. The spectrum of HEK cells has a clear maximum and two higher harmonics emphasizing the resonant character. By rescaling with the cell type specific value for r, the spectra would be shift to smaller values and exhibit a distance comparable to those in Figure 4.12B. The difference between the theoretical spectrum and the experimental one is probably induced by the divergence of the approximated waiting time density from the original depicted in Figure 4.12A leading to smaller amplitudes.

Despite these small deviations the spectra exhibit a good agreement and demonstrate both, the stochasticity of the process by the flat part of the spectrum and

the resonant character for large λs. Together with the spatial aspect of the oscillation properties demonstrated by the dependence of the nucleation rate on the buffer content shown in figure 4.8 the resonant behavior indicates AECR.

The spectral behavior is also known from experimental neuron dynamics. Theoretical studies explain the dip within the spectrum by a noisy threshold of the excitable dynamics. Most often they assume Gaussian noise, simulate a spike generating neuron model and find the corresponding dip. Other approaches use heuristic time independent probability densities [121] leading to the experimentally observed spectrum. The advantage of the probability density (4.3) is its physiological motivated origin that may also hold for neurons. Although most models assume neurons to be point objects, they are spatially extended. Action potentials are generated by cooperative behavior of ion channels and recent studies have shown that nucleation might be essential for this dynamics, too [155]. Thus the above presented results may inspire some areas of Neuroscience as well.

4.3.3 Information theory

In this section we interpret the previous results in an information theoretical way. In his famous paper [206] Shannon introduced the information entropy of a signal by the expectation value of the logarithm of its probability density $p(t)$ of a random variable I as

$$H = -k \int_0^\infty p(t) \log p(t) dt, \tag{4.27}$$

where k is a positive constant defining the units of the measurements. H measures the uncertainty about a specific realization I_i of I. In this framework, information $\mathcal{I}$ is defined as the entropy export of a system having first entropy H_1 and after a dynamical change, e.g. by a stimulation, entropy H_2 as

$$\mathcal{I} = H_1 - H_2. \tag{4.28}$$

This means for signaling in cells that the signal without stimulus should have a high entropy H_1 since in this case an external signal by a stimulus inducing an internal signal with entropy H_2 could be detected most efficiently.

From thermodynamics we know that systems in thermodynamic equilibrium are in the state of maximal entropy. The probability distribution $p(x)$ of a stochastic process with average μ and $|x| < \infty$ that exhibits the maximal entropy is the Gaussian distribution, which can be found in a variety of processes. For processes which are limited to positive values, i.e. $0 < x < \infty$, and a given mean μ the distribution with the maximal entropy is the Poisson distribution, what can be calculated by Lagrange multipliers. Consequently we expect an entropy minimization due to the

time dependence of the nucleation rate $\Lambda = \lambda(1 - e^{-\xi t})$ compared to a pure Poisson process.

In order to interpret the experimental results we are interested in the information distance of a pure (4.1) and a time dependent (Equation (4.3)) Poisson process. Instead of calculating the (not analytically solvable) entropy (Equation 4.27) for the time-dependent Poisson process, we look at the information gain by switching from one process to another one given by the Kullback entropy [85],

$$\mathcal{K}(p_0, p_{\mathrm{st}}) = k \int_0^\infty p_0(t) \log \frac{p_0(t)}{p_{\mathrm{st}}(t)} dt. \tag{4.29}$$

In a strict mathematical framework, $\mathcal{K}$ is only defined for discrete distributions, where the integral is replaced by a sum, since the integral leads to an additional integration constant that has no meaning. But here we can set the constant to zero according to [85] and use the Kullback entropy to determine the differences between two distributions in terms of information divergence.

For two pure Poisson processes with the rates λ_1 and λ_2 we determine in Section A.5 the Shannon information $\mathcal{I}_{\mathrm{poi}}$ and the Kullback entropy $\mathcal{K}_{\mathrm{poi}}$, leading to

$$\mathcal{I}_{\mathrm{poi}} = \log\left(\frac{\lambda_2}{\lambda_1}\right) \tag{4.30}$$

$$\mathcal{K}_{poi} = \frac{\lambda_1}{\lambda_2} + \log\left(\frac{\lambda_2}{\lambda_1}\right) - 1 \ , \tag{4.31}$$

which are both simple functions of the ratio of the nucleation rates. The two information measures are shown in Figure 4.14A, where we see that $\mathcal{I}_{\mathrm{poi}}$ is a monotonic function of the ratio, whereas $\mathcal{K}_{\mathrm{poi}}$ has a minimum at zero in the case of equality of the rates. Since $\mathcal{K}$ describes an entropy, it is always positive. Nevertheless, we see that both measures exhibit a similar behavior and can thus be equivalently used for information estimation, where we have to distinguish for $\mathcal{K}$ between information gain and loss from the context.

The switch between two pure Poisson processes corresponds to the experiment with astrocytes in Figure 4.8, where the nucleation rate λ was decreased by loading additional Ca^{2+} buffer into the cell. Most of these spontaneously oscillating cells stopped oscillating, which indicates low values of λ. This means that cells exhibit spontaneous oscillations with low λ leading to a high entropy $H_1 = -k_B\,[\log(\lambda) - 1]$ (see appendix A.5). In means of information theory, this is a smart way to detect external signals which induce intracellular Ca^{2+} oscillations with a smaller entropy H_2 and a narrower probability density, respectively. Assuming a limited increase of λ, $d\lambda$ due to stimulation we can calculate the information gain by Equation (4.29) leading to Figure 4.14B. Here we see that cells should have small λs in order to detect information given by a fixed increase of λ most efficiently.

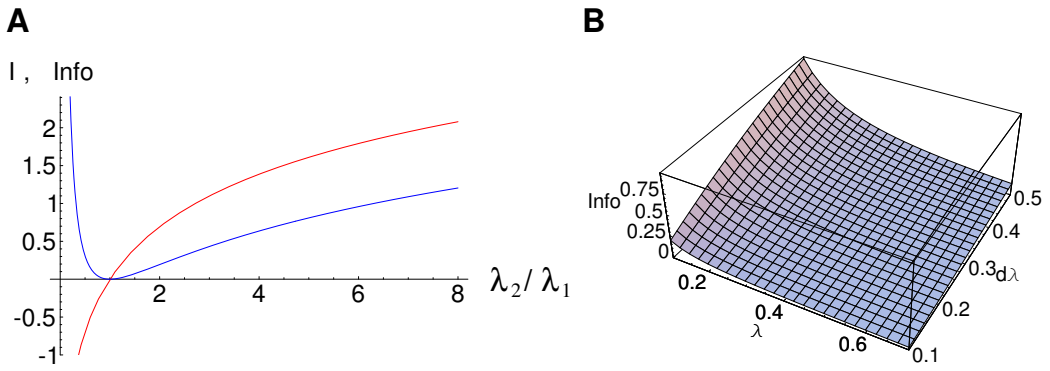

Figure 4.14: Information divergence of two Poisson processes. **A**: Comparison of the Shannon information (red) and the Kullback entropy (blue). **B**: Information divergence by a change of λ by $d\lambda$. Here we used natural units, i.e. $k = 1$.

We are now interested in the information gain by the regeneration rate ξ. By inserting $p_0(t) = \mathcal{P}_{\text{poi}}(t)$ and $p_{\text{st}}(t) = \mathcal{P}_\xi(t)$ into Equation (4.29), we find in Section A.5 the analytical solution for the information gain

$$\mathcal{K} = k \left[\mathcal{H}\left(\frac{\lambda_1}{\xi}\right) + \log\left(\frac{\lambda_1}{\lambda_2}\right) + \frac{\lambda_2 \xi}{\lambda_1(\lambda_1 + \xi)} - 1 \right] , \tag{4.32}$$

where $\mathcal{H}(\lambda/\xi)$ denotes the continuous harmonic series given by

$$\mathcal{H}(x) = \gamma + \frac{d}{dx} \log \Gamma(x+1) , \tag{4.33}$$

with the Euler-Mascheroni constant γ and the Gamma function $\Gamma(x+1)$. For $\lambda_1 = \lambda_2 = \lambda$ (4.32) reduces to

$$\mathcal{K} = k \left[\mathcal{H}\left(\frac{\lambda}{\xi}\right) + \frac{1}{\left(1 + \frac{\lambda}{\xi}\right)} - 1 \right] . \tag{4.34}$$

This means for $\xi \to \infty$, i.e. $\mathcal{P}_\xi \to \mathcal{P}_{\text{poi}}$, $\mathcal{K}$ goes to zero as expected and for $\xi \ll \lambda$ it turns out that $\mathcal{K} \to \log(\lambda/\xi)$. Note that in this description the nucleation rates λ for both processes are equal. The analysis in the previous section has shown that HEK cells act at higher λs, what additionally increases the rate of information gain and thus expression (4.34) is a lower estimate.

The expression (4.34) for $\mathcal{K}$ depends only on the ratio $r = \lambda/\xi$, as does the relation for the slope m in Equation (4.17). Thus we can estimate the information content of Ca^{2+} oscillations by the slope m. In Figure 4.15A the relations (4.17)

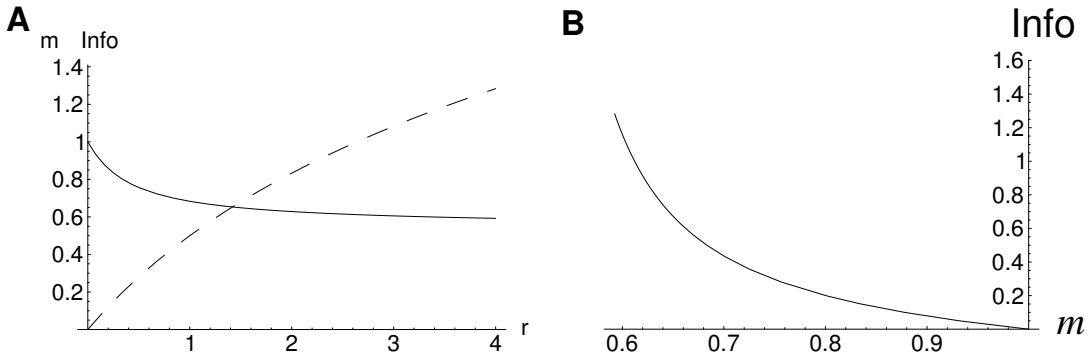

Figure 4.15: **A**: The slope $m \approx CV$ (solid line) and the information gain $\mathcal{K}$ (dashed line) in dependence of the ratio $r = \lambda/\xi$. Due to this relation we can estimate the detectable information in a signal by the experimental slope of the σ-T_{av} relation (**B**), where we used natural units, i.e. $k = 1$.

and (4.34) are shown in dependence on r, where we used natural units leading to $k = 1$. Figure 4.15B displays the dependence of $\mathcal{K}$ on m.

In this context the experimental findings make sense. The spontaneous oscillations in astrocytes and microglia might demonstrate the structure of the internal spatial signaling network within cells. From the information theoretical point of view, an ISI distribution close to a Poisson process as spontaneous oscillations exhibit, is a good choice, since it is able to detect an eventually occurring signal most sufficiently. Moreover, we can deduce from the data of stimulated HEK cells that these cells perform entropy export, i.e. information processing. In Figure 4.4C we find for the PLA cells a slope $m_{\mathrm{PLA}} = 0.7$, which is between the stimulated HEKs and the spontaneous glia cells. That result makes sense too, since these cells are stem cells in the phase of cell differentiation in which Ca^{2+} oscillations might control gene expression.

4.4 Discussion

We have shown that cells use a stochastic mechanism to generate global Ca^{2+} spikes. With about 10^4 IP_3Rs in each HEK cell (S.C. Tovey, C.W. Taylor, unpublished) and far more Ca^{2+} ions, why does random behavior play such an important role in Ca^{2+} spiking? The reason is that, as for any stochastic medium, global events are initiated by local processes. A puff changes the local free Ca^{2+} concentration by 100 to 1000-fold [249] and the gradients are so steep that only neighboring IP_3R clusters experience the change. Each puff, occurring within only a small part of the cell, is a potential wave initiation site, and the few IP_3R clusters that participate

in the initiation of each wave are too few for the process to become deterministic. These properties identify intracellular Ca^{2+} dynamics as a random medium. The existence of so called "hot spots" [167] does not change these conclusions; it simply means that P_{puff} is not spatially homogeneous.

Intracellular Ca^{2+} spikes occur randomly. But a regular regime exists if P_{trig} is high due to the existence of a deterministic part of the ISI leading to pronounced peaks in the power spectrum of the spike trains. The mean and the standard deviation of the ISI distribution depend on spatial coupling. The regular Ca^{2+} spikes are thus an example of array enhanced coherence resonance, an intrinsically stochastic phenomenon [122, 182, 60, 214, 39]. This is consistent with hierarchical recruitment of Ca^{2+} release events [135, 23]. Hence, oscillations are an emergent property of arrays of IP_3R clusters and not a property of single IP_3Rs. Ca^{2+} oscillations are the first example of the constructive use of noise in cell signaling and the first experimental verification of AECR in a biological system.

Although the randomness of blips and puffs is widely accepted [62, 169, 279, 238, 125, 91, 213, 37, 221, 126, 190], this is the first study explaining the stochasticity of global events by a founded biophysical model.

The probability of initiating a wave (P_{trig}) is determined by local properties, such as channel state dynamics, numbers of channels in a cluster, release currents, and by diffusion of free Ca^{2+} between clusters. P_{trig} sets σ of the ISI distribution. Information on local properties, like the open probability *in vivo*, can thus, in principle, be obtained from the fluctuations of the global Ca^{2+} signal.

We have shown that in different cell types IP_3-evoked Ca^{2+} spikes are caused by random wave nucleation with a regular regime arising from AECR. In this context the deterministic time T_{det} plays a key role. From our gained knowledge of the underlying mechanism we can determine the intrinsic property T_{det} from global observations.

The randomness of spike trains does not prevent Ca^{2+} oscillations from transmitting information. As long as the ISI distribution of stimulated spike trains is sufficiently different from the ISI distribution of spontaneous spiking, cells can distinguish the message from the noise as shown in Section 4.3.3. We found the slope of the σ-T_{av} relation to be a simple experimentally accessible measure for the information content of spike trains.

As a final proof of our hypotheses we may check the waiting time probability density, which characterizes the process completely as stated in Section 3.5.1. In the inset of Figure 4.16 the density defined by Equation (4.3) with the values fitted in Figure 4.5A is shown. They exhibit a very similar behavior to the distributions obtained from the merged spike trains, which are normalized to the average period T_{av} as shown in Figure 4.16.

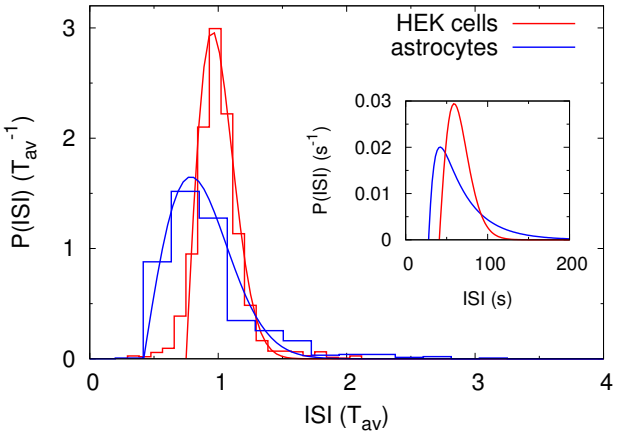

Figure 4.16: Comparison of $\mathcal{P}(t)$. The waiting time distributions for the fitted parameter values (inset) exhibit a good agreement with those obtained from merged spike trains, which are normalized to the mean T_{av}.

4.4.1 Comment on noisy limit cycle oscillators

Here we comment briefly on the assumption of Ca^{2+} oscillations being noisy limit cycle oscillators. For that purpose we analyze the σ-T_{av} relation, i.e. the CV of oscillations, occurring by a Hopf bifurcation and a saddle node bifurcation. This is classified in Neuroscience as neurons of type II and type I, respectively.

Hopf Bifurcation: A standard model for the Hopf bifurcation neuron model is the FitzHugh-Nagumo (FHN) model, which can be derived from a van-der-Pol oscillator [74, 124]. The governing equations for the spiking variable $x(t)$ and the recovery variable $y(t)$ read

$$\epsilon \dot{x} = x - x^3 - y \tag{4.35a}$$

$$\dot{y} = x + a + \sqrt{2D}\varrho(t) \ , \tag{4.35b}$$

where ϵ is the time separation parameter and $\sqrt{2D}$ is the strength of white Gaussian noise, i.e. $\langle \varrho(t) \rangle = 0$ and $\langle \varrho(t)\varrho(t') \rangle = \delta(t - t')$. The Langevin dynamics for the recovery variable $y(t)$ is a common and mathematically rigorous way to add stochastic input to the FHN model [122].

The system exhibits a Hopf bifurcation for the excitable parameter $a = -1$, at which the fixed point becomes unstable and a stable limit cycle occurs for $a > -1$. For small values of Δa and $a = -(1 + \Delta a)$, the system can be driven by noise from the stable fixed point on the limit cycle. The influence of the noise for the two different regimes is shown in the σ-T_{av} plot in Figure 4.17A. In the oscillatory regime, the noise does only lead to small variation and CV is less than 0.2, rather independent of ϵ. Values for the coefficient of variation observed in the experiments can only be found in the excitable regime, where the system runs on an unstable limit cycle. That is illustrated in Figure 4.17B, where the dependence of CV on the noise strength D and on the excitable parameter a is shown.

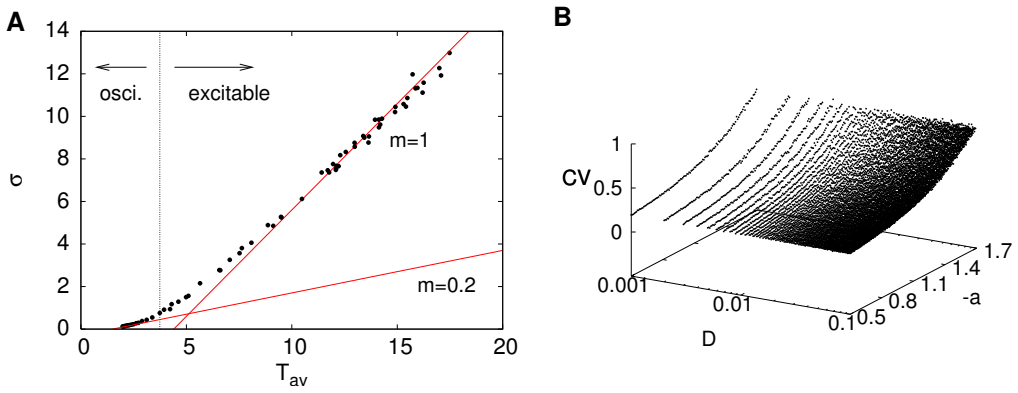

Figure 4.17: Noisy Hopf limit cycle oscillator. **A**: The σ-T_{av} relation of spike trains containing 10^5 ISIs each of a FHN neuron for $D = 0.01$, $\epsilon = 0.1$ and different as exhibits a σ-T_{av} relation comparable to those found in experiment only in the excitable regime indicated by the line $m = 1$. Close to the bifurcation point the oscillatory regime exhibits only a linear dependence with a slope of ≈ 0.2. **B**: The CV of the FHN model in dependence on D and a exhibits also for large D only in the excitable regime ($a < -1$) values comparable to the experiment. Moreover, it demonstrates that the findings in **A** are rather independently of the parameter choice.

Saddle node bifurcation: The relation for CV in a system with a saddle node bifurcation is studied in [123] in relation to a type I neuron. The complete neuron dynamics can be reduced to a one-dimensional normal form driven by a white noise input as

$$\dot{x} = \beta + x^2 + \sqrt{2D}\varrho(t) \ , \tag{4.36}$$

where again x corresponds to the spiking variable and ϱ denotes white Gaussian noise. The simple spike generator produces a spike whenever x reaches a threshold x_+, similar to the fire-diffuse fire models mentioned in Section 2.5.2. Afterwards x is set to a negative value x_-. The parameter β corresponds to the excitation parameter a in Equation (4.35).

Since the Langevin Equation (4.36) is one dimensional we can interpret it easily as a Brownian particle, i.e. as a particle that jumps randomly in a potential $V(x)$. In general the motion of x occurs through a force F that might depend on x, i.e. $\dot{x} = F(x)$. In physics a force is defined in general by the negative derivative of a potential V at the corresponding location. Hence we can determine the potential of the first two terms in Equation (4.36) by simple integration leading to

$$V(x) = -x^3/3 - \beta x \ . \tag{4.37}$$

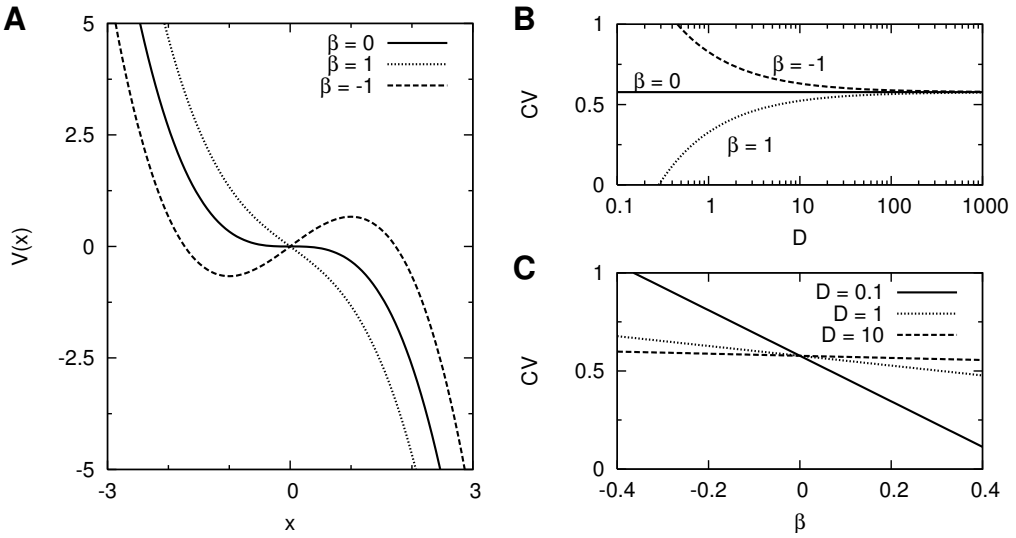

Figure 4.18: Coefficient of variation for a saddle node bifurcation. **A**: Potential $V(x)$ for different values of β. For $\beta < 0$ a minimum occurs. Thus a spike can only be initiated by noise. **B**: Strong noise approximation for CV derived in [123]. For large noise the system does not notice the different potentials, whereas for low noise the oscillatory regime ($\beta > 0$) exhibits small CV, and the spike trains of the excitable system ($\beta < 0$) have a large variability. **C**: Strong noise approximation for CV in dependence of β. In contrast to the Hopf bifurcation system, the saddle node bifurcation leads to rather high CV in the oscillatory regime, i.e. $\beta > 0$.

Integration of the noise term in Equation (4.36) yields a Wiener process that describes Brownian motion. Thus, the Langevin equation can be visualized as a Brownian particle in the potential shown in Figure 4.18A for different values of β.

For $\beta < 0$ the potential $V(x)$ exhibits a minimum at $x = -\sqrt{\beta}$ and a potential barrier at $x = +\sqrt{\beta}$. A particle that comes from the resetting value x_- is caught in the valley and can escape by noise over the barrier corresponding to the famous Kramer problem [108, 90]. That is the typical property of type I neurons. For $\beta > 0$ the system is in the oscillatory regime, since the potential has no minimum.

Lindner and coworkers analyzed the system with respect to the rate $r = 1/\mathrm{T_{av}}$ and the coefficient of variation CV in the three following relevant regimes [123]. In the excitable regime with weak noise the system corresponds to the over-damped Kramers problem as the system (4.35) does for large $\mathrm{T_{av}}$ [90]. In this case the CV is equivalent to the rare-event statistic of a Poisson process and corresponds to our wave nucleation assumption.

The widespread opinion of noisy limit cycle oscillation complies with the oscillatory regime at weak noise, i.e. with a monotonously decreasing potential $V(x)$

given by $\beta > 0$ and the condition $\beta \gg D^{2/3}$. This leads to the approximated mean period $\langle T \rangle = \pi/\sqrt{\beta}$ and the relation for the coefficient of variation $CV \propto \beta^{-3/4}$ [11]. In the buffer experiments in Figure 4.8 we observed an increase of the mean period of about 100 %, which would correspond to a scaling of β by a factor of 4. Corresponding to the above relation that would imply a decrease of CV by a factor of 0.35, which is not in accordance with the experimental findings, where the CVs stay rather constant.

The last regime of the system corresponds to strong noise, i.e $|\beta| \ll D^{2/3}$. In the large noise limit the rate can be approximated by $r \approx 0.2D^{1/3} + 0.15D^{-1/3}\beta$, and for the CV the relation $CV \approx 3^{-1/2} + 0.25D^{-2/3}\beta$ holds [123]. The latter dependence is shown in Figures 4.18B and C for different values of D and β, where we have to bear in mind the restrictions to small βs and large noise, respectively. From the relations above, we can find parameter values that exhibit a similar behavior as seen in the buffer experiments, but due to the restrictions they are not valid. Further, we observe a CV comparable to the one in experiments, but a regular behavior as observed in the measurements can not be generated in the valid range.

Noisy Ca^{2+} ODE model: For an example more related to Ca^{2+}, we return to the ODE model of Goldbeter *et al.* introduced in Section 2.5.1. To analyze the effect of noise and to comment the general opinion, that varying Ca^{2+} signals occur by noisy perturbation of limit cycles, we introduce Gaussian noise into the governing Equations (2.1) leading to the Langevin equation

$$\dot{Z} = J_0 + J_1\beta - J_2 + J_3 + k_f Y - kZ + \sqrt{2D}\varrho(t) \tag{4.38a}$$

$$\dot{Y} = J_2 - J_3 - k_f Y \ , \tag{4.38b}$$

with Gaussian noise $\varrho(t)$ and the fluxes

$$J_2 = V_{M_2} \frac{Z^n}{K_2^n + Z^n} \tag{4.39a}$$

$$J_3 = V_{M_3} \frac{Y^m}{K_R^m + Y^m} \frac{Z^p}{K_A^p + Z^p} \ , \tag{4.39b}$$

describing pumps and channels. For more details see Section 2.5.1.

The introduced noise allows for Ca^{2+} spikes also in the non oscillatory regime. We first analyze the σ-T_{av} relation for standard parameter in the oscillatory regime [84], which exhibits now varying spiking due to the noise. A typical time course of the cytosolic Ca^{2+} concentration is shown in Figure 4.19A for a rather high noise intensity $D = 0.1$.

The dependence of the standard deviation on the average period T_{av} for different $D = 0.1 \ldots 0.001$ is shown in panel B. The dependence in the oscillatory regime exhibits an opposite trend than those found in experiments: σ decreases with T_{av}.

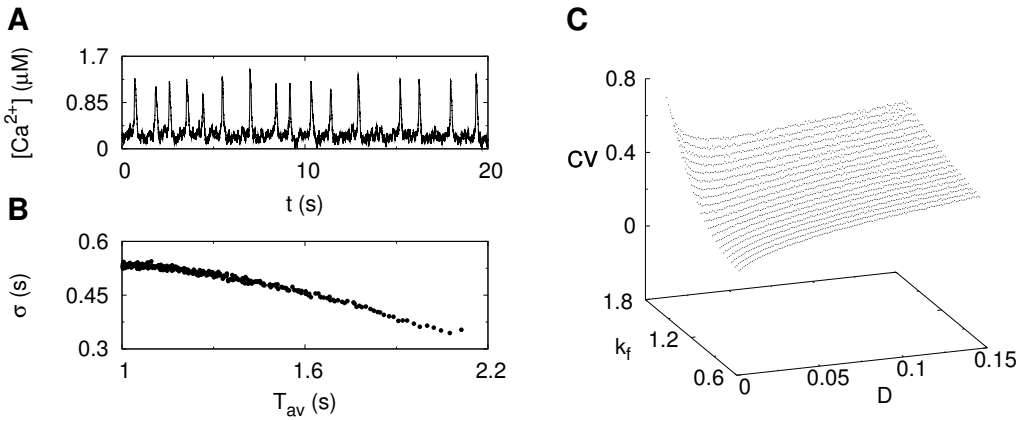

Figure 4.19: Noisy Ca^{2+} ODE model. **A**: Due noise the cytosolic Ca^{2+} oscillations become more irregular. **B**: The σ-T_{av} relation in the oscillatory regime exhibits an opposite dependence than those found in experiments. **C**: Also the coefficient of variation CV exhibits comparable values in the excitable regime, where we observe a minimum on dependence on D. This minimum indicates coherent resonance.

A more systematic analysis is shown in Figure 4.19C, where the coefficient of variation CV is determined in dependence on the noise strength D and k_f. In the oscillatory regime ($k_f <\approx 1.1$), CV increases monotonically with D and exhibits smaller values than those we observed in experiments. In the excitable regime, CV exhibits a nonlinear dependence on D. For small noise, the fluctuations are so small, that the system is merely forced on the unstable limit cycle and exhibits a Poisson like behavior, the behavior of rare events. That correspond to large CVs. For increasing D, CV exhibits a minimum, before it increases again for large noise. This minimum indicates coherent resonance, where the noise is optimal for a regular spiking.

Hence, also the Ca^{2+} specific ODE model does only exhibit a large variation in spiking in the excitable regime and noisy limit cycle oscillations demonstrates different dynamical properties than those observed in experiments.

Resonant behavior: A typical property of excitable media close to the bifurcation is a resonant behavior [257, 258]. This can be illustrated by the potential in Figure 4.18A. If a particle coming from $x_- < -\sqrt{\beta}$ has a mass M it oscillates due to inertia around the minimum until the noise pushes it over the barrier[2]. Hence the probability of escape, i.e. the waiting time density, exhibits several peaks. The particle that could not escape at the first time when it was close to the maximum

[2]For inertia effects we rely on second order ordinary differential equations (ODEs) which are mathematical equivalent to a set of two coupled ODEs such as Equations (4.35) or the Ca^{2+} model defined in (4.38).

swings back and hence its escape probability first decreases and finally increases again when coming back close to to the barrier. In the case of high friction the particle is in the over-damped limit and inertia effects are negligible leading to a unimodal waiting time distribution.

From a dynamical point of view, these two different behaviors correspond to two different kinds of fixed points: a stable focus leads to resonant characteristics and a stable node captures the over damped limit. The latter can be approximated by a one dimensional system like (4.36).

Although the probability distribution in Figure 4.16 exhibits a unimodal structure, one might tend to expect resonant dynamics, due to the peaked power spectra in Figure 4.13. In neurons both resonant and non-resonant regimes are observed [57] and studied, where no significant differences of the spectra are reported [257]. Besides the experimentally hard accessible waiting time density, the Fano factor defined in Equation (3.29) can be used to characterize the dynamics [42, 57].

While the coefficient of variation CV characterizes the variability in the range of $\mathrm{T_{av}}$, the Fano factor $F(T)$ is a measure on all time scales. $F(T)$ is calculated from the merged spike trains ς of astrocytes and HEK cells by splitting ς into non overlapping windows of time T and determining the ratio of the variance and the mean of spike numbers within T. As mentioned in Section 3.5.2, $F(T)$ decreases linearly for small T from one proportional to the inverse of $\mathrm{T_{av}}$. The time scale T_s at which the data start to deviate from the linear dependence denotes the minimal ISI, $\mathrm{T_{det}}$. Figure 4.20 depicts the theoretically expected linear decrease (thick lines) and the data (thin lines) for HEK cells (red), astrocytes (blue) and a deterministic spike train with fixed ISIs of 10 s. We see again the different regimes cells work at. The astrocytes have an averaged minimal ISI of approximately 40 s whereas the HEK cells have a slightly larger $\mathrm{T_{det}} \approx 65$ s. The Fano factor of the deterministic spike train exhibits perfect oscillation, what is in accordance with theory [146]. These oscillations are also observed between 100 s and 300 s for the more regular regime of HEK cells, whereas astrocytes exhibits a more Poisson like character. More important is the comparison with the results obtained with neurons in [57], where resonant neurons exhibit long lasting plateaus and peaks at high values of $F(T)$. The structures found here correspond to non-resonant neurons. The more regular behavior of HEK cells indicated by the oscillating Fano factor is in accordance with theoretical investigations [146] and points out a more coherent behavior, but which is still stochastic.

These examples have demonstrated that the limit cycle assumption may hold for specific experimental conditions, but it cannot be a generic model for the transition from regular to a more stochastic behavior, since it exhibits different characteristics as those observed in experiments.

Also the analysis of Ca^{2+} concentrations close to open IP_3Rs [250] has demonstrated, that stochastic opening and closing of single channels are essential for os-

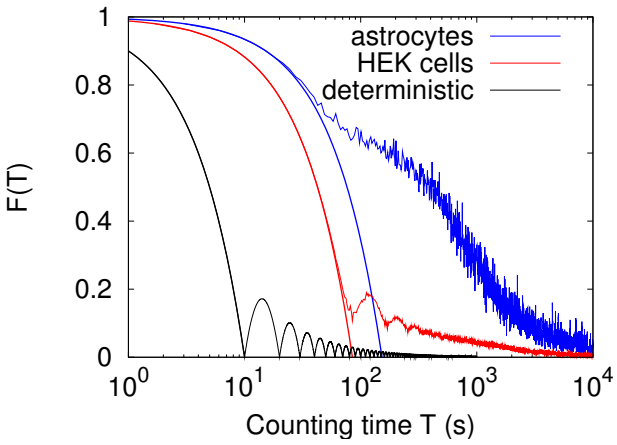

Figure 4.20: Fano factor $F(T)$ for astrocytes (blue), HEK cells (red) and a deterministic spike train with T_{av}=10 s (black). The Fano factor measures spike-count variability in dependence on the time scale, the counting time T. The time scale at which the data (thin lines) starts to differ from theoretical predictions (thick lines) denotes T_{det}.

cillations. In deterministic models with homogeneously distributed IP_3Rs which are solely controlled by IP_3 and Ca^{2+} activation and Ca^{2+} inhibition, oscillations vanish for realistic Ca^{2+} concentrations. By shifting parameters, oscillations can be re-evoked, but their properties such as amplitude and frequency are different compared to experiments.

Moreover, the ODE models are top-down approaches, which do not resolve the molecular level and cannot incorporate the microscopic fluctuations, which we have shown to be essential for the oscillation mechanism.

4.5 Summary

The major findings of this chapter describing the oscillation mechanism can be summarized as follows:

- In contrast to the current opinion for the last twenty years, Ca^{2+} oscillations are sequences of random spikes.

- The analysis suggests that spikes occur by wave nucleation, which is consistent with experimental and theoretical predictions. Hence cells use molecular noise constructively to build global signals, which are orchestrated on the level of the cell and are thus a spatial phenomenon.

- The spatial character is dominated by the interplay of the spatial inhomogeneous IP_3Rs distribution and the SERCA pumps leading in combination with the nonlinear properties of the IP_3R to a stochastic medium. The properties of the stochastic medium and the subsequent behavior of cells depend strongly on the cytosolic buffer concentration and dynamics.

- Spontaneous oscillations exhibit a rather pure Poisson character, whereas stimulated oscillations obey a time dependent Poisson process.
- The cell specific deterministic time T_{det} can be determined from single cell measurements by the model.
- The deterministic time T_{det} can lead to a rather regular regime in case of large nucleation rates λ when the stochastic time is in the same order as T_{det}. This regime is characterized by the dependence on spatial coupling and by the peaked power spectrum indicating AECR for which Ca^{2+} oscillations are a first biological example.
- Moreover, T_{det} leads to an underestimating of the traditional CV. Despite the classical definition $CV = \sigma/T_{av}$ one should estimate CV by the slope of the population line from the σ -T_{av} relation. This property seems to be cell type specific.
- Despite their randomness, Ca^{2+} oscillations can carry information in response to external conditions, which can be estimated by the population slope of the σ-T_{av} relation.
- The Ca^{2+} signaling network might be evolutionary optimized in the sense that its structure induces a Poisson process, which is the optimal choice for information processing.
- Noisy limit cycle oscillators are no good generic models for intracellular Ca^{2+} oscillations.

Chapter 5

Temperature dependence

Within the last chapter our aim was a rather general one, to decipher the oscillation mechanism of intracellular Ca^{2+} oscillations. For that purpose we analyzed oscillations of different cell types. This chapter[1] is devoted to a more specific phenomenon and is restricted to a specific cell type, astrocytes. While I performed the glia experiments regarding the oscillation mechanism in the lab of Helmut Kettenmann at the Max-Delbrück-Center, I was astonished by a paradigm claiming the difference between cultured astrocytes and astrocytes within acute brain slices.

The most predominant and obvious distinctions are the different levels of activity and the strength of Ca^{2+} signals of the two different kind of astrocytes. Cultured astrocytes exhibit rather often spontaneous Ca^{2+} oscillations with spikes having high amplitudes and a typical width of one minute or longer. In contrast, astrocytes in acute brain slices show less frequently Ca^{2+} spikes and their durations and amplitudes are significantly smaller compared to those of cultured cells.

These differences has demoted cultured astrocytes to toy models and physiological findings have always to be confirmed with measurements in acute brain slices. Feeling discontented with this situation (especially since I used cultured astrocytes in my experiments) I discussed possible reasons with many people of the lab.

Inspired by my observation that cultured cells are normally measured at room temperature whereas brain slice experiments use heated buffer solutions I started a first experiment with cultured cells, in which I changed the temperature. Indeed I found a decrease of activity for increasing temperature and even smaller amplitudes. Thus motivated I started a cooperation with Antje Heidemann, a PhD student in the Kettenmann lab, who measured astrocytic Ca^{2+} signals in acute brain slices, and the post doc Carola Schipke who supervised the work.

The work is already published and thus I will demonstrate in this chapter mainly the work I have done and refer for other details to the publication [198]. From the

[1] The chapter is adapted in parts from [198].

systems biological point of view the study of the system under different external condition might increase the knowledge and lead to new hypotheses of the control mechanisms as depicted in Figure 1.1.

5.1 Motivation

As mentioned in Section 3.2.2 Ca^{2+} signaling is the predominant form of astrocytic signaling activity. The Ca^{2+} responses in astrocytes can be elicited by transmitters and hormones but astrocytes exhibit also spontaneous Ca^{2+} activity as seen in Chapter 4. The spontaneous Ca^{2+} transients occur independently of neuronal activity, but are modulated by neuronal function such as induced epileptic activity that increases the number of astrocytes showing spontaneous Ca^{2+} signals [3]. As mentioned in Section 3.2.2, spontaneous astrocytic Ca^{2+} transients can then in turn be sensed by neurons: the Ca^{2+} increase in the astrocytes leads to a release of neurotransmitters, most prominently glutamate, which leads to the activation of NMDA receptors in neurons and neuronal excitation [173].

Spontaneous $[Ca^{2+}]_i$-activity has been reported for astrocytes in culture [68, 255, 35, 133] and acutely isolated slices of several brain regions [156, 172, 240]. The observed regions include the rat ventrobasal thalamus [171, 170], the rat [287] and the mouse hippocampus [283], and the neocortex, entorhinal cortex, striatum, cerebellum, thalamus, hypothalamus, and spinal cord of mice [3]. Pathologic events can affect the properties of spontaneous astrocytic Ca^{2+}-signaling. Reactive astrocytes surrounding stab wounds in the neocortex lack spontaneous Ca^{2+} activity. In contrast, more spontaneously active astrocytes were observed in the neocortex under epileptiform conditions [240]. This astrocytic Ca^{2+} activity has been found in brain slices obtained from mice at all ages, but was highest during the first two weeks after birth and then gradually decreased to a lower level during adulthood [3].

The spontaneous Ca^{2+} responses are quite variable including random profiles, rhythmic oscillations, as well as bursting activity with a wide range of periods from 10 to 300 seconds. In the thalamus, a small subset of so-called 'pacemaker cells' was found, which displayed rhythmic oscillatory patterns of 0.019 Hz [170]. The Ca^{2+} increases have been correlated with the release of neuroactive substances [283]. Astrocytes can release glutamate [21, 9], D-Serine [177, 165], ATP [186, 266, 86, 40, 6, 230], chemokines [56], prostaglandins [21, 284], and NO [119], many of those in a Ca^{2+}-dependent manner [176]. Ca^{2+} increases can occur over the entire cell, but have also been reported to be restricted to small cellular compartments, such as microdomains. These locally restricted elevations can spread along processes, and oscillations could occur independently of each other in different processes within a given cell [113]. Spontaneous Ca^{2+} responses involve Ca^{2+} release from internal stores, mostly mediated by IP_3Rs [170, 156], but also with a potential involvement

of RyRs [240] and influx of extracellular Ca^{2+} by capacitative Ca^{2+} entry.

Recently, spontaneous Ca^{2+} transients have also been observed *in vivo* in the mouse brain [93]. In contrast to observations from brain slices or cultured astrocytes, spontaneous Ca^{2+}-activity occurred with a rather low frequency. To this point, none of the studies in acute slices was carried out at physiological body temperature, but rather at lower temperature, mainly at room temperature. In addition to explain the differences between cultured astrocytes and cells in brain slices, we therefore address the question whether the frequency of spontaneous Ca^{2+} responses in astrocytes depends on temperature. We indeed found that the spontaneous Ca^{2+} transients in astrocytes were strongly dependent on temperature.

5.2 Results

To determine the temperature dependence of spontaneous astrocytic calcium signaling, we recorded basal activity at different temperatures or changed the temperature while recording fluo-4 fluorescence from astrocytes in cortical slices and cultured astrocytes. We either changed the temperature of the perfusate abruptly or gradually changed the temperature by modulating the heating of the recording chamber inlet. The temperature was measured directly in the recording chamber next to the slice or cover slip with a small probe connected to a digital thermometer.

5.2.1 Ca^{2+} signaling of astrocytes in cortical brain slices

In cortical slices obtained from P 10 – P 12 mouse brains, astrocytes exhibited robust spontaneous activity, i.e. oscillations with high frequencies as well as ΔF amplitudes and a long duration (Figure 5.1) when recording Ca^{2+} activity at room temperature. In contrast, we rarely recorded spontaneous activity when the brain slices were maintained at physiological temperature during recording (Figure 5.1).

To determine how rapidly a temperature change will affect the frequency of spontaneous activity and the time course of a single event, we increased the temperature while recording fluo-4 fluorescence from astrocytes in cortical brain slices. The temperature was increased from 24°C to 37°C within about 2 min and then again lowered to 24°C. As shown in Figure 5.1, the spontaneous Ca^{2+} responses decreased rapidly in frequency when the temperature increased and their activity recovered when the temperature dropped. When the heating was turned on during a recording, the overall average amplitude, i.e. the fluorescence signal averaged over all cells, decreased to $49 \pm 14\%$ ($n = 3$, average cell number/slice $= 37 \pm 18$) activity at 37°C compared to activity at room temperature (RT). Spontaneous Ca^{2+}-activity could be restored again by switching the heating off and thereby lowering the temperature back to RT ($154 \pm 70\%$).

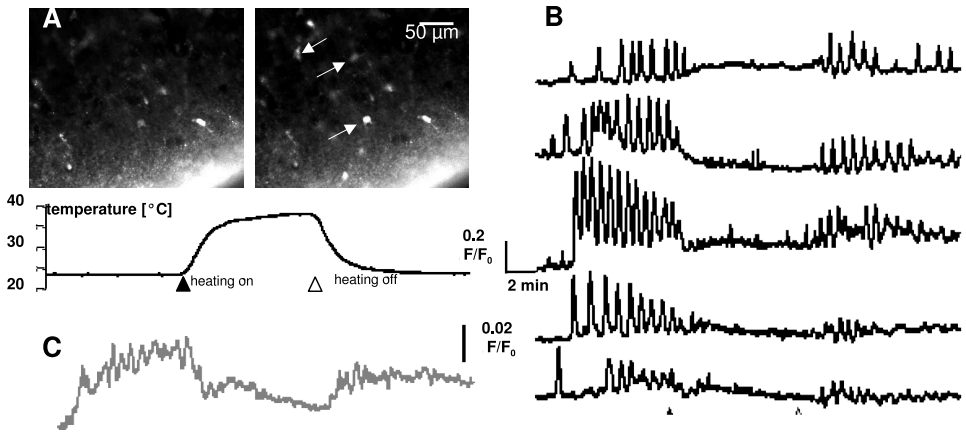

Figure 5.1: Basal calcium activity of cortical astrocytes in acute brain slices is modulated by temperature **A**: Fluorescence microscopy images of one cortical brain slice stained with Fluo4. The left image is taken at RT, the right image at 37-38°C. Arrows point to single astrocytes exhibiting a Ca^{2+} transient. **B**: Time course of change in temperature and fluorescence $\Delta F = F/F_0$ recorded from five different astrocytes within the image shown in **A**. **C**: Average ΔF traces of the five trace.

To determine temperature-frequency relationship of spontaneous Ca^{2+} activity, we compared the number of astrocytes exhibiting spontaneous activity at different temperatures. In one set of experiments, the Ca^{2+} activity was recorded while lowering the temperature from 37-38°C to 34-31°C to examine the relevance of drop-of-temperature-induced astrocytic Ca^{2+} signaling from physiological temperatures. Mild hypothermia within this temperature range [111] is used clinically to attenuate further damage after brain injury [77, 79, 187]. In addition, this temperature range is often used in experiments where the buffer solution is heated to mimic physiological conditions.

The induced activity by lowering the temperature from 37-38°C to 34-31°C was compared to the activity at RT. At 37-38°C, 18 ± 10% of the cells were active as compared to the cells being active at RT (set to 100%). At 31-33°C the number of cells exhibiting Ca^{2+} signaling increased to 40 ± 20%.

In a second set of experiments, the experimental order was reversed so that the reference period measured at RT was at the beginning of the experiment before the temperature was increased to 37-38°C. The number of cells exhibiting spontaneous Ca^{2+}-activity at RT was set to 100% and an increase of temperature to 38°C let to a decrease of the number of active cells to 26 ± 16%. At 31-34°C the number of active cells was 47 ± 26% ($n = 4$).

5.2.2 Ca^{2+} signaling in cultured cortical astrocytes

To explore if the reported differences in Ca^{2+} signals between cortical astrocytes and cultured cells are induced by the different temperatures they are measured at, we performed similar experiments with primary astrocytes cultured from the mouse cortex. Similar results as for acute brain slices were obtained in cultured astrocytes in two sets of experiments with the higher temperature set to 30°C and 28°C. In one set of experiments, the measurement started at 20°C then temperature was raised to 30°C and subsequently lowered back to 20°C. At 20°C, the majority of astrocytes showed increases in Ca^{2+}-transients (72 ± 24% of all cells). This activity decreased rapidly when increasing the temperature to 30°C and was restored by lowering the temperature again to 20°C as shown in Figure 5.2B. In terms of cell numbers, only 17 ± 5% of the cells, which have been active at 20°C exhibited Ca^{2+} transients at 30°C and the activity recovered in 92 ± 21% of the initially active cells when returning to 20°C as shown Figure 5.2C ($n = 4$ experiments).

In a second set of experiments with cultured cells, the temperature was decreased from 28°C to 20°C for one set and vice versa for another set of experiments. As for the recordings in brain slices the order had no influence on the activity change. The number of active cells at 28°C was reduced to 69 ± 8% of the cells being active at 20°C ($n = 6$, averaged active cells/total cells = 74 ± 11%) no matter in which order we recorded the activity. This reduction in activity, starting at 28°C, is significantly smaller compared to recordings with the higher temperature set to 30°C (figure. 5.2C), indicating that between 28°C and 30°C is a threshold-like temperature with regard to the start of the oscillations. An exemplary measurement for the second kind of experiment is exhibited in Figure 5.3A.

5.2.3 Temperature influence on time courses of Ca^{2+} transients

We noted that also the duration of the Ca^{2+} transient was affected by a change in temperature. To determine the time course of single Ca^{2+}-transients, we measured the spike width (SW) of individual Ca^{2+}-transients as explained in Section 3.5.3. The spike duration of the Ca^{2+} transients of astrocytes in acute brain slices decreased significantly when the temperature was raised from 24°C to 37°C, namely from 45 ± 17s to 13 ± 4s. This dependence was fully reversible, since lowering the temperature back to 24°C increased the spike duration again to 45 ± 18s (10 slices, 42 cells at $T_{24°C}$ 70 spikes; $T_{37°C}$ 53; $T_{24°C}$ 71 spikes). We also determined the spike duration at 31°C which averaged at 22 ± 5s (9 slices, 29 cells at $T_{31°C}$ 43 spikes) (Figure 5.3C).

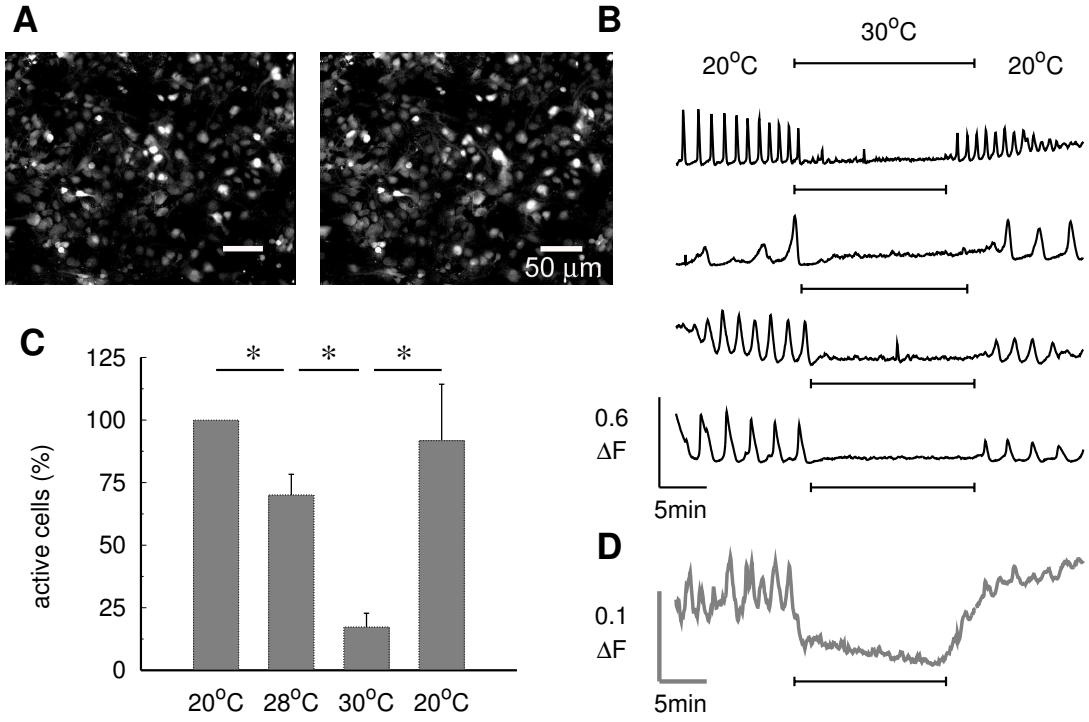

Figure 5.2: The activity of cultured astrocytes is temperature dependent. **A**: Fluorescence microscopy images of an astrocyte culture at two different temperatures, left at 20°C, right at 30°C. **B**: Fluorescence recordings from four different astrocytes in three different experiments. The temperature was varied between 20°C and 30°C (indicated by the bar). **C**: Average number of cells which respond with a fluorescence change in the field of recording (average from four different experiments). The number of responsive cells at 20°C is set to 100 % and then compared to the number of responsive cells at different temperatures or to the recovery at 20°C (bars indicate s.e.; *, $p < 0.05$;). **D**: Average trace of ΔF traces from 38 astrocytes obtained within one experiment similar as shown in **B**.

In cultured astrocytes the spike duration changed from an average of 63 ± 18s at 20°C to 21 ± 5s at 30°C. The effect of temperature on spike duration was reversible, namely 72 ± 20s at 20°C after lowering the temperature from 30°C (4 experiments; at $T_{30°C}$ 15 cells, 26 spikes; at $T_{20°C}$ 30 cells, 56 spikes) (Figure 5.3B). At 28°C, the average spike duration was 27 ± 6s as compared to 75 ± 16s at 20°C (4 experiments; 30 cells at $T_{28°C}$ 103 spikes; $T_{20°C}$ 105 spikes), (Figure 5.3B). There was no significant difference between data obtained from culture and brain slices. We therefore plotted the temperature dependence of the spike duration, pooling data points from culture and brain slices. We computed the weighted average from the individual measurements and found a dependence of the spike widths as shown in Figure 5.3D. The data can be fitted best by $f(T) = ae^{-bT}$ with $a = 620$ s and $b = 0.109/°C$ indicating an exponential dependence of the spike widths on temperature.

In most temperature-controlled perfusion systems, the inflowing buffer is heated. We noted that upon switching off a perfusion with heated buffer, an increase in the frequency of Ca^{2+} responses was induced in astrocytes in acute cortical brain slices [181]. This change in frequency was reversible when the bath perfusion was turned on again. By measuring the temperature in the bath, we found that the temperature dropped from 33°C to 26°C within 250 s (flow rate 3-4 ml/min, chamber volume ≈ 1-1.5 ml). This drop in temperature coincided with an induction of Ca^{2+}-activity in individual astrocytes. During the period of about 4 minutes, in which the perfusion was switched off, we recorded different types of Ca^{2+} responses from individual cells within the same slice, including single peak responses, oscillations, oscillations superimposed on a transient Ca^{2+} increase, plateaus, as well as plateaus with superimposed oscillations. The effect could be repetitively evoked and we commonly observed a similar activity pattern in one given cell.

5.2.4 Further pharmacological investigation

So far we can explain the observed differences of the two cell types by the temperature. To confirm that there are no other chemical side effects Antje Heidemann performed several pharmacological experiments. Their main results are listed below and we refer the interested reader to [198].

NO is involved in modulating oscillatory Ca^{2+} signalling in astrocytes: NO is a potential mediator of the observed Ca^{2+} responses in astrocytes, since NO is implicated in astrocytic Ca^{2+} signalling [119]. To block the production of NO, the nitric oxide synthase inhibitor Nω-nitro-L-arginine (L-NNA; 2 mM) was applied for 12-20 minutes. The number of spontaneously active cells was significantly reduced when compared to control (39 ± 30% with the number of cells active at control conditions set to 100%, $p < 0{,}005$; $n = 16$, averaged cell number/slice = 32 ± 16).

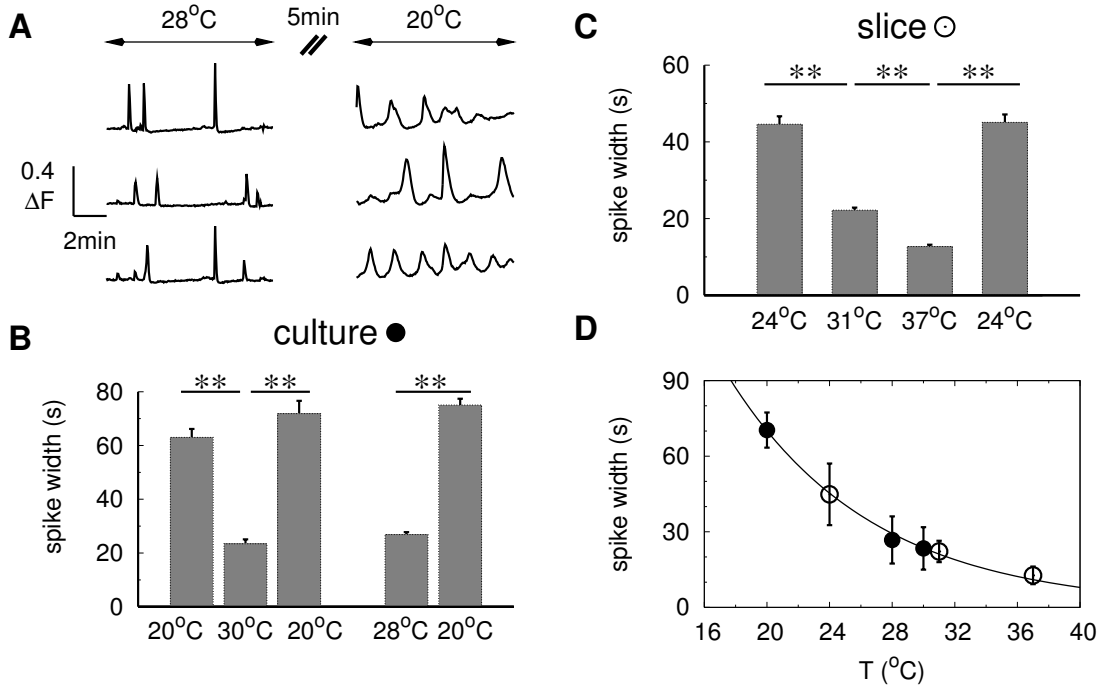

Figure 5.3: The spike width of calcium oscillations is temperature dependent for both, cultured astrocytes and cells within acute brain slices **A**: ΔF traces from three different cultured astrocytes at 28°C and 20°C. Note that the transient fluorescence changes have a smaller spike width and occur less frequently at higher temperature. The recordings were separated by 5 min. **B**: The spike widths of the fluorescence transients were determined from recordings as depicted in **A**. The histogram shows the average values for all experiments obtained from cultured astrocytes determined at different temperatures as indicated (error bars indicate s.e.). **C**: Similar values as shown in **B** but for astrocytes in brain slices. **D**: From data shown in **B** and **C** the duration of the spike width is plotted as a function of temperature for astrocytes from culture (black dots) and brain slices (circles). The data points were fitted by $f(\mathrm{T}) = 620\,\mathrm{s}\exp(-0.109\mathrm{T}/°\mathrm{C})$, where we computed the weighted average for the two lowest temperatures from the data shown in **B** and **C** (**, $p < 0.005$).

The NO-donor S-nitrosoglutathione (SNOG; 100 μM) was applied to investigate whether NO could influence the oscillatory astrocytic Ca^{2+} signalling in astrocytes in acute cortical brain slices. SNOG induced reproducible oscillatory Ca^{2+} responses in cortical astrocytes at 31°C.

The observed Ca^{2+} signalling is mainly driven by release from internal stores: The stopped flow paradigm was used to further study the properties of spontaneous Ca^{2+} activity in astrocytes. Cells were maintained in a perfusion chamber with the inflowing buffer heated to 30-33°C. Subsequently, we activated spontaneous Ca^{2+} activity by lowering the temperature via stopping the perfusion system.

First, it was tested whether spontaneous Ca^{2+} activity was due to Ca^{2+} influx from the extracellular space or due to Ca^{2+} released from intracellular stores. Therefore, Ca^{2+} was omitted in the perfusion buffer. The total number of responsive cells was slightly, but not significantly, reduced to 78 $\pm$ 34% (n = 13, averaged cell number/slice = 31 $\pm$ 15). Interestingly, only cells, which had reacted in control conditions, reacted under Ca^{2+}-free conditions. For assessing the contribution of intracellular Ca^{2+} stores, a first control recording was compared to a second one after perfusion with buffer containing 1 µM thapsigargin for approximately 15 min. After that treatment, in the presence of thapsigargin, astrocytes exhibited a largely reduced oscillatory activity .

We conclude that intracellular Ca^{2+} increase due to spontaneous activity are to a large extent controlled by Ca^{2+} release from intracellular Ca^{2+} stores and that NO is an important factor in controlling spontaneous Ca^{2+} activity also via Ca^{2+} release from internal stores.

5.3 Discussion

We have seen that a decrease in temperatures below the normal body core temperature increases the frequency of spontaneous Ca^{2+} transients in mouse astrocytes and prolongs the duration of single Ca^{2+} transients. The consistency of our findings between cultured astrocytes and astrocytes in acute brain slices, suggests that the temperature-dependence of spontaneous Ca^{2+} activity is an intrinsic property of astrocytes and is not affected by the substantial differences in astrocyte morphology in the two experimental settings.

Spontaneous increases in the cytosolic Ca^{2+} concentration of cells are generally known to play a role in development, differentiation and maturation of tissues. Especially in the nervous system it is described that spontaneous oscillatory electrical activity accompanied by Ca^{2+} oscillations underlie the establishment of connections in the CNS [274, 117, 80, 281, 280], and the astrocytic activity was hypothesized to drive those neuronal oscillations [46, 171].

All previous studies on spontaneous astrocytic Ca^{2+} signalling in culture or in acute brain slices have not been performed at the precise core temperature of 37°C. Either the temperature was not reported as for the hippocampus [156] or, when the temperature was stated, it was commonly between 20°C and 25°C, as for the studies in acute slices of the ventrobasal thalamus (20-24°C) [173] and of the neocortex (22-25°C) [3]. In epileptic tissue, the rate of spontaneous activity increased as compared to control slices in control conditions, but also in this study the temperature during the recording was not stated [240]. These results indicate that spontaneous astrocytic Ca^{2+} signalling at a high frequency could be a temperature artefact and astrocytes *in vivo* might not exhibit such frequent spontaneous activity. Indeed, the first Ca^{2+} recordings from astrocytes *in vivo* support this view [93]. In this study, it is reported that the astrocytes were either quiescent or responded with one or few events during a 10 min observation time. A similar observation was recently made *in vivo* in the barrel cortex: only two out of 93 astrocytes showed a somatic Ca^{2+} increase during a 10 min observation time [265]. Taken together, the findings indicate that the effect of temperature might explain the low frequency of spontaneous Ca^{2+} signalling *in vivo*.

The impact of temperature on Ca^{2+} signalling is most likely not an astrocyte-specific phenomenon. In cardiac muscle the incidence and frequency of Ca^{2+} spikes decreased dramatically at 37°C compared with 22°C. In other cell types as e.g. in rabbit renal tubules, hepatocytes, parenchymal, endothelial, and Kupffer cells of the liver acute hypothermia affects the intracellular Ca^{2+} homeostasis and goes along with a rise in cytosolic Ca^{2+} levels [140, 104, 87].

We found that temperature not only affected the frequency of spontaneous events, but also the time course of a single event. At physiological temperature, single events were significantly shorter as compared to lower temperature. A mechanistic explanation could be a faster inhibition of the IP_3R channels yielding in shorter opening times at higher temperatures or by the temperature dependent activity of the SERCA pumps [50, 112]. Since activity of SERCAs increases with temperature, the communication between IP_3R clusters decreases and events do not occur in synchrony within a cell, thus ceasing the global oscillations.

In Bergmann glial cells, NO triggers a transient Ca^{2+} increase, and the Ca^{2+} transient triggered by parallel fibre stimulation is mediated by NO [139]. Here we demonstrated that SNOG, an NO-donor, triggered Ca^{2+} signalling in cortical astrocytes in acute brain slices. We show a strong overlap of the cell populations exhibiting Ca^{2+} signalling upon SNOG application and at low temperatures. Whereas the NO-induced response is completely dependent on Ca^{2+} release from internal stores, the signalling induced by a drop in temperature is not completely abolished after emptying internal Ca^{2+} stores. Thus, we assume that NO is not the initial trigger of the drop-in-temperature-induced Ca^{2+} signalling but has a secondary role in its amplification. NO has already been suggested to function as an autocrine factor for

astrocytes [204, 200] and even to be an endogenous Ca^{2+} influx factor, responsible for the refill of internal stores [119]. This, together with the fact that NO-synthase is mainly activated by Ca^{2+} [106, 28], supports the possibility of an amplifying role for NO.

Methodological consequences

Many studies on astrocytic cultures or brain slices are carried out at room temperature [3] or the temperature is not even reported [156]. The results obtained here demonstrate that astrocytes show altered Ca^{2+} signalling behavior at room temperature in comparison to higher temperatures with oscillations almost absent at physiological temperatures. Therefore, any measurements on astrocytes at room temperature are prone to artefacts as Ca^{2+} signalling can account for many cellular processes possibly influencing the measured parameters. Since astrocytic Ca^{2+} signalling was demonstrated to affect neuronal activity, the same applies for measurements of neuronal parameters in brain slices or mixed cultures. On the other hand, the reproducibility of Ca^{2+} oscillations in astrocytes induced by a drop in temperature might serve as a means to introduce such activity and to further study the influence of astrocytic Ca^{2+} activity on the functionality on integrated neuron-glia networks in the brain.

5.4 Summary

This chapter has shown how temperature changes the cell behavior. Interestingly cell work counter intuitive from a physical point of view. In physics higher temperature leads to higher energy and subsequently to higher activities as for instance in threshold models discussed in Section 4.4.1. The temperature dependent SERCA activity might thus serve as another example how cells keep themselves far from thermodynamic equilibrium.

The biological aspects of the investigation within this chapter can be summarized by:

- The effect of temperature explains the low frequency of spontaneous Ca^{2+} signalling *in vivo*.
- The observed differences between cultured astrocytes and astrocytes in acute brain slices are mainly induced by the different temperatures at which cells are normally measured.
- The supposed reasons of the temperature dependence given by the higher SERCA activity and a possibly faster inhibition of IP_3Rs at higher temperatures lead to the assumption, that this effect is not astrocytes specific.

- NO effects spontaneous Ca^{2+} activity in astrocytes.

Although our phenomenological knowledge is increased and the paradox differences between the cell types are explained we end up with a further question which is related to the one of the previous chapter. Is the temperature dependence a local or a spatial phenomenon? In the case that the the activity decrease is caused by higher SERCA activity, the phenomenon would correspond to the buffer experiments in Section 4.2.3 and has therefore a spatial character. If the effect is caused by a change in the IP_3R properties, it would correspond to local character.

Hence, we have obtained a new hypotheses that can be tested in theoretical investigations. To explore whether the increased SERCA activity can lead to the observed behavior we rely on a physiological model for intracellular Ca^{2+} dynamics. That is the topic of the modeling part coming next.

Part II

Modeling

Chapter 6

A physiological model of intracellular Ca^{2+} dynamics

Within this chapter[1] we develop a detailed biophysical model for intracellular Ca^{2+} dynamics. The model includes the most important features identified in the experimental part to determine the oscillatory behavior. The dominant property is the hierarchical organization of Ca^{2+} signals. They are triggered by local stochastic opening events of single channels. These fluctuations are carried on the level of the cell by wave nucleation. To capture this structure a generic model relies on a bottom-up approach.

The variety of characteristics of Ca^{2+} oscillations in different cell types has led to a zoo of different modeling approaches as mentioned in Section 2.5. The huge modeling interest arose from an experiment by Woods and coworkers in 1986 showing that hepatocytes respond with intracellular Ca^{2+} oscillations to hormonal stimulation [275, 276]. This was explained by Goldbeter *et al.* by the model (2.1) introduced in Section 2.5.1 consisting of two coupled ordinary differential equations (ODEs) [84, 53].

The discovery of the oscillatory behavior awoke the interest of theoreticians. In theoretical physics there was a well-established theory about dynamical systems exhibiting different kinds of oscillations and transitions from oscillatory behavior to damped dynamics [54, 233]. We can rather easily determine the asymptotic behavior of a small system in dependence on model parameters from its governing differential equations by a linear stability analysis. Stability analysis is based on the determination of the eigenvalues of the Jacobi matrix. These eigenvalues describe the stability of fixed points and their characteristics. In theoretical biology this methods was already used since the late 1960s to describe glycolytic oscillations [205, 202, 92].

In this framework Ca^{2+} oscillations were assumed to be limit cycles, which are

[1] This chapter is adapted in parts from [216].

closed trajectories in the phase space. Limit cycles can arise by a variety of bifurcations. Most common bifurcations are Hopf and saddle node bifurcations, which have characteristic amplitude and period behaviors [45] some of which are discussed in Section 4.4.1.

A general problem of these models is their assumption of a well stirred cell neglecting concentration gradients within the cell. But our experimental results of Chapter 4 have demonstrated that Ca^{2+} signaling occurs by a hierarchical network given by an array of IP_3R clusters and that their spatial inhomogeneity and the ensuing concentration gradients are essential ingredients of the oscillation mechanism. Hence, Ca^{2+} oscillations consist of repeated wave nucleation and are thus a spatial phenomenon, where the spatial aspect is a major component to shape oscillations. Moreover, we have demonstrated in Section 4.4.1 that our experimental findings are not consistent with the limit cycle assumption.

Ca^{2+}-wave nucleation is theoretically studied with different approaches including buffer dynamics and different IP_3R models and arrangements. Most of them are restricted to one or two spatial dimensions and assume homogeneously distributed IP_3Rs or large numbers of IP_3Rs so that the individual behavior of a single channel is averaged out. In regards to the hierarchical signaling network, these assumptions may not be valid, since they do not allow for microscopic triggering events and the subsequent dynamics of a stochastic medium, whose existence was verified in the experimental part of this thesis. Moreover, theoretical studies have shown that systems with realistic values for dissociation constants and local concentrations do not exhibit an oscillatory regime [250].

From our experimental results we deduce that a generic model must include the following features:

- spatially extended cells
- inhomogeneous IP_3R distribution
- buffer dynamics
- microscopic IP_3R models.

The development of such a model corresponds in the context of the knowledge generation in system biology to the theoretical loop in Figure 1.1. We are interested in such a model by two reasons. Firstly, we want to verify the experimental results about the oscillation mechanism and to proof the hypotheses obtained from experiment. Therefore, we include the hierarchical structure and analyze the model's outcome. Secondly, we may find new hypotheses about the complex interplay of the involved elements, which may lead to new experimental studies and thus can be the starting point for a next knowledge generating loop.

We will model in Chapter 7 the experimental protocols used in the first part and verify both, experiments and the model by coincidence of their results. Thereby we model the buffer experiments of Chapter 4 and revive the question of the temperature dependence of Ca^{2+} oscillation found in Chapter 5. Within the latter we have hypothesized that the reversible decrease of Ca^{2+} signals at higher temperature is caused by the increased activity of SERCA pumps what we want to verify.

The model can be used as well for other signaling pathways exhibiting spatial concentration gradients such as e.g. cAMP [282, 118, 254, 271, 102]. The included spatial inhomogeneity and its stochastic property may evoke the interest of other scientific fields as pattern formation in physics and chemistry or the theory of stochastic processes.

6.1 General concept

Our modeling strategy for this coupled system is based on separation of the two involved length scales. On the microscopic scale we use a detailed model for the channels. Those will open and close in a stochastic manner due to stochastic binding of signaling molecules.

To derive a physiological model of intracellular Ca^{2+} dynamics we incorporate all three spatial dimensions and include a realistic model for the release channels. That enables us to take into account the spatial arrangement of cells and their complex regulation mechanisms described in Section 2.3. The latter is given by reactions of Ca^{2+} with buffer molecules like BAPTA or Calmodulin and by the SERCA pumps, which remove Ca^{2+} from the cytosol. The cellular dynamics is therefore described by reaction diffusion equations including the biological elements. The cellular dynamics is given by an in general nonlinear reaction diffusion system (RDS). In order to solve this RDS analytically we will linearize the equations and determine the corresponding coupled Green's functions [163, 13].

Once we have the Green's function of a reaction diffusion equation, we can calculate the concentration C at any arbitrary position $\mathbf{r}$ at time t by

$$\begin{aligned} C(\ \mathbf{r},t) = &\int_V d\ \mathbf{r}' \int_0^t dt' F_0(\ \mathbf{r}') G(\ \mathbf{r},t|\ \mathbf{r}'t') + \int_S dS' \int_0^t dt' \Phi(\ \mathbf{r}',t') G(\ \mathbf{r},t|\ \mathbf{r}'t') \\ &+ \int_V d\ \mathbf{r}' \int_0^t dt' F(\ \mathbf{r}',t') G(\ \mathbf{r},t|\ \mathbf{r}'t')\ , \end{aligned} \tag{6.1}$$

where V denotes the volume of the cell and S its surface. The first term in Equation (6.1) describes the influence of the initial concentration distribution $F_0(\ \mathbf{r}')$, the second corresponds to a possibly time dependent flux boundary condition $\Phi(S,t')$ and the last term takes volume source terms $F(\ \mathbf{r}',t')$ into account. In the case of Dirichlet boundary conditions G has to be replaced in the second term of the right hand side by its derivation to the outward-drawn normal n, i.e. by $\partial G/\partial n$.

We can calculate concentrations at arbitrary points in space without having to calculate them at all points of a numerical grid due to the Green's function. That makes the method fast, since integrations are usually faster than grid operations.

Another important property of the general solution (6.1) is that we can solve very efficiently inhomogeneous boundary problems, which are very common in biological systems as one might think about inhomogeneously distributed plasma membrane receptors.

For the intracellular Ca^{2+} dynamics we will assume in the following Neumann (no-flux) boundary condition as well as Dirichlet boundary conditions. The Ca^{2+} dynamics is mostly driven by the last term of Equation (6.1), which corresponds to the volume production $F(\mathbf{r}', t')$ given by the channel currents. To determine these currents we will use the recently developed single channel approximation to translate the states of channels into currents needed to determine the concentration dynamics.

The two parts, the microscopic channel dynamics and the cellular concentration dynamics are coupled by a hybrid version of a Gillespie algorithm [82, 5], which determines the channel transitions in dependence on the concentration dynamics.

6.2 The DeYoung-Keizer channel model

As mentioned in Section 2.4 the most important property of IP_3Rs is their nonlinear open probability dependence on the Ca^{2+} concentration found by several groups in the early 1990s [73, 20, 168]. This is the key element of CICR. The versatility and importance of IP_3Rs has led to a variety of model approaches reviewed in [224].

There are two different concepts. The mechanistic models (like the DeYoung-Keizer model [48] or the Atri model [12]) assume binding to each subunit to be independent of the state of other subunits. The different models exhibit similarities, and some are even equivalent or familiar in the sense that one model is a simplification of another one [239].

Conceptually different models assume binding to different subunits as coupled [237, 153]. All these investigations focus on the stationary behavior of the IP_3R, simply caused by the experimental restriction to resolve the fast channel dynamics well enough for non stationary models. Hence, the model developed here can be used to analyze the different channel models in a dynamic environment closing the gap between stationary behavior and physiological cell dynamics.

In this chapter we use the DeYoung-Keizer model, but the following RDS and its solution can also be used with other channel models. Motivated by atomic force microscopic pictures of the IP_3R as the one shown in Figure 2.4E, the DKM assumes each IP_3R to consist of four identical subunits. The DKM assumes 3 binding sites per subunit. One binding site for IP_3, one for Ca^{2+} activating the subunit and

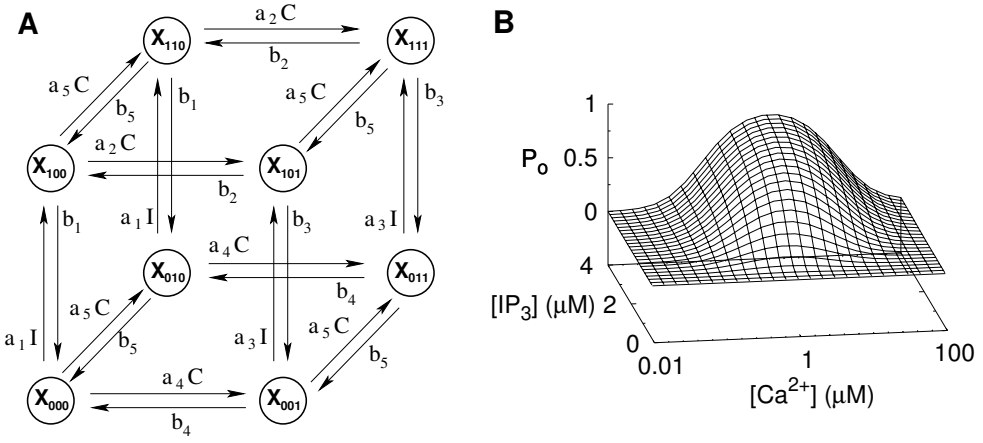

Figure 6.1: **A**: Scheme of the DeYoung-Keizer model for a single subunit. A subunit is active, if IP_3 (I) is bound and Ca^{2+} (C) is only bound to the activating site, i.e. in state X_{110}. A channel opens if at least 3 of its 4 subunits are active. See text for more details and Table 6.1 for values of rates b_i and rate constants a_i. **B**: Stationary open probability P_o defined by Equation (6.3) for the rate constants a_i and rates b_i given in Table 6.1.

another one for Ca^{2+}, which inhibits the subunit. The two binding sites for Ca^{2+} with a higher affinity for the activating site and a lower affinity for the dominant inhibiting site is a minimal choice to generate nonlinearities, which are the sources of the bell shaped open probability in Figure 2.4E and of CICR, respectively.

Since each of the 3 binding sites can be free or occupied, a single subunit has 2^3 different states X_{ijk} and 12 possible transitions, which can be visualized on a cube as shown in Figure 6.1A.

The first index of X_{ijk} specifies IP_3 binding and is 1 if IP_3 is bound and 0 otherwise. Analogously, the second index indicates Ca^{2+} binding to the activating site, and the last one corresponds to Ca^{2+} binding to the dominant inhibiting site. A subunit is active in the state X_{110} only and a channel will open if at least three of the four subunits are activated.

The transitions between the states X_{ijk} occur by stochastic binding and dissociation of signaling molecules to the corresponding binding sites. The rates for binding depend on the particular rate constants a_i and on the Ca^{2+} concentration C and the IP_3 concentration I, respectively, as shown in Figure 6.1A, whereas dissociation occurs with constant rates b_i.

The binding and unbinding of Ca^{2+} and IP_3 in an ensemble of receptors lead to a fraction of channels p_{ijk} in the state X_{ijk}. In the case of a large and homogeneous ensemble, the dynamics of p_{ijk} can be described by rate equations taking the dependence on the Ca^{2+} and IP_3 concentration into account. In general these con-

a_1	20 $(\mu Ms)^{-1}$	IP_3 binding with no inhibiting Ca^{2+} bound
b_1	20 s^{-1}	IP_3 dissociation with no inhibiting Ca^{2+} bound
a_2	0.001 $(\mu Ms)^{-1}$	Ca^{2+} binding to inhibiting site with IP_3 bound
b_2	0.03 s^{-1}	Ca^{2+} dissociation from inhib. site with IP_3 bound
a_3	2.6 $(\mu Ms)^{-1}$	IP_3 binding with inhibiting Ca^{2+} bound
b_3	20 s^{-1}	IP_3 dissociation with inhibiting Ca^{2+} bound
a_4	0.025 $(\mu Ms)^{-1}$	Ca^{2+} binding to inhib. site with no IP_3 bound
b_4	0.1 s^{-1}	Ca^{2+} dissociation from inhib. site without IP_3
a_5	10 $(\mu Ms)^{-1}$	Ca^{2+} binding to activating site
b_5	1.225 s^{-1}	Ca^{2+} dissociation from activating site

Table 6.1: Rates of the DKM used within simulations if not stated otherwise.

centrations are not constant in time, and especially the Ca^{2+} concentration changes enormously by transitions from closed to open states and vice versa. We can determine the stationary values $\bar{p}_{ijk}$ for constant Ca^{2+} and IP_3 concentrations denoted by C_{st} and I, respectively. They are given by

$$\bar{p}_{000} = \gamma_1\, d_1 d_2 d_5 \qquad \bar{p}_{100} = \gamma_1\, d_2 d_5\, I\ , \tag{6.2a}$$
$$\bar{p}_{010} = \gamma_1\, d_1 d_2\, C_{st} \qquad \bar{p}_{001} = \gamma_1\, d_3 d_5\, C_{st}\ , \tag{6.2b}$$
$$\bar{p}_{011} = \gamma_1\, d_3\, C_{st}^2 \qquad \bar{p}_{101} = \gamma_1\, d_5\, I\, C_{st}\ , \tag{6.2c}$$
$$\bar{p}_{110} = \gamma_1\, d_2\, I\, C_{st} \qquad \bar{p}_{111} = \gamma_1\, I\, C_{st}^2\ , \tag{6.2d}$$

where $\gamma_1^{-1} = (C_{st} + d5)\,(d_1 d_2 + C_{st} d_3 + C_{st} I + d_2 I)$ and $d_i = b_i/a_i$.

With these relations we can determine the stationary open probability P_o in dependence on Ca^{2+} and IP_3. Since a channel opens if three or four subunits are in the state X_{110}, the open probability takes the form

$$P_o = 4p_{110}^3 - 3p_{110}^4\ , \tag{6.3}$$

which is shown in Figure 6.1B in dependence on Ca^{2+} and IP_3 for the rates given in Table 6.1. We observe a bell shaped dependence on Ca^{2+} and the monotonic increase of P_o with increasing IP_3.

6.3 IP_3 dynamics

As seen above, both IP_3 and Ca^{2+} are essential to activate a subunit. We start with the simpler IP_3 dynamics. IP_3 is produced by PLCs at the plasma membrane in response to external stimulation by agonists. From there it diffuses into the cytosol,

where it is degraded by enzymes. In order to find an analytical solution we describe the dynamics by

$$\frac{\partial [IP_3]}{\partial t} = D_{\mathrm{IP_3}} \nabla^2 [IP_3] - \eta [IP_3] \ , \tag{6.4}$$

where $D_{\mathrm{IP_3}}$ denotes the diffusion coefficient and η is the degradation rate. The linear partial differential equation (PDE) (6.4) can be solved by the Green's formalism (6.1), where the dynamics is purely driven by the boundary condition, i.e. only the surface term in Equation (6.1) determines the concentration. As IP_3 cannot pass the membrane and we assume the cell to be a sphere, we have to specify the spherical Green's function with no-flux boundary condition. The latter may also hold for Ca^{2+} in large cells.

6.3.1 Deriving the spherical Green's function

We start with the most simple case of pure diffusion of a general species C within a sphere described by the spherical coordinates r, θ and ϕ with the initial and boundary conditions defined by

$$\frac{\partial C}{\partial t} = D_{\mathrm{C}} \nabla^2 C \tag{6.5a}$$

$$C(r, \theta, t_0) = f(r, \theta) \tag{6.5b}$$

$$\left. \frac{\partial C}{\partial r} \right|_{r=R} = j(\theta, t) \ , \tag{6.5c}$$

where D_C denotes the diffusion coefficient, R is the radius of the cell, f denotes the initial distribution of C and j describes the flux through the membrane. Due to rotational symmetry we can neglect the ϕ dependence.

The Green's function is the response of a system due to a δ source in time and space. The corresponding relation of Equation (6.5) for the Green's function $G = G(r, \theta, t | r', \theta', t')$ takes the form

$$\frac{\partial G}{\partial t} = D \nabla^2 G + \frac{1}{r'^2 \sin \theta'} \delta(r - r') \delta(\theta - \theta') \delta(t - t') \tag{6.6a}$$

$$G(r, \theta, t | r', \theta', t') = 0, \quad t \leq t' \ , \tag{6.6b}$$

where G has to fulfill the corresponding boundary condition in (6.5c). This problem can be solved by Laplace transformation and separation ansatz. After Laplace transformation with respect to t the governing equation of the transformed Green's function $\tilde{G}(r, \theta, s | r', \theta', t')$ reads

$$\tilde{G} = D \nabla^2 \tilde{G} + \frac{1}{r'^2 \sin \theta'} \delta(r - r') \delta(\theta - \theta') e^{-st'} \ . \tag{6.7}$$

We first solve the homogeneous problem being the Helmholtz equation

$$\nabla^2\psi(r,\theta) + \lambda^2\psi(r,\theta) = 0 \;, \tag{6.8}$$

where the λs are determined by the particular boundary condition. In spherical coordinates Equation (6.8) reads

$$\frac{\partial^2\psi}{\partial r^2} + \frac{2}{r}\frac{\partial\psi}{\partial r} + \frac{1}{r^2\sin\theta}\frac{\partial}{\partial\theta}\left[\sin\theta\frac{\partial\psi}{\partial\theta}\right] = -\lambda^2\psi \;, \tag{6.9}$$

which can be solved by a standard separation ansatz. We expand the space dependent part $D\nabla^2\tilde{G}$ in eigenfunctions of the Laplace operator ∇^2. The radial part leads to Bessel's differential equation and the angle dependent part obeys a Legendre differential equation. Due to convergence restrictions, the solution of the Helmholtz equation (6.8) takes the form

$$\psi_{lp}(r,\theta) = \frac{J_{l+1/2}(\lambda_{lp}r)}{r^{1/2}}P_l(\cos\theta), \quad p = 1,2,3,\ldots \;\; l = 0,1,2,\ldots \tag{6.10a}$$

$$\psi_{00}(r,\theta) = 1 \;, \tag{6.10b}$$

where $J_i(x)$ denotes the ith Bessel function of the first kind [1] and $P_l(\cos\theta)$ is the Legendre polynomial [1]. The λ_{lp}s are determined by the boundary condition

$$\frac{\partial}{\partial r}\frac{J_{l+1/2}(\lambda_{lp}r)}{r^{1/2}}\bigg|_{r=R} = \frac{l}{R\lambda_{lp}}J_{l+1/2}(\lambda_{lp}R) - J_{l+3/2}(\lambda_{lp}R) = 0 \;, \tag{6.11}$$

where for each mode l of the oscillating Bessel function $J_l(x)$ p different λ_{lp}s fulfill the condition (6.11). We can solve Equation (6.7) by inserting the ansatz

$$\tilde{G}(r,\theta,s|r',\theta',t') = \sum_{l,p=0}^{\infty}\beta_{l,p}\psi_{l,p}(r,\theta) \tag{6.12}$$

leading to

$$s\sum_{l,p=0}^{\infty}\beta_{l,p}\psi_{l,p}(r,\theta) = -D\sum_{l,p=0}^{\infty}\beta_{l,p}\lambda_{lp}^2\psi_{l,p}(r,\theta) + \frac{1}{r'^2\sin\theta'}\delta(r-r')\delta(\theta-\theta')e^{-st'} \;. \tag{6.13}$$

By applying the integral-operators

$$\int_{-1}^{+1} d\mu\, P_m(\mu) \tag{6.14a}$$

$$\int_0^b dr\, r^{3/2}J_{m+1/2}(\lambda_{mq}r) \;, \tag{6.14b}$$

we get due to orthogonality of the Legendre polynomials and of the Bessel functions [1] the relation

$$s\beta_{m,q} = -\beta_{m,q}\lambda_{mq}^2 D + \frac{1}{\mathcal{N}(m)\mathcal{N}(\lambda_{mq})}\psi_{mq}(r',\theta')e^{-st'} \ , \tag{6.15}$$

where the norms $\mathcal{N}$ are given by

$$\mathcal{N}(l) = \int_{-1}^{+1} d\mu \, P_l^2(\mu) = \frac{2}{2l+1} \tag{6.16a}$$

$$\begin{aligned}\mathcal{N}(\lambda_{lp}) &= \int_0^R dr\, r^2 \left[\frac{J_{l+1/2}(\lambda_{lp}r)}{r^{1/2}}\right]^2 \\ &= \frac{R^2}{2}\left[J_{l+1/2}^2(\lambda_{lp}R) - J_{l-1/2}(\lambda_{lp}R)J_{l+3/2}(\lambda_{lp}R)\right]\end{aligned} \tag{6.16b}$$

$$\mathcal{N}(\lambda_{00}) = \int_{-1}^{+1} d\mu \int_0^R dr\, r^2 = 2\frac{R^3}{3}. \tag{6.16c}$$

Equation (6.15) determines the unknown coefficients β_{lp}. The solution in Laplace space is thus given by

$$\tilde{G}(r,\theta,s|r',\theta',t') = \sum_{l,p=0}^{\infty} \frac{1}{\mathcal{N}(l)\mathcal{N}(\lambda_{lp})(s+D\lambda_{lp}^2)}\psi_{lp}(r',\theta')e^{-st'}\psi_{l,p}(r,\theta). \tag{6.17}$$

It can be transformed back easily to time by the residual theorem, since we have first order poles, $s + D\lambda_{lp}^2$, along the negative real axis only. The Green's function of the inhomogeneous diffusion problem (6.5) finally reads

$$\begin{aligned}G(r,\theta,t|r',\theta',t') = \sum_{l=0,p=1}^{\infty} &\frac{1}{\mathcal{N}(l)\mathcal{N}(\lambda_{lp})}\frac{J_{l+1/2}(\lambda_{lp}r')}{r'^{1/2}}P_l(\cos\theta')e^{\lambda_{lp}^2 Dt'} \\ &\frac{J_{l+1/2}(\lambda_{lp}r)}{r^{1/2}}P_l(\cos\theta)e^{-\lambda_{lp}^2 Dt} + \frac{3}{2R^3} \ .\end{aligned} \tag{6.18}$$

The Green's function describes the response in the point (r,θ) due to a delta source in (r',θ'). Thus we can rotate the coordinates, that one of the Legendre polynomials is one and G does only depend on one angle Θ. In the following we are interested in the responses of different localized sources at asymmetrically arranged points shown in Figure 6.2 for two representative points P and P'. Hence, the spherical symmetry is not valid anymore and we have to include the ϕ dependence, what can be done in an elegant way by the relation between the angles

$$\cos(\Theta) = \cos(\theta)\cos(\theta') + \sin(\theta)\sin(\theta')\cos(\phi - \phi') \ . \tag{6.19}$$

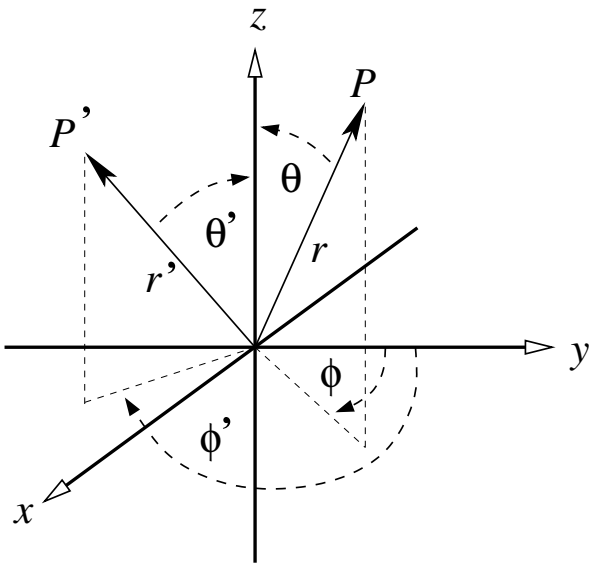

Figure 6.2: Sketch of the angles of two points P and P' in spherical coordinates. For more than two asymmetrically distributed points we have to incorporate the ϕ dependence. Since the solution (6.20) does only depend on the cosine of the angle between the two points P and P', we can use Equation (6.19) to rotate the sytem with respect to the coordinates of the two points.

The ϕ dependence induces another normalization factor of 2π, and the Green's function $G_0(r, \theta, \phi, t|r', \theta', \phi', t')$ of the IP$_3$ dynamics with $\eta = 0$ finally reads

$$G_0 = \sum_{l=0,p=1}^{\infty} \frac{J_{l+1/2}(\lambda_{lp} r) J_{l+1/2}(\lambda_{lp} r')}{2\pi \mathcal{N}(l) \mathcal{N}(\lambda_{lp}) \sqrt{r r'}} P_l(\cos\Theta) e^{-\lambda_{lp}^2 D(t-t')} + \frac{3}{4\pi R^3} , \tag{6.20}$$

with the diffusion coefficient D and the norms $\mathcal{N}$ defined in (6.16). The λs are determined by the boundary condition in Equation (6.11). The second term of the solution (6.20) corresponds to the stationary solution, where the amount of the δ source is equally distributed. Once we have determined the Green's function G_0 we can easily calculate the solution C_0 by the approach (6.1).

For non vanishing η the solution can be determined by Dankwart's method [44]. The solution of the linear reaction diffusion equation

$$\frac{\partial C}{\partial t} = D_C \nabla^2 C - \eta C \tag{6.21}$$

is given by

$$C = \eta \int_0^t C_0(t') e^{-\eta t'} dt' + C_0(t) e^{-\eta t} , \tag{6.22}$$

where C_0 denotes the solution for $\eta = 0$. Instead of integrating the solution derived by the Green's function for the second time, we can incorporate the linear degradation in the Green's function. Thus, the Green's function G_η of the IP$_3$ dynamics defined in Equation (6.4) is given by

$$G_\eta = G_0 e^{-\eta(t-t')} . \tag{6.23}$$

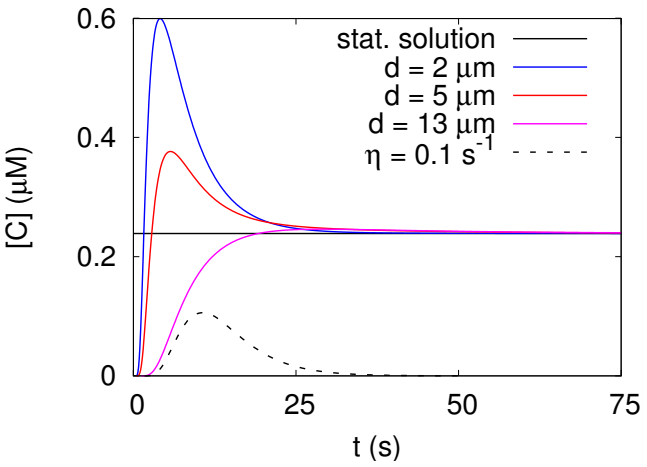

Figure 6.3: Concentrations at different distances d of a δ source with strength 1 mM. For $\eta = 0$ the concentrations (solid lines) converge to the stationary solution (black solid). For $\eta \neq 0$ the stationary solution is 0. The dashed line corresponds to the purple line with $\eta = 0.1$ s^{-1}.

To test the derived solution we calculate the response of a spatio-temporal delta source of strength $\sigma_C = 1$ mM. Due to the spatial δ function of the source, the spatial integrals in Equation (6.1) vanish and the concentration is given by the time integral over Equation (6.23).

We test the solution with a sphere of radius $R = 10$ µm and in the case $\eta = 0$, since we know that the solution should converge to the homogeneous stationary concentration $C_{st} = V^{-1}$ µm^{3}mM. This is shown in Figure 6.4, where the solid colored lines denotes the concentration at different distances of the source in the case of vanishing η. We see that the used number of modes $N_l = N_p = 30$ is sufficient to avoid an oscillating behavior and converge to the known stationary solution. Moreover, we observe a maximum in C for points close to the source, which decreases with increasing distance. For a large distance (purple line) the maximum vanishes, since C is nearly homogeneously distributed. For non vanishing η the stationary solution is zero and we expect in general smaller concentrations. Indeed, we observe such a behavior for $\eta = 0.1$ s^{-1} as indicated by the dashed line in Figure 6.4.

6.3.2 Applications of the spherical Green's function

A more physiological scenario with respect to IP_3 dynamics is the IP_3 distribution induced by plasma membrane receptor activated PLCs. If we assume the IP_3 sources in the membrane as delta functions in the angles, the surface integral in Equation (6.1) is reduced to a sum over the distinct sources at (R, θ_s, ϕ_s). Fig. 6.4 exhibits plane cuts through a cell with 42 randomly scattered IP_3 sources of strength σ_{IP} in the membrane. In each plane the IP_3 concentration is shown 200 ms after stimulation of a cell with a radius of $R = 10$ µm and typical values for the IP_3 dynamics [264] ($D_{ip_3} = 80\ \mu m^2/s$, $\eta = 10.2$ 1/s and $\sigma_{IP} = 1$ mM/s). This inho-

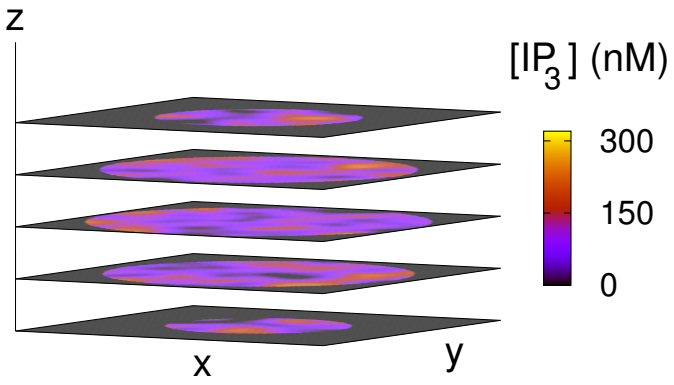

Figure 6.4: IP_3 concentration in 5 planes of a cell with 42 randomly scattered membrane receptors 200 ms after stimulation leading to a flux $\sigma_{IP} = 1\ mM/s$ of each receptor. This inhomogeneous distribution blurs after stimulation and finally vanishes due to degradation.

mogeneous distribution will blur after the stimulation has stopped and vanish for $t \to \infty$ caused by the degradation with rate η.

6.4 Ca^{2+} dynamics

In contrast to the experimental situation in the last section, intracellular Ca^{2+} dynamics is mainly driven by Ca^{2+} release from internal stores by channels. The cellular Ca^{2+} response to channel transition is determined by the spatio-temporal interplay of the cytosol and the ER connected by IP_3Rs, SERCA pumps and by a leak flux σ_l through the membrane of the ER. It was shown in both, experimental [14] and theoretical [58] studies, that buffers play an important role by shaping the Ca^{2+} signals and have the physiological function to keep the free Ca^{2+} concentration low. Due to low Ca^{2+} base level concentrations, these buffers are not saturated, and we have to take them into account explicitly.

As shown in Figure 2.4A in Section 2.4.1 the ER is a tubular network spreading throughout the whole cell. It is shown that diffusion within such a network can be described by Fick's law with a reduced diffusion coefficient [160]. Therefore we neglect the spatial structure of the ER and assume it to be spatially continuous in the whole cytosol. That leads to a two Ca^{2+} -species model (also called bi-domain model) depicted in Figure 6.5.

6.4.1 Model equations

The coupling between the cytosolic and the lumenal Ca^{2+} concentrations corresponds to a RDS of the form:

$$\frac{\partial[\mathrm{Ca}^{2+}]}{\partial t} = D_c\nabla^2[\mathrm{Ca}^{2+}] + [\sigma_l + P_c(\mathbf{r},t)]\,([E]-[\mathrm{Ca}^{2+}]) - P_p\frac{[\mathrm{Ca}^{2+}]^2}{k_d^2+[\mathrm{Ca}^{2+}]^2} + \sum_j k_j^-[CaB_j] - k_j^+[B_j][\mathrm{Ca}^{2+}] \tag{6.24a}$$

$$\frac{\partial[E]}{\partial t} = D_E\nabla^2[E] - \gamma\left\{[\sigma_l + P_c(\mathbf{r},t)]\,([E]-[\mathrm{Ca}^{2+}]) - P_p\frac{[\mathrm{Ca}^{2+}]^2}{k_d^2+[\mathrm{Ca}^{2+}]^2}\right\} + \sum_k k_k^-[EG_k] - k_k^+[G_k][E] \tag{6.24b}$$

$$\frac{\partial[B_j]}{\partial t} = D_{B_j}\nabla^2[B_j] - k_j^+[B_j][\mathrm{Ca}^{2+}] + k_j^-[CaB_j] \tag{6.24c}$$

$$\frac{\partial[G_k]}{\partial t} = D_{G_k}\nabla^2[G_k] - k_k^+[G_k][E] + k_k^-[EG_k]\,, \tag{6.24d}$$

where the first two equations describe the free Ca^{2+} concentration in the cytosol and the ER, respectively, and the other two equations correspond to a variety of cytosolic and lumenal buffers $[B_k]$ and $[G_j]$. The first terms on the right hand side characterize diffusion with the individual diffusion coefficients D_i. The following terms in Equations (6.24a) and (6.24b) describe the leak flux (with permeability σ_l) and release through channels (P_c). The space dependence of $P_c(\mathbf{r}_c,t)$ reflects the location of channel clusters and the time dependence the stochastic opening and closing of the channels described in Section 6.2. This time dependent source term is governed by stochastic simulation of the channel states as described in Section 6.4.3. γ is the volume ratio $V_{\mathrm{cyt}}/V_{\mathrm{ER}}$. The third term results from Ca^{2+} uptake into the ER from the cytosol by SERCA pumps with a flux strength P_p and the SERCA dissociation constant k_d. The remaining terms in (6.24) describe the reactions of Ca^{2+} with cytosolic and lumenal buffers $[B_k]$ and $[G_j]$, respectively, where k^+ denotes the capture rate and k^- is the dissociation rate.

The typical time scale for concentration changes at open channels upon opening is microseconds [249]. On that time scale, the concentration profile and the release current become quasi-stationary in the range of the channel molecule. Subsequent changes of the local concentration are due to changes of the bulk concentrations in the cytosol and ER. Consequently, we use here the quasi-steady approximation for a cluster current derived in [14]

$$\sigma(a_i) = \frac{8\pi F D_c}{1+\frac{D_c}{D_E}}\frac{a_i\sqrt{\frac{D_E+D_c}{D_cD_E}\sigma_c} - \tanh\left(a_i\sqrt{\frac{D_E+D_c}{D_cD_E}\sigma_c}\right)}{\sqrt{\frac{D_E+D_c}{D_cD_E}\sigma_c}}\left(\bar{E} - \left[\mathrm{Ca}^{2+}\right]\right)\,, \tag{6.25}$$

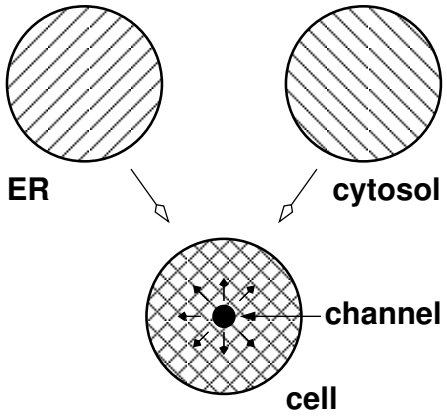

Figure 6.5: Sketch of the two compartment model. We overlay the two compartments, i.e. each point in space within our spherical cell corresponds to the ER and the cytosol simultaneously. Open channels act as source terms for the RDS of the cytosol.

where $F = 96485.34$ C/mol is the Faraday constant and σ_c denotes the channel flux constant. That approximation takes the concentration profile at and around open clusters into account [14]. The radius of the conducting area of a cluster is a_i. It is determined by the number of open channels $N_{o,i}$ in the ith cluster as $a_i = R_s N_{o,i}^{\frac{1}{3}}$ (R_s single channel radius).

On the cellular length scale, the cluster term in Equation 6.24 is described by a sum of δ-functions

$$P_c(\mathbf{r}, t) = \sum_{i=1}^{N_{\mathrm{cl}}} \sigma(a_i(t))\, \delta\left(\mathbf{r} - \mathbf{r}_i\right). \tag{6.26}$$

The location of the ith cluster is $\mathbf{r}_i$, and N_{cl} denotes the number of clusters.

One advantage of the approximation Equation 6.25 is that the current depends on the spatially averaged Ca^{2+} concentration $\bar{E}$ only. Since we are only interested in the cytosolic Ca^{2+} concentration dynamics, we can neglect the spatial Ca^{2+} dynamics within the ER. Moreover, we can determine the local Ca^{2+} concentration at an open channel cluster induced by its own current (6.25) by the corresponding relation of the approximation [14] as

$$\left[\mathrm{Ca}^{2+}\right]_{\mathrm{cluster}}^{(\mathrm{loc})}(\mathbf{r}_i, t) = \frac{1}{8F\pi D_c a_i}\sigma(a_i(t)) \,. \tag{6.27}$$

Note that the total concentration at a cluster is the sum of the concentration (6.27) and the concentrations induced by currents of other open channel clusters. The dynamics of the average ER concentration are determined by the integrated channel currents, the leak flux and the pump flux which depend on the average cytosolic Ca^{2+} concentration (see below).

Most of the Ca^{2+} within the ER is buffered, and hence the total amount of Ca^{2+} is higher than the integrated free Ca^{2+}. That can be taken into account by using the

rapid buffer approximation [263, 62]. It introduces a rescaling of the ER dynamics by a time scale factor which can be absorbed into γ. In the presence of a lumenal buffer with total concentration $[G]_T$ we obtain

$$\gamma_{\text{eff}} = \frac{V_{\text{cyt}}}{V_{\text{ER}}\left(1 + \frac{[G]_T K_G}{(E+K_G)^2}\right)}\,, \tag{6.28}$$

with the dissociation constant K_G of the buffer.

Due to mass conservation of the buffer, i.e. the total buffer amount stays constant $[B_j]_T = [B_j] + [\text{Ca}B_j] = \text{constant}$, and the reasonable assumption that free buffers have the same diffusion coefficients as the corresponding bounded buffers, we can rewrite the reaction terms as

$$R_j = -k_j^+[B_j][\text{Ca}^{2+}] + k_j^-([B_j]_T - [B_j]) \tag{6.29}$$

and substitute bounded buffers in Equations (6.24a, 6.24b).

We take besides $[\text{Ca}^{2+}]$ one mobile $[B]$ and one immobile buffer $[B_i]$ in the cytosol into account leading to the following reaction diffusion system

$$\begin{aligned}
\frac{\partial[\text{Ca}^{2+}]}{\partial t} &= D_{\text{Ca}}\nabla^2[\text{Ca}^{2+}] - \sigma_p[\text{Ca}^{2+}] + \sigma_l([E] - [\text{Ca}^{2+}]) \\
&\quad + \sum_{i=1}^{N_{\text{cl}}} \sigma(a_i(t))\,\delta\left(\mathbf{r} - \mathbf{r}_i\right) + \sum_j R_j && \text{(6.30a)} \\
\frac{\partial[B]}{\partial t} &= D_B\nabla^2[B] - k^+[B][\text{Ca}^{2+}] + k^-([B]_T - [B]) && \text{(6.30b)} \\
\frac{\partial[B_i]}{\partial t} &= -k_j^+[B_i][\text{Ca}^{2+}] + k_i^-([B_i]_T - [B_i]), && \text{(6.30c)}
\end{aligned}$$

where we used relation (6.29) for the R_j and a linearized pump flux with the pump flux constant σ_p.

Former theoretical studies [249, 60, 58] have identified steep concentration gradients in the order of up to 3 orders of magnitudes near to an open channel caused by the interplay of the SERCA pumps, buffers and of the huge concentration differences between the ER and the cytosol. These gradients require a fine spatial discretization and tiny time steps by stability criteria of explicit PDE solving methods. Both render a numerical integration with PDE solvers for non-linear PDEs computationally extremely expensive.

Rescaling of time and space		
$t \to t/T$	scaling time t with $T = 1/(k^+[B]_T)$	
$r \to r/L$	scaling space r with $L^2 = D_{\mathrm{Ca}}/(k^+[B]_T)$	
Dimensionless parameter definitions		
c	$\frac{[\mathrm{Ca}^{2+}]}{K}$	dimensionless free Ca^{2+} concentration
b	$\frac{[B]}{[B]_T}$	dimensionless free mobile buffer concentration
b_i	$\frac{[B_i]}{[B_i]_T}$	dimensionless free immobile buffer concentrations
e	$\frac{[E]}{K_E}$	dimensionless free Ca^{2+} concentration in the ER
d	$\frac{D_B}{D_{\mathrm{Ca}}}$	ratio of the diffusion coefficients
ϵ_τ	$\frac{[B]_T}{K}$	time separation of the mobile buffer
ϵ_τ^i	$\frac{[B_i]_T}{K}$	time separation of the immobile buffer
ϵ_R	$\frac{[B_i]_T k_i^-}{[B]_T k^-}$	ratio of buffer influence
σ_i'	$\frac{\sigma_i}{k^+[B]_T}$	scaled fluxes of σ_l and σ_p
σ'	$\frac{\sigma}{k^-[B]_T}\left(\frac{k^+[B]_T}{D_{\mathrm{Ca}}}\right)^{\frac{3}{2}}$	scaled channels current
κ	$\frac{K}{K_i}$	ratio of the dissociation constants of the 2 buffers

Table 6.2: Dimensionless parameter definition of the RDS (6.31).

In order to overcome these restrictions we linearize the PDEs and derive an analytical solution of the RDS (6.30) by a much-component Green's function, which enables us to calculate the concentration at arbitrary times and space points given a specific history of the opening behavior of the channels.

Thus, we use the linear pump term and linearize the non-linear buffer reaction terms around the stationary state, when all channels are closed in order to be able to apply Green's function. This is done in Section B.1. Finally, we introduce dimensionless variables as explained in detail in Section B.1 and listed in Table 6.2.

That leads to the following reaction diffusion system:

$$\frac{\partial c}{\partial t} = \nabla^2 c - \Big[(1+c_0)b + \epsilon_R(1+\kappa c_0)b_i + (b_0 + b_{i,0}\epsilon_R\kappa + \sigma_p' - \sigma_l')c\Big] + \sigma_l'\frac{\bar{e}}{\kappa_E} + \sum_{i=1}^{N_{\mathrm{cl}}}\left[\sigma'(a_i(t))\delta(\boldsymbol{r}-\boldsymbol{r}_i)\right] \tag{6.31a}$$

$$\frac{\partial b}{\partial t} = d\,\nabla^2 b - \frac{1}{\epsilon_\tau}\left[(1+c_0)b + b_0 c\right] \tag{6.31b}$$

$$\frac{\partial b_i}{\partial t} = -\frac{\epsilon_R}{\epsilon_\tau^i}\left[(1+\kappa c_0)b_i + b_{i,0}\kappa c\right]\ . \tag{6.31c}$$

Analogously to Equations (6.31) the first equation describes the dynamics of the free cytosolic Ca^{2+} concentration, the second one the free mobile buffer and the last equation corresponds to the free immobile buffer dynamics. Note that the rescaled time and space as well as all new variables and scaling parameters are now dimensionless by the definitions given in Table 6.2. The linearization leads to an overestimation of the buffers as shown in Section B.2. We switch again to spherical coordinates (r, θ, ϕ) and assume the same boundary condition at the cell membrane for all three species.

6.4.2 Deriving the Green's dyadic

We derive here the analytical solution for a single cluster[2]. The total cellular Ca^{2+} dynamics is given by the superposition of the solutions for several clusters. We start with the RDS (6.31) in matrix form,

$$\left[\begin{pmatrix}1&0&0\\0&d&0\\0&0&0\end{pmatrix}\nabla^2 - \begin{pmatrix}1&0&0\\0&\epsilon_\tau&0\\0&0&\epsilon_\tau^i\end{pmatrix}\frac{\partial}{\partial t} + \begin{pmatrix}a_{11}&a_{12}&a_{13}\\a_{21}&a_{22}&0\\a_{31}&0&a_{33}\end{pmatrix}\right]\begin{pmatrix}c\\b\\b_i\end{pmatrix} = -\mathbf{f}(\mathbf{r},t)\ , \tag{6.32}$$

where $\mathbf{f}(\mathbf{r},t)$ denotes the vector of the inhomogeneous terms of each component. In order to solve this system of coupled PDEs by means of coupled Green's functions or a Green's dyadic $\mathbf{G}$, we have to solve similar to Equation (6.6) the following problem,

$$\mathbf{LG} = \begin{pmatrix}\nabla^2 - \frac{\partial}{\partial t} + a_{11} & a_{12} & a_{13}\\ a_{21} & d_\epsilon\nabla^2 - \epsilon_\tau\frac{\partial}{\partial t} + a_{22} & 0\\ a_{31} & 0 & -\epsilon_\tau^i\frac{\partial}{\partial t} + a_{33}\end{pmatrix}\begin{pmatrix}g_{11}&g_{12}&g_{13}\\g_{21}&g_{22}&g_{23}\\g_{31}&g_{32}&g_{33}\end{pmatrix} = -\frac{1}{r'^2\sin\theta'}\delta(r-r')\delta(\theta-\theta')\delta(t-t')\begin{pmatrix}1&0&0\\0&1&0\\0&0&1\end{pmatrix}. \tag{6.33}$$

[2]For a more detailed derivation see appendix B.3.

Analogously to (6.7) the time derivative can be replaced by s due to Laplace transform leading to

$$\tilde{\mathbf{L}}\tilde{\mathbf{G}} = -\frac{1}{r'^2 \sin\theta'}\delta(r-r')\delta(\theta-\theta')e^{-st'}\mathbf{1}_{3\times 3}\ . \tag{6.34}$$

If we assume the same boundary conditions for calcium and the buffers, the system (6.32) can be solved by the spectral ansatz

$$\tilde{\mathbf{G}} = \sum_{l=0,p=0}^{\infty} \boldsymbol{\alpha}_{lp}\psi_{lp}(r,\theta), \tag{6.35}$$

where $\psi_{lp}(r,\theta)$ is the solution of the Helmholtz Equation (6.10), which respects the appropriate boundary conditions. Thus, the Green's dyadic (or matrix) is determined by the amplitude matrix $\boldsymbol{\alpha}_{lp}$. By inserting (6.35) into equation (6.34) we get

$$\sum_{l=0,p=0}^{\infty} \mathbf{M}_{lp}\ \ \boldsymbol{\alpha}_{lp}\ \ \psi_{lp}(r,\theta) = -\frac{1}{r'^2 \sin\theta'}\delta(r-r')\delta(\theta-\theta')e^{-st'}\ \mathbf{1}_{3\times 3}\ , \tag{6.36}$$

where $\mathbf{M}_{lp}$ correspond to the Laplace transform of $\mathcal{L}$. The Laplace transform is done after the Laplace operators on the diagonal of M acted on the space dependent functions as can be explicitly seen in Equation (6.47). By applying the integral operators (6.14) on both sides, the amplitude matrix is given by

$$\boldsymbol{\alpha}_{mq} = \frac{\psi_{mq}(r',\theta')e^{-st'}}{\mathcal{N}(m)\mathcal{N}(\lambda_{mq})}\ \mathbf{M}_{lp}^{-1}\ , \tag{6.37}$$

which must still be transformed back into real space. Therefore we use the property of the matrix inversion

$$\mathbf{M}^{-1} = \frac{1}{|\mathbf{M}|}\mathrm{adj}(\mathbf{M})\ , \tag{6.38}$$

which enables us to apply the residual theorem by determining the zeros of $|\mathbf{M}|$ leading to a cubic equation for s. Thus, the Green's dyadic takes the form

$$\mathbf{G}(r,\theta,t|r',\theta',t') = \sum_{l=0,p=1}^{\infty}\sum_{i=1}^{3} \frac{\mathrm{adj}(\mathbf{M}_{lp})}{\partial|\mathbf{M}_{lp}|/\partial s|_{s=s_i}} \frac{1}{\mathcal{N}(l)\mathcal{N}(\lambda_{lp})} \frac{J_{l+1/2}(\lambda_{lp}r')}{r'^{1/2}} \times$$
$$P_l(\cos\theta')e^{-s_i t'}\frac{J_{l+1/2}(\lambda_{lp}r)}{r^{1/2}}P_l(\cos\theta)e^{s_i t} + \frac{3}{2b^3}e^{s_i(t-t')}\frac{\mathrm{adj}(\ \mathbf{M}_{00})}{\partial|\mathbf{M}_{00}|/\partial s|_{s=s_i}}. \tag{6.39}$$

Similar to the Green's function for the IP_3 dynamics, we can include the ϕ dependence by the relation for the angle θ between the source sitting in (r_c,θ_c,ϕ_c) and the point (r_p,θ_p,ϕ_p) at which we want to calculate the concentrations, leading to

$$\cos(\theta) = \cos(\theta_p)\cos(\theta_c) + \sin(\theta_p)\sin(\theta_c)\cos(\phi_p-\phi_c)\ . \tag{6.40}$$

This causes again a further normalization factor of 2π. If we now assume a source density according to

$$\boldsymbol{\varrho}(r,\theta,\phi,t) = \sigma(t)\frac{\delta(r-r_c)\,\delta(\theta-\theta_c)\,\delta(\phi-\phi_c)}{r^2\sin\theta}\begin{pmatrix}1\\0\\0\end{pmatrix}\,, \tag{6.41}$$

the concentrations due to the influx of a single cluster are given by

$$\begin{pmatrix}c\\b\\b_i\end{pmatrix}(t) = \sum_{l=0,p=1}^{\infty}\frac{J_{l+1/2}(\lambda_{lp}r)}{r^{1/2}}P_l(\cos\theta)\begin{pmatrix}\chi_1^{(lp)}\\\chi_2^{(lp)}\\\chi_3^{(lp)}\end{pmatrix}(t) + \begin{pmatrix}\chi_1^{(00)}\\\chi_2^{(00)}\\\chi_3^{(00)}\end{pmatrix}(t)\,. \tag{6.42}$$

The response functions $\vec{\chi}^{(lp)}$ and $\vec{\chi}^{(00)}$ include the time integration over the source history, i.e. the scaled time dependent channel flux strength $\sigma'(t)$, and take the buffer reaction as well as the coupling with the ER into account leading to

$$\begin{pmatrix}\chi_1^{(lp)}\\\chi_2^{(lp)}\\\chi_3^{(lp)}\end{pmatrix} = \sum_{i=1}^{3}\frac{J_{l+1/2}(\lambda_{lp}r_c)}{2\pi\,\mathcal{N}(l)\,\mathcal{N}(\lambda_{lp})\,r_c^{1/2}}\int_0^t dt'\sigma'(t')e^{s_i(t-t')}\frac{\mathrm{adj}(\mathbf{M}_{lp})}{\partial|\mathbf{M}_{lp}|/\partial s|_{s=s_i}}\begin{pmatrix}1\\0\\0\end{pmatrix} \tag{6.43}$$

$$\begin{pmatrix}\chi_1^{(00)}\\\chi_2^{(00)}\\\chi_3^{(00)}\end{pmatrix} = \sum_{i=1}^{3}\frac{3}{4\pi b^3}\int_0^t dt'\sigma'(t')e^{s_i(t-t')}\frac{\mathrm{adj}(\mathbf{M}_{00})}{\partial|\ \mathbf{M}_{00}|/\partial s|_{s=s_i}}\begin{pmatrix}1\\0\\0\end{pmatrix}, \tag{6.44}$$

with the normalization factors $\mathcal{N}(l)$ and $\mathcal{N}(\lambda_{lp})$ given by Equations (6.16).

The λ_{lp}s are determined by the boundary conditions at b_c (the scaled cell radius R) which reads

$$\frac{\partial}{\partial r}\frac{J_{l+1/2}(\lambda_{lp}r)}{r^{1/2}}\bigg|_{r=b_c} = \frac{l}{b_c\lambda_{lp}}J_{l+1/2}(\lambda_{lp}b_c) - J_{l+3/2}(\lambda_{lp}b_c) = 0. \tag{6.45}$$

in the case of no-flux boundary conditions and

$$J_{l+1/2}(\lambda_{lp}b_c) = 0 \tag{6.46}$$

for Dirichlet boundary conditions, for which $\vec{\chi}^{(00)}$ vanishes and the boundary concentration C_b must be added to the solution (6.42).

The coupling of the cytosol with the ER by σ_p and σ_l as well as the coupling strengths between Ca^{2+} and the two buffers will determine the time constants s_i of the response functions (6.43, 6.44), which are implicitly given by the matrix inversion of the matrix

$$\mathbf{M}_{lp} = \begin{pmatrix}\lambda_{lp}^2 + s - a_{11} & -a_{12} & -a_{13}\\ -a_{21} & d\epsilon_\tau\lambda_{lp}^2 + s\epsilon_\tau - a_{22} & 0\\ -a_{31} & 0 & s\epsilon_\tau^i - a_{33}\end{pmatrix}\,, \tag{6.47}$$

with the matrix elements a_{ij} representing the coupling of the PDEs (6.31) given by

$$a_{ij} = \mathbf{A} = \begin{pmatrix} -b_0 - b_{i,0}\epsilon_R\kappa - \sigma_p + \sigma_l & -(1+c_0) & -\epsilon_R(1+c_0\kappa) \\ -b_0 & -(1+c_0) & 0 \\ -b_{i,0}\epsilon_r\kappa & 0 & -\epsilon_R(1+c_0\kappa) \end{pmatrix} \tag{6.48}$$

where $a_{23} = a_{32} = 0$ reflects the fact that the two buffers do not interact directly.

Note that this solution for a δ source will diverge directly at the source. We circumvent this problem by calculating the Ca^{2+} concentration 50 nm from the cluster location, which is in the range of channel spacing within clusters and use the single channel approximation for the concentration (6.27) at open clusters. The convergence of the solution is briefly discussed in appendix B.4.

In the last step we have to determine the mean Ca^{2+} concentration in the ER to quantify the channel currents (6.25). If we do not assume Ca^{2+} entry through the cell membrane, the total amount of Ca^{2+} will stay constant

$$N_{\text{tot}} = ((\bar{c}(t) - c_0) + (b_0 - \bar{b}(t)) + (b_{i,0} - \bar{b_i}(t)) + \bar{e}(t)/\gamma)V_{\text{cyt}} = const\ . \tag{6.49}$$

With the assumption that at time $t = 0$ the cell has no open channels and is in equilibrium we have also the relation

$$N_{\text{tot}} = (c_0 + (b_T - b_0) + (b_{i,T} - b_{i,0}) + \bar{e}_0/\gamma)V_{\text{cyt}}. \tag{6.50}$$

Hence, to calculate the average Ca^{2+} concentration within the ER $\bar{e}(t)$, we rely on the average concentrations $\bar{\mathbf{c}}$ of all three components. Since $V_{\text{cyt}}\bar{\mathbf{c}} = \int_{V_{\text{cell}}} dV\mathbf{c}$ we have to integrate the solution (6.42) over the entire cell:

$$\bar{\mathbf{c}} = \frac{1}{V_{\text{cyt}}} \int_0^{b_{\text{cell}}} \int_0^{\pi} \int_0^{2\pi} \vec{c} r^2 \sin(\theta) dr d\theta d\phi\ . \tag{6.51}$$

The ϕ integration simply gives a factor of 2π whereas the other two integrations lead to the equations

$$\begin{aligned} \mathcal{R} &= \int_0^R \frac{J_{l+1/2}(\lambda_{lp} r)}{r^{1/2}} r^2 dr \\ &= \frac{2^{-\left(\frac{3}{2}+l\right)}\ R^{(3+l)}\ \lambda_{lp}^{\frac{1}{2}+l}\ \Gamma\left(\frac{3+l}{2}\right)}{\Gamma\left(\frac{5+l}{2}\right)\Gamma\left(\frac{3}{2}+l\right)}\ {}_1F_2\left[\frac{3+l}{2}; \left(\frac{5+l}{2}, \frac{3+l}{2}\right); -\left(\frac{R\lambda_{lp}}{2}\right)^2\right] \end{aligned} \tag{6.52a}$$

$$\mathcal{Q} = \int_0^{\pi} P_l(\cos\theta)\sin\theta d\theta = \int_{-1}^{1} P_l(x)dx = \frac{2\sin(l\pi)}{l\pi + l^2\pi} = \begin{cases} 0 & , \quad l > 0 \\ 2 & , \quad l = 0 \end{cases}\ , \tag{6.52b}$$

where ${}_1F_2\left[x, \mathbf{y}, z\right]$ denotes the hypergeometric function [1]. Hence, only modes with $l = 0$ contribute to the global concentration and Equation (6.52a) can be simplified

to

$$\mathcal{R} = \sqrt{\frac{2}{\pi}} \frac{\sin(\lambda_{0p} R) - R\lambda_{0p} \cos(\lambda_{0p} R)}{\lambda_{0p}^{5/2}} \ . \tag{6.53}$$

With these solution we can calculate the total cell response for one cluster by

$$V_{\text{cyt}} \bar{\mathbf{c}} = 2\pi \ \mathcal{R} \ \mathcal{Q} \ \vec{\chi}_{lp} + \frac{4\pi R^3}{3} \ \vec{\chi}_{00} \ , \tag{6.54}$$

what can be used to determine $\bar{e}(t)$ by relations (6.49) and (6.50). In the case of no Ca^{2+} conservation, $\bar{e}(t)$ is given by

$$\bar{e}(t) = \bar{e}_0 - \int_0^t dt' \sigma'(t') - \bar{c}(t')\sigma_p + \sigma_l \left(\bar{e}(t') - \bar{c}(t')\right) \ , \tag{6.55}$$

this means by the difference of the initial ER concentration $\bar{e}_0$ and the difference of the released Ca^{2+} and Ca^{2+} pumped back into the ER. Also this method requires the calculation of the mean cytosolic Ca^{2+} concentration.

6.4.3 Green's cell model algorithm implementation

The analytical solution for the concentration dynamics (6.42) can now be used as a natural environment for localized IP_3R clusters to study the interplay of their nonlinear stochastic opening behavior and the feedback of Ca^{2+}. The stochastic opening and closing of the IP_3Rs is translated by the single channel approximation (6.25) to time-dependent source terms in the RDS. The stochastic transitions depend on the IP_3 and local Ca^{2+} concentrations and are modeled by a hybrid version of the Gillespie algorithm [5], which was already used by Rüdiger *et al.* in relation to Ca^{2+} dynamics [195].

Gillespie algorithm: The Gillespie algorithm allows for simulation of stochastic processes [82]. Given the actual time t, the probability that the next stochastic event occurs in the infinitesimal time interval $[t + \tau, t + \tau + dt]$ and is an event Ξ_i, is given by

$$P(\tau, i)dt = \alpha_i e^{-\alpha_0 \tau} dt \ , \tag{6.56}$$

where $\alpha_0 = \sum \alpha_j$ is the sum of all propensities. The event probability $P(\tau, i)$ can be realized by drawing two random numbers r_1 and r_2 from a uniform distribution in the interval $[0, 1]$. Then τ and i are determined by

$$\alpha_0 \tau = \ln(1/r_1) \ , \quad \sum_{j=1}^{i} \alpha_j \leq \alpha_0 \ r_2 < \sum_{j=i+1}^{n} \alpha_j \ . \tag{6.57}$$

The original Gillespie method assumes that the propensities during two events stay constant. This is not valid for our problem, since opening and closing of channels change the Ca^{2+} concentration respectively the propensities by up to three orders of magnitudes.

To resolve this problem we use the method described in [195], which adopt the hybrid version of the Gillespie algorithm [5] to Ca^{2+} dynamics. The time of the next stochastic event is determined by solving

$$\int_t^{t+\tau} \alpha_0(s,c)ds = \ln(r_1) \ , \tag{6.58}$$

where the propensities α_0 depends explicitly on time s and the concentration c. For constant α_0 Equation (6.58) simplifies to (6.57). For the determination of τ we rewrite the first equation equation in (6.57) by introducing a new variable $g(\tau)$ and solve

$$\dot{g}(s) = \alpha_0(s,c) \ , \tag{6.59}$$

with the initial condition $g(0) = 0$. A reaction occurs, when $g(s)$ reaches $\ln(r_1)$. The corresponding reaction event is determined as before by a second random number r_2 according to the second condition in Equation (6.57).

For the Ca^{2+} dynamics, the channel transitions Ξ correspond to jumps on the Markov chains representing the subunits of the DKM described in Section 6.2 and shown in Figure 6.1A. Hence, Ξ describes the transition $X_{ijk} \to X_{i'j'k'}$, where a single transition does only change one index. For a channel consisting of four subunits the X_{ijk} correspond to occupation numbers. Since each of the four subunit is in one of the states the sum over all i, j and k equals 4. In this context Ξ corresponds to an increase of X_{ijk} by 1 and a subsequently decrease of another state $X_{i'j'k'}$ by 1 according to Figure 6.1A.

Since the Ca^{2+} concentrations at open channel clusters are rather high, the Ca^{2+} concentration dependent transitions are favored at open clusters. This leads to small time steps. Moreover, the Ca^{2+} concentration changes due to channel transitions very rapidly, and consequently we have to calculate the concentrations for many times.

Parallel algorithm structure: To deal with this enormous computational requirements, I developed a parallel algorithm in C++ using the standard library for parallel computing *Message Passing Interface* (MPI) and the *Gnu Scientific Library* (GSL) for the implementation of Bessel functions $J_{l+1/2}(x)$ and Legendre polynomials $P_l(\theta)$. The two key elements of the algorithm are the determination of channel transitions and the calculation of the analytical concentration responses at the cluster locations. One benefit of the analytical solution of the linear RDS is that we only have to calculate the concentration at points where IP_3R clusters

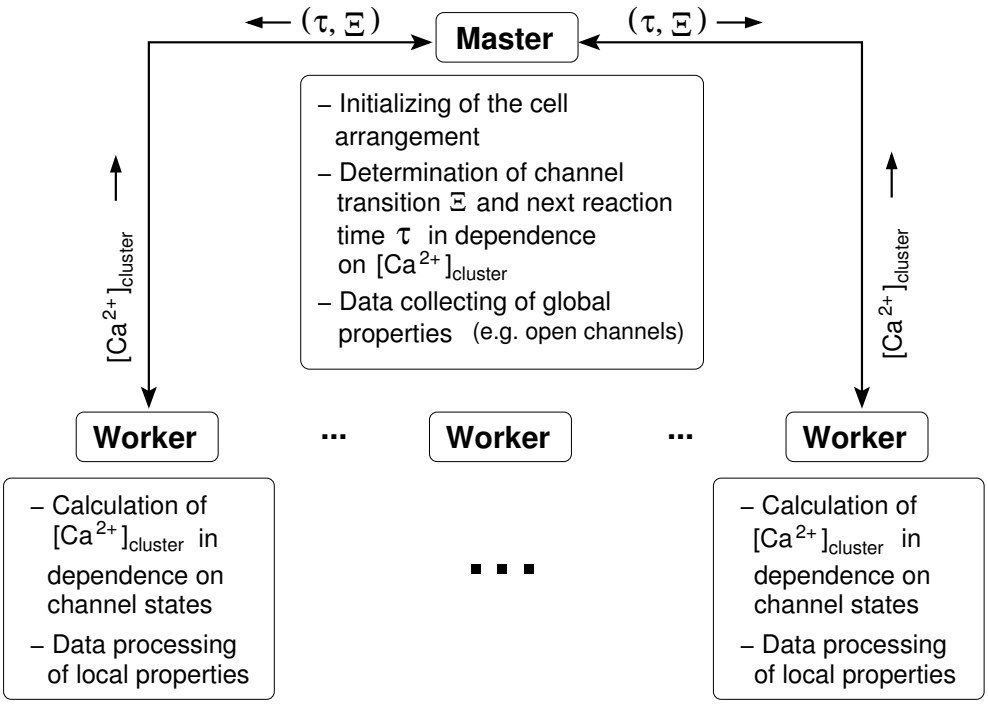

Figure 6.6: The scheme of the parallel Green's cell model algorithm. The algorithm is split into two parts. The master process determines the cell arrangement and performs the Gillespie algorithm leading to channel transitions Ξ and reaction times τ. Therefore it relies on the Ca^{2+} concentrations $[Ca^{2+}]_{\text{cluster}}$ at the cluster locations, which are calculated by the analytical solution on worker processes in dependence on the channel state history $\sigma_i(t)$ of each cluster.

are localized. Another advantage is the linearity, which enables us to calculate the concentrations of clusters independently and to superpose them in the following.

These properties can be used for a sufficiently parallelized algorithm depicted in Figure 6.6. The bottleneck of parallel computing is the communication between different processors or nodes. Consequently the amount of data transmission should be minimized. This can be achieved either by transmission of information at very few iteration steps or as less as possible information at each step. Since our problem needs an update at every time step or at least at every step, where a channel opens or closes, I minimized the information that has to be transmitted. Therefore the problem is split into two parts leading to two different kinds of processes. The *master* process is the "brain" of the algorithm, which determines the channel transitions, reaction times and collects global properties. For this tasks it requires the concentration at the IP_3R clusters. These are determined by *worker* processes, which calculate the concentration at a cluster according to Equation (6.42).

The Ca^{2+} concentration of each cluster is calculated by a single worker process for which the channel state history of all clusters is required. Therefore each worker process has a copy of the source term $\sigma(t)$ of each cluster. These source vectors are updated according to the Gillespie algorithm performed by the master process. This relies on the Ca^{2+} concentration at each cluster. Hence, in each iteration step one bidirectional communication occurs. First the master process broadcasts the time of the next reaction τ and the corresponding channel transition Ξ consisting of three integers: which reaction occurs in which channel of which cluster. Second each worker process sends the calculated Ca^{2+} concentration of the corresponding cluster to the master process, where they are used to determine the next transition Ξ and occurrence time τ.

The algorithm is inspired by [195], but exhibit some modifications due to its parallel character and the use of the analytical solution. It can be summarized as follows.

- The master process initializes the cell arrangement by reading a parameter file, which determines e.g. the cell radius R, the number of clusters N_{cl} and their locations, the Ca^{2+} base level and buffer concentrations, buffer dissociation rates and various other properties of the RDS. The clusters are set randomly, on a regular grid or at specific localization with a fixed or randomly chosen number of channels in the cell. The channel states are initialized according to the stationary probabilities defined in Equations (6.2).

- These specifications are sent to all other processes and translated into dimensionless parameters. Moreover, the λ_{lp}s and most of the response functions χ are determined and stored at each worker process with the cluster specific values.

- The master determines the next estimated reaction time by relation (6.58). For the new time $t_{\mathrm{new}} = t_{\mathrm{old}} + \tau$ the property g_{new} is calculated by (6.59). Therefore the master collects the Ca^{2+} concentrations at each cluster $[Ca^{2+}]_{\mathrm{cluster}}$ from the corresponding worker processes.

- If $g_{\mathrm{new}} < \ln r_1$ (no stochastic event occurs), the master sets $t_{\mathrm{old}} = t_{\mathrm{new}}$ and determines the next time step τ, which is broadcasted to the worker processes.

- If $g_{\mathrm{new}} \geq \ln r_1$ (a stochastic event occurs in $[t_{\mathrm{old}} = t_{\mathrm{new}}]$), the event time t_s and the corresponding $[Ca^{2+}]_{\mathrm{cluster}}$ are determined by linear interpolation. The master process draws a random number r_2 and determines the stochastic event Ξ according to Equation (6.57) and updates the channel states. The next time step τ is determined and sent together with the channel transition Ξ to the worker processes. Then $g_{\mathrm{new}} = 0$ is set and a new random number r_1 is drawn on the master process.

6.5 Results

Before we use the *Green's cell algorithm* (GCA) in the next chapter for cell specific simulations regarding the experimental findings, we first introduce the observables which can be determined by the method. We will analyze the cell behavior in dependence on the IP_3 and Ca^{2+} concentrations.

6.5.1 Cell observables

As a first example for a physiological cell simulation, we put randomly 31 IP_3R clusters separated by at least 1.4 µm in a cell with a radius of $R = 10$ µm as shown in Figure 6.7A. Each cluster has a randomly chosen number of channels between 3 and 13 leading to a total number of 237 channels within the cell. We set the IP_3 concentration to a constant value of $[IP_3] = 95$ nM and choose for the Ca^{2+} base level $[Ca^{2+}]_0 = 75$ nM. The volume ratio between the cytosol and the ER was set to $\gamma = 15$. We assume no-flux boundary condition and set the other parameters of the RDS as listed in Table 6.3.

Parameter values		
R	10 µm	cell radius
a	8 nm	channel radius
D_{Ca}	220 $\mu m^2/s$	diffusion coefficient of cytosolic Ca^{2+}
D_E	70 $\mu m^2/s$	diffusion coefficient of lumenal Ca^{2+}
D_B	95 $\mu m^2/s$	diffusion coefficient of mobile buffer
$[B]_T$	25 µM	total mobile buffer concentration
k_B^+	600 $(\mu Ms)^{-1}$	on rate of the mobile buffer
k_B^-	100 s^{-1}	dissociation rate of the mobile buffer
$[B_i]_T$	30 µM	total immobile buffer concentration
$k_{B_i}^+$	600 $(\mu Ms)^{-1}$	on rate of the immobile buffer
$k_{B_i}^-$	100 s^{-1}	dissociation rate of the immobile buffer
P_p	100 s^{-1}	pump rate
σ_c	$4.3 \cdot 10^6$ s^{-1}	channel flux constant
σ_l	≈ 0.01 s^{-1}	leak flux constant given by P_l and $[Ca^{2+}]_0$

Table 6.3: Standard parameters of the cell arrangement used in simulations if not stated otherwise.

Direct observables of the GCA are the number of open channels and inhibited subunits, which are shown in panel B. The number of open channels (black) exhibits a rather regular oscillatory behavior. We can also identify inhibition as the mechanism which terminates a spike, since the number of inhibited subunits (purple)

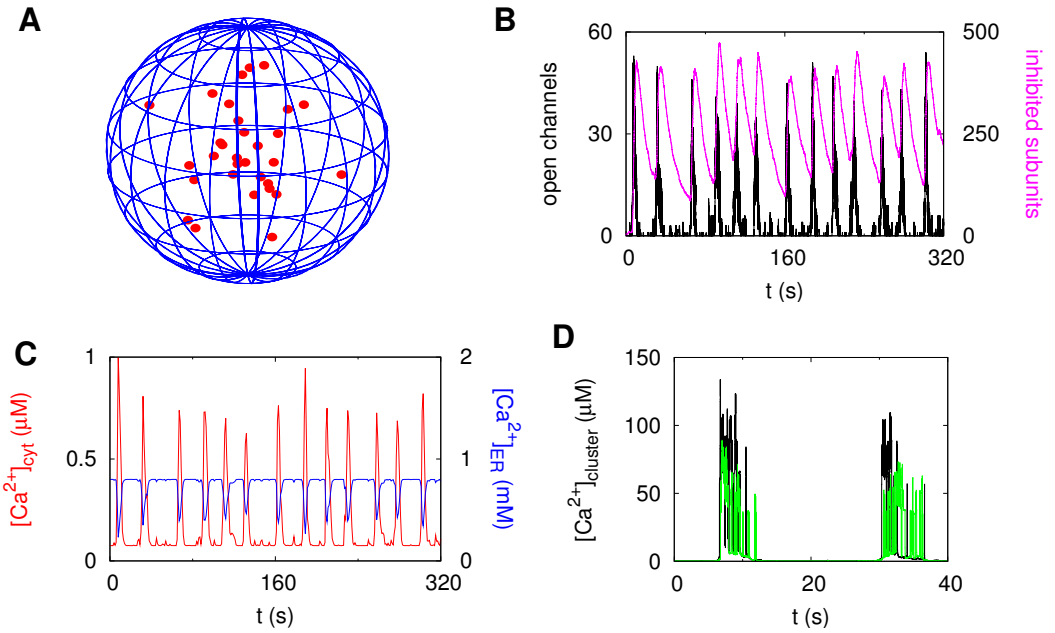

Figure 6.7: Green's cell simulation and its observables. The simulation corresponds to a cell with 31 randomly distributed clusters as depicted in panel **A**. Each cluster has between 3 and 13 channels. The GCA determines the channel states (**B**) in dependence on the Ca^{2+} concentrations $[Ca^{2+}]_{cluster}$ at the corresponding clusters, which is shown in panel **D** for two representative clusters. Panel **C** exhibits the averaged cytosolic (red) and the lumenal (blue) Ca^{2+} concentration.

increases drastically during a spike and all channels close again. In the following the number of inhibited subunits relaxes slowly towards its resting level. The inhibition blocks further channel openings for several seconds, what corresponds to the deterministic time T_{det} described in Sections 4.3.1 and 4.3.2. Thus, we observe only very few channel openings directly after a spike and that opening of several channels do not initiate a new spike if the number of inhibited subunits is still to high (approximately higher than 200). Moreover, the amplitude of the spike of open channels seems to be smaller if the spike is initiated at times where the number of inhibited subunits is still high. This is reasonable, since inhibited channels cannot contribute to a spike. The regular behavior of the two observables and their relation shown in panel B points to array enhanced coherent resonance (AECR) which was also found in the experimental results. The IP_3 and Ca^{2+} concentrations seem to be in the range where a spike is initiated as soon as the system is in the excitable state again and before the cell has reached its resting level, which would correspond to a low number of inhibited subunits comparable to the initial number of around ten.

In experiments, we do not observe the number of open channels directly but their

effect on the cytosolic Ca^{2+} concentration $[Ca^{2+}]_{cyt}$. This can be determined by Equation (6.54) and is shown in Figure 6.7C for the corresponding channel behavior in panel B. The cytosolic Ca^{2+} concentration exhibits an oscillatory behavior similar to the number of open channels, but the lagged behavior is smeared due to diffusion. Furthermore, we see that the uncoordinated opening of channels between the spikes leads to very small fluctuations in the concentrations only.

We can also determine the time dependent lumenal Ca^{2+} concentration $[Ca^{2+}]_{ER}$ (blue). Since we do not assume Ca^{2+} influx through the plasma membrane, the cytosolic Ca^{2+} spikes are accompanied by lumenal Ca^{2+} concentration decreases, and hence $[Ca^{2+}]_{ER}$ and $[Ca^{2+}]_{cyt}$ are coupled directly. Although this picture has large similarities with results of the ODE model developed by Goldbeter *et al.* shown in Figure 2.5, it is qualitatively different. First, the two concentrations in the two compartments differ by more than three orders of magnitude in the Green's cell model, whereas they are in the same range in the ODE model, what is not in accordance with physiology. Second, and more important, there is a structural difference. Within the ODE model, oscillations arise by repeated emptying and refilling of the ER, which occur by a bifurcation leading to a limit cycle as mentioned in Section 2.5.1. In this model the oscillatory behavior of the lumenal Ca^{2+} concentration is essential, what could not be verified in experiments. In the Green's cell model, the decrease of $[Ca^{2+}]_{ER}$ is not required for oscillations to occur as can be seen in Figure 6.9, where γ was set to one and the lumenal concentration exhibits subsequently only a very small decrease, what does not stop "oscillations".

Another major difference is the spatial inhomogeneity, which leads to the properties of a stochastic medium and the hierarchical organization of Ca^{2+} signals as introduced in Section 2.5.2 and discussed in Chapter 4. The discrete IP_3R cluster combined with the SERCA pumps leads to steep gradients close to open channel clusters. That can be seen immediately by comparison of the average cytosolic Ca^{2+} concentration shown in Figure 6.7C and the Ca^{2+} concentrations at open channel clusters depicted for two representative clusters in Figure 6.7D. While $[Ca^{2+}]_{cyt}$ is in the range of less than 1 μM, the typical concentrations at clusters $[Ca^{2+}]_{cluster}$ during a spike are in the range of tens of μM as shown in panel D for two representative clusters with 7 and 11 channels, respectively, for the first two spikes in panel B and C. The large concentration increases at IP_3R clusters due to single channel opening are a key element of the self amplifying effect that allows for CICR.

An illustration for the Ca^{2+} gradients is shown in Figure 6.8, where the isoconcentration surface of 2 μM is visualized during a spike. The initial puff releases Ca^{2+}, which diffuses to adjacent clusters and activates them, too. Thus, Ca^{2+} release spreads through the entire cell, until inhibition closes the channels and Ca^{2+} is removed into the ER by SERCAs.

The Ca^{2+} signal shown in Figure 6.7 exhibits a rather regular behavior, even though it is not deterministic. Moreover, the spike generation before the subunits

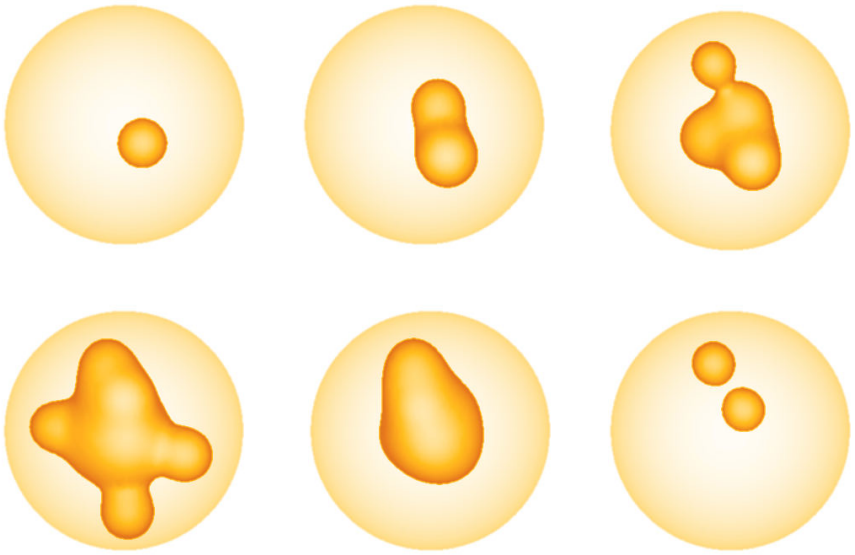

Figure 6.8: Iso-concentration surface of 2 μM during a spike. The initial puff (left upper picture) activates adjacent clusters (upper row of pictures). After most of the channels were activated, inhibition closes channels, and Ca^{2+} is pumped back into the ER (lower row of pictures).

have reached their resting level indicates a regime, where the probability P_{trig} to initiate a Ca^{2+} wave just after the deterministic time has passed is high and allows for a regular behavior by AECR. This is caused by the high concentrations of IP_3 and Ca^{2+} as well as by the strong spatial coupling. The observed behavior might be comparable with the one of stimulated HEK cells in Chapter 4. They exhibit small regeneration rates ξ as determined in Figure 4.5, meaning that a Ca^{2+} spike occurs before the cell has recovered to its resting state again. This corresponds in the simulation to spike initiation before the number of inhibited subunits has relaxed to its resting level as shown in Figure 6.7B.

Such a regular behavior might also be described by noisy limit cycle oscillators. But a generic model must cover as well the other dynamical regime, where Ca^{2+} spikes occur more irregularly, and the cell relaxes to the resting state between spikes. This is the regime of more irregular spiking, which is observed mainly in the case of spontaneous oscillations in the experimental part. To model this, we use the same cell setup with a decreased $[Ca^{2+}]_0$ of 35 nM. We set $\gamma = 1$ and the lumenal Ca^{2+} concentration to 400 μM to demonstrate that oscillations do not occur by the repeated emptying and refilling of the ER. The behavior of open channels, inhibited subunits and Ca^{2+} concentrations is shown in Figure 6.9.

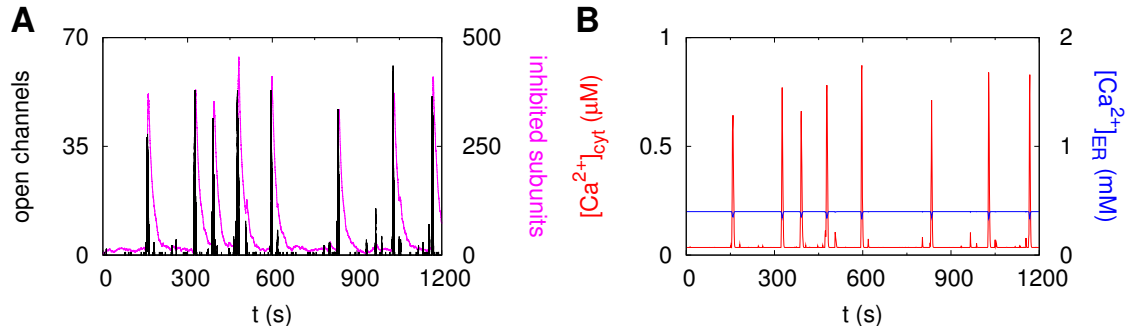

Figure 6.9: Lower $[Ca^{2+}]_0$ leads to more irregular oscillations. Simulation of the same cell setup as in Figure 6.7 with $[Ca^{2+}]_0$=0.35 nM, $\gamma = 1$ and $[Ca^{2+}]_{ER}$=400 µM exhibits prolonged and more irregular ISIs. These are caused by the lower Ca^{2+} concentration leading to less frequent triggering events. The channel behavior shown in panel **A** indicates a full regeneration during two successive spikes, since the number of subunits relaxes totally. The cytosolic Ca^{2+} concentration spikes (red) in panel **B** have a similar height than those in Figure 6.7, but due to the different volume ratio $\gamma = 1$ the lumenal Ca^{2+} concentration (blue) stays rather constant. Hence, oscillating $[Ca^{2+}]_{ER}$ is not required for oscillations in the Green's cell model.

Panel A exhibits the channel behavior. The oscillations are more irregular than those in Figure 6.7A caused by the lower $[Ca^{2+}]_0$, which decreases P_{trig}. Hence, the cell does not exhibit a spike directly after the deterministic time T_{det} and relaxes into the resting state, in which the number of inhibited subunits exhibits a constant level. The height of the open channel spikes is slightly increased compared to the simulation in Figure 6.7, because less channels are inhibited. Panel B shows the average cytosolic (red) and lumenal (blue) Ca^{2+} concentrations. The lumenal Ca^{2+} concentration exhibits only very small deviations from its base level, since we set the volume ratio to $\gamma = 1$. This stresses the conceptual difference to the ODE model. The feedback loop needed to build oscillations is given in the ODE model by the lumenal Ca^{2+} concentration, whereas the feedback in the Green's cell model is included by the local properties of the IP_3R.

In experiments, the Ca^{2+} concentration is not determined directly, but by fluorescent dyes. The recorded fluorescent signals change their intensities by binding of Ca^{2+} to dyes and the subsequent change of their molecular configuration leading to different fluorescent properties. These dyes correspond to a mobile buffer b in the RDS (6.24) and we can calculate its dynamics by the solution (6.42) for b. This is shown in the upper panel of Figure 6.10A for a cell with 15 randomly located clusters each having between 5 and 20 channels. Here, the ratio of time dependent Ca^{2+} bound buffer $b(t)$ and the initially bound buffer b_0 is plotted over time with

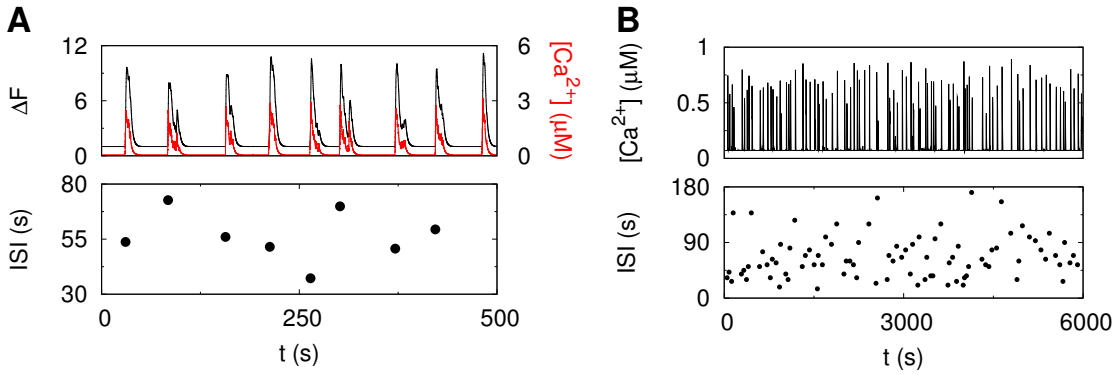

Figure 6.10: Influence of the lumenal base level and ISI determination. The upper panel in **A** exhibits the cytosolic Ca^{2+} concentration (red) and the corresponding amount of Ca^{2+} bound mobile buffer normalized to the initially bound buffer. That corresponds to the fluorescent signal ΔF recorded in experiments. The buffer signal is smoother than the Ca^{2+} signal caused by diffusion and reaction rates. The simulation used a cell with 15 randomly located clusters each having between 5 and 20 channels and a rather high lumenal Ca^{2+} base level of 3 mM. The ensuing large channel currents induce rather high cytosolic Ca^{2+} concentrations of up to 3 μM. If we simulate the same cell with a lower lumenal base level of 800 μM, the currents and subsequently the average Ca^{2+} concentration decrease as shown in panel **B**. This corresponds to a weaker coupling of the channels and leads to single puff activity between global spikes and subsequently larger deviation in the ISIs as shown in the lower panel.

the definition $\Delta F = b(t)/b_0$ (black line). Additionally, the corresponding cytosolic Ca^{2+} concentration $[Ca^{2+}]_{cyt}$ (red) is shown. Comparison of the two corresponding observables demonstrates that the fluorescent signal is more smeared out than the original Ca^{2+} signal.

The IP_3 concentration was set to $[IP_3]$=100 nM and $[Ca^{2+}]_0$=0.55 nM. The ER base level concentration of 3 mM leads to rather large single channel currents $\sigma = 0.45$ pA by relation (6.25). These large currents lead again to a rather regular behavior although the mobile buffer concentration was increased to $[B]_T = 60$ μM. The regular behavior can be seen in the lower panel, where analogously to the experimental time series in Figures 4.3 and 4.8 the length of the ISIs is shown. The ISIs vary between 35 s and 75 s. The large currents lead to high mean cytosolic Ca^{2+} concentrations during a spike of approximately 3 μM. Subsequently, ΔF exhibits large values. Another property induced by the large currents is the absence of single puffs, which would lead to small deviations from the base levels of $[Ca^{2+}]_{cyt}$ as those shown in Figure 6.9B. The large currents lead to a high coupling between channels of different clusters and the resulting high cytosolic concentrations lead to

full inhibition of the channels. If the cell is in the excitable state again, a triggering event, i.e. opening of a single channel, will lead to a global signal very likely, since the corresponding large current leads to high $[Ca^{2+}]_{\text{cluster}}$, activating other channels of the cluster. The locally amplified triggering event induces opening of other clusters, since it increases $[Ca^{2+}]_{\text{cyt}}$ and subsequently the open probability P_o of IP_3Rs. Hence, the variability of the ISI shown in the lower panel of A is caused by the stochasticity of the first channel opening in the cell.

If we assume a lower Ca^{2+} base level in the ER the currents decrease and we expect a more irregular spiking, since not every initial event induces a global signal. This behavior is shown in Figure 6.10B, where the same cell setup was simulated with a lumenal Ca^{2+} base level of 800 μM. Indeed we observe a lower maximal cytosolic Ca^{2+} concentration $[Ca^{2+}]$ during a spike of around 0.9 μM (upper panel) and slower and more irregular ISIs (lower panel) in Figure 6.10B. Here, the ISIs vary between 20 s and 180 s. The $[Ca^{2+}]$ in the upper panel demonstrates also the fact that not every local event triggers a global signal, since the concentration exhibits some tiny peaks, especially during long ISIs. These small peaks correspond to isolated puffs which do not initiate a global signal.

The example in panel B further demonstrates the power of the Green's cell model, since it allows for long real time simulations covering up to thousands of seconds even with spatially resolved IP_3Rs each described by a detailed channel model. This simulation runs 3 day on the computer cluster *Dirac*[3] using 8 processors. Comparable simulations in two spatial dimensions using *Finite Element Solver* (FES) [195] to solve the coupled PDE system (6.24) need up to six weeks for 300 s real time. Hence, the GCA leads to a speeding up of a factor of hundred, and the parallel algorithm structure allows for detailed cell simulation within one day.

For an example with Dirichlet boundary conditions, we assume a cell with 31 randomly distributed channel clusters separated by at least 1.5 μm. Each cluster has a random number of channels between 2 and 12 yielding 214 channels in total. The volume ratio was set to $\gamma = 5$ and the lumenal Ca^{2+} concentration to 2 mM. Other parameters were chosen as in the simulations above with a IP_3 concentration of 85 nM and a deviating mobile buffer concentration of 15 μM.

We now study the influence of a in time-dependent boundary condition leading to a varying base level concentration $[Ca^{2+}]_0$. The behavior of the cytosolic Ca^{2+} concentration is shown in Figure 6.11 in red and the oscillating base level concentration is depicted in black. We see how the spiking behavior of the cytosolic Ca^{2+} concentration is influenced by the oscillating boundary condition. Bursting-like behavior for higher $[Ca^{2+}]_0$ alternates with parts exhibiting only few or no spikes for low base level concentrations.

[3]For technical details of the cluster see appendix B.5 and
`http://www.helmholtz-berlin.de/angebote/it/dienste/dirac/index_de.html`.

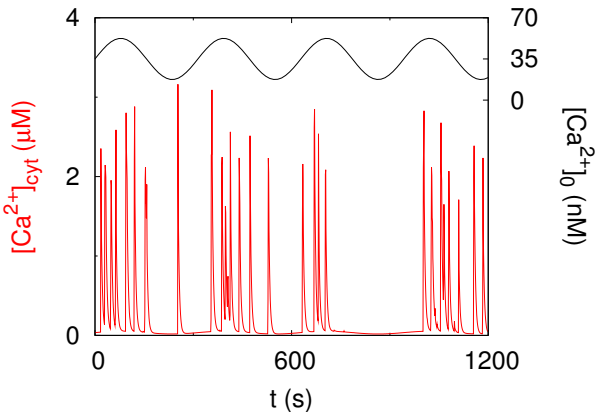

Figure 6.11: Influence of oscillating boundary condition. The oscillating boundary condition leads to an oscillating base level $[Ca^{2+}]_0$ (black). Due to the local nonlinearities of the channel, the rather small variations in $[Ca^{2+}]_0$ have a large influence on the cellular Ca^{2+} dynamics (red) which exhibits bursts.

These first examples have demonstrated that we can simulate the intracellular Ca^{2+} dynamics sufficiently with the Green's cell model. With this modeling approach we have access to properties, which are determined in experiments such as the cytosolic Ca^{2+} concentration as well as to internal properties which can not be determined in experiments like the number of open channels or of inhibited subunits.

6.5.2 Oscillations in dependence on the Ca^{2+} and IP_3 concentrations

We now can investigate the properties of the IP_3 pathway using the Green's cell algorithm. First, we are interested in the the dependence of Ca^{2+} signals on the Ca^{2+} and IP_3 concentrations. For this reason we used a fixed setup of a cell with 47 randomly distributed clusters, which are separated by a minimal cluster distance of 1.4 µm and have between 4 and 16 channels each. The standard parameters of the RDS are given in Table 6.3.

This prototype of a cell was simulated with different values of the cytosolic Ca^{2+} base level $[Ca^{2+}]_0$ and IP_3 concentration leading to distinct channel behaviors as shown in Figure 6.12.

If both concentrations are high as in panel A, the channels do not exhibit a cooperative signal, since due to high $[Ca^{2+}]_0$ most channels are inhibited, and as soon as they are excitable, they will open again and return into the inhibited state leading to the shown noisy signal. This mechanism also holds for very low $[IP_3]$ (D), but now the total amount of sensitized, inhibited and open channels is decreased.

If we switch $[Ca^{2+}]_0$ to physiological concentrations at high $[IP_3]$, i.e. going from A to B, we observe very regular oscillations, which occur by AECR. Due to the high IP_3 concentration, most channels are in the excitable state, and as soon as a single IP_3R opens, a global wave travels through the system, synchronizing the inhibition of the channels and terminating the Ca^{2+} release. As soon as the inhibiting Ca^{2+}

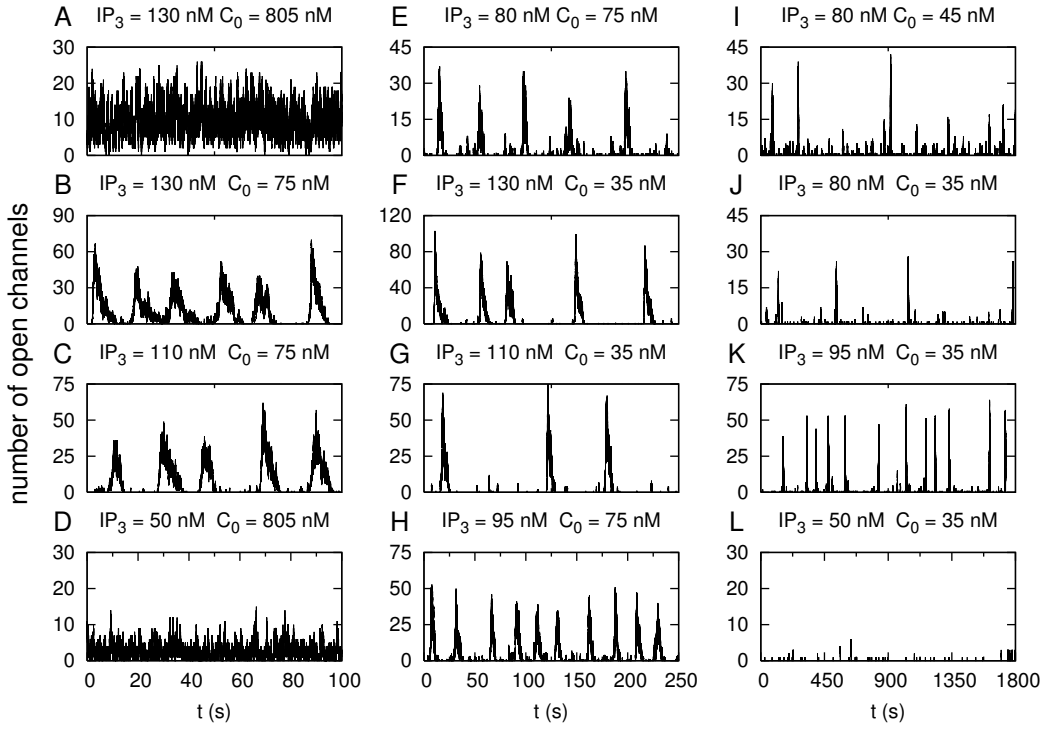

Figure 6.12: Channel signals of a specific cell with 47 randomly scattered clusters having between 4 and 16 channels for different Ca^{2+} base level concentrations $[Ca^{2+}]_0$ and IP_3 concentrations $[IP_3]$. For very high (A) and low (L) concentrations, no constructive signal of the total 405 channels is observed, whereas in the intermediate parameter region, the nonlinear properties of the IP_3R combined with those of the RDS serve for fast and regular oscillations (such as in B) or slower irregular oscillations with smaller amplitudes (J). Note the different time ranges for each column and see text for more details.

dissociates from the corresponding binding site, one channel will open again since $[Ca^{2+}]_0$ respectively the open probability is high.

For a further decrease of $[Ca^{2+}]_0$, means going to B and F, the oscillations become slower and more irregular, as the probability of an initial event decreases (note the different time ranges for each column in Figure 6.12). In both cases (B and F) only rare single events, as blips or puffs, are observed, caused by full inhibition and additionally by low $[Ca^{2+}]_0$ in panel F.

This dynamic difference is also reflected in the amplitudes. The fast repeating spikes in B have smaller amplitudes than those in F and the last one in B, which occurs after a longer refractory period. That ensures a more complete recovery and minimizes the effect of inhibition.

Lowering the IP_3 concentration for fixed $[Ca^{2+}]_0$ from B to C, H and E) or

from F to G, K and J, causes an increase of T_{av} and shrinks the amplitudes, as the channels are less sensitized and the nucleation probability decreases. In these less sensitized regimes, $[Ca^{2+}]_0$ sets the probability for the initial events, as can be seen by comparing E, I and J, where puff sizes decrease with decreasing $[Ca^{2+}]_0$, but the amplitudes of the less frequent spikes at $[Ca^{2+}]_0$= 45 nM are similar to those with 75 nM but shrink for a even lower concentration of 35 nM.

Finally, if we go to very low concentrations of both IP_3 an Ca^{2+}(L), no spikes are observed, and the resulting signal is the random overlay of single uncoordinated blips. From a physiological point of view, oscillations evolve from the last depicted case of low concentrations by increasing $[IP_3]$ caused by external or internal signals inducing PLCs.

To characterize the oscillations, we determine the mean period T_{av} by averaging over the ISIs, here given by the time between to successive maxima of open channels. Thereby we can explore the concentration dependence of the oscillations shown in Figure 6.13. For physiologically reasonable high concentrations, the cells exhibit fast and quite regular oscillations. If we lower one of the signaling molecule concentrations, the oscillation character depends strongly on the other concentration. If this concentration is low, too, oscillation will become slower and more irregular, i.e. they will have higher T_{av} and standard deviations, what is in comply with our experimental results. If the complementary concentration is high, oscillations remain fast and more regular also for smaller concentrations, but the amplitudes decrease. For even smaller values of the complementary concentration, the oscillations become slower and more irregular, too.

From these simulations we can determine the dependence of the standard deviation σ on T_{av} as done for the experimental oscillations shown in Figures 4.4 and 4.9 in the experimental part. This is shown in Figure 6.14, where each dot corresponds to a spike train of one cell. The shown linear regression line is given by $\sigma(T_{av}) = 0.98\ T_{av} - 25$ s. These results are in good agreement with experiments and indicate the wave nucleation phenomenon.

6.6 Summary

In this chapter we developed a tool to simulate intracellular Ca^{2+} dynamics by a bottom-up approach, which combines stochastic simulation on a microscopic scale and analytical solutions for the deterministic dynamics on the macroscopic length scale. The analytical solution is based on Green's functions, and hence we refer to the model as the *Green's cell model* (GCM) and to its implementation as the *Green's cell algorithm* (GCA). The model structure and its implementation as well as the first obtained results can be summarized as follows:

- The GCM splits the cellular dynamics into two parts.

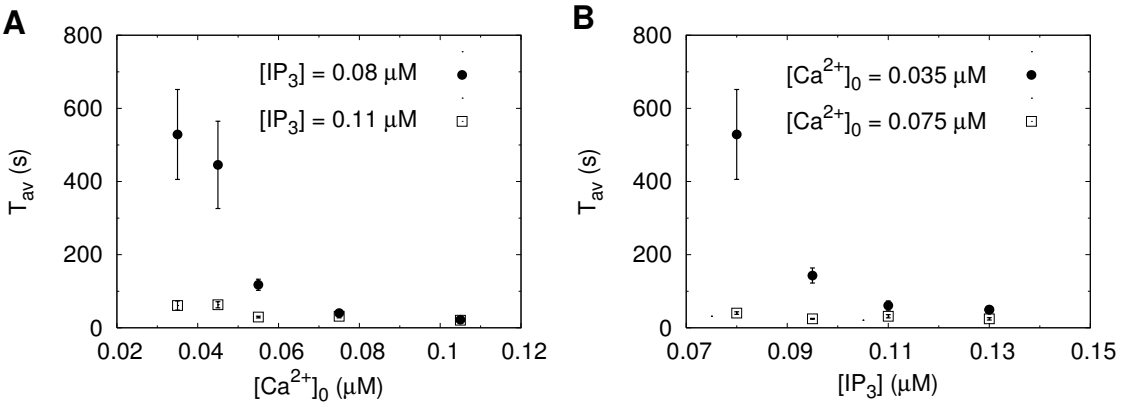

Figure 6.13: Dependence of the oscillation period on $[Ca^{2+}]_0$ and $[IP_3]$ **A**: Dependence of T_{av} on the cytosolic Ca^{2+} base level concentration $[Ca^{2+}]_0$. For high IP_3 concentrations the oscillations are rather fast for a large region, whereas for low $[IP_3]$ T_{av} increases with decreasing $[Ca^{2+}]_0$. **B**: Dependence of T_{av} on the IP_3 concentration $[IP_3]$ for fixed $[Ca^{2+}]_0$. For lower $[Ca^{2+}]_0$ the oscillation become slower with decreasing $[IP_3]$. For even smaller concentrations, the fast oscillations become slower and more irregular, too. (Error bars denote s.e.)

  - On the microscopic scale the IP_3R states are characterized by the DeYoung-Keizer model (DKM).
  - On the global scale the cellular dynamics is described by a linear reaction diffusion system (RDS).

- The stochastic binding of Ca^{2+} and IP_3 to IP_3R molecules is determined by a hybrid version of the Gillespie algorithm.

- The corresponding channel states are translated into source fluxes of the RDS (6.31) by the single channel approximation defined in Equation (6.25).

- The RDS is solved analytically by means of coupled Green's functions, also known as Green's dyadic.

- The resulting concentrations at the cluster locations influence the channel transitions and lead to CICR.

- The GCM was implemented as a parallel algorithm using C++ and MPI routines. It is based on the length scale separation. The microscopic dynamics of channel transitions and the time steps are determined by one process relying on the Ca^{2+} concentration at the cluster locations, which are determined by worker processes on other processors.

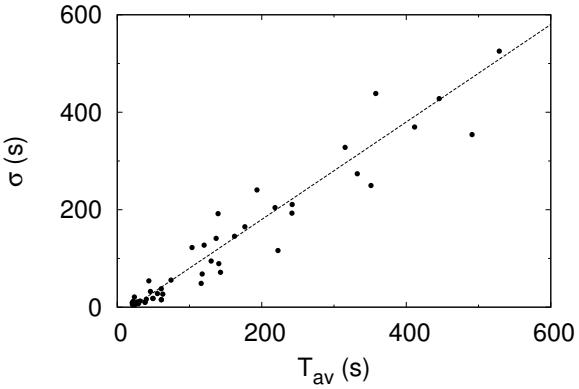

Figure 6.14: Simulated σ-T_{av} relation. From simulations as those shown in Figure 6.12 we determine σ and T_{av}. The observed linear relation between them is in accordance with the experimental findings in Figure 4.4 and points to wave nucleation.

- The algorithm allows for sufficient long time simulations within one day. We can simulate a real time of hundreds of seconds for typical physiological cell properties within 24 hours, what is a speedup factor of around hundred compared to straight forward methods like Finite Element Solvers.
- With this algorithm we have access to experimental observables like the cytosolic Ca^{2+} concentration as well as to internal properties such as the number of open channels and inhibited subunits.
- We can observe the hierarchical structure of CICR given by the inhomogeneous concentration distribution and determine different cellular regimes. These different regimes ranging from rather regular to highly stochastic behavior emerge naturally from the GCM for different parameters. This demonstrates the generic character of the model.
- In the representative simulations we have seen, how large channel currents lead to stronger coupling of clusters and subsequently to more regular spiking.
- As a first systematic example, we have analyzed the dependence of the IP_3 pathway on the Ca^{2+} and IP_3 concentration and found different regimes: the rather regular regime for high $[IP_3]$ and moderate $[Ca^{2+}]_0$ as well as the more irregular regime for lower concentrations.
- The simulated oscillations exhibit a similar behavior of the σ-T_{av} relation as the experimentally measured oscillations.

Taken all together, we have a powerful tool to simulate intracellular dynamics. The developed Green's cell algorithm (GCA) can generate easily the versatile forms of Ca^{2+} signals in dependence on physiologically motivated parameters and can now be used to study different aspects of Ca^{2+} signaling, what is the topic of the next chapter.

Chapter 7

Cell simulations

In this chapter[1], we use the Green's cell algorithm (GCA) developed in the last chapter for cell specific simulations. We start with using the GCA to simulate the experiments of the experimental part of this thesis. In the second part of this section, we simulate situations which are hardly accessible in experiments leading to new hypotheses and insights into the system.

First we focus on the buffer experiments of Section 4.2.3, which have demonstrated the spatial character of Ca^{2+} signals. Then we return to the question of Chapter 5 how temperature influences Ca^{2+} signaling and whether the effects can be caused by the changed spatial coupling due to increased SERCA activity.

In a next step, we go beyond the experimental possibilities by analyzing the cellular behavior under different physiological conditions, which cannot be changed directly in experiments. Thus, we investigate the influence of IP_3R clustering using the GCA by distributing a fixed number of channels on a varying number of clusters and analyzing the cellular behavior.

While the investigations mentioned so far analyzed the spatial dependence of Ca^{2+} signals, we use the method in Section 7.4 to study the dependence of the global cell behavior on intrinsic channel properties. This is motivated by very recent results of Rahman *et al.* [188] demonstrating different stationary open probabilities P_o of IP_3Rs in dependence on their spatial arrangement. They find a doubled P_o for lone IP_3Rs compared to single channels within IP_3R clusters.

In this context the theoretical findings might be the starting point for new experimental investigations and new insights into the system.

[1]This chapter is adapted in parts from [217] and [188].

7.1 Buffer simulations

In Chapter 4 of the experimental part, we used additional cytosolic buffers to characterize the oscillation mechanism. Former studies have described the hierarchical structure of Ca^{2+} signals [26, 253, 24], which originate from opening of single IP_3Rs leading to CICR. In order to demonstrate the spatial character of CICR, we first measured Ca^{2+} oscillations in cells for several minutes yielding in a reference value for T_{av} and σ. Next we loaded additional Ca^{2+} buffers into the cell and restarted the measurements. From our hypotheses of the underlying wave nucleation mechanism, we expected an increase of both T_{av} and σ of the oscillations due to the decreased spatial coupling between IP_3R clusters. This was found in the experiments as shown in Figure 4.8.

7.1.1 Motivation and methods

A disadvantage of the experimental protocol used in the experiments shown in Figure 4.8 is a possible effect of the buffers on the cytosolic Ca^{2+} base level $[Ca^{2+}]_0$. Due to their buffering capacity, they could decrease $[Ca^{2+}]_0$. A smaller $[Ca^{2+}]_0$ would lead to less frequent activation of IP_3Rs and hence the increased T_{av} and σ could be caused by local properties instead of the spatial effect we expect from our model.

As discussed in Section 4.2.3, this objection is probably inapplicable, since we loaded small buffer concentrations in presence of extracellular Ca^{2+}. We expect that in this case the Ca^{2+} regulating elements, especially SERCAs and PMCAs, accomplish a constant base level $[Ca^{2+}]_0$.

Nevertheless we might confirm the spatial origin of the increased oscillation characteristics, T_{av} and σ, by simulations, in which we can fix $[Ca^{2+}]_0$. We start with a simulation of an experiment according to Figure 4.8. We simulate a given cell with

Parameter values for buffer simulations		
$[IP_3]$	60 nM	IP_3 concentration
$[B_i]_T$	30 µM	total immobile buffer concentration
$k^+_{B_i}$	1 $(\mu Ms)^{-1}$	on rate of the immobile buffer
$k^-_{B_i}$	2 s^{-1}	dissociation rate of the immobile buffer
P_p	52 s^{-1}	pump rate
σ_c	$4.31 \cdot 10^6$ s^{-1}	channel flux constant

Table 7.1: Standard parameters of the cell deviating from those given in Table 6.3 used for buffer simulations if not stated other wise. The dissociation constant K is given by the ratio of the dissociation rate k^- and the capture rate k^+.

a fixed cell arrangement for different buffer concentrations to characterize the effect

of buffers. The prototype of a cell used in the simulation had 15 randomly scattered channel clusters separated by at least 1.5 μm. Each cluster consists of a random number of channels between 3 and 16 leading to 117 channels in total. We used different parameters corresponding to different types of buffers. Most simulations were done with parameters for BAPTA or EGTA for the mobile buffer $[B]$, since they were used in experiments. For the stationary buffer $[B_i]$ a dissociation constant of $K_d = k^-/k^+ = 2$ μM was chosen. The main properties of the most common buffer types are summarized in Table 7.2.

buffer type	D_B [μm^2/s]	k^+ [(μM s)$^{-1}$]	k^- [s^{-1}]
BAPTA	95	600	100
EGTA	113	1.5	0.3
Calmodulin	32	500	470
Parvalbumin	36	6	1
stationary buffer	0	1	2

Table 7.2: Typical parameters for different buffer types.

Similar to the experiments, we determine the ISIs of the oscillation pattern of each cell. To mimic the experimental protocol of Figure 4.8, we compare the simulations of a given cell with two different mobile buffer concentrations. This is shown in Figure 7.1 for two representative examples, where the upper panels exhibit the ratio of the spatially integrated mobile buffer to the resting level b_0, which corresponds to the experimental observable $\Delta F = b(t)/b_0$. The lower panels show analogously to the experiments the individual interspike intervals following each spike. In panel A the EGTA concentration was increased from 25 μM (red) to 250 μM (blue), yielding an increase of the average period T_{av} from 98 s to 288 s. In panel B the same cell was simulated with 5 μM BAPTA for the reference period (red) and with 18 μM BAPTA for the second period (blue). The increase of 13 μM BAPTA causes an increase of of the period from 78 s to 295 s.

Since BAPTA has a larger capture rate k^+ than EGTA, the period is more sensitive to a concentration increase. This is in accordance with the wave nucleation assumption, as the characteristic length scale, the diffusion length $L \propto (k^+[B]_T)^{-1}$, depends on k^+ of the mobile buffer concentration $[B]$. Hence, increasing the mobile buffer concentration decreases L and subsequently the coupling between the clusters more efficiently with BAPTA. That requires lower BAPTA concentrations for an effect comparable to large EGTA application.

The different heights of ΔF are also caused by the different k^+ values of the two buffers and the smaller concentrations of BAPTA used in simulations. An increase of the cytosolic Ca^{2+} concentration leads to a nearly complete binding of BAPTA to Ca^{2+}. The smaller k^+ value for EGTA yields less bound Ca^{2+} and therefore

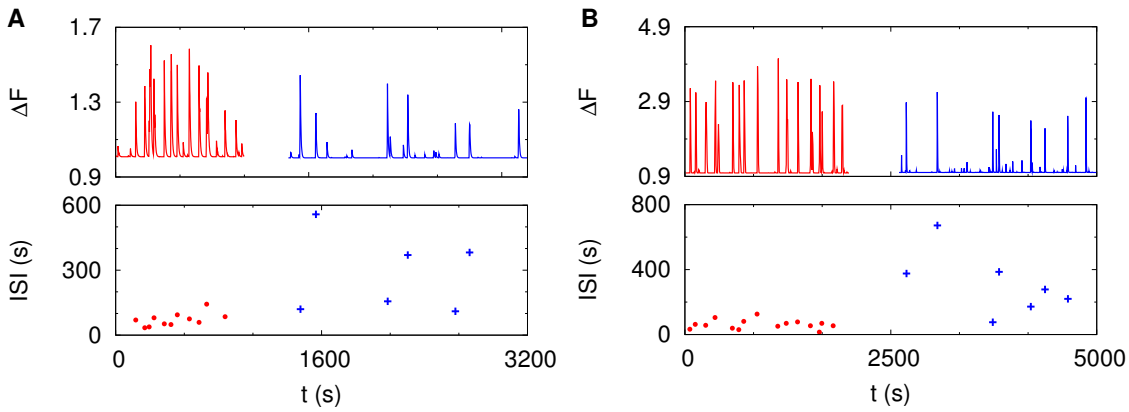

Figure 7.1: The simulated influence of Ca^{2+} buffers on the spiking behavior is in accordance with the experiments shown in Figure 4.8. The upper panels exhibit the corresponding theoretical fluorescent signal ΔF. The lower panels show the individual interspike interval following each spike. **A**: An increasing EGTA concentration from 25 µM (red) to 250 µM (blue) leads to an increase of T_{av} from 78 s to 288 s. **B**: The same simulation was performed with 5 µM (red) and 18 µM (blue) BAPTA, respectively. The increased BAPTA concentration effects an increase of T_{av} from 94 s to 295 s.

smaller ΔF values. This is the reason why fluorescent dyes should have large k^+, since smaller concentrations lead to larger signals.

7.1.2 Simulations are consistent with experiments

For a more detailed comparison with the experiment, we simulated different cell setups by varying the EGTA concentration (from 10 µM to 250 µM), the minimal distances between two clusters (from $d_{\min} = 1.5$ µm to $d_{\min} = 2.5$ µm) and different base level Ca^{2+} concentrations $[Ca^{2+}]_0$ (from 35 nM to 65 nM).

This has led to 44 cell pairs with an EGTA concentration difference of 10 µM in total, from which 35 pairs exhibit analyzable oscillations. The dependence of σ on T_{av} of these oscillations is shown in Figure 7.2A, where in accordance to the experiments shown in Figures 4.8 and 4.9, the values for the reference oscillations with the lower EGTA concentration are shown by red dots, and the values for the increased buffer concentration are depicted by blue crosses.

The σ-T_{av} dependence exhibits an analog behavior as those observed in the experiments. The population slope for both cases is around one, i.e. the data points are shifted by the increased buffer concentration in the direction of the population slope of the reference measuring period with a lower buffer concentration. This is in line with the experimental results summarized in Table 4.1.

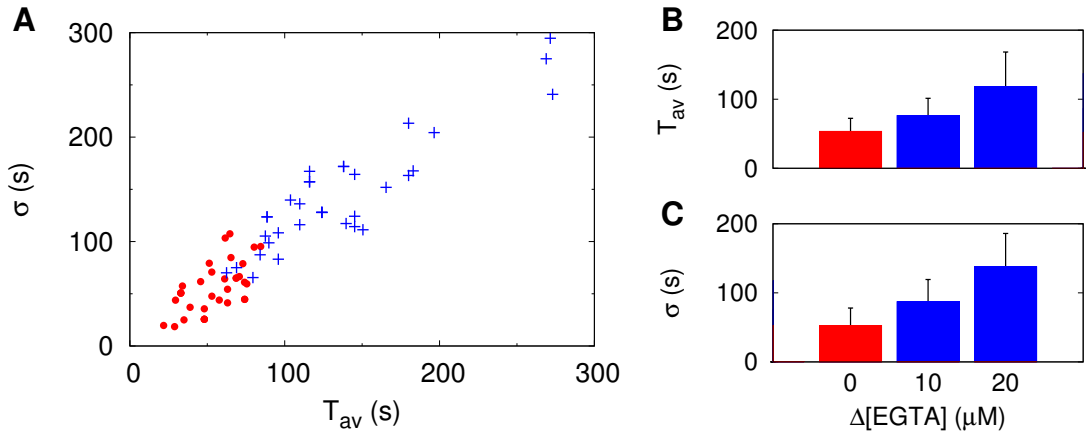

Figure 7.2: Simulations of the corresponding buffer experiments shown in Figures 4.8 and 4.9. Cells were simulated for two different mobile buffer concentrations, each corresponding to an increase in the cytosolic EGTA concentration of $\Delta\,[\mathrm{EGTA}] = 10\ \mu\mathrm{M}$. **A**: The σ-$\mathrm{T_{av}}$ relation for simulated buffer experiments. The red dots denote the reference measurements, and the blue crosses correspond to the oscillations after increasing the EGTA concentration by 10 µM. **B**: From such simulations we determine the population average of $\mathrm{T_{av}}$ and σ. The data shown in panel A corresponds to a $\Delta\,[\mathrm{EGTA}] = 10\ \mu\mathrm{M}$ leading to an increase from 53 ± 18 s to 76 ± 25 s. For simulations with an increase of $\Delta\,[\mathrm{EGTA}] = 20\ \mu\mathrm{M}$ the period prolonged to 118 ± 50 s. **C**: σ increases from 52 ± 25 s to 82 ± 25 s and to 137 ± 48 s, respectively.

From these simulations we can also extract 25 pairs with an EGTA concentration difference of 20 µM. For the different setups we performed the population averages of $\mathrm{T_{av}}$ and σ shown in Figure 7.2B and C, respectively. $\mathrm{T_{av}}$ increases from 53 ± 18 s to 76 ± 25 s for a 10 µM increase of EGTA and to 118 ± 50 s for $\Delta\,[\mathrm{EGTA}] = 20\ \mu\mathrm{M}$. This corresponds to a relative increase of 43 % and 123 %, respectively. The standard deviation changes from 52 ± 25 s to 82 ± 25 s and to 137 ± 48 s, fitting to relative changes of 57 % and 163 % for the two different concentration differences. All together, this behavior is in accordance with the experimental findings in Figures 4.8 and 4.9.

An open question is the influence of the different k^+ values of EGTA and BAPTA and the smaller slope of the σ-$\mathrm{T_{av}}$ relation of stimulated HEK cells observed in Figure 4.4 and 4.9. For the first purpose we simulate a fixed cell setup of 31 channel clusters having on average 10 channels with $[\mathrm{Ca^{2+}}]_0 = 0.55$ nM and $d_{\mathrm{min}} = 1.5$ µm for different concentrations of EGTA and BAPTA. From the yielding spiking $\mathrm{Ca^{2+}}$ time series, $\mathrm{T_{av}}$ and σ were obtained leading to the dependencies shown in Figure 7.3A

by the blue and red squares for EGTA and BAPTA, respectively. Both relations exhibit a slope close to one and a deterministic part of 18 s and 21 s, respectively, as shown by the corresponding linear regression lines.

The dependence of T_{av} on the buffer concentration is shown in Figure 7.3B by the blue squares for the cell with EGTA and by the red squares for the cell with BAPTA as mobile buffer. The dependence on the buffer concentration exhibits a nonlinear behavior for both buffer types, where the concentrations are in different ranges as shown by the two distinct x-axis labels, blue for EGTA and red for BAPTA. This is a consequence of the different k^+ values of the two buffers. Small concentrations of BAPTA have a similar effect as high EGTA concentrations as can be seen for the largest T_{av} of approximately 300 s which is caused by 18 µM BAPTA and 250 µM EGTA. This concentration difference was also found in buffer experiments with astrocytes in Section 4.2.3.

A common property is a fast increase of T_{av} for smaller buffer concentrations. The relative increase becomes smaller for moderate buffer concentrations before increasing again for larger concentrations. This behavior is caused by the interplay of the linear reaction diffusion system (RDS) and the nonlinear property of the channel's dynamics. The rather large region of the smaller rise of the relative increase between 10 µM and 15 µM BAPTA and between 60 µM and 160 µM EGTA is probably caused by the fact that the resulting concentrations at neighbouring clusters are mainly in the range where the open probability of IP_3Rs exhibits a rather linear Ca^{2+} concentration dependence.

The other open question regards the smaller slopes of the σ-T_{av} relation. Motivated by the observation in Figure 6.7, where higher currents have led to more regular behavior, we simulated the same cellular arrangement as above with BAPTA as mobile buffer and an artificially high lumenal Ca^{2+} concentration of 8 mM, as well as with an increased IP_3 concentration of 90 nM. The increased Ca^{2+} concentration in the ER leads to a ten times larger single channel current of $\sigma = 1.1$ pA compared to the standard parameters. Indeed, we observe in Figure 7.3A a dependence of σ on T_{av} with a fitted slope of 0.62 for the red dots, what is in the range of the experimental results for stimulated HEK cells. The deterministic part given by the offset of the regression line from origin is in the same range like for the cells with the smaller single channel currents, since recovery does not depend on the flux strength.

The larger currents cause higher BAPTA concentrations for periods comparable to the ones obtained with the standard current of 0.11 pA as shown in Figure 7.3B by the red dots. Moreover, we see that the linear region is prolonged caused by concentrations at adjacent clusters for which P_o exhibits a more linear dependence on the Ca^{2+} concentration. These results were substantiated by simulations, where the ER concentration was kept at 800 µM, but the currents were increased by increasing the channel radius to 0.1 µm, yieding a single channel current of 1.4 pA. These simulations exhibit a similar behavior as the red dots in Figure 7.3.

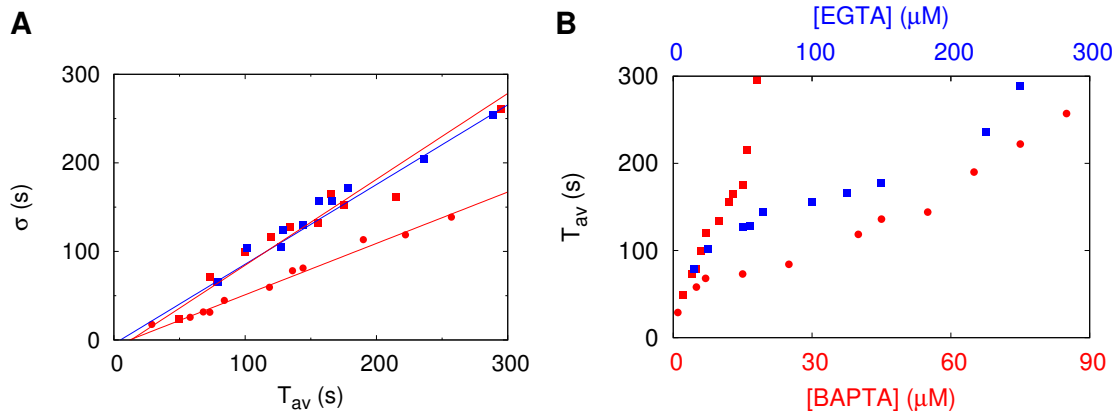

Figure 7.3: Increasing concentrations of BAPTA and EGTA increase σ and T_{av} in simulations. **A**: σ-T_{av} relation for a cell wih different concentrations of EGTA (blue) and BAPTA (red), respectively. The decreased slope of the relation for the dots compared to the squares is caused by an increased single channel current from 0.11 pA to 1.1 pA due to a ten times higher lumenal Ca^{2+} concentration. **B:** Dependence of T_{av} on the EGTA (blue) and BAPTA (red) concentration for cells with a single channel current of 0.11 pA (squares) and of 1.1 pA (dots), respectively.

Further simulations analyzing the σ-T_{av} relation were done with respect to cluster and channel densities as well as to higher IP_3 concentations. Simulations with a decreased cluster distance of $d_{min} = 0.5$ μm but with the same average number of channels per cluster as in the simulations above exhibit faster oscillations but the dependence of σ on T_{av} has still a slope close to one. For these cell setups varying only in the BAPTA concentration, an increased IP_3 concentration of 1 μM leads merely to a shift along the σ-T_{av} relation with slope one in direction to faster and more regular oscillation. Only if we increase the average number of channels per cluster to 30 and use the high IP_3 concentration of 1 μM, we find a decreased slope of 0.58 for the σ-T_{av} dependence. The rather large number of channels per cluster and the high IP_3 concentration lead again to large local cluster currents. Hence, the decreased slope illuminates once more the role of large flux strengths.

Thus, we can explain the buffer experiment on a more detailed basis. In experiments we observed smaller slopes of the σ-T_{av} relation for stimulated HEK cells compared to spontaneous oscillations in glia cells as shown in Figures 4.4 and 4.9 and faced in Table 4.1. The stimulated hepatocytes exhibit also a smaller slope of the relation as shown in Figure A.4A. This points to the reasonable assumption of larger fluxes caused by stimulation. To clarify this issue, further experiments with a ratiometric dye like fura2 are needed. These experiments should measure the global cytosolic Ca^{2+} concentrations as well as determine the local concentrations of single

puffs, what was recently done in SH-SY5Y cells [222].

Although the findings here fit the experimental data of the experimental part rather well, we still have some open tasks. The different concentration ranges yielding similar increases of σ and T_{av} for different cell types could not be totally clarified. Possible reasons are different permeabilities of the plasma membrane for the additional buffer, different IP_3R subtypes with different radii or different SERCA expression levels yielding different lumenal Ca^{2+} concentrations.

7.2 Temperature simulations

We now revive the findings of the experiments of Chapter 5, where we found that the differences between cultured astrocytes and astrocytes in acute brain slices are predominantly caused by the different temperatures at which cells are normally measured.

7.2.1 Hypothesis and methods

The hypothesized explanation is based on the reported temperature dependent SERCA pump activity [50, 112]. The authors report a rather linear increase of the pump strength with increasing temperature from 5 °C to 38 °C. Thus, the Ca^{2+} uptake at 5 °C amounts only 5 % of the uptake at 38 °C.

From this knowledge, we expect that a temperature increase leads to a similar effect as an increased cytosolic buffer concentration: it decreases the spatial coupling between IP_3R clusters and therefore we observe less cooperative Ca^{2+} signals. A difference to the situation with an increased buffer concentration is given by the fast removal of Ca^{2+} from the cytosol.

An increased buffer concentration acts first and foremostly by suppressing the creation of a critical nucleus of puffs. The probability that a triggering event, i.e. the opening of a first channel cluster, activates adjacent channel clusters, is decreased, since the free Ca^{2+} concentration is lowered by the additional buffer. But once the global wave is set off, moderate buffer concentrations do not modify the global Ca^{2+} signal too much as the buffers saturate and stop to bind free Ca^{2+}. Both, the experimental and simulated results of the buffer experiments only show small changes in the spike form compared to the increase of the mean period T_{av} and the standard deviation σ.

This behavior is different for a decreased spatial coupling caused by increased SERCA activity. The pumps do not stop to remove Ca^{2+} at high concentration, only the pump rate saturates. Hence, the individual spike form is influenced by the stronger pumping as demonstrated experimentally by the decreased spike width for larger temperatures shown in Figure 5.3D. Moreover, the spike widths of the two

different cell types could be fitted nicely by an exponential function of the temperature. The spike amplitudes of the representative Ca^{2+} time series in Figures 5.1 and 5.2 seem also to be reduced, what is in contradiction to previous theoretical studies [62], in which the influence of SERCA pumps was studied.

We use here the GCA to illuminate whether the experimentally observed temperature dependence is in line with an increased SERCA activity. Motivated by the observation that the astrocytic Ca^{2+} signals do not change significantly in Ca^{2+} free medium, we assume no-flux boundary conditions at the cell membrane. In the following simulations, the local Ca^{2+} concentration at a channel cluster induced by its own current was not determined by the single channel approximation given by Equation (6.27), but by the analytical solution 30 nm apart from the cluster. On the one hand this prevents a systematic error, since the approximation does not include the pump strength, and on the other hand we can estimate the quality of the approximation with respect to the pump strength.

Furthermore, we use a fixed lumenal Ca^{2+} concentration of 800 µM by adjusting the leak flux and a cell setup with 31 randomly distributed IP_3R clusters having a random number of channels between 2 and 16, yielding 258 channels in total. The clusters are seperated by at least 1.5 µm. Other parameters deviating from the standard parameters given in Table 6.3 are listed in Table 7.3. This prototype of a cell was simulated with different pump strengths P_p.

Parameter values for temperature simulation		
$[Ca^{2+}]_0$	55 nM	cytosolic Ca^{2+} base level
$[IP_3]$	80 nM	IP_3 concentration
$[B]_T$	52 µM	total mobile buffer concentration (EGTA)
k_B^+	0.3 $(\mu Ms)^{-1}$	on rate of the mobile buffer
k_B^-	1.5 s^{-1}	dissociation rate of the mobile buffer
$[B]_T$	32 µM	total immobile buffer concentration
σ_c	$4.31 \cdot 10^6$ s^{-1}	channel flux constant

Table 7.3: Standard parameters of the cell deviating from those given in Table 6.3 used for temperature simulations if not stated otherwise.

7.2.2 Influence of the pump strength

Figure 7.4 shows the global cell dynamics, where panel A exhibits the number of open channels and panel B shows the resulting cytosolic Ca^{2+} concentration for pump strengths P_p varying between 22 s^{-1} and 200 s^{-1}.

A first conspicious property shown in panel A is that the amplitudes of open channels during a spike are similar. They all exhibit heights between 25 and 30,

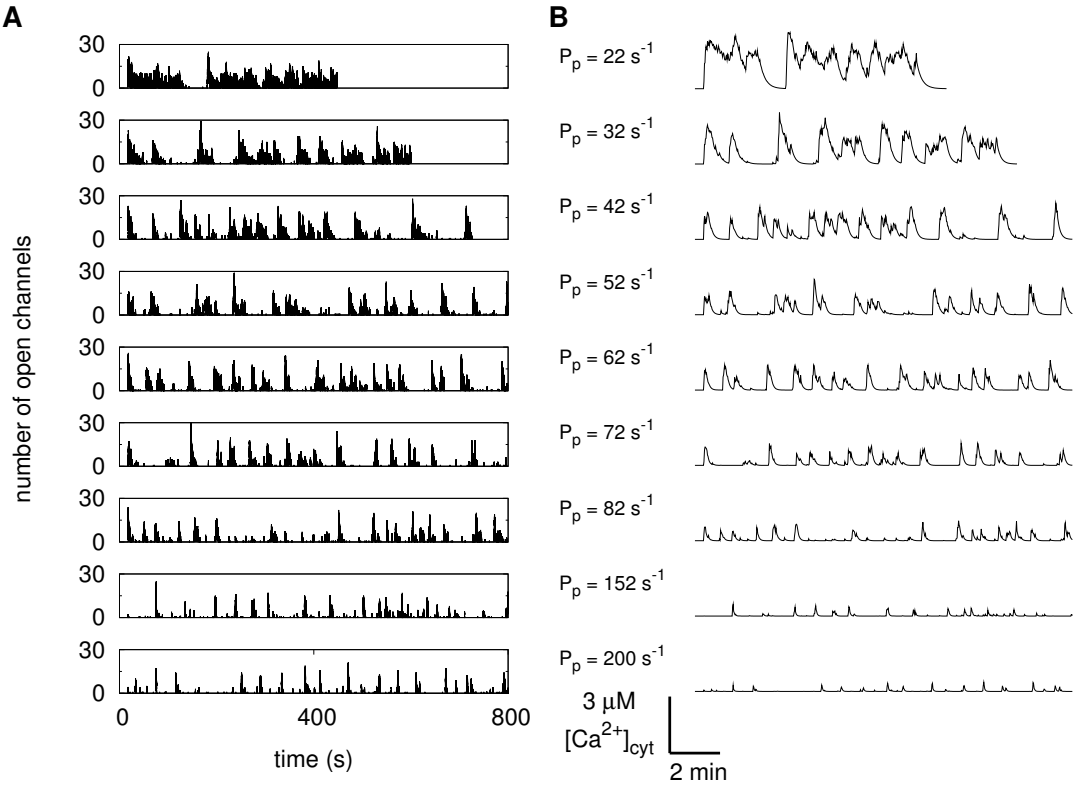

Figure 7.4: Dependence of Ca^{2+} signals on the pump strength. The temperature dependent activity of SERCA leads to higher pump rates P_p for higher temperatures. This influences the Ca^{2+} signals as shown by the number of open channels (**A**) and the corresponding Ca^{2+} concentrations (**B**). For the two smallest strengths the simulations ended before the shown real time of 800 s caused by run time restrictions on the compute cluster.

rather independently of the pump strengths P_p. Nevertheless, P_p has a huge influence on the time course. For low pump strengths, Ca^{2+} is removed from the cytosol too slow for a coordinated signal. If a channel recovers from inhibition, the cytosolic Ca^{2+} concentration is still high enough to activate the channel or to inhibit it again. This leads to plateaus for the two lowest pump strengths.

This behavior is also reflected by the cytosolic Ca^{2+} concentrations. For $P_p = 22\ s^{-1}$, the cell exhibits a plateau response and a plateau with superimposed oscillations, which are often observed in experiments with astrocytes from acute brain slices [198, 8, 175, 68, 113]. For $P_p = 32\ s^{-1}$, the shorter plateaus of open channels are translated into a more oscillatory behavior of the cytosolic Ca^{2+} concentration which exhibits rather different amplitudes of the spikes. The concentration is in a similar range as the cell with the lowest pump strength, indicating a regime where

local channel inhibition and spatial coupling determined by pumps have an equal influence on the cellular dynamics.

For increasing P_p, the cells exhibit an even more spiking behavior since long lasting channel activity is absent, and therefore $[Ca^{2+}]_{cyt}$ shows more pronounced peaks. This can be again explained by the interplay of inhibition and Ca^{2+} removal. After a spike has occured and most channels are inhibited, the SERCAs decrease the cytosolic Ca^{2+} concentration sufficently fast that $[Ca^{2+}]_{cyt}$ is on the base level again when channels recover from inhibition. Subsequently, the cell relaxes to its resting level, from which it can be activated again by CICR, i.e. by triggering opening of a channel cluster.

For very large pump strengths, the spikes of the number of open channels have still a similar height to those for smaller P_p, but their widths decrease drastically. This induces low and slim peaks of the cytosolic Ca^{2+} concentration.

So far, the simulations seem to approve the hypothesis of the decreased SERCA activity leading to an increased Ca^{2+} activity at lower temperatures. In terms of the findings in Chapter 5, a temperature increase in the experiments and the oberved changes of the Ca^{2+} signals corresponds to an increase of the pump rate from the region between 42 s^{-1} to 62 s^{-1} to 152 s^{-1} or higher.

The here observed change of Ca^{2+} signals in dependence on the pump strength exhibits some similarities with experimental studies changing long lasting cytosolic Ca^{2+} plateaus into an oscillatory behavior by increasing the buffer capacity of hepatocytes [194]. An experimental investigation demonstrating directly the influence of SERCA expression levels on Ca^{2+} signals is still missing but might be animated by the experimentally found temperature dependence and the simulations regarding the influence of the pump strength.

For a further detailed analysis, we determine the spike widths of the simulated cytosolic Ca^{2+} peaks as done for the experimental data in Figure 5.3D. Figure 7.5A exhibits the dependence of the spike width on the pump strength P_p.

The analysis of the spike width (SW) yields an exponential dependence on the pump rate P_p as shown by the line defined by $\mathrm{SW} = 61 \cdot \exp(-0.012\mathrm{s} \cdot P_p)$. At second glance we observe that the spike width become most regular for $P_p = 62$ s^{-1} as depicted by the smallest errorbar. For large P_p the errorbars become also small but the relative variation is still larger. This might indicate an optimal dynamical regime.

An analogue behavior can be found for the average amplitudes in panel B. The dependence on P_p can be fitted by the exponential relation $2.9 \cdot e^{-0.011\mathrm{s} \cdot P_p}$, and again the mean amplitude for $P_p = 62$ s^{-1} exhibits the smallest relative variations. The amplitude behavior obtained from simulations have a similar trend like those seen in the experiments of Chapter 5, but contradicts former theoretical results where the amplitude stayed constant [65]. A probable reason of this difference is the constant lumenal Ca^{2+} concentration used here. Higher pump rates do not lead to higher

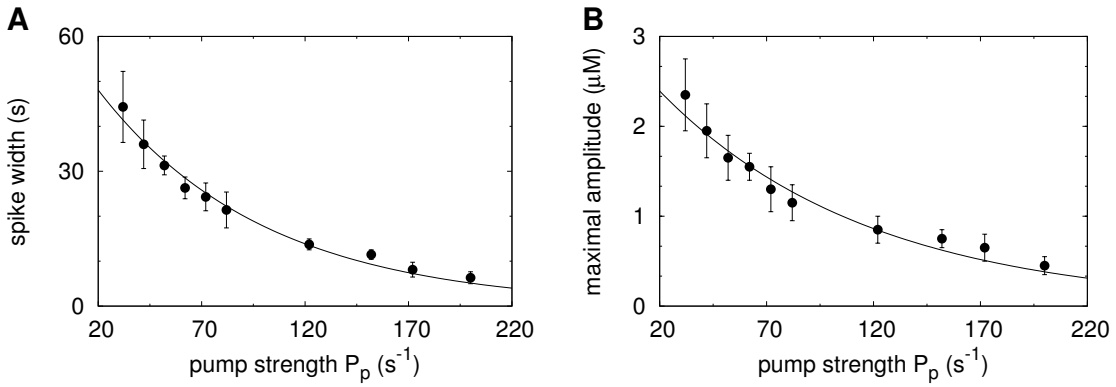

Figure 7.5: Spike width and amplitude in dependence on the pump strength for the Ca^{2+} signal shown in Figure 7.4. **A**: The spike width exhibits an exponential dependence on P_p. This is in good agreement with the experimental findings in Figure 5.3D. **B:** Also the amplitude dependence on P_p obeyes an exponential relation. (Error bars denote s.e.)

Ca^{2+} concentrations in the ER, since they are compensated by a larger leak flux, and subsequently the channel currents are not affected. Thus, the decrease of the amplitudes with increasing pump strength indicates a regulation of the ER filling level. That might be achieved by Ca^{2+} transport into the extracellular space or by buffering. More detailed experiments using ratiometric dyes are needed to clearify this contradiction.

To analyze the hinted optimal regime, we determine again the oscillation characteristics T_{av} and σ. Indeed, T_{av} exhibits a minimum of 42 s for a pump rate of 62 s^{-1} as shown in Figure 7.6A. Panel B shows the dependence of σ on T_{av} which exhibits again a slope close to one and indicates a deterministic time of 20 s. The spread of the data points is only caused by the different pump strengths. The standard deviation of the fastest oscillation has the largest deviation from that linear relation indicating AECR. Note that this does not occur for an extreme value of the pump rate, but for the moderate value of $P_p = 62$ s^{-1}.

Similar simulations with smaller buffer concentrations have shown an analogue behavior with a shift of the minimum of T_{av} to larger P_p. This is in line with our consideration, since a lower buffer concentration leads to a larger spatial coupling what can be compensated by higher pump rates.

The nonlinear dependence of T_{av} on the pump strength might indicate a possible control mechanism. A recent study [30] has demonstrated how frequency-modulation controles gene regulation. If we therefore assume that the ability to spike and to use frequency coding is the purpose of the Ca^{2+} signaling pathway, cells can control that by the expression level of SERCA. From the findings above, we expect a negative

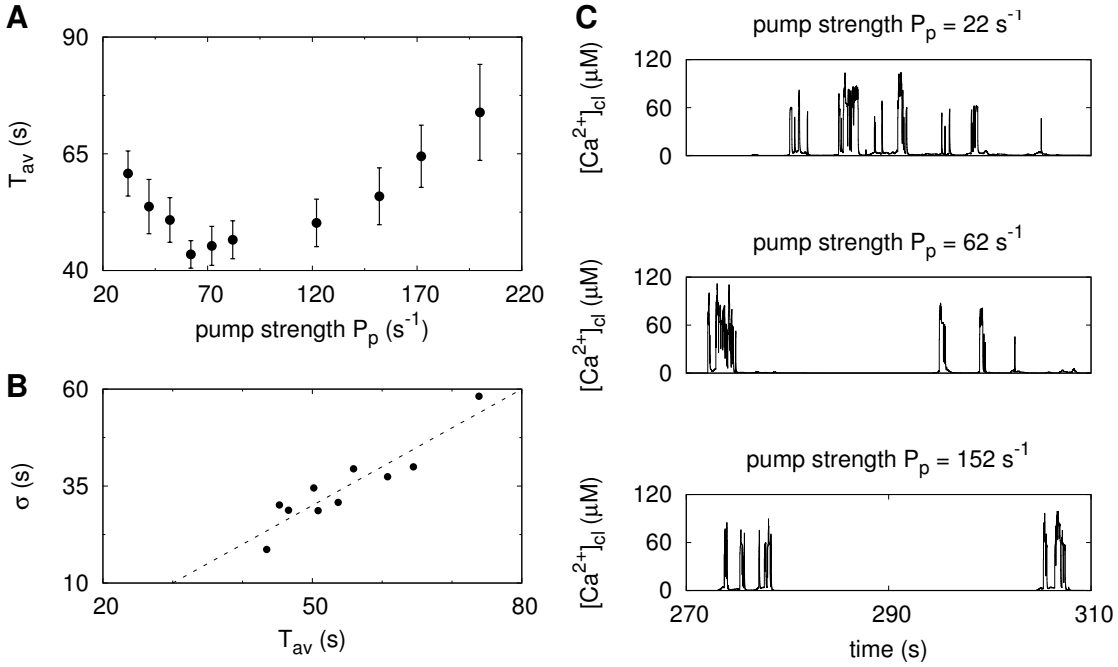

Figure 7.6: Dependence of the mean period T_{av} on the pump strength P_p. **A**: T_{av} exhibits a nonlinear dependence on the pump strength with a minimal mean period of 42 s for $P_p = 62$ s^{-1}. This might illuminate a possible control mechanism cells can use to tune their oscillations. **B**: The σ-T_{av} relation exhibits a population slope close to one and a deterministic time of approximately 20 s. **C**: The height of the local Ca^{2+} concentration $[Ca^{2+}]$ close to a cluster is hardly affected by P_p as demonstrated by the representative example of the same cluster in different simulations using different pump rates. Hence, the differences in the cytosolic Ca^{2+} oscillations in Figure 7.4B are spatially induced.

feedback of SERCA expression on fast oscillations and a positive feedback on slow oscillations with high concentration peaks and plateaus.

For a last check of our conception, we look in Figure 7.6C at the local Ca^{2+} concentrations at channel clusters. For all cases the concentration peaks are in the range of 100 μM independently of P_p. Hence, the different cytosolic Ca^{2+} signals shown in Figure 7.4B are not caused by different local properties but are a spatial phenomenon. Thus, the results of the temperature experiments in Chapter 5 are consistant with a spatial control mechanism. Due to the wide distribution of SERCA and the universality of Ca^{2+} signaling, this mechanism might be used in many temperature sensitive cellular processes, what would make SERCAs a key temperature sensor.

A more detailed view on the data shows that the widest local spike is observed

for the moderate pump rates, since for lower pump rates the longer remaining Ca^{2+} leads to partial inhibition of the channel clusters, and subsequently less channels can participate in the spike. At large P_p, Ca^{2+} is removed so fastly, that after a random closing the Ca^{2+} concentration decreases rapidly and hence the open probability of channels within the cluster is lower. This illuminates how the local nonlinearity of the IP_3R open probability can lead to a nonlinear cell response, although the global dynamics is described by a linear RDS.

Remember that we do not use the single channel approximation defined in Equation (6.27) for the concentration at a cluster induced by its own current but calculate the response to the current by the analytical solution. We see that the peaks are only barely influenced by an increase of the pump rate by a factor of eight. Besides the spatial mode of action of temperature, this demonstrates the quality of the approximation (6.27).

7.3 Clustering simulations

So far we have seen that the developed phsiological model and the corresponding algorithm can reproduce the experimental data and illuminate some of the cellular properties leading to distinct behaviors. We now turn to a task that goes beyond the experimental properties, the role of IP_3R clustering.

7.3.1 The role of IP_3R clustering

As described in Section 2.3 and experimentally shown in Chapter 4, clustering leads to a rich dynamical spectrum. The question is now why cells build distinct channel cluster and do not use a diffuse arrangement of channels or work with one huge cluster. While the influence of IP_3R clustering has been studied on the level of a single cluster [141] and in two dimensions with a reduced model of the IP_3R [214], an investigation of this issue in three dimensions and in the hierarchical picture still lacks. Thus, we use the GCA in this section to close this gap.

To explore the influence of IP_3R clustering, we vary the number of clusters N_{cl} in the cell arranged on a regular grid with a grid constant d as depicted in figure 7.7A. The unphysiological regular arrangement excludes possible artefacts induced by different random cluster configurations. But the findings regarding the separation will in general also hold for more irregular arrangements. The standard parameters used in the following investigation deviating from those given in Table 6.3 are listed in Table 7.4.

Our results do not depend qualitatively on this explicit choice, but can differ in a quantitative manner for different parameters.

The grid constant influences the spatial coupling between the clusters as the

Parameter values for clustering simulations		
$[Ca^{2+}]_0$	50 nM	cytosolic Ca^{2+} base level
$[IP_3]$	90 nM	IP_3 concentration
$[B]_T$	25 µM	total mobile buffer concentration
k_B^+	600 $(\mu Ms)^{-1}$	on rate of the mobile buffer
k_B^-	100 s^{-1}	dissociation rate of the mobile buffer
$[B_i]_T$	30 µM	total immobile buffer concentration
$k_{B_i}^+$	3 $(\mu Ms)^{-1}$	on rate of the immobile buffer
$k_{B_i}^-$	6 s^{-1}	dissociation rate of the immobile buffer
P_p	86 s^{-1}	pump rate

Table 7.4: Standard parameters of the cell deviating from those given in Table 6.3 used for clustering simulations if not stated other wise.

Ca^{2+} signals at adjacent clusters decrease with increasing separation d and thus decrease the probability for a global event.

7.3.2 Clustering increases the capability to oscillate

Figure 7.7B and C exhibits two representative examples of the cooperative channel behavior for a cell with 128 channels distributed equally on N_{cl} clusters separated by $d = 1$ µm. The upper panels show the number of open channels N_{open} and the lower panels depict the degree of inhibition R_{inh}, which is zero if no subunit is inhibited and one for total inhibition. We observe for two clusters each consisting of 64 channels a relatively regular spiking caused by the self amplifying character of CICR. If one channel of a cluster opens, it will open other channels of the cluster, too, leading to an increase of the cytosolic Ca^{2+} concentration, which will activate the second cluster. The resulting high $[Ca^{2+}]$ leads to an almost complete inhibition of channels terminating the spike. If we distribute the 128 channels on 32 clusters, i.e. each cluster has 4 channels, the amplitude and frequency decrease, since the spatial coupling is decreased. Thus we observe a higher uncoordinated background activity, i.e. opening events of very few channels that rarely lead to global events, as the puffs are too small to nucleate a global wave. To characterize such oscillations, we will determine in the following the mean amplitude and the mean period T_{av} by averaging over the ISIs, here given by the time between two successive maxima of open channels.

Cells can control the number of IP_3R and the degree of clustering [34, 272]. Thus, we are interested in how cells can tune spiking with these two variables. We compare a stimulated cell with the above mentioned high $[IP_3]$ and a cell with a lower IP_3 concentration. It turned out that cells with high $[IP_3]$ and a sufficiently high number of channels exhibit a saturated behavior as can be seen in Figure 7.8.

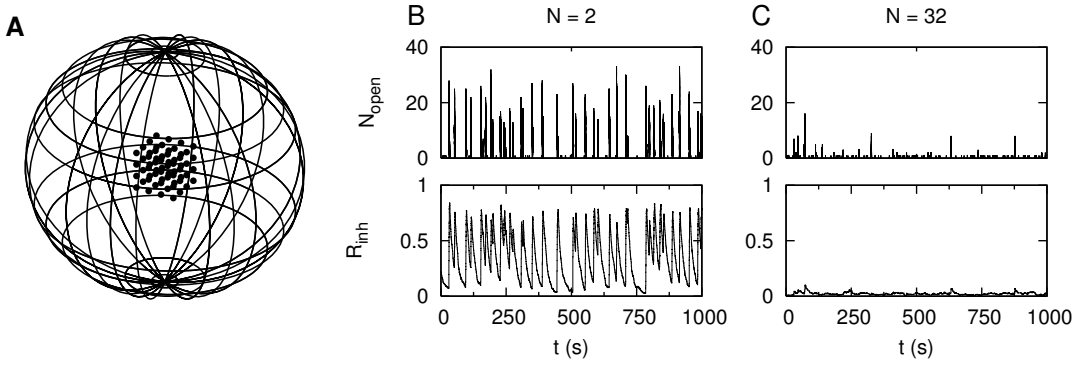

Figure 7.7: **A**: Sketch of the spatial arrangement for the clustering analysis. Clusters are put on a regular grid around the origin. **B** and **C**: Representative examples of the channel dynamics. Upper panels show number of open channels and the lower panels the amount of inhibited subunits for a cell with 128 channels in total, which are distributed on N clusters.

This fits the results of Section 6.5.2.

The squares in Figure 7.8 show T_{av} in panel A and the number of open channels in panel B for a cell with a fixed number of channels $N_{ch} = 320$, which are distributed equally on N_{cl} clusters separated by $d = 1$ µm. Both, T_{av} and the amplitude exhibit only small fluctuations indicating the strong coupling between the clusters. This behavior changes if we switch to low IP_3 concentrations as can be seen by the dots in Figure 7.8. Here each cluster contains 100 channels, i.e. by increasing the number of clusters we increase the number of channels as well. The amplitudes increase by increasing the number of clusters. Thereby T_{av} decreases from about 50 s for 2 clusters to about 20 s for 15 clusters. That is in the range of the mean period of the saturated cell and is due to the increase of the nucleation probability due to the increased number of channels. For even more clusters, T_{av} increases again since inhibition obstructs the more regular behavior. That is a consequence of the increased amplitudes shown in Figure 7.8B for higher amounts of clusters and channels leading to higher Ca^{2+} concentrations. We observe a steep increase of the amplitudes up to the level of the saturated cell of about 45 channels. From that point on, a further expression of channels is less sufficient as the amplitude increases slower and exhibits larger variations. Interestingly this cross over point of the amplitudes coincides with the fastest oscillation period in 7.8A.

To analyze the effect of channel distribution further we use a grid with a grid constant $d = 1.5$ µm and less channels to avoid a saturated behavior. Figure 7.9 exhibits T_{av} and the amplitude for two different cell setups. The dots correspond to N_{ch}= 128 and the squares mark N_{ch}= 256. The mean periods in Figure 7.9A exhibit a pronounced change for less than ten channels per cluster. Another prop-

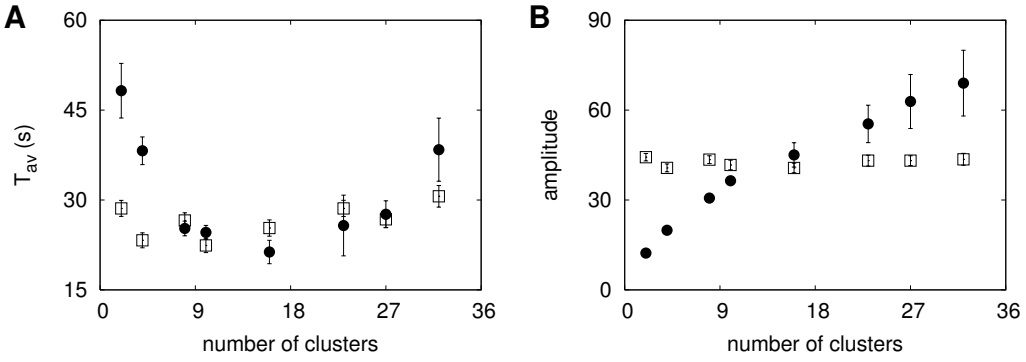

Figure 7.8: Comparison of a cell with [IP_3]=50 nM and a fixed number of channels distributed equally on clusters (squares) with a cell with [IP_3]=10 nM, where each cluster consists of 100 channels (dots). **A**: Dependence of the mean period T_{av} on the number of clusters. **B**: Averaged maximal amplitude of number of open channel. (All error bars denote s.e.)

erty is shown by the amplitudes. Although the squares have the double amount of channels compared to the dots, the average maximal amplitude is only slightly increased caused by self inhibition. These results suggest that cells with 128 channels have a larger dynamic range for frequency coding. In addition T_{av} exhibits a more pronounced change than the amplitude and could be used for a robust control mechanism.

We now return to the question about diffusive arranged channels. In a third approach to the analysis of the cluster distribution, we preserve the channel density by scaling the grid constant with the cubic root of the number of channels per cluster, i.e. $d = d_1 \, (N_{\mathrm{ch}}/N_{\mathrm{cl}})^{1/3}$, where d_1 denotes the minimal grid constant for one channel per cluster. In Fig. 7.10 we compare two cells with the same [IP_3] and Ca^{2+} base level concentration but with two different number of channels N_{ch} and minimal grid constants d_1. Both setups, the one with $N_{\mathrm{ch}} = 128$ and $d_1^{(1)}$=1 μm denoted by the squares and the setup with $N_{\mathrm{ch}} = 256$ and $d_1^{(2)}$=1.5 μm shown by the dots, exhibit a minimum in T_{av}, as shown in Fig. 7.10A.

That means, cells with a more diffusive arrangement of channels can decrease T_{av} and increase the amplitude by clustering of IP_3Rs. That is due to the existence of an optimal coupling strength for systems with discrete excitable stochastic elements [214, 212, 100]. Once the minimal T_{av} is reached, further clustering results again in slower oscillations, since inhibition blocks the channel clusters. Further we see that oscillations with lower channel density (dots) are slower compared to those with a higher density (squares). The two minima of T_{av} for the two setups occur at distinct cluster numbers and T_{av} values, but in both minima each cluster has 16 channels. We observe for both realizations a plateau of the amplitudes for

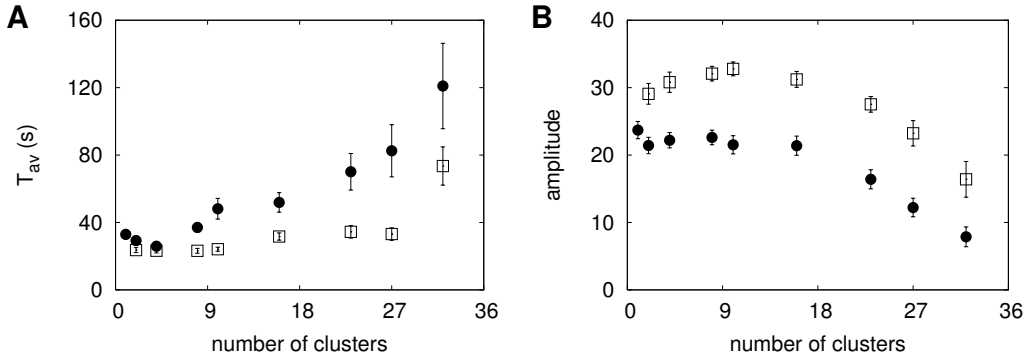

Figure 7.9: Influence of clustering with a conserved number of channels (triangles denote N_{ch}=128 and squares $N_{\mathrm{ch}} = 256$, i.e. each square has doubled amount of channels as the corresponding dots) and a fixed grid constant $d = 1.5$ µm . **A**: Mean period T_{av} against the number of clusters. **B**: The corresponding amplitude dependence.

a relatively large range from about 8 to 23 clusters. In this range the cell with the larger amount of channels exhibits a nearly doubled average amplitude, whereas the amplitude is only slightly higher for few clusters due to inhibition and goes to zero for a diffusive arrangement of channels at larger cluster numbers. Interestingly the minimal periods are in this range of constant amplitudes what might indicate a stabilized regime.

In this section we used the GCA to investigate the role of IP_3R clustering. We found that spike amplitudes and ISIs depend on the degree of clustering, the cluster configuration and the number of clusters.

We found optimal configurations and numbers of channels with respect to a variety of properties. Reliable fast spiking can be obtained with about 10 channels per cluster and cluster densities of about 0.01 $\mu\mathrm{m}^{-3}$. That would wean numbers of channels per cell which are about one order of magnitude smaller than those estimated from IP_3 binding experiments (see [136] and references therein). Remarkably, expressing move IP_3 or increasing the degree of clustering does not improve regularity or accelerate spiking. It is currently believed that Ca^{2+} oscillations use frequency encoding, what was recently confirmed in relation to gene regulation [30]. Small channel numbers appear more suitable for that purpose than large ones. Clustering of channels consistently improved spiking with respect to regularity of ISI and amplitude of spikes.

If we assume that the ability to spike and to use frequency coding is the purpose of the Ca^{2+} signaling pathway, our results indicate that it can be achieved with surprisingly small channel numbers and if channels cluster. A recent experimentally study [222] reports even such a low number of release sites.

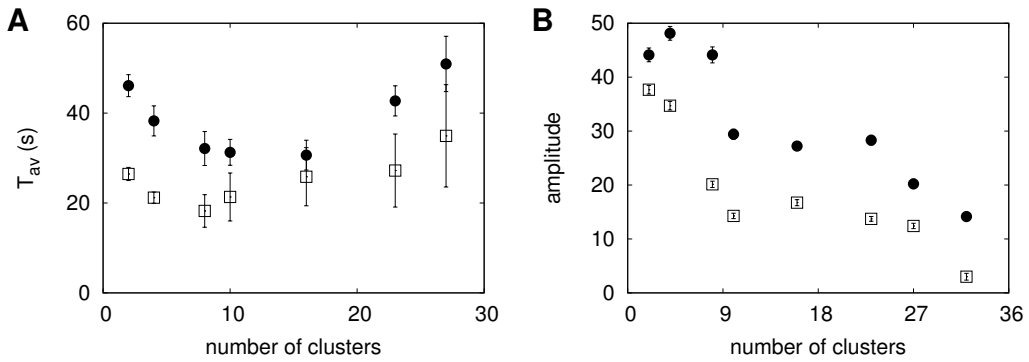

Figure 7.10: Influence of clustering with a conserved channel density. **A**: The comparison of T_{av} for a cell with $N_{ch} = 128$ channels and d_1=1 µm (squares) and a cell with $N_{ch} = 256$ channels and d_1=1.5 µm (dots) demonstrate that the minimal T_{av} is not a simple effect of the density. **B**: The amplitudes exhibit a constant region and show, that diffusively arranged channels do not create global oscillations for physiological regions, as the period increases and the amplitude goes to zero for increasing number of clusters.

7.4 Intrinsic channel properties

An advantage of the GCA is its modularity in respect of different channel models. The structure of the algorithm enables the implementation of different channel models rather easily, since the channel states are translated into currents acting as source term of the reaction diffusion system. Hence, the structure of the analytical solution of the system is uneffected, and distinct channel models lead only to a modified Gillespie algorithm determining the channel states of the master process of the parallel algorithm depicted in Figure 6.6.

In this section, we analyze the effect of different open times of IP_3Rs and give a representative example how to test channel models with respect to the cellular dynamics.

7.4.1 Open times of IP_3Rs depend on their arrangement

Very recently Rahman *et al.* have found experimentally a change in the open probability P_o of IP_3Rs in dependence on their arragement [188]. They measured the channel behavior by patch clamp techniques. To exclude side effects induced by varying lumenal Ca^{2+} concentrations, they isolated the patch from the membrane and put it into a bath solution enabling constant conditions. From the resulting patch clamp records they determined the open and close times.

They found a difference in the open times τ_o between IP_3Rs within clusters and

isolated channels. Lone IP_3R exhibit an open time of $\tau_0 = 10$ ms and single channels within clusters have a τ_0 of 5 ms. The question arose if this change on a very short time scale has an influence on global oscillations. To explore the implication of this effect and its possible physiological role, we used the GCA to perform simulations comparable to those of the last section, in which we analyzed the effect of clustering with a decreased open probability for clustered channels.

We start with simulations on a regular grid as done in Section 7.3 and analyze also cell behaviors for a random distribution of channel clusters. To illustrate the ramification of both, clustering and a decreased open probability, we contrast three situations for a fixed numer of IP_3Rs and a conserved channel density.

Analogously to the last section we compare a cell with 32 lone IP_3Rs seperated by 1.5 µm and a cell with eight clusters sperated by 2.48 µm, each having four IP_3Rs. These arrangements lead to the same channel density and are shown in Figure 7.11A where red corresponds to lone IP_3Rs and blue denotes the clustered channel locations. The cell with the clustered IP_3Rs was simulated with two different parameter sets for the channel properties describing the different open times τ_o.

The active state of the IP_3R in the DeYoung-Keizer model (DKM) corresponds to a burst of a single channel. For the DKM, the current averaged over a burst I_{burst} is given by

$$I_{\text{burst}} = I_s \frac{\tau_o}{\tau_o + \tau_{\text{cl}}} \,, \tag{7.1}$$

where I_s denotes here the single channel current defined by Equation (6.25) and τ_{cl} is the closing time of IP_3R. To allow burst length to be changed in accord with the experimental observations (i.e. decreased by 50 % for clustered IP_3R) within the framework of the DKM, the Ca^{2+} dissociation rate k^-_{Ca} was adjusted. It depends on τ_o by the relation

$$k^-_{\text{Ca}} = \text{b}_5 \frac{\tau_{\text{cl}}}{\tau_o + \tau_{\text{cl}}} \,, \tag{7.2}$$

where b_5 denotes the rate of dissociation of Ca^{2+} from the activating binding site of the DKM as shown in Figure 6.1A and described in Table 6.1.

We incorporate the halved open time into the GCA by scaling the single channel current in accordance with Equation (7.1) with the two different open times τ_o and the unaffected closing time τ_{cl} of roughly 21 ms. The decreased open time was considered in the channel dynamics by using a modified value of b_5 obtained by Equation (7.2). As shown in Figure 7.11B, this leads to shorter bursts with decreased amplitudes for the smaller open probability (blue) compared to the standard values (black).

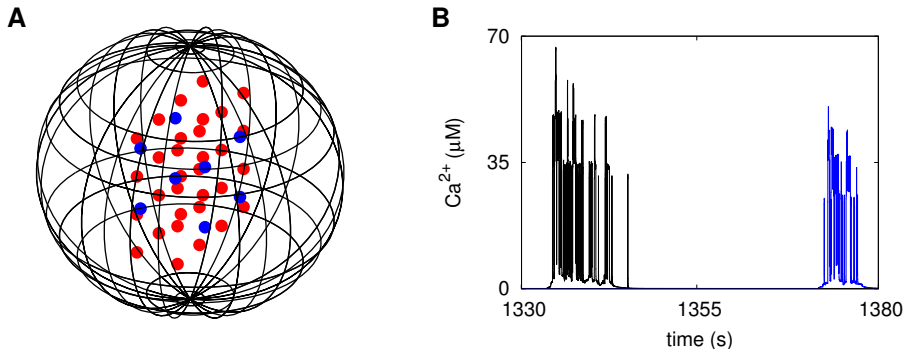

Figure 7.11: Decreased open times lead to shorter bursts with smaller amplitudes. **A**: Typical channel arrangement on a regular grid. The 32 lone IP_3Rs are separated by 1.5 µm (red), and the eight clusters each consisting of 4 channels have a distance of 2.48 µm, yielding to the same channel density. **B**: Typical concentration at a cluster during a spike for a cell with channels with IP_3R properties of lone IP_3R (black) and clustered IP_3R (blue). The decreased open times lead to shorter bursts with smaller amplitudes.

7.4.2 Decreased open times increase the dynamical range

To analyze the effect of the decreased open time τ_o, we performed several parallel simulations for the cellular arrangement shown in Figure 7.11A in which we varied the mobile buffer concentration between 45 µM and 65 µM. A representative example for 65 µM is shown in Figure 7.12 where panel A shows the number of open channels and panel B exhibits the corresponding cytosolic average concentration.

We see that the lone IP_3Rs (red) do not exhibit a cooperative signal since the coupling between them is too small. The cell with clustered IP_3Rs and a smaller open time of $\tau_o = 5$ ms (blue) exhibits in this example a single spike in both, the number of open channel (A) and the Ca^{2+} concentration (B). The same setup with an open time equivalent to lone IP_3R of $\tau_o = 10$ ms shows a rather frequent spiking (black). Moreover, the concentration spikes have higher amplitudes than those with the decreased open probability.

Thus, we found again the fact of the last section that clustering enables cells to oscillate more properbly than a diffusive arrangement of channels. From ten of these simulations we could determine the mean period T_{av} for the two clustered arrangements with different τ_o. We found for the smaller τ_0 (blue) an average ISI of 223 s and for an average over the same setups with the larger open time (black) a period of 67 s as shown in Figure 7.12C. The variations of T_{av} within one group corresponding to one of the two different open times are caused by the different buffer concentrations. The smaller errorbar for the faster oscillations indicates a more regular behavior, i.e. the cell is in the stable oscillating regime and not as

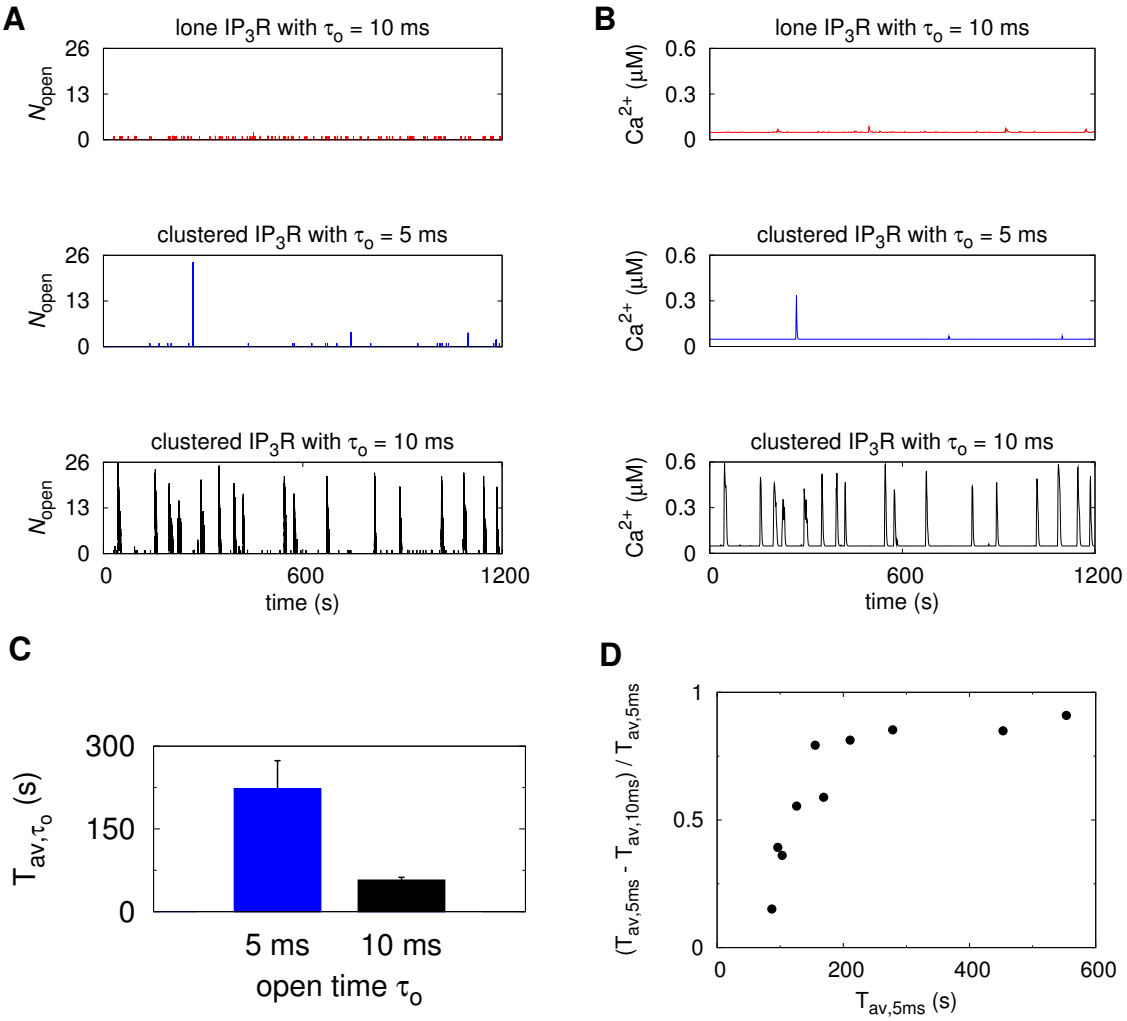

Figure 7.12: Influence of clustering and decreased open times for 32 lone IP_3Rs separated by 1.5 μm and $\tau_0 = 10$ ms (red), clustered IP_3Rs with $\tau_0 = 5$ ms (blue) and $\tau_0 = 10$ ms (black). **A**: The number of open channels demonstrates that cell can generate spikes due to clustering and that the decreased open time leads to less frequent spikes. **B**: This is also shown in the average cytosolic Ca^{2+} concentrations, where we observe a decrease in the spike height for shorter open times (blue) compared to the clustered IP_3Rs with larger τ_o (black). **C**: By varying the mobile buffer concentration between 45 μM and 65 μM, we could compare the effect of the two different open times leading to different mean periods T_{av}. **D**: The relative change of the different T_{av} depends on the regime. For stronger coupled clusters and subsequently faster oscillations of the cell with IP_3Rs having $\tau_o = 5$ ms the relative change is rather small whereas for slow oscillations the effect is up to 100 %.

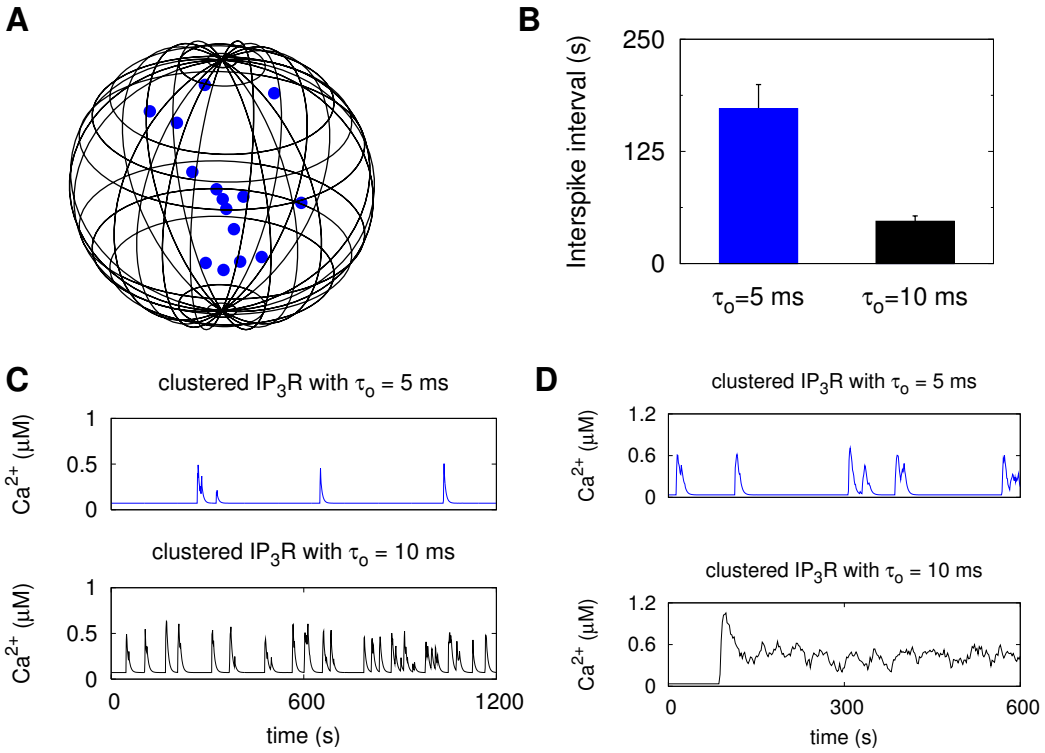

Figure 7.13: Effect of decreased τ_o in random setups. **A**: Representative example of a random realization of cluster distribution. **B**: The average period T_{av} for parallel simulations of five random setups with the two different open times exhibits larger values for smaller τ_o. **C**: Representative example of parallel simulations for an identical setup of a cell with $\tau_o = 5$ ms (blue) and $\tau_o = 10$ ms (black). **D**: The example for large stimulation and strong coupling demonstrates that a decreased τ_o induces a larger regime for oscillations.

senitive to the mobile buffer concentration as the cell with smaller τ_o.

To study this effect in more detail, we determine for each pair of simulations the relative change induced by decreasing τ_o. This is shown in panel D where the relative difference of T_{av} for the two different open times is plotted over the mean period of the smaller τ_o. The relative difference $(T_{av,5ms} - T_{av,10ms})/T_{av,5ms}$ exhibits a saturated behavior for large $T_{av,5ms}$ of approximately 100 % and only a small deviation for fast oscillations of the cell having IP_3Rs with a decreased open probability. This demonstrates how smaller τ_os increases the dynamical range of the cell.

In a next step, we compared the oscillatory behavior of cells with different kinds of IP_3Rs arranged in randomly scattered channel clusters. Figure 7.13A exhibits a representative example. For each of the five random configuration with 15 clusters

having a random number of channels between 2 and 10, we simulate the cell with both open times. We set the Ca^{2+} base level concentration to 40 nM and choose an IP_3 concentration of 80 nM. Panel C exhibits a representative example of the spiking behavior of the cytosolic Ca^{2+} concentration where blue and black corresponds again to $\tau_0 = 5$ ms and $\tau_0 = 10$ ms, respectively.

From the resulting parallel time series, we determined again the average interspike intervals shown in Figure 7.13B. For the lower open probability, we find a mean period of 168 s, and for cells containing IP_3Rs with $\tau_o = 10$ ms, the mean interspike interval equals 58 s. Here, the variation within one group occur due to the intrinsic channel stochasticity and, more important, due to due to the different spatial arrangements. An analysis of the relative change exhibits a similar relation as for the simulations on the regular grid shown in Figure 7.12D (data not shown) indicating again an increase of the dynamical range.

For a final demonstration of the advantage of a changed open probability, we repeated the simulation leading to the representative examples in Figure 7.13C with a high IP_3 concentration of 1 µM, a Ca^{2+} base level of 35 nM and a doubled number of IP_3Rs per cluster. The resulting time series are shown in panel D. We see that in the case of strong stimulation and larger coupling which is caused by the additional channels, the cell with the reduced open times (blue) still exhibits spiking whereas the cytosolic Ca^{2+} concentration of the cell with the higher open probability does not oscillate but shows a plateau.

Recent studies suggest the property of an oscillating cytosolic Ca^{2+} concentration to be essential for the cell [30]. In this context, the findings of a change in τ_o make sense. As we have seen in this and in the previous section, clustering increases the capability to spike. Hence, the higher open times for lone IP_3Rs increase their contribution to a spike since it increases the local currents and acts as an amplifying effect on the one hand. On the other hand, we have found that a decreased open time of clustered IP_3Rs increases the dynamical range of the cell. Especially in the situation of strong stimulation and coupling between clusters, this mechanism leads to oscillations while higher open probabilities generate long lasting cytosolic Ca^{2+} responses.

These findings demonstrate also that the experimentally found temperature dependence of Ca^{2+} signals could also be caused by a change of the IP_3R properties. But we have seen in Section 7.2 that the experiments can be explained rather perfectly by an increased SERCA pump activity, for which a strong experimental evidence exists[112, 50]. The modeling investigation of SERCA activity has shown that the change in the global signal is a spatial effect, since the local Ca^{2+} concentrations close to clusters are nearly unaffected by larger pump rates P_p. However, a local change in the IP_3R property leading to a similar effect on the global scale is indispensably connected with a decrease of local currents and concentrations. This could be verified easily in experiments.

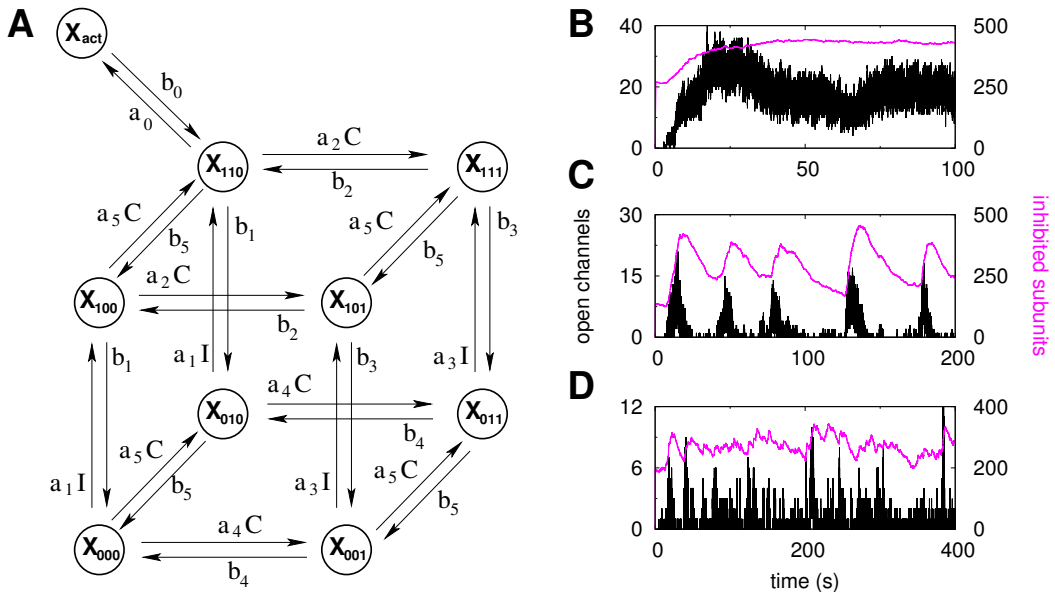

Figure 7.14: Representative channel model test. **A**: Scheme of a modified DeYoung-Keizer model for a subunit. Deviating from the DKM, a subunit is not active in the state X_{110} but in the state X_{act}, which is achieved by a transition from X_{110} with a constant rate a_0 and leaved only back to X_{110} with rate b_0. **B**-**D**: Representative examples of the behavior of open channels (black) and inhibited subunits (purple) demonstrating the dominance of a steady state where open channels and inhibited subunits are in equilibrium as in (B) and (D) for $[Ca^{2+}]_0$=35 nM and $[Ca^{2+}]_0$=5 nM, respectively. Only for a small parameter regime, the channel model allows for fast and regular oscillations (C) with $[Ca^{2+}]_0$=15 nM.

7.4.3 Representative channel model test

As mentioned above, the GCA is compatible with respect to different channel models. A great future task will be the test of different channel models. Usually, these models are derived from patch clamp experiments of single IP_3Rs. A disadvantage of these experiments is that the spatio-temporal interaction with other channels and channel clusters with respect to the cellular dynamics cannot be studied.

Here comes the GCA into the game. Due to its biophysical bottom-up approach, it is able to translate the single molecule properties into global cell responses. We demonstrate the method for a single example that might serve as an outlook for future projects. We analyze a modified DeYoung-Keizer model recently developed by Rüdiger *et al.* in relation to single channel records. They introduced a fast time scale into the model by an extra state for each subunit representing the active state which is denoted by X_{act} in Figure 7.14A. The active state is reached from the

former active state X_{110} by a fast transition with the constant rate $a_0 = 540\ s^{-1}$. From state X_{act}, the system only can go back to state X_{110} with rate $b_0 = 80\ s^{-1}$. For more details of the DKM see Section 6.2 and for the modified model [195].

A typical behavior in terms of open channels (black) and inhibited subunits (purple) is shown in Figure 7.14B-D for a cell with 23 channel clusters each having on average 7 channels and which are separated by at least 3 µm. We use Ca^{2+} base level concentrations of 35 nM (B), 15 nM (C) and 5 nM (D). The IP_3 concentrations was fixed to 70 nM in the shown examples. Other parameters are the standard parameters listed in Table 6.3.

We see that the modified DKM does only lead to a rather regular spiking for a narrow parameter range (C). For most parameters the cell exhibit a steady state where open channels and inhibited subunits are in equilibrium. This is not a feature of the specific parameter choice but is stable for a large parameter region. Slow and irregular oscillations were never found in the extensive simulations scanning a large parameter range of buffer concentrations and properties as well as pump strengths and base level concentrations. Decreasing $[IP_3]$ and $[Ca^{2+}]_0$ from the regular regime has always led to an uncoordinated activity of single channels and clusters similar to the behavior shown in panel D.

A possible reason for the limited capability to spike is very likely a missing transition from the active to the inhibited state. If the subunits of a channel are in the state X_{act}, the channel is open and the local Ca^{2+} concentration is subsequently high. But since there is no transition to an inhibited state, the channel closes independently of the Ca^{2+} concentration with the fixed rate b_0. Once the channel is closed, the Ca^{2+} concentration decreases rapidly due to diffusion, SERCA pumps and buffers. Hence, the probability to become inhibited is low and the channel more probably opens again rather than becomes inhibited leading to the observed steady state with a high level of inhibited subunits. This assumption is supported by first simulations with another channel model that has also no direct transitions from open to inhibited states and exhibits a similar steady state.

Although this short example has not led to a complete new channel model, we have demonstrated the power of the GCA since the simulation of the global cell response originating from single molecule properties have suggested a general structural feature of future models.

7.5 Summary

In this chapter, we used the GCA to simulate different tasks. We started with the simulation of the corresponding experiments of the first part of this thesis almost perfectly fitting the experimental data. This demonstrates the power of the developed method. In the second part of this chapter, we went beyond the experimental

possibilities and studied the role of clustering and of intrinsic channel properties. The main findings of these cell specific simulations can be summarized as follows:

- The simulations of the buffer experiment are in accordance with the experimental data of Chapter 4 and demonstrate that the findings are probably not induced by a decrease of the cytosolic base level caused by additional buffers.
  - Increasing the mobile buffer concentration leads to slower and more irregular oscillations in accordance to the experimental findings shown in Figure 4.8.
  - In simulations we find a decreased slope of the σ-T_{av} relation for large channel currents. This might be proved by further experiments.

- The simulations regarding the experimentally found temperature dependence of Ca^{2+} signals in Chapter 5 demonstrate that the hypothesized reason of an increased SERCA pump activity is in line with both, the experimental and modeling data.
  - An increased pump strength changes the global cytosolic Ca^{2+} signals from long lasting plateaus to a spiking behavior.
  - The average period T_{av} exhibits a non-monotonic dependence on the pump strength. This suggests a negative feedback of fast oscillations on SERCA expression in order to preserve the ability to oscillate.
  - The spike width decreases exponentially with increasing pump strength fitting the experimental results of Figure 5.3D.
  - The local concentrations at clusters are barely influenced by large pump rates demonstrating that the change of the global Ca^{2+} signal is a spatial phenomenon. Moreover, this result justifies the use of the single channel approximation given by Equation (6.27).

- The analysis of IP_3R clustering has shown how the local self amplifying effect due to clustering leads to more stable oscillations in a wider parameter regime.
  - Diffusive arranged channels exhibit only in a rather small parameter range oscillations. Due to clustering, the same number of channels leads to fast oscillations.
  - The sensitivity to IP_3 depends on the number of channels. For low concentrations, a large number of channels N_{ch} preserve the capability to oscillate. A further increase of N_{ch} leads to higher amplitudes but induces longer periods.

  - There is an optimal configuration and number of channels with respect to oscillation behavior. The found small number of channels serving for a rather regular behavior contradicts the currently believed numbers.
  - From these results, we expect a negative feedback of fast oscillations on IP_3R expression.

- The recently experimentally found decreased open time τ_o of IP_3Rs localized in channel clusters compared to lone IP_3Rs leads to a larger dynamical range of the cell.
  - Even with a smaller open probability of clustered IP_3Rs, clustering increases the capability to spike.
  - Parallel simulations of cells with clustered IP_3Rs having different τ_os exhibit larger T_{av} for smaller open times. The difference decreases for fast oscillations in both setups.
  - With respect to the temperature dependence, the two different hypothesized mechanisms, increased SERCA activity or change in IP_3R properties, could be easily distinguished by measurements of the local currents and concentrations of single IP_3Rs and clusters, respectively.

Altogether, these simulations have substantiated the designed picture of the Ca^{2+} oscillating mechanism. The simulations fit almost perfectly the experimental results of the first part of this thesis and grant a deeper insight into the system. The final example has demonstrated how the GCA will be used in future to develop and test new IP_3R models.

Chapter 8

Conclusion

Standing on the basis of systems biology, this work uses an interdisciplinary approach to understand Ca^{2+} oscillations. The starting point of the investigation is a critical review of established modeling approaches. Most of these models simplify cells to homogeneous reactors, neglect their spatial inhomogeneity and describe intracellular Ca^{2+} oscillations as deterministic limit cycles. But theoretical studies have demonstrated that channel clustering and the yielding large concentration gradients do not allow for limit cycle oscillations but might induce the experimentally observed spiking behavior by exploiting channel fluctuations.

These two different approaches touch the basics of cell signaling. How do cells generate predictable signals from single molecule dynamics? The assumption of a homogeneous topology induces an averaging over all the involved active molecules. In the case of Ca^{2+} signaling this corresponds to merging all open channels into one single cytosolic Ca^{2+} influx. Predictability arises from the deterministic behavior due to the law of large numbers within this paradigm. The random opening and closing of IP_3Rs caused by the stochastic binding of Ca^{2+} and IP_3 to the channels leads in combination with their spatially heterogeneous distribution to a stochastic medium. In this picture, the coordinated global signal is orchestrated on the level of the cell only and a local and deterministic dynamics does not exist. In many cases, cells dispense with predictability. But if it exists, it arises from a tight control of the open probability P_o in this paradigm. P_o is first kept low and then increased till the event happens. .

To clarify the question of the oscillation mechanism, this works starts from the level of hypothesis in the scheme of the iterative knowledge generating process in systems biology depicted in Figure 1.1. In the first part, we investigated Ca^{2+} oscillations experimentally and focused on the hypothesized spatial character of Ca^{2+} signals and their stochastic characteristics. We developed in the second part a detailed biophysical model the simulation of which were compared with the experimental findings and fit them almost perfectly. The insights into the IP_3 pathway

obtained by modeling lead to the suggestion of new experiments.

I. Experimental investigation of Ca^{2+} oscillations

Starting from the theoretical assumption of a nucleation process of localized events, namely the opening of channel clusters, we studied Ca^{2+} oscillations of different cell types in Chapter 4. We analyzed these oscillations with respect to their mean period T_{av} and standard deviations σ and compared the outcome with the theoretical prediction. It turned out that Ca^{2+} oscillations are indeed stochastic and that the origin of the stochasticity is the hierarchical organization of Ca^{2+} signalling. Thus, molecular fluctuations in terms of random channel behavior are carried on the level of the cell by wave nucleation leading to a spiking behavior. Hence, Ca^{2+} oscillations have therefore a spatial character.

That contradicts the current opinion claiming Ca^{2+} oscillations to be noisy limit cycle oscillations. Consequently Ca^{2+} is not a good representative example of a cellular oscillator but demonstrates how cells can use their spatial dimensions to orchestrate different kinds of signals by using spatial concentration gradients. From this observation, we expect the findings to be generic for other signal pathways such as cAMP. Moreover, we have demonstrated how we can extract intrinsic properties from global observations and introduced a method to estimate the information content of Ca^{2+} oscillations.

The observed regular regime of Ca^{2+} spikes was predicted to occur by array enhanced coherent resonance (AECR), a phenomenon known from statistical physics to occur in stochastic media. We have proven this mechanism by sophisticated data analysis methods. That makes Ca^{2+} to a first biological example of AECR.

A main result of the experimental study is the observation that the oscillations seem to be describable by two parameters λ and ξ of the corresponding probability density. λ denotes the nucleation rate determined by the puff activity as well as by the spatial coupling, and ξ is the regeneration rate that describes recovery from inhibition. It turned out that different cell types exhibit different ξs and cells of one type differ mainly in λ leading to cell type specific slopes of the σ-T_{av} relation.

A more specific experimental investigation was done in Chapter 5, where the influence of temperature on Ca^{2+} signals in astrocytes was studied. The results demonstrate that the reported differences between cultured astrocytes and cells in acute brain slices are mainly caused by the different temperatures cells are used to be measured at. This result resolves the unsatisfying fact of the diverse behavior of cells from the same cell type in respect of Ca^{2+} signals. Contemporaneously, the question of the physiological mechanism of this phenomenon arose. Is it caused by a temperature induced change of the local IP_3R dynamics? Or is the effect caused by an increased SERCA activity and has therefore a spatial character? To illuminate this questions and to undergird other experimental results, we used a modeling

approach in the second part of the thesis.

II. Bottom-up modeling approach

To investigate the physiological basis of Ca^{2+} signals, we developed a biophysical model in terms of a reaction diffusion system (RDS) including a detailed model for the channel dynamics in Chapter 6. The RDS is solved analytically by means of coupled Green's functions. The analytical solution is driven by the stochastic opening and closing of the channels, the Markovian dynamics of which depends on the response of the RDS. The two parts are coupled by a hybrid version of the Gillespie algorithm.

The developed Green's cell model allows for an elegant parallel algorithm enabling sufficiently fast simulations of the spatially resolved Ca^{2+} dynamics. The implemented Green's cell algorithm (GCA) was used to analyze the IP_3 pathways with respect to different conditions in Chapter 7. Here we simulated the experimental protocols of the experimental part. Thus, we found in buffer simulations a similar dependence of the oscillations on the buffer concentration as in the experiments with regards to the spiking behavior of single cells as well as in the population behavior of the σ-T_{av} relation. Furthermore, we observe a decreased slope of the σ-T_{av} relation for large channel fluxes that is comparable to the slope of stimulated cells in experiments. That indicates a possible reason of cell specific ξ values what can be tested in future experiments.

Simulations regarding the found temperature dependence have demonstrated that the findings are in line with the hypothesized increased SERCA pump activity. Moreover, the oscillation period exhibits a minimum in dependence on the pump strength. From this we expect a negative feedback of SERCA expression on fast oscillations. This is another example how cells can use the spatial dimensions to shape their Ca^{2+} oscillations.

The GCA was also used to go beyond the experimental possibilities. We studied the influence of IP_3R clustering and how intrinsic channel properties act on the global signal. It turned out that cells can build regular oscillations with a number of channels that is by one to two orders of magnitudes smaller than currently believed. This result is confirmed by very recent experimental findings. The oscillations exhibit a minimal period for an optimal configuration with respect to channels per cluster. This might be used as a mechanism controlling IP_3R expression and clustering.

Simulations of the experimentally observed reduction of the open probability of clustered IP_3Rs compared to lone IP_3Rs have demonstrated that this leads to an increased dynamical range of cells regarding Ca^{2+} oscillations. That means that cells preserve their ability to spike for higher levels of IP_3R expression and clustering. In this sense, the retuned open probability might represent a robustness mechanism.

Altogether, this work has shown that Ca^{2+} oscillations are stochastic and consist of repeated wave nucleation. In this framework, the spatial coupling of stochastically activated release sites are essential for the hierarchical organization of Ca^{2+} signals. Intracellular Ca^{2+} models have to include even these characteristics to reflect physiology. The developed Green's cell model deals sufficiently with these requirements and generates the experimentally known spectrum of Ca^{2+} signals in a natural way in dependence on physiological related parameters such as IP_3R cluster localization, Ca^{2+} and IP_3 base level concentrations, SERCA activity and cytosolic buffer content. Moreover, the GCA allows for investigation which are hardly accessible for experiments. Thus, the studies of the oscillation behavior in dependence on SERCA activity and IP_3R clustering have illuminated new possible control feedbacks within the cell. The GCA will be used in future to develop and test IP_3R models and for a deeper understanding of the IP_3 pathway.

Although this work uses Ca^{2+} dynamics as a representative example, we expect the results also to be valid for other signaling pathways exhibiting spatial gradients such as cAMP. The basic principle to generate global signals from molecular dynamics by diffusion induced aggregation will probably found in many other signaling processes. Furthermore, the developed methods and simulation tool can be used in other disciplines of science.

Appendix A

Biological appendix

This appendix contains supporting informations and figures, which illustrate further aspects and may lead to a deeper understanding of the topics mentioned in the main text. Moreover, we give details for some of the calculations used in the main text.

A.1 Ca^{2+} oscillations are mediated by IP_3R

Evidence for IP_3Rs evoking Ca^{2+} oscillations in astrocytes, microglia and HEK cells is presented in [72, 67, 210].

Spontaneous Ca^{2+} oscillations in PLA cells stop upon application of thapsigargin (data not shown[1]). We conclude that thapsigargin-sensitive intracellular Ca^{2+} stores are required for Ca^{2+} oscillations.

For antibody staining cells were fixed with 4% formaldehyde in PBS (pH 7.4) for 20 min. After washing three times with medium we used a primary rabbit purified polyclonal anti-IP_3R antibody (1:200; Chemicon), which was visualized with anti-rabbit IgG (1:100, Sigma) using a confocal laser-scanning microscope (LSM 510 Meta, Zeiss). Measuring the fluorescence reveals the presence of IP_3Rs as shown in Figure A.1A and B. Low concentrations (≤ 1 mM) of caffeine had no effect on Ca^{2+} oscillations. The phospholipase C antagonist U73122 abolished oscillations while its inactive derivative U73433 had no effect (Figure A.1C and D). The IP_3R antagonist 2-aminoethoxydiphenyl borate (2-APB) also abolished oscillations (Figure A.1E). We conclude that spontaneous oscillations in PLA cells are driven by Ca^{2+} release via IP_3Rs.

[1] This experiment as well as the PLC antagonist experiment were done by H. Sauer for the cooperative publication [219].

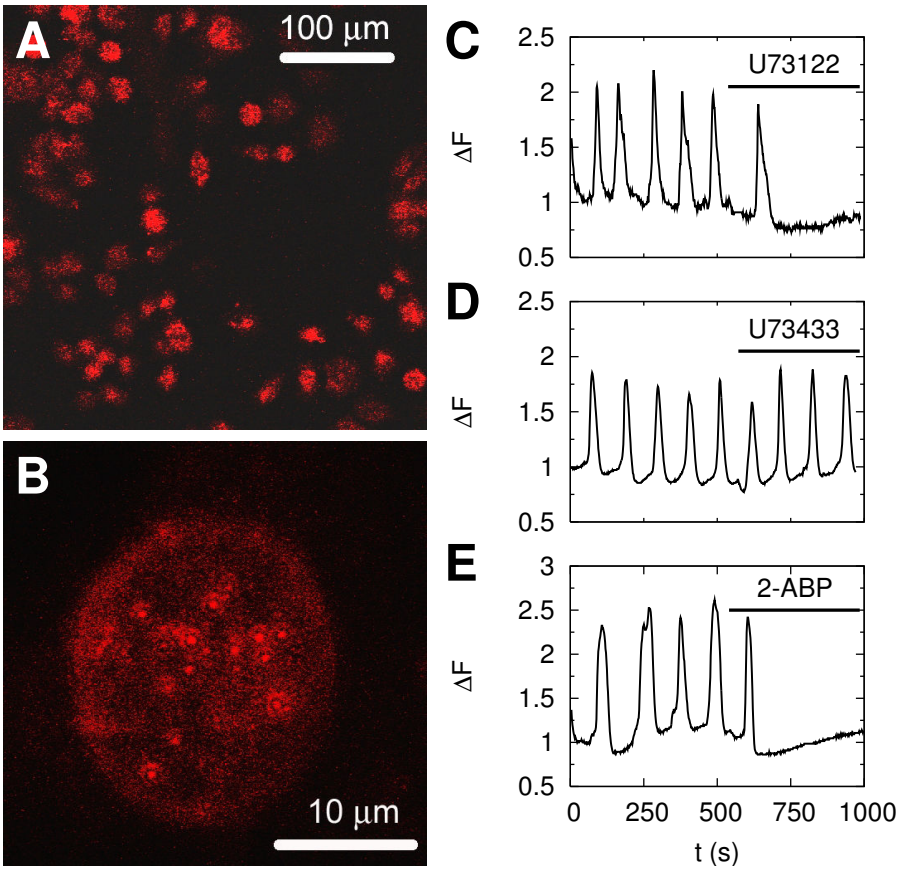

Figure A.1: IP_3R mediate spontaneous Ca^{2+} signals in PLA cells. Antibody staining of PLA cells with purified rabbit anti-IP_3R antibody visualized with anti-rabbit IgG. The results show expression of IP_3Rs in all cells (**A**) and clustering of IP_3Rs within single cells (**B**). The phospholipase C inhibitor U73122 (20 µM) immediately inhibited spontaneous Ca^{2+} oscillations (**C**), while its inactive derivative analogue U73433 (20 µM) had no effect (**D**). The IP_3R antagonist 2-APB (10 µM) abolished spontaneous Ca^{2+} oscillations (**E**).

A.2 Serial correlation coefficient

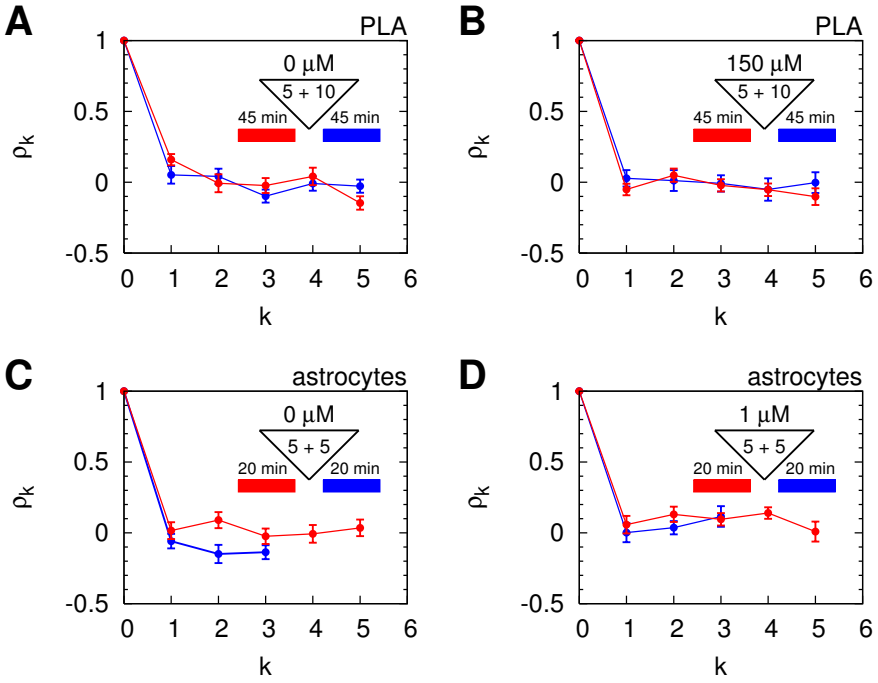

Figure A.2: Successive ISIs in PLA cells and astrocytes are not correlated. See text for details.

The figure shows correlations between the ith and $(i+k)$th ISI averaged across n time series. Correlations of the first and second measuring period of the experiments described in Figure 4.8 are shown in red and blue, respectively. The corresponding measurement durations of the experiments presented in Figure 4.8 are shown above the colored bars and the loading and wash out times are denoted within the triangles. Panel **A** shows control for PLA cells ($n_1 = 27$, $n_2 = 20$), i.e. without addition of buffer before the second measuring period. Panel **B** shows results with 150 µM EGTA-AM added before the second measurement period ($n_1 = 35$, $n_2 = 18$). Control for astrocytes ($n_1 = 36$, $n_2 = 35$) (**C**) and with 1 µM EGTA-AM added before the second measurement period ($n_1 = 33$, $n_2 = 23$) (**D**).

The vanishing serial correlation coefficient (SCC) is not an artefact of averaging. The individual SCC are close to zero and do not exceed a level of 0.5. This is shown on the representative example of 35 HEK cells in Figure A.3.

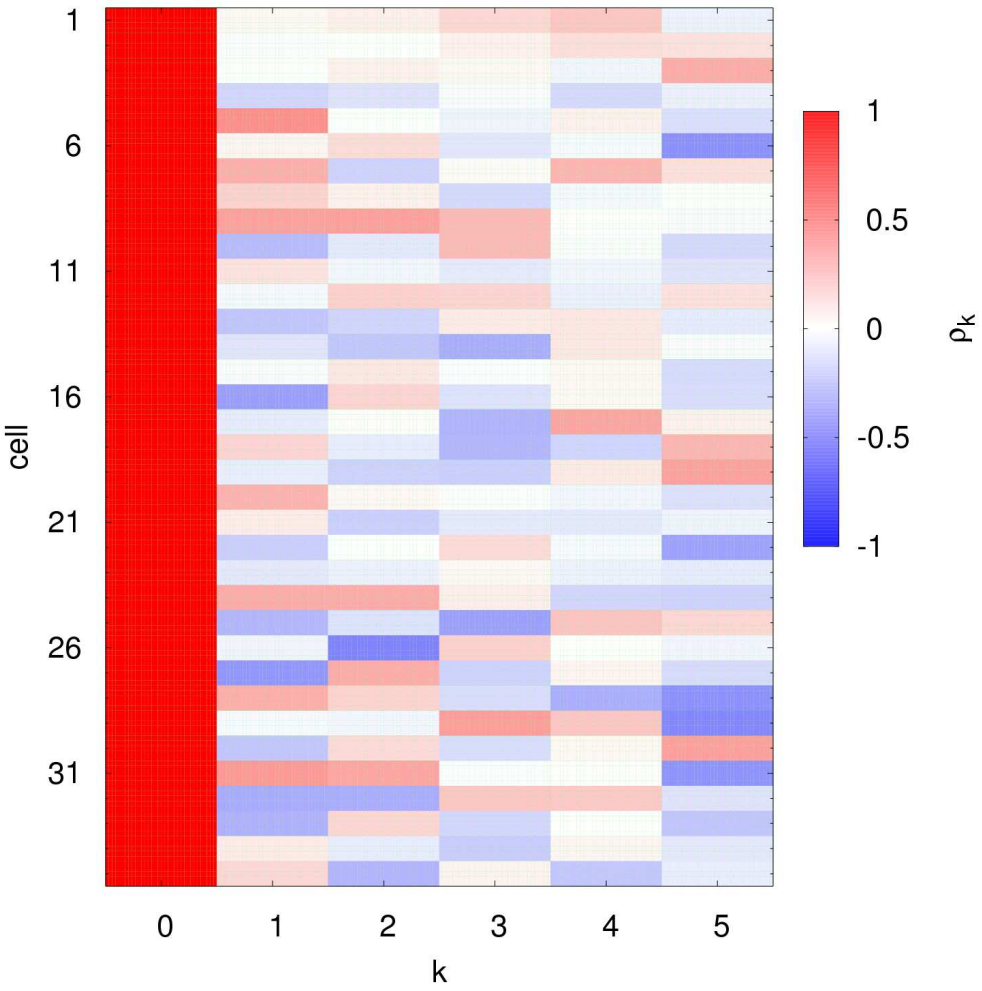

Figure A.3: Representative serial correlation coefficients of individual HEK cells.

A.3 Further σ-T_{av} relation

For supplement to the results in Figures 4.4 and 4.11 we show here another example of stimulated Ca^{2+} oscillations. The data obtained from Andrew Thomas corresponds to hepatocytes stimulated with 0.1 µM noradrenaline. The σ-T_{av} relation (A) exhibits a similar behavior like the stimulated HEK cells in Figure 4.4 indicating that stimulation leads to low regeneration rates ξ in the waiting time density (4.3).

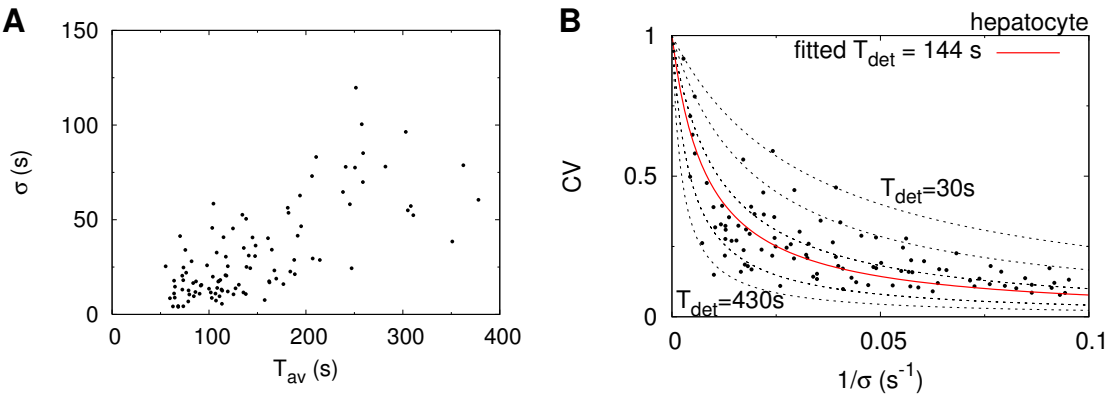

Figure A.4: σ-T_{av} relation of hepatocytes. **A**: For stimulated hepatocytes the σ-T_{av} relation exhibits a linear dependence. Analogously to stimulated HEK cells in Figure 4.4 the slope is around 0.5 indicating that they work at similar ξ values. **B**: The influence of the deterministic time leads to a decrease of the coefficient of variation CV for increasing $\lambda \approx \sigma^{-1}$ as predicted in Section 4.3.2 and shown for spontaneous oscillations in PLA cells in Figure 4.11.

The CV decreases with increasing nucleation rate λ, which is proportional to the inverse standard deviation σ, since for large λs the nucleation time is in the range of the deterministic time and subsequently leads to a more regular regime via AECR as mentioned in Section 4.3.2.

A.4 Interpretation of T_{det} within the σ-T_{av} relation

The scattering of the data points in the σ-T_{av} relation (Figures 4.4, 4.9 and A.4A) is on the one hand caused by different nucleation rates λ. On the other hand the deviations in direction of the T_{av} axis might be caused by different deterministic times T_{det}, by small ξ values in the density (4.3) or by both of them.

For astrocytes with a large ξ we expect that the scattering occurs by different T_{det}. We therefore determine T_{det} of each cell by relation (4.16) and bin cells with similar deterministic times. For each of these subpopulations we determined the subpopulation slope and find slopes very close to one for all cells as shown in Figure A.5A. With this assumption we can explain more than 96 % of the original data shown in Figure 4.4A.

If we do the same procedure for HEK cells we end up with a typical result shown in Figure A.5B. The naive use of the pure Poissonian assumption fails, since the subpopulation slope exhibit large deviations from one and explain the data in a rather artificial way.

Together with the buffer experiments and the consistency of population and shifting slopes in table 4.1, this demonstrates the different regimes for spontaneous and stimulation induced oscillations.

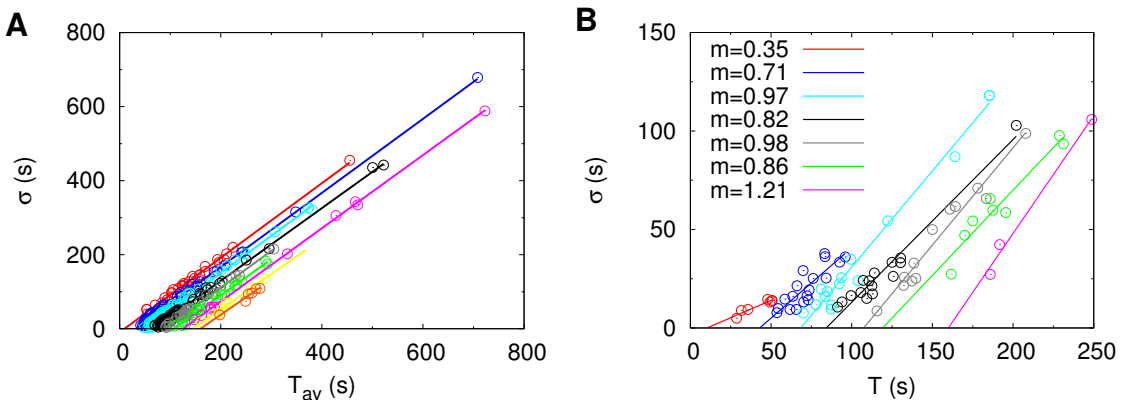

Figure A.5: Interpretation of T_{det} within the σ-T_{av} relation. Cells with similar T_{det} were put into a subpopulation and the population slope was determined by linear regression. For astrocytes (**A**) these slopes are all close to one as expected and more than 96 % of the data can be explained in that way. For HEK cells (**B**) this approach fails, since the population slopes m exhibit large variations as stated in the figure legend.

A.5 Calculation for information theory

Here we demonstrate how to derive the formulas of the information content used in Section 4.3. For the Shannon information caused by a change of the rate λ, i.e. $\lambda_1 \to \lambda_2$ of a Poisson process we rely on the integral

$$\begin{aligned} H_{\text{poi}} &= -k \int_0^\infty p(t) \log p(t)\, dt = -k \int_0^\infty \lambda e^{-\lambda t} \log\left(\lambda e^{-\lambda t}\right) dt \\ &= -k \int_0^\infty \lambda e^{-\lambda t} \log \lambda dt - k \int_0^\infty \lambda e^{-\lambda t} \log e^{-\lambda t}\, dt \\ &= -k \log \lambda \int_0^\infty \lambda e^{-\lambda t} dt + k\lambda \int_0^\infty t\lambda e^{-\lambda t}\, dt \\ &= -k \log \lambda \int_0^\infty p(t)\, dt + k\lambda \int_0^\infty t p(t)\, dt \\ &= -k \left[\log \lambda - 1\right] , \end{aligned} \tag{A.1}$$

where we used the property of the probability density $\int p(t)\, dt = 1$ and of the Poisson process $\mathrm{T}_{\text{av}} = \int_0^\infty t p(t)\, dt = 1/\lambda$. The Shannon information is thus given by

$$\mathcal{I}_{\text{poi}} = H(\lambda_1) - H(\lambda_2) = -k \left[\log \lambda_1 - 1 - \log \lambda_2 + 1\right] = k \log\left(\frac{\lambda_2}{\lambda_1}\right) . \tag{A.2}$$

The Kullback entropy of two Poisson processes $p_1(t)$ and $p_2(t)$ is given by

$$\begin{aligned} \mathcal{K}_{\text{poi}} &= k \int_0^\infty p_2 \log \frac{p_2}{p_1} dt = k \int_0^\infty p_2 \left(\log p_2 - \log p_1\right) dt \\ &= k \int_0^\infty p_2 \log p_2\, dt - k \int_0^\infty p_2 \log p_1\, dt \\ &= k \left[\log(\lambda_2) - 1\right] - k \log \lambda_1 \int_0^\infty p_2\, dt + k\lambda_1 \int_0^\infty t p_2\, dt \\ &= k \left[\log(\lambda_2) - 1 - \log(\lambda_1) + \frac{\lambda_1}{\lambda_2}\right] \\ &= k \left[\log\left(\frac{\lambda_2}{\lambda_1}\right) + \frac{\lambda_1}{\lambda_2} - 1\right] \end{aligned} \tag{A.3}$$

To determine the information divergence $\mathcal{K}_\xi$ between a pure Poisson process $p(t) = \lambda_1 e^{-\lambda_1 t}$ and a time dependent Poisson process

$$p_\xi(t) = \lambda_2 \left(1 - e^{-\xi t}\right) \exp\left[-\int_0^t \lambda_2 \left(1 - e^{-\xi t'}\right) dt'\right]$$

we set $p_2 = p(t)$ and $p_1 = p_\xi(t)$. Hence, $\mathcal{K}_\xi$ is given by

$$\begin{aligned}
\mathcal{K}_\xi &= k \int_0^\infty p \log \frac{p}{p_\xi} dt = k \int_0^\infty p \left(\log p - \log p_\xi\right) dt \\
&= k \int_0^\infty p \log p \; dt - k \int_0^\infty p \log p_\xi \; dt \\
&= k \left[\log(\lambda_1) - 1\right] \\
&\quad - k\lambda_1 \int_0^\infty e^{-\lambda_1 t} \log \left(\lambda_2 \left(1 - e^{-\xi t}\right) \exp \left[- \int_0^t \lambda_2 \left(1 - e^{-\xi t'}\right) dt' \right] \right) dt \\
&= k \left[\log(\lambda_1) - 1\right] \\
&\quad - k \log(\lambda_2) \int_0^\infty p \; dt - k\lambda_1 \int_0^\infty e^{-\lambda_1 t} \log \left(1 - e^{-\xi t}\right) \; dt \\
&\quad - k\lambda_1 \int_0^\infty e^{-\lambda_1 t} \log \left(\exp \left[- \int_0^t \lambda_2 \left(1 - e^{-\xi t'}\right) dt' \right] \right) dt \\
&= k \left[\log(\lambda_1) - 1 - \log(\lambda_2)\right] \\
&\quad - k \int_0^\infty \lambda_1 e^{-\lambda_1 t} \log \left(1 - e^{-\xi t}\right) \; dt \\
&\quad + k\lambda_1 \int_0^\infty e^{-\lambda_1 t} \int_0^t \lambda_2 \left(1 - e^{-\xi t'}\right) dt' \; dt \\
&= k \left[\log(\lambda_1) - 1 - \log(\lambda_2)\right] + k\mathcal{H}\left(\frac{\lambda_1}{\xi}\right) \\
&\quad + k \int_0^\infty \frac{\lambda_1 \lambda_2}{\xi} \left(1 - e^{-\xi t} - t\xi\right) e^{-\lambda_1 t} \; dt \\
&= k \left[\log(\lambda_1) - 1 - \log(\lambda_2) + \mathcal{H}\left(\frac{\lambda_1}{\xi}\right) \right] + k \frac{\lambda_2 \xi}{\lambda_1(\lambda_1 + \xi)} \\
&= k \left[\mathcal{H}\left(\frac{\lambda_1}{\xi}\right) + \log\left(\frac{\lambda_1}{\lambda_2}\right) + \frac{\lambda_2 \xi}{\lambda_1(\lambda_1 + \xi)} - 1 \right] ,
\end{aligned} \tag{A.4}$$

where $\mathcal{H}(x) = \gamma + \frac{d}{dx} \log \Gamma(x+1)$ denotes the continuous harmonic series with the Euler-Mascheroni constant γ and the Gamma function $\Gamma(x)$ [1].

Appendix B

Theoretical appendix

This appendix gives supporting information for the theoretical part of the thesis. We demonstrate some calculations which may disturb the readability of the main text, but are essential for the method. Moreover, some supporting results are presented.

B.1 Deriving the nondimensional reaction diffusion system

According to Smith [220] we rewrite the system in dimensionless form for further simplification. Therefore we introduce new time and length scales T and L, redefining the time $t \to t/T$ and space $r \to r/L$, and we re-scale the concentrations by

$$c = \frac{[Ca^{2+}]}{K},\ b = \frac{[B]}{[B]_T},\ b_i = \frac{[B_i]}{[B_i]_T},\ e = \frac{[E]}{K_E}. \tag{B.1}$$

Thus, the RDS (6.30) can be rewritten as

$$\begin{aligned}
\frac{1}{Tk^+[B]_T}\frac{\partial c}{\partial t} &= \frac{D_{Ca}}{L^2k^+[B]_T}\nabla^2 c - bc + (1-b) + \frac{\sigma_l}{k^+[B]_T}(\bar{e}-c) - \frac{\sigma_p}{k^+[B]_T}c \\
&\quad + \frac{[B_i]_T k_i^-}{[B]_T k^-}\left(1 - b_i - b_i c\frac{K}{K_i}\right) + \frac{\sigma}{L^3k^-[B]_T}\delta(\boldsymbol{r}-\boldsymbol{r}_0) && \text{(B.2a)} \\
\frac{1}{Tk^-}\frac{\partial b}{\partial t} &= \frac{D_B}{L^2k^-}\nabla^2 b - bc + (1-b) && \text{(B.2b)} \\
\frac{[B_i]_T}{T[B]_T k^-}\frac{\partial b_i}{\partial t} &= \frac{[B_i]_T k_i^-}{[B]_T k^-}\left(1 - b_i - b_i c\frac{K}{K_i}\right)\ . && \text{(B.2c)}
\end{aligned}$$

To obtain a dimensionless system we choose

$$\frac{D_{Ca}}{L^2 k^+ [B]_T} = 1 \Rightarrow L^2 = \frac{D_{Ca}}{k^+ [B]_T} \tag{B.3a}$$

$$\frac{1}{T k^+ [B]_T} = 1 \Rightarrow T = \frac{1}{k^+ [B]_T} \tag{B.3b}$$

defining the diffusion length L and the reaction time T. Similarly the remaining quantities in (B.2) can be subsumed in dimensionless parameters shown in table 6.3. Thus Equation (B.2) takes the form

$$\frac{\partial c}{\partial t} = \nabla^2 c - (bc + b - 1) - \epsilon_R \left(b_i c \kappa + b_i - 1\right) - \sigma_p' c + \sigma' \delta(\boldsymbol{r} - \boldsymbol{r}_0) \tag{B.4a}$$

$$\epsilon_\tau \frac{\partial b}{\partial t} = d_\epsilon \nabla^2 b - (bc + b - 1) \tag{B.4b}$$

$$\epsilon_\tau^i \frac{\partial b_i}{\partial t} = -\epsilon_R \left(b_i c \kappa + b_i - 1\right) \ . \tag{B.4c}$$

In order to solve these equations analytically, we linearize them around the initial state, which is assumed to be the resting state. The resting state corresponds to the equilibrium, where all channels are closed, Ca^{2+} and buffers are homogeneously distributed and in equilibrium. The scaled concentrations of the initial condition are given by

$$c_0 = \frac{[Ca^{2+}]_0}{K}, \quad b_0 = \frac{1}{c_0 + 1}, \quad b_{i,0} = \frac{1}{c_0 \kappa + 1}, \tag{B.5a}$$

where K is the dissociation constant of the mobile buffer and $\kappa = \frac{K}{K_i}$ denotes the ratio of the dissociation constants of the mobile and immobile buffer, respectively. Applying a small perturbation by setting $c = c_0 + \delta c$, $\bar{e} = \bar{e}_0 + \delta \bar{e}$, $b = b_0 + \delta b$ and $b_i = b_{i,0} + \delta b_i$ into Equations (B.4), we get

$$\begin{aligned} \frac{\partial \delta c}{\partial t} = \nabla^2 \delta c - \Big[& (1 + c_0)\delta b + \epsilon_R (1 + \kappa c_0)\delta b_i + (b_0 + b_{i,0}\epsilon_R \kappa + \sigma_p' - \sigma_l')\delta c \\ & + \delta c \delta b + \epsilon_R \kappa \delta c \delta b_i \Big] + \sigma' \delta(\boldsymbol{r} - \boldsymbol{r}_0) + \sigma_l' \frac{\delta \bar{e}}{\kappa_E} \end{aligned} \tag{B.6a}$$

$$\epsilon_\tau \frac{\partial \delta b}{\partial t} = d_\epsilon \nabla \delta b - \left[(1 + c_0)\delta b + b_0 \delta c\right] - \delta c \delta b \tag{B.6b}$$

$$\epsilon_\tau^i \frac{\partial b_i}{\partial t} = -\epsilon_R \left[(1 + \kappa c_0)\delta b_i + b_{i,0} \kappa \delta c\right] - \epsilon_R \kappa \delta c \delta b_i \ . \tag{B.6c}$$

Here, the time derivatives of the constant parts vanish. We now neglect all nonlinear terms in (B.6) and end up with the linearized dimensionless system of the form

$$\frac{\partial \delta c}{\partial t} = \nabla^2 \delta c - \Big[(1+c_0)\delta b + \epsilon_R(1+\kappa c_0)\delta b_i + (b_0 + b_{i,0}\epsilon_R\kappa + \sigma_p' - \sigma_l)\delta c\Big] + \sigma'\delta(\boldsymbol{r}-\boldsymbol{r}_0) + \sigma_l'\frac{\delta\bar{e}}{\kappa_E} \tag{B.7a}$$

$$\epsilon_\tau \frac{\partial \delta b}{\partial t} = d_\epsilon \nabla^2 \delta b - [(1+c_0)\delta b + b_0 \delta c] \tag{B.7b}$$

$$\epsilon_\tau^i \frac{\partial b_i}{\partial t} = -\epsilon_R\left[(1+\kappa c_0)\delta b_i + b_{i,0}\kappa\delta c\right] \ . \tag{B.7c}$$

For more convenient reading we drop the δs of the concentrations, and after some simple algebra we find Equation (6.31).

B.2 Influence of linearization

Kajetan Bentele analyzed in his diploma thesis the influence of the buffer linearization. Therefore he solved the full nonlinear and the linearized problem numerically. He took only one mobile buffer into account and neglected pumps and leak fluxes leading to the equations:

$$\frac{\partial c}{\partial t} = \nabla_r^2 c - (bc + b - 1) + \sigma' \frac{\Theta(a-r)}{\frac{4}{3}\pi a^3} \tag{B.8a}$$

$$\frac{\partial b}{\partial t} = d\nabla_r^2 b - \frac{1}{\epsilon_\tau}(bc + b - 1) \ , \tag{B.8b}$$

where Θ denotes here the Heavy side function, since he assumed a spherical source with radius a. For simplicity, he chose spherical symmetry and assumed Dirichlet boundary conditions in order to obtain stationary solutions for $t \to \infty$. The nondimensional parameters are analogously defined as in table 6.2 by $d = D_B/D_{Ca}, \epsilon_\tau = [B]_T/K = [B]_T k^+/k^-$ and $\sigma' = \sigma/(L^3 k^- [B]_T)$, the timescale was chosen to be $T = (k^+[B]_T)^{-1}$ and the length scale according to $L^2 = D_{Ca}T$.

He analyzed the stationary solution of the nonlinear equation and its linearized form for different parameter values numerically. A representative example is shown in Figure B.1 where he compared the nonlinear equation (red) with the linearized form (green) and with a pure diffusion equation which corresponds to vanishing buffer concentrations. Near to the source located at the origin, the three situations only exhibit small differences, since the buffer is saturated. For increasing distance from the source r, we observe smaller Ca^{2+} concentrations for the system with non vanishing buffer concentrations, as expected. The linearized system exhibits a larger decrease of c from the pure diffusion equation than the nonlinear system does. Hence, the linearization overestimates the influence of buffers.

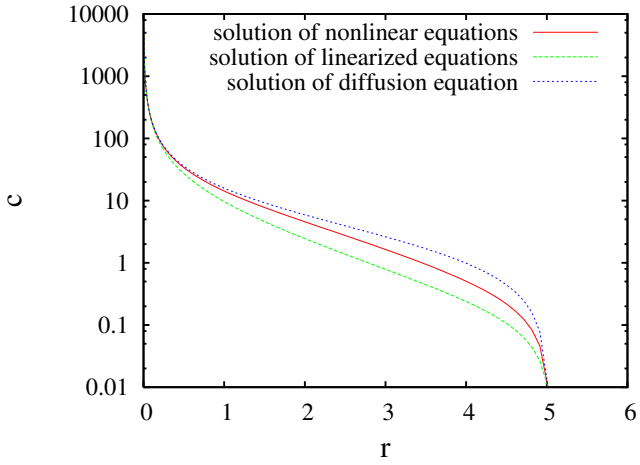

Figure B.1: Linearization overestimates the influence of buffers as can be seen by the larger deviation of the stationary concentration of the linear system from the pure diffusion equation compared to the nonlinear equation. (Figure kindly provided by K. Bentele.)

B.3 More detailed derivation of the Green's dyadic

Here we demonstrate how to derive the Green's dyadic of the RDS (6.31) in more detail. We start with RDS (6.31) in matrix form,

$$\left[\begin{pmatrix}1&0&0\\0&d&0\\0&0&0\end{pmatrix}\nabla^2-\begin{pmatrix}1&0&0\\0&\epsilon_\tau&0\\0&0&\epsilon_\tau^i\end{pmatrix}\frac{\partial}{\partial t}+\begin{pmatrix}a_{11}&a_{12}&a_{13}\\a_{21}&a_{22}&0\\a_{31}&0&a_{33}\end{pmatrix}\right]\begin{pmatrix}c\\b\\b_i\end{pmatrix}=-\begin{pmatrix}f_c(\mathbf{r},t)\\f_{b_m}(\mathbf{r},t)\\f_{b_i}(\mathbf{r},t)\end{pmatrix}. \tag{B.9}$$

In order to solve this system of coupled PDEs by means of coupled Green's functions or a Green's matrix $\mathbf{G}$, we have to solve analogously to Equation (6.6) the following problem,

$$\begin{aligned}\mathbf{LG}&=\begin{pmatrix}\nabla^2-\frac{\partial}{\partial t}+a_{11}&a_{12}&a_{13}\\a_{21}&d_\epsilon\nabla^2-\epsilon_\tau\frac{\partial}{\partial t}+a_{22}&0\\a_{31}&0&-\epsilon_\tau^i\frac{\partial}{\partial t}+a_{33}\end{pmatrix}\begin{pmatrix}g_{11}&g_{12}&g_{13}\\g_{21}&g_{22}&g_{23}\\g_{31}&g_{32}&g_{33}\end{pmatrix}\\&=-\frac{1}{r'^2\sin\theta'}\delta(r-r')\delta(\theta-\theta')\delta(t-t')\begin{pmatrix}1&0&0\\0&1&0\\0&0&1\end{pmatrix}.\end{aligned} \tag{B.10}$$

After Laplace transformation we have

$$\begin{aligned}\tilde{\mathbf{L}}\tilde{\mathbf{G}}&=\begin{pmatrix}\nabla^2-s+a_{11}&a_{12}&a_{13}\\a_{21}&d_\epsilon\nabla^2-s\epsilon_\tau+a_{22}&0\\a_{31}&0&-s\epsilon_\tau^i+a_{33}\end{pmatrix}\begin{pmatrix}\tilde{g}_{11}&\tilde{g}_{12}&\tilde{g}_{13}\\\tilde{g}_{21}&\tilde{g}_{22}&\tilde{g}_{23}\\\tilde{g}_{31}&\tilde{g}_{32}&\tilde{g}_{33}\end{pmatrix}\\&=-\frac{1}{r'^2\sin\theta'}\delta(r-r')\delta(\theta-\theta')e^{-st'}\begin{pmatrix}1&0&0\\0&1&0\\0&0&1\end{pmatrix}.\end{aligned} \tag{B.11}$$

With the same boundary conditions for all species, the system (B.9) can be solved by the ansatz

$$\begin{pmatrix} \tilde{g}_{11} & \tilde{g}_{12} & \tilde{g}_{13} \\ \tilde{g}_{21} & \tilde{g}_{22} & \tilde{g}_{23} \\ \tilde{g}_{31} & \tilde{g}_{32} & \tilde{g}_{33} \end{pmatrix} = \sum_{l=0,p=0}^{\infty} \begin{pmatrix} \alpha_{11}^{(lp)} & \alpha_{12}^{(lp)} & \alpha_{13}^{(lp)} \\ \alpha_{21}^{(lp)} & \alpha_{22}^{(lp)} & \alpha_{23}^{(lp)} \\ \alpha_{31}^{(lp)} & \alpha_{32}^{(lp)} & \alpha_{33}^{(lp)} \end{pmatrix} \psi_{lp}(r,\theta), \tag{B.12}$$

where $\psi_{lp}(r,\theta)$ is the solution for the Helmholtz Equation (6.10), which respects the appropriate boundary conditions by the determination of the corresponding λs. By inserting (B.12) into equation (B.11) we get

$$\begin{aligned} \sum_{l=0,p=0}^{\infty} \begin{pmatrix} -\lambda_{lp}^2 - s + a_{11} & a_{12} & a_{13} \\ a_{21} & -d_\epsilon \lambda_{lp}^2 - s\epsilon_\tau + a_{22} & 0 \\ a_{31} & 0 & -s\epsilon_\tau^i + a_{33} \end{pmatrix} \begin{pmatrix} \alpha_{11}^{(lp)} & \alpha_{12}^{(lp)} & \alpha_{13}^{(lp)} \\ \alpha_{21}^{(lp)} & \alpha_{22}^{(lp)} & \alpha_{23}^{(lp)} \\ \alpha_{31}^{(lp)} & \alpha_{32}^{(lp)} & \alpha_{33}^{(lp)} \end{pmatrix} \psi_{lp} \\ = -\frac{1}{r'^2 \sin\theta'} \delta(r-r')\delta(\theta-\theta') e^{-st'} \begin{pmatrix} 1 & 0 & 0 \\ 0 & 1 & 0 \\ 0 & 0 & 1 \end{pmatrix}. \end{aligned} \tag{B.13}$$

By applying the integral operators (6.14) on both sides we find the equations to determine the coefficients $\alpha_{ij}^{(lp)}$

$$\begin{aligned} \begin{pmatrix} -\lambda_{mq}^2 - s + a_{11} & a_{12} & a_{13} \\ a_{21} & -d_\epsilon \lambda_{mq}^2 - s\epsilon_\tau + a_{22} & 0 \\ a_{31} & 0 & -s\epsilon_\tau^i + a_{33} \end{pmatrix} \begin{pmatrix} \alpha_{11}^{(mq)} & \alpha_{12}^{(mq)} & \alpha_{13}^{(mq)} \\ \alpha_{21}^{(mq)} & \alpha_{22}^{(mq)} & \alpha_{23}^{(mq)} \\ \alpha_{31}^{(mq)} & \alpha_{32}^{(mq)} & \alpha_{33}^{(mq)} \end{pmatrix} \\ = -\frac{\psi_{mq}(r',\theta') e^{-st'}}{\mathcal{N}(m)\mathcal{N}(\lambda_{mq})} \begin{pmatrix} 1 & 0 & 0 \\ 0 & 1 & 0 \\ 0 & 0 & 1 \end{pmatrix}. \end{aligned} \tag{B.14}$$

Thus α is given by

$$\begin{aligned} &\begin{pmatrix} \alpha_{11}^{(mq)} & \alpha_{12}^{(mq)} & \alpha_{13}^{(mq)} \\ \alpha_{21}^{(mq)} & \alpha_{22}^{(mq)} & \alpha_{23}^{(mq)} \\ \alpha_{31}^{(mq)} & \alpha_{32}^{(mq)} & \alpha_{33}^{(mq)} \end{pmatrix} = \\ &\frac{\psi_{mq}(r',\theta') e^{-st'}}{\mathcal{N}(m)\mathcal{N}(\lambda_{mq})} \begin{pmatrix} \lambda_{mq}^2 + s - a_{11} & -a_{12} & -a_{13} \\ -a_{21} & d_\epsilon \lambda_{mq}^2 + s\epsilon_\tau - a_{22} & 0 \\ -a_{31} & 0 & s\epsilon_\tau^i - a_{33} \end{pmatrix}^{-1}. \end{aligned} \tag{B.15}$$

For the inverse Laplace transform we use the property of the matrix inversion

$$\mathbf{M}^{-1} = \frac{1}{|\mathbf{M}|} \mathrm{adj}(\mathbf{M}) \tag{B.16}$$

by determining the zeros of $|\mathbf{M}|$ leading to a cubic equation for s. Thus

$$\begin{pmatrix} g_{11} & g_{12} & g_{13} \\ g_{21} & g_{22} & g_{23} \\ g_{31} & g_{32} & g_{33} \end{pmatrix} = \sum_{l=0,p=1}^{\infty} \sum_{i=1}^{3} \frac{\mathrm{adj}(\mathbf{M}_{lp})}{\partial|\mathbf{M}_{lp}|/\partial s|_{s=s_i}} \frac{1}{\mathcal{N}(l)\mathcal{N}(\lambda_{lp})} \frac{J_{l+1/2}(\lambda_{lp} r')}{r'^{1/2}} \times$$
$$P_l(\cos\theta') e^{-s_i t'} \frac{J_{l+1/2}(\lambda_{lp} r)}{r^{1/2}} P_l(\cos\theta) e^{s_i t} + \frac{3}{4\pi b^3} e^{s_i (t-t')} \frac{\mathrm{adj}(\mathbf{M}_{00})}{\partial|\mathbf{M}_{00}|/\partial s|_{s=s_i}}. \tag{B.17}$$

With a source density according to

$$\boldsymbol{\varrho}(r,\theta,t) = \sigma(t) \frac{\delta(r-r_c)\delta(\theta)}{r^2 \sin\theta} \begin{pmatrix} 1 \\ 0 \\ 0 \end{pmatrix} \tag{B.18}$$

the response due to the influx of a single cluster is given by

$$\begin{pmatrix} \delta c \\ \delta b \\ \delta b_i \end{pmatrix} = \sum_{l=0,p=1}^{\infty} \frac{J_{l+1/2}(\lambda_{lp} r)}{r^{1/2}} P_l(\cos\theta) \begin{pmatrix} \chi_1^{(lp)} \\ \chi_2^{(lp)} \\ \chi_3^{(lp)} \end{pmatrix}(t) + \begin{pmatrix} \chi_1^{(00)} \\ \chi_2^{(00)} \\ \chi_3^{(00)} \end{pmatrix}(t) \tag{B.19}$$

with

$$\begin{pmatrix} \chi_1^{(lp)} \\ \chi_2^{(lp)} \\ \chi_3^{(lp)} \end{pmatrix}(t) = \sum_{i=1}^{3} \frac{1}{\mathcal{N}(l)\mathcal{N}(\lambda_{lp})} \frac{J_{l+1/2}(\lambda_{lp} r_c)}{r_c^{1/2}} \int_0^t dt' \sigma(t') e^{s_i (t-t')} \frac{\mathrm{adj}(\mathbf{M}_{lp})}{\partial|\mathbf{M}_{lp}|/\partial s|_{s=s_i}} \begin{pmatrix} 1 \\ 0 \\ 0 \end{pmatrix} \tag{B.20}$$

$$\begin{pmatrix} \chi_1^{(00)} \\ \chi_2^{(00)} \\ \chi_3^{(00)} \end{pmatrix}(t) = \sum_{i=1}^{3} \frac{3}{2b^3} \int_0^t dt' \sigma(t') e^{s_i (t-t')} \frac{\mathrm{adj}(\mathbf{M}_{00})}{\partial|\mathbf{M}_{00}|/\partial s|_{s=s_i}} \begin{pmatrix} 1 \\ 0 \\ 0 \end{pmatrix}, \tag{B.21}$$

where we used $P_l(\cos 0) = P_l(1) = 1$. If the source is calculated at some arbitrary point (r_c, θ_c, ϕ_c), the solution can be obtained by rotating the coordinate system such that the source is located at $(r_c, 0, 0)$ as described in the main text.

B.4 Convergency

The convergency of the spectral solution is a crucial requirement of the GCM algorithm. The contribution of the different modes shown in Figure B.2A might indicate a slow convergency of the solution.

But for the solution this product is multiplied with exponentials of the time constants $s_{l,p}$ for each species i and the product of $J_{l+1/2}(\lambda_{l,p} r_c) P_l(\cos\theta_c)$ from the

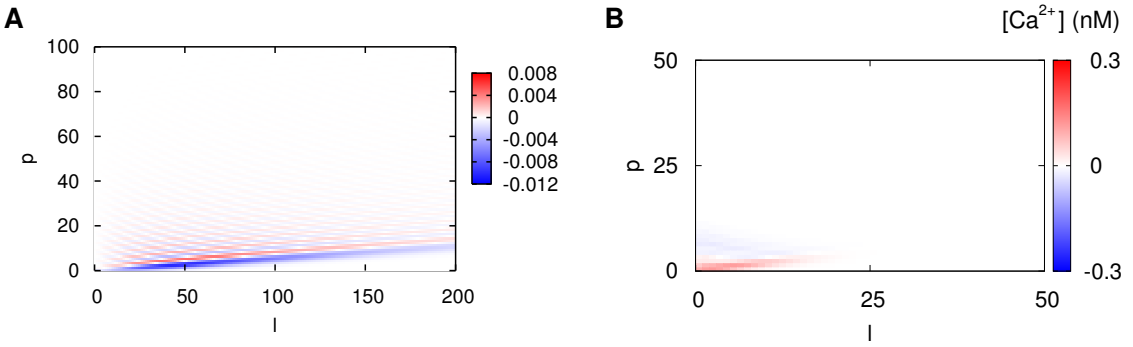

Figure B.2: Convergency of the analytical solution. **A**: Spectral contribution of products of Bessel functions $J_{l+1/2}(\lambda_{l,p}r)$ and Legendre polynomial $P_l(\theta)$ to the solution in dependence on the modes l and p, for $r = 6$ µm and $\theta = 0.1$. **B**: Spectral contribution of the solution for a cell with $R_{cell} = 10$ µm. The contribution to the Ca^{2+} concentration is shown in dependence on the mode number. For typical times of $t = 0.02$ ms and a distance of $d = 0.5$ µm , 30 modes in l and p are enough for convergency.

source. This is shown in Figure B.2B for the Ca^{2+} concentration at $r = 0.6\,R_{cell}$, $\Theta = 0.3$ in a distance of 0.5 µm of the source after $t = 0.02$ ms. For longer times and larger distances the number of modes needed for convergency decreases faster. Hence, for clusters which are set within a sphere with radius $r_{conv} = 0.8\,R_{cell}$ in the cell, 30 modes for l and p are sufficient for convergency.

B.5 Technical details of the computing cluster *Dirac*

The cluster *Dirac* is a compute cluster at the Helmholtz Center Berlin (Hahn-Meitner Institute). It consists of a control unit with two 1.8 GHz Dual-Core 64-Bit AMD 265 CPUs and two GB RAM. The computing nodes (node1–node6) are each equipped with four 1.8 GHz Dual-Core 64-Bit AMD 865 CPUs and 16 GB RAM. The cluster is configured with *OpenSuse 10.1 (64 bit)*. The nodes are connected by 100 Mbit/s ethernet cables. This means that communication between 8 processors is fast, since they are located on the same board. Communication of more than eight processors must pass the bottleneck of the ethernet communication and is only useful for jobs with very high computational requirements. Furthermore, it is reasonable to use multiples of eight for the number of processors. Note, that MPI can start more than one process on one processor.

Bibliography

[1] M. Abramowitz and A. Stegun. *Handbook of Mathematical Functions*. Dover Publication, New York, 1970.

[2] C.E. Adkins and C.W. Taylor. Lateral inhibition of Inositol 1,4,5-trisphosphate receptors by cytosolic Ca^{2+}. *Current Biology*, 9:1115–1118, 1999.

[3] F. Aguado, J.F. Espinosa-Parrilla, M. Carmona, and E. Soriano. Neuronal activity regulates correlated network properties of spontaneous calcium transients in astrocytes in situ. *The Journal of Neuroscience*, 22(21):9430–9444, 2002.

[4] B. Alberts, D. Bray, J. Lewis, M.Raff, K.Roberts, and J.D. Watson. *Molecular Biology of the Cell*. Garland Publishing, Inc., New York & London, 3rd edition, 1994.

[5] A. Alfonsi, E. Cancès, G. Turinici, B. Di Ventura, and W. Huisinga. Exact simulation of hybrid stochastic and deterministic models for biochemical systems. *INRIA Rapport de Recherche, Thèmes NUM et BIO*, 5435, 2004.

[6] C.M. Anderson, J.P. Bergher, and R.A. Swanson. Atp-induced atp release from astrocytes. *J. Neurochem.*, 88:246–256, 2004.

[7] C.M. Anderson and M. Nedergaard. Astrocyte-mediated control of cerebral microcirculation. *Trends Neurosci.*, 26:340–344, 2003.

[8] A. Araque, G. Carmignoto, and P.G. Haydon. Dynamic signaling between astrocytes and neurons. *Annu.Rev.Physiol.*, 63:795–813, 2001.

[9] A. Araque, R.T. Doyle, and P.G. Haydon. Snare protein-dependent glutamate release from astrocytes. *J. Neurosci.*, 20:666–673, 2000.

[10] A. Araque, V. Parpura, R.P. Sanzgiri, and P.G. Haydon. Tripartite synapses: glia, the unacknowledged partner. *Trends Neurosci.*, 22:208–215, 1999.

[11] F.T. Arecci and A. Politi. Transient fluctuations in the decay of an unstable state. *PRL*, 45:1219, 1970.

[12] A. Atri, J. Amundson, D. Clapham, and J. Sneyd. A single pool model for intracellular calcium oscillations and waves in the Xenopus laevis oocyte. *Biophys.J.*, 65:1727–1739, 1993.

[13] J.V. Beck, K.D: Cole, A. Haji-Sheikh, and B. Litkouhi. *Heat Conduction Using Green's Function.* Series in Computational and physical processes, New York, 1992.

[14] K. Bentele and M. Falcke. Quasi-steady approximation for ion channel currents. *Biophys.J.*, 93:2597–2608, 2007.

[15] M. Berridge. Elementary and global aspects of calcium signalling. *J.Physiol.*, 499:291–306, 1997.

[16] M.J. Berridge. Calcium oscillations. *J.Biol.Chem.*, 265(17):9583–9586, 1990.

[17] M.J. Berridge, M.D. Bootman, and P. Lipp. Calcium - a life and death signal. *Nature*, 395:645–648, 1998.

[18] M.J. Berridge, P. Lipp, and M.D. Bootman. The versatility and universality of calcium signalling. *Nature Rev. Mol. Cell Biol.*, 1:11–22, 2000.

[19] I. Bezprozvanny. The inositol 1,4,5-trisphosphate receptors. *Cell Calcium*, 38:261–272, 2005.

[20] I. Bezprozvanny, J. Watras, and B.E. Ehrlich. Bell-shaped calcium-response curves of Ins(1,4,5)P_3- and calcium-gated channels from endoplasmatic reticulum of cerebellum. *Nature*, 351:751–754, 1991.

[21] P. Bezzi, G. Carmignoto, and L. Pasti. Prostaglandins stimulate calcium-dependent glutamate release in astrocytes. *Nature*, 391:281–285, 1998.

[22] D. Boehning and S.K. Joseph. Functional properties of recombinant type I and type III Inositol 1,4,5-trisphosphate receptor isoforms expressed in COS-7 cells. *J.Biol.Chem.*, 275(28):21492–21499, 2000.

[23] M. Bootman, M. Berridge, and P. Lipp. Cooking with calcium: The recipes for composing global signals from elementary events. *Cell*, 91:367–373, 1997.

[24] M. Bootman, E. Niggli, M. Berridge, and P. Lipp. Imaging the hierarchical Ca^{2+} signalling in HeLa cells. *J.Physiol*, 499(2):307–314, 1997.

[25] M.D. Bootman, T.J. Collins, C.M. Peppiatt, L.S. Prothero, L. MacKenzie, P. DeSmet, M. Travers, S.C. Tovey, J.T. Seo, M.J. Berridge, F. Ciccolini, and P. Lipp. Calcium signalling - an overview. *Seminars in Cell & Developmental Biology*, 12(1):3–10, 2001.

[26] M.D. Bootman, P. Lipp, and M.J. Berridge. The organisation and functions of local Ca^{2+} signals. *J.Cell Science*, 114(12):2213–2222, 2002.

[27] M.D. Bootman, L. Missiaen, J.B. Parys, H. De Smedt, and R. Casteels. Control of inositol 1,4,5-trisphosphate-induced Ca^{2+} release by cytosolic Ca^{2+}. *Biochem.J.*, 306(2):445–451, 1995.

[28] D.S. Bredt and S.H. Snyder. Nitric oxide mediates glutamate-linked enhancement of cgmp levels in the cerebellum. *PNAS*, 86:9030–9033, 1989.

[29] S.E. Burk, J. Lytton, D.H. MacLennan, and G.E. Shull. cdna cloning, functional expression, and mrna tissue distribution of a third organellar Ca^{2+}-pump. *J.Biol.Chem.*, 264:18561–18568, 1989.

[30] L. Cai, C.K. Dalal, and M.B. Elowitz. Frequency-modulated nuclear localization bursts coordinate gene regulation. *Nature*, 455:485–490, 2008.

[31] N. Callamaras and I. Parker. Phasic characteristics of elementary Ca^{2+} release sites underlies quantal responses to IP_3. *The EMBO Journal*, 19(14):3608–3617, 2000.

[32] A.M. Cameron, J.P. Steiner, and A.J. Roskams. Calcineurin associated with the inositol 1,4,5-trisphosphate receptor-fkbp12 complex modulates Ca^{2+} flux. *Cell*, 83:463–472, 1995.

[33] E. Carafoli. Calcium signaling: A tale for all seasons. *PNAS*, 99:1115–1122, 2002.

[34] M. Chalmers, M.J. Schell, and P. Thorn. Agonist-evoked inositol trisphosphate receptor IP_3R clustering is not dependent on changes in the structure of the endoplasmic reticulum. *Biochem.J.*, 394(1):57–66, 2006.

[35] A.C. Charles. Glia-neuron intercellular calcium signalling. *Dev.Neurosci.*, 16:196–206, 1994.

[36] A.C. Charles, E.R. Dirksen, J.E. Merrill, and M.J. Sanderson. Intercellular signalling in glial cells: calcium waves and oscillations in response to mechanical stimulation and glutamate. *Neuron*, 6:983–992, 1991.

[37] H. Cheng, W.J. Lederer, and M.B. Cannel. Calcium-sparks: elementary events underlying excitation-contraction coupling in heart muscle. *Science*, 262:740–744, 1993.

[38] G.C. Churchill, J.S. O'Neil, R. Masgrau, S. Patel, J.M. Thomas, A.A. Genazzani, and A. Galione. Sperm deliver a new second messenger: NAADP. *Curr.Biol.*, 13:125–128, 2003.

[39] S. Coombes and Y. Timofeeva. Sparks and waves in a stochastic fire-diffuse-fire model of Ca^{2+} release. *Phys.Rev.E*, 68:021915, 2003.

[40] M.L. Cotrina, J.H. Lin, A. Alves-Rodrigues, S. Liu, J. Li, H. Azmi-Ghadimi, J. Kang, and M. Nedergaard. Connexins regulate calcium signaling by controling ATP release. *Proc.Nat.Acad.Sci.USA*, 95(26):15735–15740, 1998.

[41] D.R. Cox. *Renewal Theory*. Chapman and Hall, London, 1967.

[42] D.R. Cox and V. Isham. *Point Processes*. Chapman and Hall, London, 1980.

[43] D.R. Cox and L. Lewis. *The Statistical Analysis of Series and Events*. Wiley, New York, 1966.

[44] J. Crank. *The Mathematics of Diffusion*. Oxford Press, London, 1956.

[45] M.C. Cross and P.C. Hohenberg. Pattern formation outside of equilibrium. *Rev. Mod. Phys.*, 65(3):851, Jul 1993.

[46] V. Crunelli, K.L. Blethyn, and D.W. Cope. Novel neuronal and astrocytic mechanisms in thalamocortical loop dynamics. *Philos. Trans. R. Soc. Lond. B Biol. Sci.*, 357:1675–1693, 2002.

[47] A. Demuro and I. Parker. Optical single-channel recording: imaging Ca^{2+} flux through individual N-type voltage-gated channels expressed in Xenopus oocytes. *Cell Calcium*, 34(6):499–509, 2003.

[48] G.W. DeYoung and J. Keizer. A single-pool inositol 1,4,5-trisphosphate-receptor-based model for agonist-stimulated oscillations in Ca^{2+} concentration. *Proc.Natl.Acad.Sci USA*, 89:9895–9899, 1992.

[49] S. Schumacher D.H. Mauch, K. Nagler and F.W. Pfrieger. Cns synaptogenesis promoted by glia-derived cholesterol. *Science*, 294:1354–1357, 2001.

[50] L. Dode, K. Van Baelen, F. Wuytack, and W.L. Dean. Low temperature molecular adaptation of the skeletal muscle sarco(endo)plasmic reticulum Ca^{2+}-atpase 1 (serca 1) in the wood frog (rana sylvatica). *J. Biol. Chem.*, 276:3911–3919, 2001.

[51] R.E. Dolmetsch, K. Xu, and R.S. Lewis. Calcium oscillations increase the efficiency and specificity of gene expression. *Nature*, 392:933–936, 1998.

[52] G. Dupont, A. Abou-Lovergne, and L. Combettes. Stochastic aspects of oscillatory calcium dynamics in hepatocytes. *Biophys. J.*, 95:2193–2202, 2008.

[53] G. Dupont and A. Goldbeter. One-pool model for Ca^{2+} oscillations involving Ca^{2+} and inositol 1,4,5-trisphosphate as co-agonists for Ca^{2+} release. *Cell Calcium*, 14:311–322, 1993.

[54] W. Ebeling, H. Engel, and H. Herzel. *Selbstorganisation in der Zeit*. Akademie-Verlag Berlin, 1990.

[55] W. Ebeling and R. Feistel. *Prinzipien der Evolution*. Spectrum, Berlin, 1994.

[56] M. Eddleston and L. Mucke. Molecular profile of reactive astrocytes–implications for their role in neurologic disease. *Neuroscience*, 54:15–36, 1993.

[57] T.A. Engel, L. Schimansky-Geier, A.V.M. Herz, S. Schreiber, and I.A. Erchova. Subthreshold membrane-potential resonances shape spike-train patterns in the entorhinal cortex. *J. Neurophysiol.*, in press, 2008.

[58] M. Falcke. Buffers and oscillations in intracellular Ca^{2+} dynamics. *Biophys.J.*, 84(1):28–41, 2003.

[59] M. Falcke. Deterministic and stochastic models of intracellular Ca^{2+} waves. *New Journal of Physics*, 5:96.1–96.28, 2003.

[60] M. Falcke. On the role of stochastic channel behavior in intracellular Ca^{2+} dynamics. *Biophys.J.*, 84(1):42–56, 2003.

[61] M. Falcke. Period distributions of intracellular Ca^{2+} oscillations. *Proceedings of the Fourth International Workshop on Bioinformatics and Systems Biology, May 31 - June 3, 2004, Kyoto, Japan*, Short papers, 2004.

[62] M. Falcke. Reading the patterns in living cells - the Physics of Ca^{2+} signaling. *Advances in Physics*, 53(3):255–440, 2004.

[63] M. Falcke, H. Engel, and M. Neufeld. Cluster formation, standing waves, and stripe patterns in oscillatory active media with local and global coupling. *Phys.Rev.E*, 52(1):763–771, 1995.

[64] M. Falcke, J.L. Hudson, P. Camacho, and J.D. Lechleiter. Impact of mitochondrial Ca^{2+} cycling on pattern formation and stability. *Biophys.J.*, 77:37–44, 1999.

[65] M. Falcke, Y. Li, J.D. Lechleiter, and P. Camacho. Modeling the dependence of the period of intracellular Ca^{2+} waves on SERCA expression. *Biophys.J.*, 85:1474–1481, 2003.

[66] U. Fano. Ionization yield to radiation. ii. the fluctuation of the random number. *Phys. Rev.*, 72(1):26–29, 1947.

[67] K. Färber and H. Kettenmann. Functional role of calcium signals for microglial function. *Glia*, 54:656–665, 2006.

[68] A. Fatatis and J.T. Russell. Spontaneous changes in intracellular calcium concentration in type i astrocytes from rat cerebral cortex in primary culture. *Glia*, 5:95–104, 1992.

[69] C.J. Favre, J. Schrenzel, J. Jaquet, D.P. Lew, and K.-H. Krause. Highly supralinear feedback inhibition of Ca^{2+} uptake by the Ca^{2+} load of intracellular stores. *J.Biol.Chem.*, 271(25):14925–14930, 1996.

[70] Federal Ministry of Education and Research. Systems biology, 2002.

[71] T. Fellin and G. Carmignoto. Neurone-to-astrocyte signalling in the brain represents a distinct multifunctional unit. *J. Physiol*, 559:3–15, 2004.

[72] T.A. Fiacco and K.D. McCarthy. Astrocyte calcium elevations: Properties, propagation, and effects on brain signaling. *Glia*, 54:676–690, 2006.

[73] E.A. Finch, T.J. Turner, and S.M. Goldin. Calcium as coagonist of Inositol 1,4,5-trisphosphate-induced calcium release. *Science*, 252:443–446, 1991.

[74] R. Fitzhugh. Impulses and physiological states in theoretical models of nerve membrane. *Biophys. J.*, 1:445–466, 1961.

[75] J.K. Foskett, C. White, K.H. Cheung, and D.O. Mak. Inosistol trisphosphate receptor calcium release. *Physiol. Rev.*, 87:593–658, 2007.

[76] R. Foyouzi-Youssefi, S. Arnaudeau, Ch. Borner, W.L. Kelley, J. Tschopp, D.P. Lew, N. Demaurex, and K.-H. Krause. Bcl-2 decreases the free Ca^{2+} concentration within the endoplasmic reticulum. *Proc.Nat.Acad.Sci.USA*, 97(11):5723–5728, 2000.

[77] H.G. Fritz and R. Bauer. Traumatic injury in the developing brain–effects of hypothermia. *Exp. Toxicol. Pathol.*, 96:91–102, 2004.

[78] I. Fujino, N. Yamada, A. Miyawaki, M. Hasegawa, T. Furuichi, and K. Mikoshiba. Differential expression of type 2 and type 3 inositol 1,4,5-trisphosphate receptor mRNAs in various mouse tissues: in situ hybridization study. *Cell Tissue Res.*, 280:201–210, 1995.

[79] L. Gaohua and H. Kimura. A mathematical model of intracranial pressure dynamics for brain hypothermia treatment. *J. Theor. Biol.*, 238:882–900, 2006.

[80] O. Garaschuk, J. Linn, J. Eilers, and A. Konnerth. Large-scale oscillatory calcium waves in the immature cortex. *Nat. Neurosci.*, 3:452–459, 2003.

[81] C.W. Gardiner. *Handbook of Stochastic Methods*. Springer, Berlin, 1985.

[82] D.T: Gillepsie. Exact stochastic simulation of coupled chemical reactions. *J. Phys. Chem.*, 8:2340–2354, 1977.

[83] A. Goldbeter. *Biochemical Oscillations and Cellular Rhythms*. Cambridge University Press, Cambridge, 1996.

[84] A. Goldbeter, G. Dupont, and M.J. Berridge. Minimal model for signal induced Ca^{2+} oscillations and for their frequency encoding through protein phosphorylation. *Proc.Nat.Acad.Sci.USA*, 87:1461–1465, 1990.

[85] I. Goychuk and P. Hänggi. Stochastic resonance in ion channels characterized by information theory. *Phys.Rev.E*, 61:4272–4280, 1999.

[86] P.B. Guthrie, J. Knappenberger, M. Segal, M.V.L. Bennet, and S.B. Kater. ATP released from astrocytes mediates glial calcium waves. *J.Neurosci.*, 19:520–528, 1999.

[87] P. Haddad, J.C. Cabrillac, L. Musallam, and P.M. Huet. Changes in intracellular calcium induced by acute hypothermia in parenchymal, endothelial, and kupffer cells of the rat liver. *Cryobiology*, 39:69–79, 1999.

[88] R.E. Hagar, A.D. Burgstahler, M.H. Nthanson, and B.E. Ehrlich. Type III $InsP_3$ receptor channel stays open in the presence of increased calcium. *Nature*, 396:81–84, 1998.

[89] H. Haken. *Synergetics*. Springer, Berlin, 1983.

[90] P. Hänggi, P. Talkner, and M. Borkovec. Reaction-rate theory: fifty years after kramers. *Rev. Mod. Phys.*, 62:251–342, 1990.

[91] J.W.M. Heemskerk, G.M. Willems, M.B. Rook, and S.O. Sage. Ragged spiking of free calcium in ADP-stimulated human platelets: regulation of puff-like calcium signals in vitro and ex vivo. *J.Physiol.*, 535(3):625–635, 2001.

[92] R. Heinrich and S. Schuster. *The Regulation of Cellular Systems.* Chapman and Hall, 1996.

[93] H. Hirase, L. Qian, P. Bartho, and G. Buzsaki. Calcium dynamics of cortical astrocytic networks in vivo. *PLoS Biol.*, 2:E96, 2004.

[94] M. Iino. Effects of adenine nucleotides on inositol 1,4,5-trisphosphate-induced Ca^{2+} release in vascular smooth muscle cells. *J.Gen.Physiol.*, 98:681–689, 1991.

[95] G. Inesi, M. Kurzmack, and D. Lewis. Kinetic and equilibrium characterization of an energy dependent enzyme and its partial reactions. *Methods Enzymol.*, 157:154–190, 1988.

[96] B. Innocenti, V. Parpura, and P.G. Haydon. Imaging extracellular waves of glutamate during calcium signaling in cultured astrocytes. *J. Neurosci.*, 20:1800–1808, 2000.

[97] R.C. Janzer. The blood-brain barrier: The cellular basis. *J. Inherit. Metab. Dis.*, 16:639–647, 1993.

[98] S.K. Joseph, H.L. Rice, and J.R. Williamson. The effect of external calcium and pH on inositol trisphosphate-mediated calcium release from cerebellum microsomla fractions. *Biochem. J.*, 258:261–265, 1989.

[99] P. Jung and G. Mayer-Kress. Spatiotemporal stochastic resonance in excitable media. *Physical Review Letters*, 74(11):2130–2133, 1995.

[100] P. Jung and J.W. Shuai. Optimal sizes of ion channel clusters. *Europhys.Lett.*, 56(1):29–35, 2001.

[101] Jr. J.W. Putney˙ Recent breakthroughs in the molecular mechanism of capacitative calcium entry (with thoughts on how we got here). *Cell Calcium.*, 42:103–110, 2007.

[102] J. Karpen and T. Rich. Resolution of camp signals in three-dimensional microdomains using novel, real-time sensors. *Proc. West Pharmacol. Soc.*, 47, 2003.

[103] J.P. Keener and J. Sneyd. *Mathematical Physiology.* Springer, New York, 1998.

[104] J.S. Kim and J.H. Southard. Alteration in cellular calcium and mitochondrial functions in the rat liver during cold preservation. *Transplantation*, 65:369–375, 1998.

[105] H. Kitano. Systems biology: A brief overview. *Science*, 295:1662–1664, 2002.

[106] R.G. Knowles, M. Palacios, R.M. Palmer, and S. Moncada. Formation of nitric oxide from l-arginine in the central nervous system: a transduction mechanism for stimulation of the soluble guanylate cyclase. *PNAS*, 86:5159–5162, 1989.

[107] C. Koch. *Methods of Neural Modeling - from Ions to Networks*. MIT Press, 1998.

[108] H.A. Kramer. Brownian motion in a field of force and the diffusion modek of chemical reactions. *Physica*, 7:284, 1940.

[109] M. Kukley, E. Capetillo-Zarate, and D. Dietrich. Vesicular glutamate release from axons in white matter. *Nature Neurosci.*, 10(3):311–320, 2007.

[110] Y. Kuramoto. *Chemical Oscillations, Waves and turbulence*. Dover Publications, New York, 1988.

[111] Y. Kurokawa, K. Inaba H. Kano, and T. Uede. Brain hypothermia relieves severe brain swelling following acute major cerebral artery occlusion. *Neurol. Med. Chir. (Tokyo)*, 41:53–61, 2001.

[112] A.M. Landeira-Fernandez, J.M. Morrissette, J.M. Blank, and B.A. Block. Temperature dependence of the Ca^{2+}-atpase (serca2) in the ventricles of tuna and mackerel. *Am. J. Physiol. Regul. Integ. Comp. Physiol.*, 286:R398–R404, 2004.

[113] A.D. Laskey, B.J. Roth, P.B. Simpson, and J.T. Russell. Images of Ca^{2+} flux in astrocytes: evidence for spatially distinct sites of Ca^{2+} release and uptake. *1998*, 23:423–432, Cell Calcium.

[114] A.M. Lawrie, E.C. Toescu, and D.V. Gallacher. Two different spatiotemporal patterns for Ca^{2+} oscillations in pancreatic acinar cells: evidence for a role of protein kinase C in Ins(1,4,5)P_3-mediated Ca^{2+} signalling. *Cell Calcium*, 14:698–710, 1993.

[115] A. LeBeau, D.I. Yule, G.E. Groblewski, and J. Sneyd. Agonist-dependent phosphorylation of the inositol 1,4,5-trisphosphate receptor - a possible mechanism for agonist-specific calcium oscillations in pancreatic acinar cells. *J.Gen.Physiol.*, 113:851–871, 1999.

[116] J.D. Lechleiter, S. Girard, D. Clapham, and E. Peralta. Subcellular patterns of calcium release determined by g-protein-specific residues of muscarinic receptors. *Nature*, 350:505–508, 1991.

[117] X. Leinekugel, I. Medina, Y.B. Ari, and R. Khazipov. Calcium oscillations mediated by the synergistic excitatory actions of gaba(a) and nmda receptors in the neonatal hippocampus. *Neuron*, 18:243–255, 1997.

[118] J. Leroy, A. Abi-Gerges, V.O. Nikolaev, W. Richter, P. Lechene, J.Mazet, M. Conti, R. Fischmeister, and Gregoire Vandecasteele. Spatiotemporal dynamics of beta-adrenergic camp signals and l-type Ca^{2+} channels regulation in adult rat ventricular myocytes: Role of phophodiesterase. *Circ. Res.*, 102:1091–1100, 2008.

[119] N. Li, J.Y. Sul, and P.G. Haydon. A calcium-induced calcium influx factor, nitric oxide, modulates the refilling of calcium stores in astrocytes. *J. Neurosci.*, 23:10302–10310, 2003.

[120] W. Li, J. Llopis, M. Whitney, M. Zlokarnik, and R.Y. Tsien. Cell-permeant caged $InsP_3$ ester shows that Ca^{2+} spike frequency can optimize gene expression. *Nature*, 392:936–941, 1998.

[121] B. Lindner. Superposition of many independent spike trains is generally not a poisson process. *PRE*, 73:022901–1–022901–4, 2006.

[122] B. Lindner, J. Garcia-Ojalvo, A. Neimann, and L. Schimansky-Geier. Effects of noise in excitable systems. *Physics Reports*, 392(6):321–424, 2004.

[123] B. Lindner, A. Longtin, and Adi Bulsara. Analytical expression for rate and cv of a type i neuron driven by white gaussian noise. *Neural Comp.*, 15:1761–1788, 2003.

[124] B. Lindner and L. Schimansky-Geier. Analytical approach to the stochastic fitzhugh-nagumo system and coherence resonance. *Phys. Rev. E*, 60:7270–7276, 1999.

[125] P. Lipp, D. Thomas, M.J. Berridge, and M.D. Bootman. Nuclear calcium signalling by individual cytoplasmic calcium puffs. *The EMBO Journal*, 16(23):7166–7173, 1997.

[126] V. Lukyanenko and S. Györke. Ca^{2+} sparks and Ca^{2+} waves in saponin-permeabilized rat ventricular myocytes. *J.Physiol.*, 521(3):575–585, 1999.

[127] S. Lyon and H. Kettenmann. Oligodendrocytes and microglia are selectively vulnerable to combined hypoxia and hypoglycemia injury in vitro. *J. Cereb. Blood Flow Metab*, 18:521–530, 1998.

[128] J. Lytton, M. Westlin, S.E. Burk, G.E. Shull, and D.H. MacLennan. Functional comparisons between isoforms of the sarcoplasmic or endoplasmic reticulum family of calcium pumps. *J.Biol.Chem.*, 267(20):14483–14489, 1992.

[129] N. Maeda, T. Kawasaki, S. Nakade, N. Yokota, T. Taguchi, M. Kasai, and K. Mikoshiba. Structural and functional characterization of inositol 1,4,5-trisphosphate receptor channel from mouse cerebellum. *J.Biol.Chem.*, 266:1109–1116, 1991.

[130] D.D. Mak, S. McBride, and J.K. Foskett. Inositol 1,4,5-tris-phosphate activation of inositol tris-phosphate receptor Ca^{2+} channel by ligand tuning of Ca^{2+} inhibition. *Proc.Nat.Acad.Sci.USA*, 95:15821–15825, 1998.

[131] D.D. Mak, S. McBride, and J.K. Foskett. ATP regulation of type 1 inositol 1,4,5-trisphosphatereceptor channel gating by allosteric tuning of Ca^{2+} activation. *J.Biol.Chem.*, 274(32):22231–22237, 1999.

[132] D.D. Mak, S. McBride, and J.K. Foskett. Spontaneous channel activity of the inositol 1,4,5-trisphosphate ($InsP_3$) receptor ($InsP_3R$). application of allosteric modeling to calcium and $InsP_3$ regulation of the $InsP_3R$ single-channel gating. *J.Gen.Physiol.*, 122:583–603, 2003.

[133] T.J. Manning and H. Sontheimer. Spontaneous intracellular calcium oscillations in cortical astrocytes from a patient with intractable childhood epilepsy (rasmussen's encephalitis). *Glia*, 21:332–337, 1997.

[134] A.R. Maranto. Primary structure, ligand binding, and localization of the human type 3 inositol 1,4,5-trisphosphate receptor expressed in intestinal epithelium. *J.Biol.Chem.*, 269:1222–1230, 1994.

[135] J.S. Marchant, N. Callamaras, and I. Parker. Initiation of IP_3-mediated Ca^{2+} waves in Xenopus oocytes. *The EMBO J.*, 18(19):5285–5299, 1999.

[136] J.S. Marchant and I. Parker. Role of elementary Ca^{2+} puffs in generating repetitive Ca^{2+} oscillations. *The EMBO Journal*, 20(1 & 2):65–76, 2001.

[137] B. Marchetti. Cross-talk signals in the cns: role of neurotrophic and hormonal factors, adhesion molecules and intercellular signaling agents in luteinizing hormone-releasing hormone (lhrh)-astrogial interactive network. *Front Biosci.*, 2:88–125, 1997.

[138] A. Martinez-Hernandez, K.P. Bell, and M.D. Norenberg. Glutamine synthetase: glial localization in brain. *Science*, 195:1356–1358, 1977.

[139] V. Matyash, V. Filippov, K. Mohrhagen, and H. Kettenmann. Nitric oxide signals parallel fiber activity to bergmann glial cells in the mouse cerebellar slice. *Mol. Cell. Neurosci.*, 18:664–670, 2001.

[140] J.F. McAnulty, M.S. Ametani, J.H. Southard, and F.O. Belzer. Effect of hypothermia on intracellular calcium in rabbit renal tubules suspended in uw-gluconate preservation solution. *Cryobiology*, 33:196–204, 1996.

[141] L. Meinhold and L. Schimansky-Geier. Analytic description of stochastic calcium-signaling periodicity. *Phys.Rev.E*, 66:050901–1–4, 2002.

[142] J. Meldolesi and T. Pozzan. The endoplasmic reticulum Ca^{2+} store: a view from the lumen. *Trends in Biochemical Sciences*, 23:10–14, 1998.

[143] T. Meyer and L. Stryer. Transient calcium release induced by succesive increments of inositol 1,4,5-trisphosphate. *Proc.Nat.Acad.Sci.USA*, 87:3841–3845, 1990.

[144] M. Michalak, R.E. Milner, K. Burns, and M. Opas. Calreticulin. *Biochem.J.*, 285:681–692, 1992.

[145] T. Michikawa, H. Hamanaka, H. Otsu, A. Yamamoto, A. Miyawaki, T. Furuichi, Y. Tashiro, and K. Mikoshiba. Transmembrane topology and sites of n-glycosylation of Inositol 1,4,5-trisphosphate receptor. *J. Biol. Chem.*, 269:9184–9189, 1994.

[146] J.W. Middleton, M.J. Chacron, B. Lindner, and A. Longtin. Firing statistics of a neuron model driven by long-range correlated noise. *Physical Review E (Statistical, Nonlinear, and Soft Matter Physics)*, 68:021920, 2003.

[147] G.A. Mignery and T.C. Südhof. The ligand binding site and transduction mechanism in the inositol 1,4,5-trisphosphate receptor. *EMBO J.*, 9:3893–3898, 1990.

[148] G.A. Mignery, T.C. Südhof, K. Takei, and P. DeCamilli. Putative receptor for inositol 1,4,5-trisphosphate similar to ryanodine receptor. *Nature*, 342:192–195, 1989.

[149] K. Mikoshiba. Inositol 1,4,5-trisphosphate receptor. *Trends in Pharmacolical Sciences*, 14(3):86–89, 1993.

[150] L. Missiaen, J.B. Parys, I. Sienaert, K. Maes, K. Kunzelmann, M. Takabashi, K. Tanzawa, and H. DeSmedt. Functional properties of the type-3 $InsP_3$ receptor in 16HBE140-bronchial mucosal cells. *J. Biol. Chem.*, 273(15):8983–8986, 1998.

[151] T. Miyakawa, A. Maeda, T. Yamazawa, K. Hirose, T. Kurosaki, and M. Iino. Encoding of Ca^{2+} signals by differential expression of IP_3 receptor subtypes. *EMBO J.*, 18(5):1303–1308, 1999.

[152] A. Miyawaki, J. Llopis, R. Heim, J.M. McCaffery, J.A. Adams, M. Ikura, and R. Tsien. Fluorescent indicators for Ca^{2+} based on green fluorescent proteins and calmodulin. *Nature*, 388:882–887, 1997.

[153] I.I. Moraru, E.J. Kaftan, B.E. Ehrlich, and J. Watras. Regulation of type 1 Inositol 1,4,5-trisphosphate-gated calcium channels by $InsP_3$ and calcium. *J.Gen.Physiol.*, 113:837–849, 1999.

[154] S.J. Mulligan and B.A. MacVicar. Calcium transients in astrocyte endfeet cause cerebrovascular constrictions. *Nature*, 431:195–199, 2004.

[155] B. Naundorf, F. Wolf, and M. Volgushev. Unique features of action potentials in cortical neurons. *Nature*, 440:1060–1063, 2006.

[156] W.J. Nett, S.H. Oloff, and K.D. McCarthy. Hippocampal astrocytes in situ exhibit calcium oscillations that occur independent of neuronal activity. *J. Neurophysiol.*, 87:528–537, 2002.

[157] C.L. Newton, G.A. Mignery, and T.C. Südhof. Co-expression in vertebrat tissue and cell lines of multiple inositol 1,4,5-trisphosphate ($IinsP_3$) recptors with distinct affinities for $IinsP_3$. *J. Biol. Chem.*, 269:28613–28619, 1994.

[158] G. Nicolis and I. Priogine. *Exploring Complexity.* W.H. Freeman and Company, New York, 1989.

[159] A. Nishiyama, M. Yu, J.A. Drazba, and V.K. Tuohy. Normal and reactive ng2+ glial cells are distinct from resting and activated microglia. *J. Neurosci. Res.*, 48(4):299–312, 1997.

[160] B.P. Ölveczky and A.S. Verkman. Monte carlo analysis of obstructed diffusion in three dimensions: Application to molecular diffusion in organelles. *Biophys.J.*, 74:2722–2730, 1998.

[161] S. Orrenius, B. Zhivotovsky, and P. Nicotera. Regulation of cell death: the calcium-apoptosis link. *Nat. Rev. Mol. Cell Biol.*, 4:552–565, 2003.

[162] T.S. Otis and M.V. Sofroniew. Glia get excited. *Nature Neurosci.*, 11(4):379–380, 2008.

[163] M. Özisik. *Heat conduction*. John Wiley and sons, New York, 1993.

[164] H.L. Pahl. Signal transduction from the endoplasmic reticulum to the cell nucleus. *Physiol.Rev.*, 79:683–701, 1999.

[165] A. Panatier, D.T. Theodosis, and J.P. Mothet. Glia-derived d-serine controls nmda receptor activity and synaptic memory. *Cell*, 125:775–784, 2006.

[166] A.B. Parekh and R. Penner. Store depletion and calcium influx. *Physiol.Rev.*, 77:901–903, 1997.

[167] I. Parker, J. Choi, and Y. Yao. Elementary events of $InsP_3$-induced Ca^{2+} liberation in Xenopus oocytes: hot spots, puffs and blips. *Cell Calcium*, 20(2):105–121, 1996.

[168] I. Parker and I. Ivorra. Inhibition by Ca^{2+} of inositol-trisphosphate-mediated Ca^{2+} liberation: A possible mechanism for oscillatory Ca^{2+} release. *Proc.Nat.Acad.Sci.USA*, 87:260–264, 1990.

[169] I. Parker and Y. Yao. *Calcium puffs in Xenopus oocytes*. in Calcium Waves, Gradients and Oscillations, Ciba F. Symposium. Wiley, Chichester, England, 1995.

[170] H.R. Parri and V. Crunelli. Pacemaker calcium oscillations in thalamic astrocytes in situ. *Neuroreport*, 12:3897–3900, 2001.

[171] H.R. Parri and V. Crunelli. Astrocytes, spontaneity, and the developing thalamus. *J. Physiol. Paris*, 96:221–230, 2002.

[172] H.R. Parri and V. Crunelli. The role of Ca^{2+} in the generation of spontaneous astrocytic Ca^{2+} oscillations. *Neuroscience*, 50:979–992, 2003.

[173] H.R. Parri, T.M. Gould, and V. Crunelli. Spontaneous astrocytic Ca^{2+} oscillations in situ drive nmdar-mediated neuronal excitation. *Nat. Neurosci.*, 4:803–812, 2001.

[174] J.B. Parys, L. Missiaen, H. DeSmedt, and R. Casteels. Loading dependence of inositol 1,4,5-trisphosphate-induced calcium release in the clonal cell line a7r5. *J.Biol.Chem.*, 268:25206–25212, 1993.

[175] L. Pasti, T. Pozzan, and G. Carmignoto. Long-lasting changes of calcium oscillations in astrocytes. a new form of glutamate-mediated plasticity. *J. Biol. Chem.*, 270:15203–15210, 1995.

[176] L. Pasti, A. Volterra, T. Pozzan, and G.Carmignoto. Intracellular calcium oscillations in astrocytes: a highly plastic, bidirectional form of communication between neurons and astrocytes in situ. *J. Neurosci.*, 17:7817–7830, 1997.

[177] L. Pasti, M. Zonta, S. Vicini, and G. Carmignoto. Cytosolic calcium oscillations in astrocytes may regulate exocytotic release of glutamate. *J. Neurosci.*, 21:477–487, 2001.

[178] S. Patel, S.K. Joseph, and A.P. Thomas. Molecular properties of inositol 1,4,5-trisphosphate receptors. *Cell Calcium*, 25(3):247–264, 1999.

[179] L. Pellerin, G. Pellegri, and P.J. Magistretti. Evidence supporting the existence of an activity-dependent astrocyteneuron lactate shuttle. *Dev. Neurosci.*, 20:291–299, 1998.

[180] V.H. Perry and S. Gordan. Macrophages and microglia in the nervous system. *Trends in Neurosci.*, 11:273–277, 1988.

[181] O. Peters, C.G. Schipke, Y. Hashimoto, and H. Kettenmann. Different mechanisms promote astrocyte Ca^{2+} waves and spreading depression in the mouse neocortex. *J. Neurosci.*, 23:9888–9896, 2003.

[182] Arkady S. Pikovsky and Jurgen Kurths. Coherence resonance in a noise-driven excitable system. *Phys.Rev.Lett.*, 78(5):775–778, 1997.

[183] S. Ponce-Dawson, J. Keizer, and J. Pearson. Fire-diffuse-fire model of dynamics of intracellular calcium waves. *Proc.Nat.Acad.Sci.USA*, 96:6060–6063, 1999.

[184] J.W. Putney and G.S.J. Bird. The inositolphosphate-calcium signaling system in nonexcitable cells. *Endocrine Reviews*, 14(5):610–631, 1993.

[185] Q.-X-Jiang, E.C. Thrower, D.E. Chester, B.E. Ehrlich, and F.J. Sigworth. Three-dimensional structure of the type 1 insositol 1,4,5-trisphosphate receptor at 24 a resolution. *EMBO J.*, 21:3575–3581, 2002.

[186] G. Queiroz, P.J. Gebicke-Haerter, A. Schobert, and K. Starke. Release of atp from cultured rat astrocytes elicited by glutamate receptor activation. *Neuroscience*, 78:1203–1208, 1997.

[187] A.A. Rabinstein. Treatment of cerebral edema. *Neurolo.*, 12:59–73, 2006.

[188] T.U. Rahman, A. Skupin, M. Falcke, and C.W. Taylor. Clustering of IP_3 receptors by IP_3 retunes their regulation by IP_3 and Ca^{2+}. *accepted at Nature*, 2008.

[189] B.R. Ransom and H. Sontheimer. The neurophysiology of glial cells. *J. Clin. Neurophysiol.*, 9, 1992.

[190] J. Rengifo, R. Rosales, A. González, H. Cheng, M.D. Stern, and E. Ríos. Intracellular Ca^{2+} release as irreversible markov process. *Biophys.J.*, 83:2511–2521, 2002.

[191] R. Rizzuto, P. Bernardi, and T. Pozzan. Mitochondria as all-round players of the calcium game. *J.Physiol.*, 529(1):37–47, 2000.

[192] H.L. Roderick, M.J. Berridge, and M.D. Bootman. *Understanding Calcium Dynamics - Experiments and Theory*, volume 623 of *Lecture Notes in Physics*, chapter 2, pages 17–35. Springer, Berlin Heidelberg New York, 2003.

[193] T.A. Rooney, S.K. Joseph, C. Queen, and A.P. Thomas. Cyclic GMP induces oscillatory calcium signals in rat hepatocytes. *J.Biol.Chem.*, 271:19817–19825, 1996.

[194] T.A. Rooney, E.J. Sass, and A.P. Thomas. Characterization of cytosolic calcium oscillations induced by phenylephrine and vasopressin in single fura-2-loaded hepatocytes. *J.Biol.Chem.*, 264:17131–17141, 1989.

[195] S. Rüdiger, J.W. Shuai, W. Huisinga, C. Nagaiah, G. Warnecke, and M. Falcke. Hybrid stochastic and deterministic simulations of calcium blips. *Biophys. J.*, 93:1847–1857, 2007.

[196] H. Sakaguchi, S. Shinomoto, and Y. Kuramoto. Phase transitions and their bifurcation analysis in a large population of activ rotators with mean-field coupling. *Progress of Theoretical Physics*, 79:600, 1988.

[197] H.J. Schatzmann. The calcium pump of the surface membrane and of the sarcoplasmic reticulum. *Annu.Rev.Physiol.*, 51:473–485, 1989.

[198] C.G. Schipke, A. Heidemann, Alexander Skupin, O. Peters, M. Falcke, and H. Kettenmann. Temperature and nitric oxide controle spontaneous calcium transients in astrocytes. *Cell Calcium*, 43:285–295, 2008.

[199] C.G. Schipke and H. Kettenmann. Astrocyte responses to neuronal activity. *Glia*, 47:226–232, 2004.

[200] F. Schliess, N. Foster, R. Reinehr, and D. Haussinger. Hypoosmotic swelling increases protein tyrosine nitration in cultured rat astrocytes. *Glia*, 47:21–29, 2004.

[201] E. Schrödinger. *What is life?* Cambridge University Press, Cambridge, 1944.

[202] T. Schulmeister and H.P. Herzel. Chaos in forced selkov systems. *ZAMM*, 66:375, 1986.

[203] S. Schuster, M. Marhl, and T. Höfer. Modelling of simple and complex calcium oscillations. *Eur.J.Biochem.*, 269:1333–1355, 2001.

[204] J. Segieth, L. Fowler, P.S. Whitton, and B. Pearce. Arginine release from rat cerebellar astrocytes: autocrine roles for glutamate and nitric oxide? *Neurosci. Lett.*, 372:262–265, 2004.

[205] E.E. Selkov. Self-oscillations in glycolysis. a simple kinetic model. *Europ. J. Biochem.*, 4:79, 1968.

[206] C.E. Shannon. A mathematical theory of communication. *Bell Syst. Tech. J.*, 27:379–423, 1948.

[207] S. Shinomoto and Y. Kuramoto. Cooperative phenomena in two-dimensional active rotator systems. *Prog. Theo. Phys.*, 75:1319, 1986.

[208] S. Shinomoto and Y. Kuramoto. Phase transition in aktive rotator system. *Prog. Theo. Phys.*, 75:1105, 1986.

[209] A.D. Short and C.W. Taylor. Parathyroid hormone controls the size of the intracellular Ca^{2+} stores available to receptors linked to inositol trisphosphate formation. *J.Biol.Chem.*, 275(3):1807–1813, 2000.

[210] A.D. Short, G.P. Winston, and C.W. Taylor. Different receptors use inositol trisphosphate to mobilize Ca^{2+} from different intracellular pools. *Biochem.J.*, 351:683–686, 2000.

[211] J. Shuai, H.J. Rose, and I. Parker. The number and spatial distribution of IP_3 receptors underlying calcium puffs in Xenopus oocytes. *Biophys. J.*, 91:4033–4044, 2006.

[212] J.W. Shuai and P. Jung. Optimal intracellular calcium signalling. *Phys.Rev.Lett.*, 88(6):068102–1–4, 2002.

[213] J.W. Shuai and P. Jung. Stochastic properties of Ca^{2+} release of inositol 1,4,5-trisphosphate receptor clusters. *Biophys.J.*, 83(1):87–97, 2002.

[214] J.W. Shuai and P. Jung. Optimal ion channel clustering for intracellular calcium signaling. *Proc.Nat.Acad.Sci.USA*, 100(2):506–510, 2003.

[215] M. Simard and M. Nedergaard. The neurobiology of glia in the context of water and ion homeostasis. *Neuroscience*, 129:877–896, 2004.

[216] A. Skupin and M. Falcke. Greens matrix method for the concentration dynamics of intracellular Ca^{2+} release. *submitted*, 2008.

[217] A. Skupin and M. Falcke. The influence of IP_3R clustering in Ca^{2+} signaling. *Gen. Inform.*, in press, 2008.

[218] A. Skupin and M. Falcke. Statistical properties and information content of Ca^{2+} oscillations. *Gen. Inform.*, 19:69–79, 2008.

[219] A. Skupin, H. Kettenmann, U. Winkler, M. Wartenberg, H. Sauer, S.C. Tovey, C.W. Taylor, and M. Falcke. How does intracellular Ca^{2+} oscillate: By chance or by the clock? *Biophys. J.*, 94:2404–2411, 2008.

[220] G.D. Smith, L. Dai, R.M. Miura, and A. Sherman. Asymptotic analysis of buffered calcium diffusion near a point source. *SIAM J.Appl.Math.*, 61(5):1816–1838, 2001.

[221] G.D. Smith, J. Keizer, M.D. Stern, W.J. Lederer, and H. Cheng. A simple numerical model of calcium spark formation and detection in cardiac myocytes. *Biophys.J.*, 75:15–32, 1998.

[222] I.F. Smith, S.M. Witgen, and I. Parker. Localization of puff sites adjacent to the plasma membrane: Functional and spatial characterization of Ca^{2+} signaling in SH-SY5Y cells utiliting membrane-permeant IP_3. *Cell Calcium*, page in press, 2008.

[223] J. Sneyd, P.D. Dale, and A. Duffy. Traveling waves in buffered systems: Applications to calcium waves. *SIAM J. on Applied Mathematics*, 58:1178–1192, 1998.

[224] J. Sneyd, M. Falcke, J.-F. Dufour, and C. Fox. Mathematical models of the inositol trisphosphate receptor. *Progress in Biophysics and Molecular Biology*, 85:121–140, 2004.

[225] J. Sneyd, S. Girard, and D. Clapham. Calcium wave propagation by calcium induced calcium release: An unusual excitable system. *Bull.Math.Biol.*, 55:315–344, 1993.

[226] J. Sneyd, J. Keizer, and M.J. Sanderson. Mechanisms of calcium oscillations and waves: a quantitative analysis. *FASEB Journal*, 9:1463–1472, 1995.

[227] J. Sneyd and J. Sherrat. On the propagation of calcium waves in an inhomogeneous medium. *SIAM J.Appl.Math.*, 57(1):73–94, 1997.

[228] J. Sneyd, K. Tsaneva-Atanasova, J.I.E. Bruce, S. Straub, D.V. Giovannucci, and D.I. Yule. A model of calcium waves in pancreatic and parotid acinar cells. *Biophys.J.*, 85:1392–1405, 2003.

[229] J. Sneyd, M. Wilkins, A. Strahonja, and M. Sanderson. Calcium waves and oscillations driven by an intercellular gradient of inositol (1,4,5)-trisphosphate. *Biophys.Chem.*, 72:101–109, 1998.

[230] C.E. Stout, J.L. Constantin, C.C.G. Naus, and A.C. Charles. Intercellular calcium signaling in astrocytes via ATP release through connexin hemichannels. *J.Biol.Chem.*, 277(12):10482–10488, 2002.

[231] C.E. Stout, J.L Costantin, C.C. Naus, and A.C. Charles. Intercellular calcium signaling in astrocytes via atp release through connexin hemichannels. *J. Biol. Chem.*, 277:10482–10488, 2002.

[232] R.L. Stratonovich. *Topics in the Theory of Random Noise*. Gordan and Breach, New York & London, 1963.

[233] S.H. Strogatz. *Nonlinear Dynamics and Chaos*. Westview, 2000.

[234] W. Suhara, M. Kobayashi, H. Sagara, K. Hamadad, Touichiro Goto, I. Fujimoto, K. Torimitsu, and K. Mikoshiba. Visualization of inositol 1,4,5-trisphosphate receptor by atomic force microscopy. *Neuroscience Letters*, 391:102–107, 2006.

[235] J.E. Swatton, S.A. Morris, T.J. Cardy, and C.W. Taylor. Type 3 inositol trisphosphate receptors in rinm5f cells are biphasically regulated by cytosolic Ca^{2+} and mediate quantal Ca^{2+} mobilization. *Biochem.J.*, 344:55–60, 1999.

[236] J.E. Swatton and C.W. Taylor. Fast biphasic regulation of type 3 inositol trisphosphate receptors by cytosolic calcium. *J.Biol.Chem.*, 277:17571–17579, 2002.

[237] S. Swillens, P. Champeil, L. Combettes, and G. Dupont. Stochastic simulation of a single inositol 1,4,5-trisphoasphate-sensitive Ca^{2+} channel reveals repetitive openings during blip-like Ca^{2+} transients. *Cell Calcium*, 23(5):291–302, 1998.

[238] S. Swillens, G. Dupont, and P. Champeil. From calcium blips to calcium puffs: Theoretical analysis of the requirements for interchannel communication. *Proc.Nat.Acad.Sci.USA*, 96(24):13750–13755, 1999.

[239] Y. Tang and H.G. Othmer. Simplification and analysis of models of calcium dynamics based on IP_3-sensitive calcium channel kinetics. *Biophys.J.*, 70:246–263, 1996.

[240] A. Tashiro, J. Goldberg, and R. Yuste. Calcium oscillations in neocortical astrocytes under epileptiform conditions. *J. Neurobiol.*, 50:45–54, 2002.

[241] P.A. Tass. Effectiv desynchronization with bipolar double-pulse stimulation. *Phys. Rev. E*, 66:36226, 2002.

[242] P.A. Tass. Effectiv desynchronizing with a stimulation technique based on soft phase resetting. *Europhys Lett.*, 57:164–170, 2002.

[243] P.A. Tass. Stochastic phase resetting of two coupled phase oscillators stimulated at different times. *Phys. Rev. E*, 67:51902, 2003.

[244] Y. Tateishi, M. Hattori, T. Nakayama, M. Iwai, H. Bannai, T. Nakamura, T. Michikawa, T. Inoue, and K. Mikoshiba. Cluster formation of inositol 1,4,5-trisphosphate receptor requires its transition to open state. *J.Biol.Chem.*, 280(8):6816–6822, 2004.

[245] C.W. Taylor. Inositol trisphosphate receptors: Ca^{2+}-modulated intracellular Ca^{2+} channels. *Biochimica and Biophysica Acta*, 1436:19–33, 1998.

[246] C.W. Taylor and A.J. Laude. IP_3 receptors and their regulation by calmodulin and cytosolic Ca^{2+}. *Cell Calcium*, 32(5-6):321–334, 2002.

[247] C.W. Taylor and J.E. Swatton. *Understanding Calcium Dynamics - Experiments and Theory*, volume 623 of *Lecture Notes in Physics*, chapter 1, pages 1–16. Springer, Berlin Heidelberg New York, 2003.

[248] D. Thomas, P. Lipp, M.J. Berridge, and M.D. Bootman. Hormone-evoked elementary Ca^{2+} signals are not stereotypic, but reflect activation of different size channel clusters and variable recruitment of channels within a cluster. *J.Biol.Chem.*, 273(42):27130–27136, 1998.

[249] R. Thul and M. Falcke. Release currents of IP_3 receptor channel clusters and concentration profiles. *Biophys.J.*, 86:2660–2673, 2004.

[250] R. Thul and M. Falcke. Stability of membrane bound reactions. *Phys.Rev.Lett.*, 93(18):188103–1–188103–4, 2004.

[251] R. Thul and M. Falcke. Frequency of elemental events of intracellular Ca^{2+} dynamics. *Phys.Rev.E*, 73:061923, 2006.

[252] Y. Timofeeva and S. Coombes. Wave bifurcation and propagation failure in a model of Ca^{2+} release. *J.Math.Biol.*, 2003. http://dx.doi.org/10.1007/s00285-003-0205-y.

[253] S.C. Tovey, P. de Smet, P. Lipp, K. W. Young, L. Missiaen, H. De Smedt, J.B. Parys, M.J. Berridge, J. Thuring, A. Holmes, and M.D. Bootman. Calcium puffs are generic $InsP_3$-activated elementary calcium signals and are downregulated by prolonged hormonal stimulation to inhibit cellular calcium responses. *J.Cell Science*, 114(22):3979–3989, 2001.

[254] S.C. Tovey, S.G. Deodes, E.J.A. Taylor, J.E. Church, and C.W. Tayor. Selective coupling of type 6 adenylyl cyclase with type 2 IP_3 receptors mediates direct sensitization of IP_3 receptors by camp. *J. Cell Biol.*, page in press, 2008.

[255] A. Van den Pol, S.M. Finkbeiner, and A.H. Cornell-Bell. Calcium excitability and oscillations in suprachiasmatic nucleus neurons and glia in vitro. *J.Neurosci.*, 12:2648–2664, 1992.

[256] N.G. van Kampen. *Stochastic processes in physics and chemistry.* North-Holland, Amsterdam, 2001.

[257] T. Verechtchaguina, L. Schimansky-Geier, and I. M. Sokolov. Spectra and waiting-time densities in firing resonant and nonresonant neurons. *Physical Review E (Statistical, Nonlinear, and Soft Matter Physics)*, 70(3):031916, 2004.

[258] T. Verechtchaguina, I. M. Sokolov, and L. Schimansky-Geier. First passage time densities in resonate-and-fire models. *Physical Review E (Statistical, Nonlinear, and Soft Matter Physics)*, 73:03108, 2004.

[259] A. Verkhratsky and H. Kettenmann. Calcium signalling in glial cells. *Trends Neurosci.*, 19:346–352, 1996.

[260] A. Verkhratsky, R.K. Orkand, and H. Kettenmann. Glial calcium: homeostasis and signaling function. *Physiol Rev.*, 78:99–141, 1998.

[261] A. Vernadakis. Glia-neuron intercommunications and synaptic plasticity. *Prog. Neurobiol.*, 49:185–214, 1996.

[262] A. Volterra, P. Magistretti, and P. Haydon, editors. *Tripartite synapses: Synaptic transmission with glia.* Oxford University Press, Oxford, 2002.

[263] J. Wagner and J. Keizer. Effects of rapid buffers on Ca^{2+} oscillations and Ca^{2+} diffusion. *Biophys.J.*, 67:447–456, 1994.

[264] S.S. Wang, A.A. Alousi, and S.H. Thompson. The lifetime of inosistol 1,4,5-triphosphate in single cells. *J. Gen. Physiol.*, 105:149–171, 1995.

[265] X. Wang, N. Lou, and Q. Xu. Astrocytic Ca^{2+} signaling evoked by sensory stimulation in vivo. *Nat. Neurosci.*, 9:816–823, 2006.

[266] Z. Wang, P.G. Haydon, and E.S. Yeung. Direct observation of calcium-independent ATP siganling in astrocytes. *Analytical Chemistry*, 72(9):2001–2007, 2001.

[267] N. Westergaard, U. Sonnewald, and A. Schousboe. Metabolic trafficking between neurons and astrocytes: the glutamate/glutamine cycle revisited. *Dev. Neurosci.*, 17:, 203–211, 1995.

[268] J.A. White, R. Klink, A. Alonso, and A.R. Kay. Noise from voltage-gated ion channels may influence neuronal dynamics in the entorhinal coretex. *J. Neurophysiol.*, 80(1):262–269, 1998.

[269] J.A. White, J.T. Rubinstein, and A.R. Kay. Channel noise in neurons. *Trends Neurosci.*, 23:131–137, 2000.

[270] T. Wilhelm. Analysis of structures causing instabilities. *Physical Review E (Statistical, Nonlinear, and Soft Matter Physics)*, 76:011911, 2007.

[271] D. Willoughby and D.M.F. Cooper. Organization and Ca^{2+} regulation of adenylyl cyclase in camp microdomains. *Physiol. Rev.*, 87(3):965–1010, 2007.

[272] B.S. Wilson, J.R. Pfeiffer, A.J. Smith, J.M. Oliver, J.A. Oberdorf, and R.J.H. Wojcikiewicz. Calcium-dependent clustering of inositol 1,4,5-trisphosphate receptors. *Mol.Biol.Cell*, 9:1465–1478, 1998.

[273] R.J.H. Wojcikiewicz. Type I, II and III inositol 1,4,5-trisphosphate receptors are unequally susceptible to down-regulation and are expressed in markedly different proportions in different cell types. *J.Biol.Chem.*, 270:11678–11683, 1995.

[274] R.O. Wong, A. Chernjavsky, S.J. Smith, and C.J. Shatz. Early functional neural networks in the developing retina. *Nature*, 374:716–718, 1995.

[275] N.M. Woods, K.S. Cuthbertson, and P.H. Cobbold. Repetitive transient rises in cytoplasmic free calcium in hormone-stimulated hepatocytes. *Nature*, 319:600–602, 1986.

[276] N.M. Woods, K.S. Cuthbertson, and P.H. Cobbold. Agonist-induced oscillations in cytoplasmic free calcium in single rat hepatocytes. *Cell Calcium*, 8:79–100, 1987.

[277] P.F. Worley, J.M. Barabant, J.M. Colvin, and S.H. Snyder. Inositol trisphosphate receptor localization in brain: variable stoichiometry wiht protein kinase C. *Nature*, 325:159–161, 1987.

[278] P.F. Worley, J.M. Barabant, S. Supattapone, V.S. Wilson, and S.H. Snyder. Characterization of inositol trisphosphate receptor binding in brain. *J.Biol.Chem.*, 262(5):12132–12136, 1987.

[279] Y. Yao and I. Parker. Quantal puffs of intracellular Ca^{2+} evoked by inositol trisphosphate in Xenopus oocytes. *J.Physiol.(Cambridge)*, 482(3):533–553, 1995.

[280] R. Yuste. Introduction: spontaneous activity in the developing central nervous system. *Semin. Cell. Dev. Biol.*, 4:1–8, 1997.

[281] R. Yuste, A. Peinado, and L.C. Katz. Neuronal domains in developing neocortex. *Science*, 257:665–669, 1992.

[282] Manuela Zaccolo and Tullio Pozzan. Discrete microdomains with high concentration of cAMP in stimulated rat neonatal cardiac myocytes. *Science*, 295(5560):1711–1715, 2002.

[283] M. Zonta, M.C. Angulo, and S. Gobbo. Neuron-to-astrocyte signaling is central to the dynamic control of brain microcirculation. *Nat. Neurosci.*, 6:43–50, 2003.

[284] M. Zonta, A. Sebelin, T. Pozzan, and G. Carmignoto. Glutamate-mediated cytosolic calcium oscillations regulate a pulsatile prostaglandin release from cultured rat astrocytes. *J. Physiol.*, 553:407–414, 2003.

[285] P.A. Zuk, M. Zhu, P. Ashjian, D.A. De Ugarte, and J.I. Huang. Human adipose tissue is a source of multipotent stem cells. *Mol.Biol.Cell*, 13:4279–4295, 2002.

[286] P.A. Zuk, M. Zhu, H.M. Mizuno, J. Huang, J.W. Futrell, A.J. Katz, H.P. Lorenz, and M.H. Hedrick. Multilineage cells from human adipose tissue: Implication for cell-based therapies. *Tissue Eng.*, 7:211–256, 2001.

[287] N.R. Zur and J.W. Deitmer. The role of metabotropic glutamate receptors for the generation of calcium oscillations in rat hippocampal astrocytes in situ. *Cereb Cortex*, 16:676–687, 2006.

List of publications

A. Skupin and M. Falcke.
From IP_3R cluster dynamics to cellular Ca^{2+} dynamics.
To appear in Chaos.

A. Skupin and M. Falcke.
A new approach in modeling Ca^{2+} in three dimensions.
In preparation.

T.U. Rahman, A. Skupin, M. Falcke and C.W. Taylor.
Clustering of IP_3 receptors by IP_3 retunes their regulation by IP_3 and Ca^{2+}.
Nature, 458, 655–659 (2009).

A. Skupin and M. Falcke.
The influence of IP_3R clustering in Ca^{2+} signaling.
Gen. Inform., 20, 24–34 (2009).

A. Skupin, H. Kettenmann, U. Winkler, M. Wartenberg, H. Sauer, S.C. Tovey, C.W. Taylor and M. Falcke.
How does intracellular Ca^{2+} oscillate: By chance or by the Clock?
Biophys. J., 94, 2404–2411 (2008).

A. Skupin and M. Falcke.
Statistical properties and information content of Ca^{2+} oscillations.
Gen. Inform., 19, 69–79, (2008).

C.G. Schipke*, A. Heidemann*, A. Skupin*, O. Peters, M. Falcke and H. Kettenmann.
Temperature and nitric oxide control spontaneous calcium transients in astrocytes.
Cell Calcium, 43, 285–295, (2008).

* contributed equally

Acknowledgement

An interdisciplinary study like this thesis is only possible with a bright support of many people. My gratefully thanks belong to my supervisor Martin Falcke, who has made this project possible by his huge engagement. He opened a lot of doors and was always a source of inspiration. I was often expressed by his deep understanding of nonlinear dynamics and its relation to Ca^{2+} dynamics. I really enjoyed our joint trip through experimental cell biology.

Without my experimental cooperation partners this investigation would not has been possible. I am very thankful to Prof Helmut Kettenmann for opening the doors of his laboratory for a theoretician like me and for the warmly affiliation of his group which has accepted me as a full member. I want to thank especially Carola Schipke and Antje Heidemann for teaching me biological experiments, their support and patient. From them I have learned to work experimentally and how to really think biologically. For cell preparation of glia cells I thank Irene Haupt.

The cooperation with Prof Colin W. Taylor and his group was and is of unpayable value. His deep understanding of molecular biology and especially of the IP_3R have deeply impressed me. For the data of HEK cells I thank Steve C. Tovey.

I thank Prof Maria Wartenberg for allowing me the experiments with PLA cells in her lab and her whole group for support. My special thanks belong to Stefanie Kunath for cell preparation and help with the IP_3R-antibody staining.

Moreover, I want to thank all former and actual members of the Mathematical Physiology group. The joint work on Green's functions stuff with the former diploma student Kajetan Bentele became a key element of the modeling part of this work. For this and the nice time we spend together I am indebted to him. The time I shared the office with Rüdiger Thul taught me the basics of modeling Ca^{2+} dynamics. Our combination of a guinea pig and a lab rat has bonded us. The BAPTA-EGTA discussions with Sten Rüdiger and our tea times has deepen my understanding of Ca^{2+} dynamics significantly.

For the support and fruitful discussions regarding the data analysis I am much obligated to Tatjana Engel and Prof Lutz Schimansky-Geier the experiences of them has helped me a lot.

I really would like to thank Prof Reinhardt Heinrich for installing such an inspir-

ing scientific environment in Berlin and hope that he would have enjoyed this work. In this context I would like to thank the *International Research Training Group* (IRTG) of the German Research Foundation (DFG) for being such a great platform for interdisciplinary research and system biological approaches and for financial support. I want to express my gratitude to Prof Hermann-Georg Holtzhütter and Prof Hans-Peter Herzel for their great effort for the IRTG after the abrupt and tragic death of Prof Heinrich.

Without the correction readers this thesis would not be as readable as it is. Therefore I thank Kevin Thurley, Rüdiger Thul, Kajetan Bentele, Udo Erdmann and Peter Bone.

Without the help and baby sitting of friends the thesis would not have achieved its current state. Thanks for that. My deep gratitude due my parents for their unconditional support during my study and all other times.

I thank my mare Lydia Müller for her love and for keeping my options open. She has appreciated my temporally absence of mind during writing this thesis. Meinen Töchtern Pina und Sira danke ich, dass sie mir die wesentlichen Dinge des Lebens immer wieder vor Augen führen.

Selbständigkeitserklärung

Hiermit erkläre ich, dass ich die vorliegende Arbeit selbstständig und nur mit den angegebenen Hilfsmitteln erstellt habe.

Alexander Skupin Berlin, den 12.1.2009